University of Wollongong

Research Online

University of Wollongong Thesis Collection 2017+

University of Wollongong Thesis Collections

2023

Engineering order-disorder transitions at the surface of topological insulators to manipulate electronic transport

Abuduliken Bake

University of Wollongong

Follow this and additional works at: https://ro.uow.edu.au/theses1

University of Wollongong

Copyright Warning

You may print or download ONE copy of this document for the purpose of your own research or study. The University does not authorise you to copy, communicate or otherwise make available electronically to any other person any copyright material contained on this site.

You are reminded of the following: This work is copyright. Apart from any use permitted under the Copyright Act 1968, no part of this work may be reproduced by any process, nor may any other exclusive right be exercised, without the permission of the author. Copyright owners are entitled to take legal action against persons who infringe their copyright. A reproduction of material that is protected by copyright may be a copyright infringement. A court may impose penalties and award damages in relation to offences and infringements relating to copyright material. Higher penalties may apply, and higher damages may be awarded, for offences and infringements involving the conversion of material into digital or electronic form.

Unless otherwise indicated, the views expressed in this thesis are those of the author and do not necessarily represent the views of the University of Wollongong.

Recommended Citation

Bake, Abuduliken, Engineering order-disorder transitions at the surface of topological insulators to manipulate electronic transport, Doctor of Philosophy thesis, School of Physics; Institute for Superconducting and Electronic Materials, University of Wollongong, 2023. https://ro.uow.edu.au/theses1/1726

Research Online is the open access institutional repository for the University of Wollongong. For further information contact the UOW Library: research-pubs@uow.edu.au

Engineering order-disorder transitions at the surface of topological insulators to manipulate electronic transport

Abuduliken Bake (Ablikim Baqi, ئابلىكىم باقى)

Supervisors:
Dr. David Cortie
Dr. Mitchell Nancarrow
Prof. Xiaolin Wang
Prof. Roger Lewis

This thesis is presented as part of the requirement for the conferral of the degree:
Doctor of Philosophy

University of Wollongong
School of Physics/ Institute for Superconducting and Electronic Materials (ISEM)

June 2023

Abstract

The theoretical discovery and experimental realisation of topological insulators, a new state of matter, has brought enormous research interest in the field of condensed matter physics. The novel and fascinating phenomenon in topological insulators (TIs) is the existence of gapless surface states (or edge states) while the bulk interior has an energy gap. These states are intriguing because they enable the transport of charges with no backscattering, which means less heat generation than ordinary conductors. The unique transport in TIs arises because of the spin-momentum locking of the surface states. Thus, the promising properties of the TIs have the potential for applications in low-energy quantum electronics and spintronics.

The research is motivated by a recent series of theories discussing the existence of amorphous topological materials and exploring the practical applications of the TIs in the semiconductor industry. The current research has extensively studied the feasibility of ion-beam patterning of a 3D strong topological insulator Sb_2Te_3. Subsequently, both in experiment and theory, this thesis proposes a novel method of engineering topological surface and edge states based on controlling the topological phase transition of Sb_2Te_3 with a focused ion-beam.

This thesis gives an introduction and overview of topological insulators in Chapter 1. Then, Chapter 2 reviews some of the essential and basic concepts and developments in recent years to help understand the field of topological insulators. It is worth mentioning that some of the experimental methodology described in Chapter 3 has been uniquely developed during the course of this thesis to characterize the Sb_2Te_3 or similar layered chalcogenide materials. This might provide guidelines to some of the researchers working in the field. The following chapters lay the foundation for transport measurements on prototype devices fabricated from Sb_2Te_3 single crystals.

Sb_2Te_3 is a 3D strong topological insulator and is a layered chalcogenide material. One discovery of the current work is that Sb_2Te_3 is sensitive to ion beam damage and easily can be amorphized with a certain fluence of ion-beam. Chapter 4 discusses minimising ion-beam-induced microstructural damage to characterise Sb_2Te_3 samples at the atomic

resolution scale. Naturally, ion-beams can also be used to introduce disorder in the crystals in a controlled manner. This provides an opportunity for patterning the surface of TIs for integrated circuitry applications. Thus, Chapter 5 explores the possibility of engineering the surface and edge states of TIs with an ion-beam by controlled surface disorder/amorphization. A particular focus is on the details of the experimental design and parameters and calculations to support the main results presented in Chapter 6. In Chapter 6, based on robust experimental and theoretical evidence, we concluded that Sb_2Te_3 topological states collapse upon amorphisation. Further, highly conducting surface and edge states emerge at the boundary of crystalline and amorphous Sb_2Te_3. This provides a viable avenue for engineering surface and edge states by controlling the phase transition of Sb_2Te_3.

Chapter 7 discusses the effect of magnetic ion-beam doping in Sb_2Te_3 and its magnetic properties. This possibly continues the work in previous Chapters 5 and 6 and provides some guidelines for magnetic ion beam patterning of TIs. The final Chapter concludes by summarizing the main findings and highlighting avenues for future work.

Acknowledgments

First and foremost, I would like to thank my supervisor and mentor Dr. David Cortie, for his unwavering support throughout my PhD studies. His knowledge, expertise, and passion made it possible for me to accomplish my research objectives and goals. David has been a great friend, talented supervisor, and caring mentor to me. His support and encouragement always motivated me, not only in my academic life but also in my personal life. His broad scientific knowledge, amiable character, and personality taught me much. I am grateful for his invaluable contribution to my career.

Dr. Mitchell Nancarrow, my co-supervisor and mentor, played an essential role in enabling me to complete my PhD research, especially my research work in the Electron Microscopy Centre at the University of Wollongong. I thank him for sharing his expert knowledge, ideas, and experiences in electron microscopy. I enjoyed many discussions with him and was inspired by his ideas in research. I am truly grateful for his support and supervision.

As my co-supervisors, Prof. Xiaolin Wang and Prof. Roger Lewis significantly contributed to the successful completion of my PhD research. I benefited from discussions with them about the underlying physics. Their suggestions and guidance shaped my research, allowing for continuous improvement. I am grateful for their kind support throughout my PhD studies.

I also would like to thank my AINSE co-supervisor Dr. Zeljko Pastuovic from ANSTO. He has been very helpful in planning projects and performing ion beam implantation experiments at the Centre for Accelerator Science (CAS) at the Australian Nuclear Science and Technology Organisation (ANSTO). I also want to thank Dr. Peter Evans from ANSTO for helping with the atomic layer deposition (ALD) coating of crystals and some ion implantation using the Metal Vapor Vacuum Arc (MEVVAA) implanter. I appreciate the help from my co-supervisor from within the ARC Centre for Excellence in Future Low Energy Electronics Technologies (FLEET) Dr. Julie Karel at Monash University, and her research team members, Dr. Golrokh Akhgar and Dr. Weiyao Zhao for providing thin films and crystal samples. Dr. Weiyao Zhao helped with the initial

transport measurements and data processing when he was at UOW. I also want to thank Dr. Jared Cole and Dr. Cong Son Ho from RMIT for supporting the theoretical calculations of the research in collaboration with my supervisor. I also would like to thank Dr. Peggy Zhang and Prof. Nagarajan Valanoor from UNSW for helping with the conducting atomic force microscopy (CAFM) measurements.

I want to thank the help and support from our research group members Dr. Sheik Md Kazi Nazrul Islam, Mr. Rezoan Rahman, and Mr. Caleb Stamper. It was a great experience working along with them and learning from each other.

I also would like to thank Dr. David Mitchell for providing help in atomic resolution imaging on the scanning transmission electron microscope (STEM) and always sharing his insightful comments whenever I sought help. I am grateful for Dr. David Mitchell, Dr. Lachlan Smillie and Dr. Qiang Zhu for training me on the JEOL ARM 200F, F200 and 2010 microscopes respectively at the EMC at UOW. I would also like to thank Prof. Germanas Peleckis for training me on some research facilities at the Australian Institute for Innovative Materials (AIIM), UOW.

My sincere thanks go to everyone who helped me through my PhD journey. I am thankful for the AINSE Post-graduate Research Award.

Last but not least, I would like to wholeheartedly thank my wife, Reyhangul Kerim, for her unwavering support. My family members` support and encouragement were invaluable to completing this rewarding journey.

Certification

I, Abuduliken Bake (Ablikim Baqi), declare that this thesis, which has been submitted in fulfilment of the requirements for the conferral of the degree Doctor of Philosophy from the University of Wollongong, is wholly my own work unless otherwise referenced or acknowledged. This document has not been submitted for qualifications at any other academic institution. My supervisor Dr. David Cortie, Dr. Jared Cole, and Dr. Cong Son Ho have contributed to the theoretical calculations. Dr. Peggy Zhang contributed to conducting atomic force microscopy measurements.

____

Abuduliken Bake

10 June 2023

Publications during PhD studies [1-18]

1. Bake, A., et al., *Top-down patterning of topological surface and edge states using a focused ion beam.* Nature Communications, 2023. **14**(1): p. 1693.

2. Bake, A., et al., *Lamellae preparation for atomic-resolution STEM imaging from ion-beam-sensitive topological insulator crystals.* Journal of Vacuum Science & Technology A: Vacuum, Surfaces, and Films, 2022. **40**(3): p. 033203.

3. Bake, A., et al., *Ultra-small cobalt particles embedded in titania by ion beam synthesis: Additional datasets including electron microscopy, neutron reflectometry, modelling outputs and particle size analysis.* Data in Brief, 2022. **40**: p. 107674.

4. Bake, A., et al., *Structure and magnetism of ultra-small cobalt particles assembled at titania surfaces by ion beam synthesis.* Applied Surface Science, 2021. **570**: p. 151068.

5. Nguyen, A., et al., *Increased phase coherence length in a porous topological insulator.* Physical Review Materials, 2023. **7**(6): p. 064202.

6. Rahman, M.R., et al., *Interplay between Thermal and Magnetic properties of Polymer Nanocomposites with Superparamagnetic Fe_3O_4 Nanoparticles.* Journal of Magnetism and Magnetic Materials, 2023: p. 170859.

7. Guo, L., et al., *Antiferromagnetic topological insulating state in $Tb_{0.02}Bi_{1.08}Sb_{0.9}Te_2S$ single crystals.* Physical Review B, 2023. **107**(12): p. 125125.

8. Abualgassem, E., et al., *Effect of Cr concentration on the optical and magnetic properties of Cr‐TiN thin films grown by reactive magnetron sputtering.* physica status solidi (a).

9. Chen, L., et al., *Topological Insulator $V_xBi_{1.08-x}Sn_{0.02}Sb_{0.9}Te_2S$ as a Promising n-type Thermoelectric Material.* Journal of Alloys and Compounds, 2022: p. 165550.

10. Abualgassem, E., et al., *Optical and magnetic properties of cobalt doped TiN thin films grown by RF/DC magnetron sputtering.* Journal of Magnetism and Magnetic Materials, 2022. **550**: p. 169023.

11. Chen, L., et al., *Magnetotransport and Berry phase tuning in Gd-doped Bi_2Se_3 topological insulator single crystals.* Physical Review Materials, 2022. **6**(5): p. 054202.

12. Khan, S., et al., *Iron oxide-palladium core-shell nanospheres for ferromagnetic resonance-based hydrogen gas sensing.* International Journal of Hydrogen Energy, 2022. **47**(12): p. 8155-8163.

13. Yang, G., et al., *Enhanced thermoelectric performance and mechanical strength of n-type BiTeSe materials produced via a composite strategy.* Chemical Engineering Journal, 2022. **428**: p. 131205.

14. Zhao, W., et al., *Massive Dirac fermions and strong Shubnikov–de Haas oscillations in single crystals of the topological insulator Bi_2Se_3 doped with Sm and Fe.* Physical Review B, 2021. **104**(8): p. 085153.

15. Yue, Z., et al., *Observation of itinerant ferromagnetism and coupled magnetoresistance in a spinel $CuCo_2S_4$.* Journal of Materials Chemistry C, 2021. **9**(28): p. 8874-8881.

16. Ahmed, A.J., et al., *Significant Reduction in Thermal Conductivity and Improved Thermopower of Electron‐Doped $Ba_{1-x}La_xTiO_3$ with Nanostructured Rectangular Pores.* Advanced Electronic Materials, 2021. **7**(4): p. 2001044.

17. Yue, Z., et al., *Cross-over from weak localization to anti-localization in rare earth doped TRS protected topological insulators.* Physics Letters A, 2021. **385**: p. 126953.

18. Cortie, D., et al., *Creating thin magnetic layers at the surface of Sb_2Te_3 topological insulators using a low-energy chromium ion beam.* Applied Physics Letters, 2020. **116**(19): p. 192410.

Under preparation

1. Bake A. et al., *Focused ion-beam assisted device fabrication from van der Waals layered structure materials for transport measurements* (chapter 3 of the thesis).

2. Bake A. et al., *High temperature magnetic order and superparamagnetism in Mn-doped Sb_2Te_3 topological insulators* (chapter 7 of the thesis).

3. Bake A. et al., *Magnetic and transport properties of amorphous Sb_2Te_3 thin films* (follow up study of chapters 5 and 6).

4. Bake A. et al., *Proximity effect induced change in magnetic and transport properties of NiFe coated on the surface of Sb_2Te_3.*

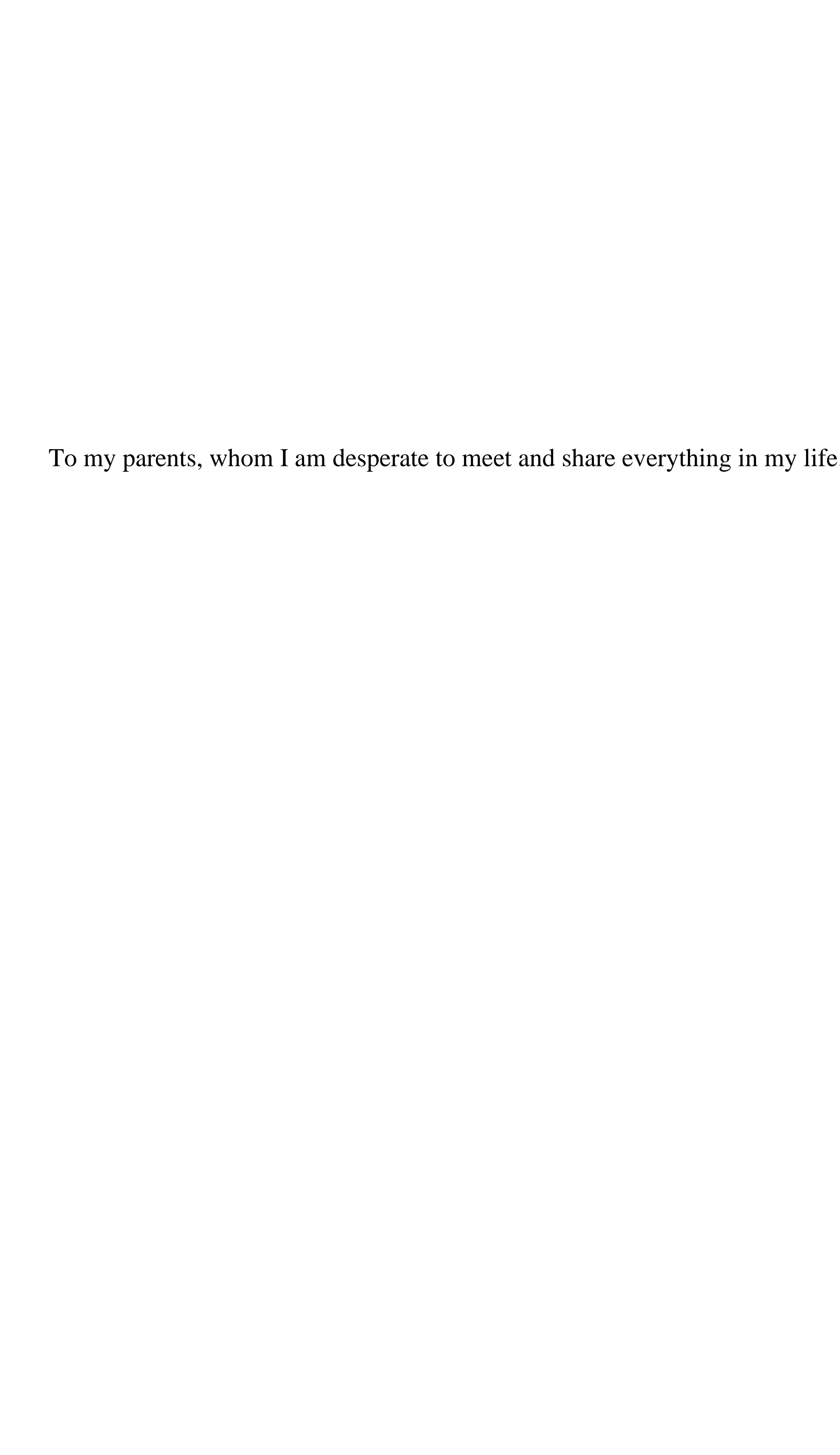

To my parents, whom I am desperate to meet and share everything in my life.

List of Names or Abbreviations

TIs	topological insulators
QHE	quantum Hall effect
SOC	spin-orbit coupling
TRS	time-reversal symmetry
BZ	Brillouin zone
STI	Strong topological insulator
WTI	Weak topological insulator
FET	Field effect transistor
ARPES	Angle-resolved photoemission spectroscopy
STM	Scanning tunnelling microscopy
PPMS	Physical property measurement system
VSM	Vibrating sample magnetometry
TKNN	Thouless, Kohmoto, Nightingale, and Nijs
SHE	Spin Hall effect
QSH/QSHE	Quantum spin Hall/ Quantum spin Hall effect
AHE	Anomalous Hall effect
QAHE	Quantum anomalous Hall effect
DOS/LDOS	Density of states/Local density of states
FIB	Focused ion beam
SEM	Scanning electron microscopy
EDS	Energy dispersive spectroscopy
SE	Secondary electrons
BSE	Backscattered electrons
EBSD	Electron backscattering diffraction
ADF/HAADF	Annular dark-field/high-angle annular dark field
BF	Bright field
XRD	X-ray diffraction
XRR	X-ray reflectometry
PNR	Polarized neutron reflectometry
DFT	Density functional theory
FC/FCW	Field cooling/Field cooling warming

ZFC/ZFCW	Zero field cooling/Zero field cool warming
SS	Surface states
Sdh	Shubnikov-de Haas
HLN	Hikami-Larkin-Nagaoka
WAL	Weak antilocalization
WL	Weak localization
MR/MC	Magnetoresistance/magnetoconductivity
HLN	Hikami-Larkin-Nagaoka

Table of Contents

Abstract 1
Acknowledgments 3
Certification 5
Publications during PhD studies [1-18] 6
List of Names or Abbreviations 9
Table of Contents 11
List of Tables, Figures, and Illustrations 14
Chapter 1. Introduction to Topological Insulators 23
1.1 Introduction and overview 23
1.2 Disorder in topological insulators 26
1.3 The emergence of amorphous topological insulators 26
1.4 Applications of topological insulators 27
1.5 Aims, objectives and hypothesis 30
References 32
Chapter 2. Literature Review 35
2.1 Order and disorder in solid state physics 35
2.2 Quantum Hall effect (QHE) 36
2.3 Topological band theory 38
2.3.1 Topology and topological invariant 38
2.3.2 Bulk-boundary correspondence 41
2.3.3 Berry Phase 42
2.4 $\mathbb{Z}_2$ classification of topological insulators 46
2.5 Quantum spin Hall (QSH) insulator 47
2.6 Quantum anomalous Hall effect (QAHE) and magnetic TIs 48
2.7 Two-dimensional (2D) to three-dimensional (3D) topological insulators 50
2.8 Overview of available methods for topological insulator electronic structure 53
2.9 Magnetotransport of topological insulators and surface states 55
2.9.1 Quantum oscillations 55
2.9.2 Weak antilocalization and weak localization 56
2.9.3 Landau level quantization 57
2.10 Types of disorder (magnetic and non-magnetic) 58
2.11 Disorder effects in topological insulators: Anderson localisation and the fate of surface states under strong disorder 60
2.12 Amorphous topological insulators? 62
2.13 Hypothesis: Methods to control order and disorder in TIs with ion beam techniques will enable surface engineering 64
References 66

Chapter 3. Methodology and Characterization techniques 70
3.1 Materials structure characterisation 70
3.1.1 Scanning electron microscopy imaging.. 70
3.1.2 Electron back-scattering diffraction (EBSD).. 71
3.1.3 X-ray analysis/ Energy dispersive spectroscopy.. 73
3.1.4 Transmission electron microscope (TEM)/ Scanning transmission electron microscope (STEM) 74
3.1.5 X-ray diffraction (XRD) 76
3.1.6 X-ray reflectometry (XRR) 77
3.1.7 X-ray photoelectron spectroscopy (XPS) 78
3.1.8 Polarized neutron reflectometry (PNR) 79
3.2 Ion beam modification.. 82
3.2.1 FIB lamellar preparation methods 82
3.2.2 Magnetic ion implantation (Broad-beam accelerator based ion mplantation)...83
3.3 Electronic and magnetic characterisation 84
3.3.1 Transport measurements using PPMS.. 84
3.3.2 Vibrating sample magnetometry measurements.. 85
3.4 Transport measurement device fabrication with a focused ion-beam 86
3.4.1 Overview 86
3.4.2 Introduction 88
3.4.3 Results and discussions.. 91
3.4.4 Conclusions 98
References 100
Chapter 4. Lamellae preparation for atomic-resolution imaging from topological insulator crystals.. 103
4.1 Overview 103
4.2 Introduction 104
4.3 Experimental.. 106
4.4 Results and discussion 109
4.4.1 SRIM calculations.. 109
4.4.2 STEM imaging.. 111
4.5 Summary and conclusions 114
References 115
Chapter 5. Feasibility for controlled patterning of Sb_2Te_3 surfaces 117
5.1 Overview 117
5.2 Monte Carlo calculations 117
5.2.1 Validation of the ion beam stopping depth calculations against STEM images 119
5.2.2 Lateral feature size from the ion beam writing process.. 122

5.2.3 The crystallinity of the underlying Sb_2Te_3 crystal after ion implantation 123
5.3 Additional data for the effect of irradiation fluences and geometries 123
5.3.1 High fluence irradiation leading to sputtering 123
5.3.2 Patterning of circular and dot geometries 126
5.4 Additional CAFM characterization 128
5.4.1 Line profiles through a region patterned using high Ga fluences 129
5.4.2 I-V characterization 129
5.4.3 Line profile showing edge conductivity 130
5.4.4 Characterizing the anisotropy in the CAFM scans 131
5.5 Details of transport measurements for the FIB devices and thin films 133
5.5.1 Details on the focused-ion beam device preparation methodology 133
5.5.2 Crystallinity of an as-prepared device 134
5.5.3 Shubnikov-de-Haas oscillations of the as-prepared crystalline device 135
5.5.4 Effect of irradiation and post-annealing in the FIB-fabricated device 136
5.5.5 Lumped-element model for the FIB fabricated devices 138
5.5.6 Complementary thin film devices 139
References 143
Chapter 6. Top-Down Patterning of Topological Surface and Edge States using an Ion Beam 144
6.1 Overview 144
6.2 Introduction 144
6.3 Results 147
6.4 Discussion 155
6.5 Methods 156
References 159
Chapter 7. High temperature magnetic order and superparamagnetism in Mn-doped Sb_2Te_3 topological insulators 162
7.1 Overview 162
7.2 Introduction 162
7.3 Synthesis and structural characterisation 164
7.4 Magnetic properties 168
7.5 Conclusion 171
References 173
Chapter 8. Conclusions and outlook 175
8.1 Summary of main results 175
8.2 Benefits to the broader research fields of 2D materials and surface electronics 178
8.3 Future directions and unresolved questions: 179

List of Tables, Figures, and Illustrations

Table 2.1. Analogies of Berry Phase: 45

Table 5.1. Identity of irradiated regions in Figure 5.6, with corresponding ion fluences irradiated within the microscope at 8 keV (C/µm^2) and conversion to the standard unit (ions/cm^2). 126

Table 5.2. Pattern ID and size with corresponding ion fluence irradiated within the FIB microscope (C/µm^2) at 8 keV and conversion to the standard unit (ions/cm^2). 127

Table 5.3. Total resistance calculation of the FIB device based on the lumped element model. 139

Table 7.1. Mn atomic percentage (at%) and elemental composition of Mn-Sb_2Te_3 165

Figure 1.1. Signatures of the exotic metallic surface states in topological insulators. (a) The electronic structure of Bi_2Se_3 measured using Angle-resolved photoemission spectroscopy (ARPES) [5]. (b) Theoretical idealization of the electronic structure of Bi_2Se_3, showing the rotation of the spin degree of freedom (red arrows) as an electron (with energy E) moves around the Fermi surface (with Fermi energy E_F) [5]. 25

Figure 1.2. Physical principle of topological spin-orbit torque (SOT) [26]. 28

Figure 1.3. Benchmarking topological field effect transistors [25]. 30

Figure 2.1. Hall and longitudinal resistivity as a function of the magnetic field for GaAs/AlGaAs heterostructures at 1.5 K. [3] 37

Figure 2.2. Landau level energy separation of a two-dimensional electron gas (2DEG). 37

Figure 2.3. Illustrates topologically equivalent objects in (a) g=0, (b) g=1, and (c) g=2 and shows the distinction between each set of objects that are topologically inequivalent. (Topological invariant = number of “holes”, in this case) 38

Figure 2.4. An illustration of the analogy between electronic band-structure topology and real-space topology. (a)–(c) The atomic insulating state is a topologically trivial state. The simplest example of a topologically non-trivial state is the Quantum Hall State in (d) which has a band-structure in (e). Like the two surfaces (c and f) which differ in their genus, the band-structures (b) and (e) are also distinguished from one another by a topological invariant, the Chern number, similar to the genus.[5] 40

Figure 2.5. Schematic illustrations showing the differences and similarities between various Hall effects. While any semiconductor may exhibit the Hall effect, and any magnetic material may exhibit the Anomalous Hall effect, the Quantum anomalous Hall effect is uniquely realized in topological insulators. Adapted from Ref. [6]. 41

Figure 2.6. Gapless states at the interface of two topologically different phases (Ref.

(https://blogs.iu.edu/sciu/2020/11/14/can-you-turn-a-baseball-into-a-donut/)).............42

Figure 2.7. Parallel transport of a vector ν around a closed loop (from O to A to B and back to O) on the sphere..43

Figure 2.8. (a) On a lens with antireflection coating, light waves reflected by the top (blue line) and the bottom (red line) surfaces interfere destructively, which leads to suppressed reflection. (b) A quantum spin Hall edge state can be scattered in two directions by a nonmagnetic impurity. Going clockwise along the blue curve, the spin rotates by π; counterclockwise along the red curve, by −π. A quantum mechanical phase factor of −1 associated with that difference of 2π leads to destructive interference of the two paths—the backscattering of electrons is suppressed in a way similar to that of photons off the antireflection coating [14]. 48

Figure 2.9. Evolution of the subband structure upon increasing the exchange field. The solid lines denote the subbands that have even parity at Γ point, and dashed lines denote subbands with odd parity at Γ point. The blue colour denotes the spin down electrons; red, spin up electrons. (A) The initial subbands are not inverted. When the exchange field is strong enough, a pair of inverted subbands appears (red dashed line and blue solid line). (B) The initial subbands are already inverted. The exchange field releases the band inversion in one pair of subbands (red solid line and blue dashed line) and increases the band inversion in the other pair (red dashed line and blue solid line) [16]. 49

Figure 2.10. (a) Bi_2Te_3 crystal structure and corresponding (b) rhombohedral Brillouin zone. [34]..51

Figure 2.11. Bulk band structure of Bi_2Se_3 (a) without consideration of spin-orbit coupling (SOC), and (b) with spin-orbit coupling. [24] 52

Figure 2.12. The surface local density of states (LDOS) on the (111) plane for (a) Sb_2Se_3, (b) Sb_2Te_3, (c) Bi_2Se_3, and (d) Bi_2Te_3 systems. [24]...52

Figure 2.13. Standard transport measurement configuration where a sample's resistance and Hall resistance are measured at different temperatures and magnetic fields. 55

Figure 2.14. The electronic structure of a topological insulator and of a magnetic topological insulator. a. The massless Dirac-like dispersion of the surface state with spin–momentum locking in a 3D topological insulator. b. Real-space picture of the surface state in a 3D topological insulator. Electrons with spins pointing up and down (red arrows) move in opposite directions. c. The gapped Dirac-like dispersion of the surface state in a magnetic topological insulator. d. The chiral edge mode that appears in a magnetic topological insulator when the Fermi level, E_F, is located in the mass gap induced by the magnetic exchange interaction.[43] 59

Figure 2.15. Disorder depth-dependent transport illustrated in a disordered surface layer of depth d=5. (a) W=4.5, topological state pinned to bottom surface. (b) W=7.5 near W_c, fully depinned from bottom surface. (c) W=9, under strong disorder, the disorder region is no longer topological. [52] 61

Figure 3.1. Electron microscopes used in the thesis for the characterization. a. JEOL JSM-6490LV SEM used for regular imaging and EDS analysis. b. FEI Helios G3 FIB-SEM used for imaging, EDS and EBSD analysis, FIB lamella and transport device fabrication.

....71

Figure 3.3. (a, b) Electron scattering acts as a divergent source of electrons within a specimen. These electrons are incident upon a lattice plane satisfying Bragg's equation. The resulting diffraction forms a pair of cones at the front and back end of the plane. (c) Diffracted rays are formed along the surface of cones and strike the phosphor screen resulting in a pair of lines for each set of lattice planes. (d) Schematic illustration of electron beam interaction with the lattice planes giving rise to Kikuchi bands on a phosphor screen [1]. 72

Figure 3.2. Monte Carlo simulation of X-ray generation intensity and depth in Sb_2Te_3 under at the beam energy range of 5-30 kV. X-ray generation depth and intensity at a. 0° specimen tilt, b. 50° specimen tilt, c. 70° specimen tilt, show that by tilting specimen x-ray generation could be brought to near surface of specimen. 73

Figure 3.4. TEM/STEM models used for characterisation in the thesis (a) JEOL JEM-F200 TEM/STEM and (b) JEOL JEM-ARM200F aberration-corrected TEM/STEM...75

Figure 3.14. Bragg-Brentano geometry, as used in many powder x-ray diffractometers. 77

Figure 3.16. Information provided by a X-ray reflectometry profile [6]. 78

Figure 3.15. A simple schematic shows the XPS instrument's main components and working principle. 79

Figure 3.19. Schematic of the PNR setup shows the working principles and application in various materials systems [7]. 80

Figure 3.20. Information provided by a typical neutron reflectometry profile showing how layer thickness, chemical composition and magnetization can affect the observed signal [8]. 81

Figure 3.5. FIB lamella preparation process. (a) Schematic illustration shows a summarised procedure for FIB lamella preparation. (b) An SEM image shows a thick protecting layer deposited on to sample before trenching. (c) Low-magnification TEM image shows the remaining~300 nm protecting coating. 83

Figure 3.17. (a) Low energy ion implanter (LEII), and corresponding (b) vacuum management and control system showing the simplified schematic of LEII based at CAS, ANSTO. 84

Figure 3.. Physical properties measurements system used for transport measurements a. 14 T PPMS, and b. DynaCool 9T PPMS showing the VSM option attached. c. Sourcemeter and break out box apparatus used for high resistance measurements........85

Figure 3.13. Commercially available chips used for transport measurement device fabrication. Left chip (FEI MEMS chip can be used to conduct in-situ biasing and heating in a FEI Helios G3 microscope). 85

Figure 3.18. Schematic diagram of a. VSM measurement setup and b. types of sample holders used in VSM showing in-plane and out-of-plane configurations. [15] 86

Figure 3.5. (a-c) A few custom-designed gold electrical contacts for four-probe measurements (d) Pt deposition at higher currents and voltages also induces significant milling damage on a rectangular geometry device, (e) Burnt electrical legs and disk geometry in the inset image. (f) Electrical contacts were fabricated for four-probe measurements and Sb_2Te_3 rectangular geometry was placed on the pre-fabricated contacts. (g) Broken chip due to the fast approaching of the manipulator during placing the lift-out geometry on the contacts. (h) Damaged device due to high current during testing. (i) Overheated device due to high current. 87

Figure 3.6. Using EDS and EBSD to identify composition and crystal phase. Poor quality single crystals showing the formation of Sb_2Te_3 and Te single crystal phase in a piece of crystal (a) SE image, (b) EDS overlayer image, (c) Band contrast image, (d) Phase colour image, (e) Euler colour image collectively showing Sb_2Te_3 and Te crystal phases present in the crystal pieces being analysed. (f) and (g) are Kikuchi patterns for Sb_2Te_3 and Te single crystals. In contrast, (b) SE image of a high-quality single crystal Sb_2Te_3 and corresponding (i) Band contrast image, (j) Phase colour image, (k) Euler colour, and (l) Pole figure from EBSD mapping indicates the pure single crystalline phase of Sb_2Te_3.92

Figure 3.7. Device fabrication through controlled fracturing, (a) A geometry milling, (b) Controlled fracturing, (c) Transferring on a chip, and (d) Electrical contact fabrication. Column 2 shows the controlled fracturing of the rectangular geometry process, and column 3 shows the illustration of each step. 93

Figure 3.8. EBSD mapping shows the degree of amorphisation of Sb_2Te_3 single crystal surfaces as ion beam milling continues. (a)-(b) EDS and EBSD mapping at intervals during the different levels of trenching. 95

Figure 3.9. Four -probe and Hall measurement device fabrication process using a combination of ex-situ exfoliation and FIB milling. (a) and (b) Rectangular transport device contacted on custom-made electrical contacts and commercial chip. 96

Figure 3.10. Transport of a surface amorphized Sb_2Te_3 of the device during fabrication. (a) Resistance versus temperature curve, (b) Magnetoresistance at various temperatures, (c) Hall measurement at various temperatures. 97

Figure 3.11. Transport of the Sb_2Te_3 device with the surface crystallinity preserved during fabrication. (a) Resistance versus temperature curve, (b) Magnetoresistance at various temperatures, (c) SdH oscillation pattern after background subtraction, (d) Oscillation frequency versus magnitude after performing Fast Fourier transform (FFT) on (c), and (c) Hall measurement at various temperatures. (f) Angle-dependent magnetoresistance at various temperatures, (g) SdH oscillation pattern after background subtraction, (h) Oscillation frequency versus magnitude after performing Fast Fourier transform (FFT) on (g). 98

Figure 4.1. (a) and (b) Comparison of a general FIB lamella preparation procedure and the modified procedure for ion-beam-sensitive crystals used in this work. (c) Schematic illustration of the key steps for the preparation of an electron-transparent specimen including the deposition of the protective carbon layer, trenching, lift out and thinning steps. 107

Figure 4.2. (a) Cross-sectional SEM image of a FIB lamella from a Sb_2Te_3 single crystal

welded onto a Cu TEM grid and inset shows the ~ 500 nm protective C layer (appearing lighter grey) is intact at the last step of surface polishing. (b) Cross-sectional STEM image showing subdivided panels in a FIB lamella. 109

Figure 4.3. Vacancy versus target depth at Ga ion beam energies from 0.5 - 16 keV for (a) Sb_2Te_3, (b) Bi_2Te_3. (Angle between the ion beam and lamella side surface is 5° for 0.5-2keV and 1.5° for 5-16 keV) (c) Vacancy versus target depth in Sb_2Te_3 for different Ga ions incident angles. (At 90°, the ion beam is perpendicular to the specimen surface.) 111

Figure 4.4. STEM HAADF images of a Sb_2Te_3 single crystal taken at the edge of stripes irradiated with Ga ion of various energies (shown inset Figure 4.4 b). The unirradiated region (left) shows the original crystalline structure while the irradiated region (right) is amorphous:(a) A region irradiated with 30 keV ion beam energy where certain areas were protected from irradiation by the additional protective coating and inset image from unirradiated region, and (b) high-resolution STEM image taken from the unirradiated region of (a). (c) and (d) are STEM HAADF images irradiated with 16 keV and 8 keV, respectively. In contrast, (e) and (f) shows STEM HAADF images of FIB lamella prepared by the standard, unrefined method showing a case of beam damage at the surface from over milling. 113

Figure 5.1. Ga^+ ions stopping range and energy loss in Sb_2Te_3. (a) The energy loss for various incident ion energies. (b) The projected ion range as a function of the incident ion energy. (c) The longitudinal and lateral straggle. 118

Figure 5.2. Monte Carlo calculations of the ion-beam irradiation process in Sb_2Te_3 showing the Ga concentration and total damage profiles. (a)-(d) Accumulated damage profiles for Ga ion beam energies between 8–40 keV for the selected fluences of 10^{15}, 5×10^{15}, and 10^{16} ions/cm^2, respectively. (e)-(h) The variation of the Ga concentration in Sb_2Te_3 at Ga ion beam energies between 8–40 keV for the selected fluence of 10^{15}/cm^2. 119

Figure 5.3. (a) STEM HAADF image showing distinct amorphous and crystalline regions. The inset shows an enlarged image of the quintuple atomic layered structure of Sb_2Te_3 superimposed with Sb and Te atoms. (b) Low magnification image surveying the cross-section of the Ga-irradiated region of the Sb_2Te_3 surface. The ion beam energy was 8 keV, and the fluence was 2.18×10^{15} ions/cm^2. (c) Detail of the boxed region in b) showing the lateral and depth scale of the amorphous region near the edge of the irradiated area. (d) EDS elemental maps of (c). (e) Ga, Sb, and Te line profiles are taken along the line shown in (a). (f) Monte Carlo calculations of the displacement per atom and Ga atomic concentration within Sb_2Te_3 for 8 keV Ga^+ ions at a fluence of 10^{15} ions/cm^2. (g) HAADF image showing a detail of the boxed region in (c). (h) Bright-field image of (g) showing strong diffraction contrast (dark) from the crystalline regions, which were not exposed to the Ga ion beam. 121

Figure 5.4. (a) 3D distribution of the Damage-Per-Atom profile in a Sb_2Te_3 crystal for a Ga beam with energy 8 keV, as calculated from the Monte Carlo calculations. (b) Secondary electron image showing Ga ion beam irradiated lines of various widths (top to bottom, input pattern width of 100, 50 and 20 nm and z depth set to 110 pm at beam energy of 30 kV and current of 1.1 pA) and (c) corresponding EBSD band contrast image. (d) Vertical intensity profile through the band contrast image measures the actual width

of the amorphized regions as (top to bottom), 200, 184 and 166 nm. 122

Figure 5.5. The XRD diffraction pattern of a c-axis orientated Sb_2Te_3 crystal was irradiated with $1x10^{17}$ /cm^2 Ga ions at 40 keV. The strong (00L) diffraction peaks show that the crystallinity is preserved below the nanometer-scale implanted region. The much smaller peak marked with a* is from Cu K_β. 123

Figure 5.6. (a) Secondary electron image of the 3×3 grid of irradiated regions labelled R1 – R9. Only the higher fluence regions (R7-R9) show topography due to sputtering effects. (b) AFM topography image labelled with the matching pattern ID (Note: the scan direction and imaging angle is different in the SEM/AFM images, as EBSD measurements require using an inclined surface). (c) Band contrast image obtained through an EBSD scan on the same region of interest, where amorphous regions appear black. (d) Phase color image showing the crystalline Sb_2Te_3 in blue and the non-indexable regions (amorphous) as black. 125

Figure 5.7. (a) Scanning electron image with each pattern ID labelled on it, and (b) Band contrast image from EBSD scan. (c) Phase color image. (d) High-magnification band contrast image. (e) Corresponding phase color image. (f) Kikuchi patterns taken at R3, R4, and R5. (g) High-magnification band contrast image of the patterns with higher Ga irradiation dose. (h) Corresponding phase color image. (i) Kikuchi patterns within patterns R6, R7, and R8. 128

Figure 5.8. (a) Line profiles through the array of irradiated grid squares (see Figure 5.6 (a) and Table 5.1 for details) for cAFM measurement at a scanning bias of 1V. (b) Current response along the line profile scans in (a) showing that the current decreases to zero within the most heavily irradiated grid squares (R4 – R9). 129

Figure 5.9. I-V characteristics. (a) Comparison of an ion-beam irradiated area (inside the midpoint of the square for an A-V boundary), with the A-C boundary (edges of the square), and unirradiated area at the crystallinity C-V boundary (outside the square). (b) CAFM image with colored arrow labels indicate the irradiated area, boundary, and crystalline area where I-V scans have been performed. (c-e) A series of repeated I-V scans at multiple patterned areas, edges, and crystalline regions to confirm the reliability of the measurements. 130

Figure 5.10. The current line scan profile shows the high conductivity at the edges at the boundary between ion-beam irradiated and unirradiated areas. (Note: the CAFM image is rotated so that the line profile direction matches the x-axis of the figure.) 131

Figure 5.11. Current mapping using 1V DC bias for an individual irradiated box. (a) CAFM scans with a fast-scanning direction parallel to the probe. (b) CAFM scans with a fast scanning direction perpendicular to the probe. 132

Figure 5.12. CAFM images of a patterned logo with edges at different angles to the scan direction. (a) Topography. (b) Current mapping of an individual irradiated FLEET logo pattern. 132

Figure 5.13. Device fabrication procedure for crystalline FIB devices. (a) A thin exfoliated flake region is selected, and a single cut is made to remove a bar-like section and weld it to a nanomanipulator. (b) The flake is placed on prefabricated gold contacts.

(c) Platinum contacts are deposited, linking the gold contacts to the surface of the Sb_2Te_3 bar (thickness=500-600 nm). 133

Figure 5.14. EDS and EBSD characterization of the rectangular lift-out on a chip shows that the device is crystalline. (a) EDS layered image. (b) EDS elemental map taken from the white box in (a) (SE image at the top), and corresponding (c) EBSD and crystal orientation map with (d) inverse pole figure (IPF) coloring key. 134

Figure 5.15. Representative Kikuchi patterns for sections of the device showing it to be crystalline. (b) and (c) Electron back-scattered Kikuchi Patterns (EBSD) (with simulated solutions generated within the Aztec software) from point B and point C on the SE image in (a). (d) The 3D phase view of the unit cell shows the orientation is identical for points B and C, indexed to the hexagonal crystal structure of Sb_2Te_3. 135

Figure 5.16. Transport measurement of the FIB fabricated device. (a) RT measurement. (b) Magnetoresistance at 2, 3, and 4 K. (c) Shubnikov-de Hass (SdH) oscillation extracted by subtracting the background from the magnetoresistance measurement. (d) Fast Fourier transform (FFT) magnitude of the SdH oscillations measured at 2−4K. 136

Figure 5.17. In-situ characterization of a Sb_2Te_3 bar before irradiation, post-irradiation and post-heating. (a) EDS and EBSD scan of a rectangular lift-out section welded on an FEI heating chip before irradiation. The EBSD and unit cell image indicate the lift-out surface's crystalline nature. (b) EDS and EBSD scan after the 5x3 μm area (indicated in the red box on the SE image) was irradiated with a Ga ion beam. The EBSD scan highlights the amorphous nature of the irradiated area. (c) After in-situ heat treatment at 400 °C for 30 minutes, the EBSD images show the recrystallization of the Sb_2Te_3 region via the disappearance of the dark amorphous region in the band contrast images. Images were generated within the Aztec software. 137

Figure 5.18. Schematic illustration showing the configuration for the four-probe contact measurements and the corresponding lumped element model of a Ga-FIB device with an amorphous surface layer, and a parallel bulk conducting channel............................... 139

Figure 5.19. Temperature-dependent resistivity of (a) the as-grown crystalline and (b) amorphized Sb_2Te_3 thin film grown by molecular beam epitaxy. (c) Cross-sectional TEM images of the starting film illustrating the clear lattice fringes from the crystalline order. D) Image of the same film after Ga-ion irradiation using a broad beam Low Energy Ion Implanter. 140

Figure 5.20. X-ray reflectometry of (a) MBE-grown Sb_2Te_3 film before and after ion-beam irradiation. (a) ~28 nm thick film before irradiation (b) MBE-grown Sb_2Te_3 film (~10 nm) before and after ion-beam irradiation. (c) and (d) SLD profiles for (a) and (b), respectively. 141

Figure 5.21. (a) Neutron reflectometry of MBE-grown Sb_2Te_3 film (~30 nm) before and after ion-beam irradiation (b) Corresponding SLD profiles. 142

Figure 5.22. a) Polarised neutron reflectometry pattern for 10 nm Sb_2Te_3 thin films at 5 K in a field of 0.1 T. b) The neutron spin asymmetry, and best fit to the data. c) The best fit SLD model to the neutron data at 5 K.. 142

Figure 6.1. The crystalline state of the topological insulator Sb_2Te_3 can be modified using

a focused-ion beam. (a) Illustration of the ordered crystalline R3m phase of Sb_2Te_3 which has $\mathbb{Z}_{2s}$ =1. (b) The disordered C2/m phase has random Sb/Te sites and has $\mathbb{Z}_{2s}$ = 0. (c) Amorphous Sb_2Te_3 shares similarities with the disordered crystalline phase. (d) Schematic illustration of the ion-beam assisted amorphization process. (e) Cross-sectional scanning transmission image in HAADF mode of the irradiated region at the surface of the crystal. (f) High-resolution HAADF image showing the amorphous and crystalline regions where the irradiation used was 2.2×10^{15} ions/ cm^2 at 8 keV. (g) Secondary electron image of a plane view of the surface showing the ion-beam irradiated patterns (inset image shows the EBSD band contrast image of a selected region). (h) EBSD band contrast image from a region in (g) (pink dashed line). Electron backscattered diffraction patterns (i) from lightly irradiated pattern and (j) from the highly irradiated pattern in (h), showing the transition from order to disorder as the ion fluence is increased. (see Table 5.2 and Figure 5.7 in Chapter 5). 147

Figure 6.2. The disordered regions modified by the ion beam have a suppressed surface conductivity. (a) Schematic of the AFM configuration showing how current and topography is measured over a patterned region. (b) Mapping of surface currents of a Sb_2Te_3 single crystal showing that the 3×3 rectangular grid sections, which were modified by the ion beam, are less conducting. Each square received a sequentially increasing ion beam dose. The measurement bias was 2.5 V. (c) Height map over the same region as in (b) showing that topography is modified for higher fluences. (d) Integrated current and height of each Sb_2Te_3 grid point irradiated with increasing dose of Ga^+ ions, measured using cAFM with a scanning bias of 2.2 V. (e) Current mapping using a 1V DC bias for an individual irradiated box (see *Figure 5.9* in Chapter 5 for IV characterization) showing additional conductivity at the edges of the pattern, and on surface terraces. (f) Four-probe temperature-dependent resistance of a Sb_2Te_3 device before and after amorphization, showing the increase resistance. The inset shows the measurement configuration. 150

Figure 6.3. Theoretical calculations show that while crystalline Sb_2Te_3 hosts Dirac surface states, the amorphous version does not, consistent with the $\mathbb{Z}_2 = 1 \rightarrow \mathbb{Z}_2 = 0$ transition (a) The electronic density of states of an amorphous Sb_2Te_3 surface exhibits a bandgap with no states crossing the Fermi level. The inset shows the atomic model of the amorphous Sb_2Te_3 surface slab generated from the molecular dynamics quench, used to calculate the electronic structure with a 15 Å vacuum boundary in the c-direction. (b) The electronic density of states of the crystalline Sb_2Te_3 surface has states crossing the Fermi level. The inset shows the crystalline surface slab used to calculate the electronic structure. (c) The band structure of the crystalline surface shows the characteristic Dirac surface states crossing the Fermi level. (d) The real-space image of the defect-free crystal shows the electron density calculated with the model Hamiltonian, and exhibits surface states at the crystal-vacuum interface. (e) A moderate level of defects does not remove the surface state position. Each white dot represents a defect in the system. (f) At a critical threshold of disorder, the disordered region becomes non-topological ($\mathbb{Z}_2$=0) as the surface states then reposition to wrap around the new topological vacuum region.......... 153

Figure 7.1. EDS analysis of the 2×10^{16} Ions/cm^2 Mn doped Sb_2Te_3 at 0° tilt. a. SE image displays the region analysed by EDS. b-d. EDS elemental mapping for Sb, Te, Mn, respectively. e. EDS spectroscopy clearly shows the Mn K_α peak. f. X-ray intensity and generation depth in Sb_2Te_3 for different beam energy at various specimen tilt............ 165

Figure 7.2. Magnetic patterning of Sb_2Te_3 surfaces. a. SEM image of a Cu grid used for implanting Mn through the Cu grid. b. SEM image of Sb_2Te_3 surface patterned through the Cu grid with Mn implantation at energy of 40 kV, and fluence of 3×10^{16} ions/cm^2. c. SEM image of the region where EDS mapping was acquired. d-f. EDS elemental mapping for Mn, Sb, and Te, respectively. 166

Figure 7.3. X-ray photoelectron spectroscopy analysis of Mn-Sb_2Te_3. a. XPS survey scan for all five Mn-Sb_2Te_3 samples, b. Mn 2p spectra, and c. fitting of Mn 2p spectrum of the Mn-Sb_2Te_3 with Mn implantation fluence of 5×10^{16} ions/cm^2. 167

Figure 7.4. TEM imaging and EDS analysis performed on a 2×10^{16} ions/cm^2 Mn-Sb_2Te_3 sample. a-c. TEM images from different regions on the lamella. d. The HRTEM image taken from the region shown in b shows the quintuple layered structure of Sb_2Te_3. f-h. EDS mapping analysis from the region shown in e. i. EDS line scan as shown in e. SRIM calculation showing Mn distribution in Sb_2Te_3 calculated for 10^5 Mn ions. 168

Figure 7.5. Magnetisation versus magnetic field (MH) measurements of the Mn-Sb_2Te_3 samples with Mn fluence of a. 5×10^{16} ions/cm^2, b. 2×10^{16} ions/cm^2, c. 1×10^{16} ions/cm^2, d. 5×10^{15} ions/cm^2. The inset figures at the top left corners show without background correction and inset figures in the bottom right corners show an enlarged region of hysteresis loop after the diamagnetic correction (only for the temperature of 5, 300K). 169

Figure 7.6. a. Coercive field with respect to Mn implantation fluence for Mn-Sb_2Te_3 samples measured at 5 K. b. Saturation magnetisation (with and without diamagnetic background subtraction) with respect to Mn fluence for Mn-Sb_2Te_3 samples measured at 5K. 170

Figure 7.7. Magnetisation versus temperature for a. 5×10^{16} ions/cm^2 Mn-Sb_2Te_3, and b. 5×10^{15} ions/cm^2 Mn-Sb_2Te_3. Corresponding field cooled zero field cooled (FC ZFC) magnetisation curves for c. 5×10^{16} ions/cm^2 Mn-Sb_2Te_3, and d. 5×10^{15} ions/cm^2 Mn-Sb_2Te_3 171

Chapter 1. Introduction to Topological Insulators

1.1 Introduction and overview

Condensed-matter physics aims to understand how order arises from the interactions between many simple constituents, such as ions, magnetic moments, or electrons. Order in materials like crystals, superconductors, and magnets is typically described as a result of spontaneous symmetry breaking, where the continuous symmetry of space or spin space is disrupted [1]. For example, spontaneous symmetry breaking can be observed in the formation of ferromagnets, which have a net magnetic moment despite the symmetry of the interactions between their constituent magnetic moments. This symmetry breaking occurs when the magnetic moments align in a specific direction, leading to an asymmetry in the ground state of the system.

In the 1980s, it was discovered that electrons confined to two dimensions and subjected to a strong magnetic field exhibit a different type of order, known as topological order, which underlies the quantum Hall effect [2]. Following this, studies of the quantum Hall effect (QHE) have led to a new classification of materials based on topological order rather than spontaneous symmetry breaking [3, 4]. The QHE does not break any symmetries. However, it has fascinating quantized Hall resistance and conducting edge modes that are not sensitive to changes in materials parameters except in the rare case of a quantum phase transition. This order leads to phenomena like dissipationless transport and emergent particles with fractional charge and statistics [5]. In the past few years, it has been found that topological order can also occur in some three-dimensional materials due to spin-orbit coupling (SOC), an intrinsic property of all solids [6-8]. These materials are called topological insulators (TIs). The discovery of the TIs has refuelled the research interest in topological order [8-17].

Topological insulators (TIs) are a new type of quantum matter that was first theoretically proposed in the early 2000s and later realized experimentally. The concept of TIs was introduced by Charles Kane and Eugene Mele in 2005, who predicted the existence of a class of two-dimensional materials insulating in the bulk but with conducting surface states [9]. These materials, called quantum spin Hall insulators, were characterized by a

topological invariant known as the Z_2 topological index [8]. In 2007, the existence of two-dimensional TIs in HgTe/CdTe quantum wells was experimentally demonstrated by a team led by Shoucheng Zhang [11]. In the following years, topological insulators were also discovered in three-dimensional materials, such as Bi_2Se_3, Bi_2Te_3, and Sb_2Te_3 [17, 18]. The theoretical discovery and experimental [8, 10, 11, 17] realization of topological insulators (TIs) opened a new paradigm of classification in condensed matter physics, as TIs are new states of quantum matter.

Topological insulators can be viewed as a type of semiconductor with the existence of conducting surface states while the bulk is insulating due to an energy gap resulting from strong spin-orbit coupling (SOC) and protected by time-reversal symmetry (TRS). The surface states of a topological insulator are made up of electrons with a particular spin orientation. These surface states are protected by a topological invariant, a mathematical quantity that characterizes the topology of materials. The surface states of a topological insulator are insensitive to certain types of perturbations, such as disorder or impurities, because the topological invariant is robust against these types of perturbations. At sufficiently high temperature, many of the topological insulators become conducting due to thermal activation across their small bulk gaps, like narrow-gap semiconductors. However, at low enough temperatures, the non-surface regions of TIs behave as insulators with a bulk energy gap separating the conduction band and valence band with the Fermi energy in between, as shown in Figure 1.1 a. The existence of topologically protected gapless electronic states at the surface (in 3D systems) or edges (in 2D systems) makes them unique, unlike any other known electronic system. Figure 1.1 a shows the surface bands/states crossing the bulk bandgap enclose a single Dirac point/cone at the Brillouin-zone centre (Γ), which is the signature of a topological insulator. In a topological insulator, the band is inverted, meaning that the conduction band has contributions from the band that made the valence band originally. This inversion is caused by the strong spin-orbit coupling in the material, which mixes the electron's spin and momentum. At 3D TI surfaces, there is a clear connection between the momentum and the spin state on the Fermi surface. As illustrated in Figure 1.1 b, each crystal momentum vector (**k**) for the surface states only has a single spin state at the Fermi level, and the spin direction rotates as the momentum moves around the Fermi surface [5]. Even when disorder or impurities are present, the topological properties of the bulk insulator prevent the metallic surface state from disappearing or becoming localized. This has led to a significant

amount of research and experimentation on 3D topological insulators in recent years.

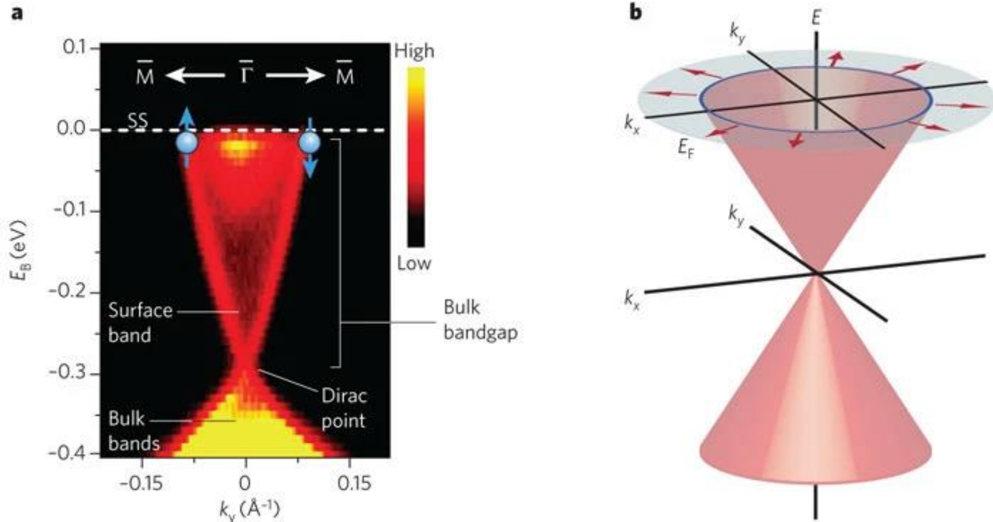

Figure 1.1. Signatures of the exotic metallic surface states in topological insulators. (a) The electronic structure of Bi_2Se_3 measured using Angle-resolved photoemission spectroscopy (ARPES) [5]. (b) Theoretical idealization of the electronic structure of Bi_2Se_3, showing the rotation of the spin degree of freedom (red arrows) as an electron (with energy E) moves around the Fermi surface (with Fermi energy E_F) [5].

The topology classification of electronic structure of crystalline materials has been a major research theme in condensed matter physics for the past decade. Topological nontrivial electronic structures have been found in various materials [19]. Some of the most well-known topological insulators include Bi_2Se_3, Bi_2Te_3, and Sb_2Te_3, all composed of layers of atoms bonded with van der Waals (vdW) forces. These materials are known as three-dimensional topological insulators because the surface states are present on all surfaces of the material. The discovery of topological insulators has opened up a new field of research known as topological matter, which was later expanded beyond TIs to include Dirac, nodal and Weyl semimetals, and topological superconductors. This field focuses on understanding these materials' fundamental properties at the quantum level and exploring their potential applications. Their unique electronic properties, which are derived from the material's topology, make them attractive for use in various applications. Some of the potential applications of topological insulators include spintronic devices, which use the spin of the electron rather than its charge to store and process information; quantum computing, which uses quantum mechanical phenomena to perform calculations; and sensors, which use the unique properties of topological insulators to detect magnetic fields or other quantities.

The identification of topological materials has been greatly aided using crystalline symmetries. Through the application of symmetry indicators and band representations, a classification scheme for crystalline topological materials has been developed, facilitating the discovery of many such materials. Very recently, frontier theoretical studies have discussed the possible existence of amorphous TIs which lie beyond the normal classification schemes based on crystalline symmetries, but potentially could offer a much greater range of topological materials [20-22].

1.2 Disorder in topological insulators

Topological insulators are believed to be immune to certain types of perturbations. However, the effect of the disorder on TIs depends on the types of disorder and its strength. Non-magnetic disorder (or charge disorder) refers to cases where the spatial positions of the atoms are disrupted, or dopant atoms are added, which may introduce changes in the chemical potential but does necessarily lead to a quantum transition. Topological insulator crystals in the chalcogenide family have charged defects such as vacancies and anti-sites, due to intrinsic features in their chemistry. Those defects make a critical contribution to the unintentional bulk conductivity of binary and ternary topological insulators. In most of the cases, however, this does not cause collapse of the topological states, merely shifting the Fermi level into the bulk bands which coexist with ungapped Dirac surface-states [23]. Apart from native defects referred as charge disorder due to non-uniform distribution of charges, there are other types of disorder. In contrast, magnetic disorder involves a local magnetic moment, or dopant, which breaks time reversal symmetry. This is generally believed to have a dramatic effect on the TI and can introduce a gap into the Dirac surface states, and even a transition into a different quantum phase such as the Quantum Anomalous Hall insulator. More discussion of disorder and its effect on topological insulators is given in in the Chapter 2 literature review.

1.3 The emergence of amorphous topological insulators

Amorphous topological insulators (TIs) are materials with topological insulators' properties, but with an amorphous structure rather than a crystalline structure. Amorphous materials do not have a long-range periodic structure, unlike crystalline materials, which

have a regularly repeating structure. Amorphous TIs have attracted great interest because they can create topological insulating behavior in a more flexible and tuneable form than crystalline TIs.

According to recent theories, amorphous materials, which lack the regular structure of a crystal lattice, can still exhibit topological properties due to non-spatial symmetries such as time-reversal symmetry. Even in the presence of disorder, topological insulator crystals can maintain their robustness. This means that in a randomly arranged lattice of atoms with disordered electron hopping, topologically protected edge states and quantized Hall conductivity can still be potentially observed, similar to that of a crystalline topological insulator [20, 21, 24].

1.4 Applications of topological insulators

Topological insulators have potential applications in various fields, including spintronic devices, quantum computing, quantum sensing, thermoelectrics and energy-efficient classical computing, discussed briefly in the sub-sections below.

Spintronic devices: The surface states of topological insulators have a fixed spin orientation with respect to their travelling direction, namely spin-momentum locking, making them attractive for use in spintronic devices and magnetic devices. These devices use the spin of the electron rather than its charge to store and process information. For example, the operation of magnetic random-access memory (MRAM) which is now commercially available uses the principle of spin-transfer torques (STTs) by injecting spin-polarized carriers to change the magnetic moment orientation in the recording layer. For a similar purpose, a reversal invariant TI, in which spin is perpendicular to the momentum along the Fermi surface, would provide an avenue to utilize the intrinsic spin-orbit interaction to generate a large spin Hall current using unpolarized carrier injection. The spin Hall current from a TI would have an analogous effect to STT devices in which spin polarized current modulates the magnetic layers, commonly referred to as spin-orbit torque (SOT) [25]. The working principle of SOT is illustrated in Figure *1.2*

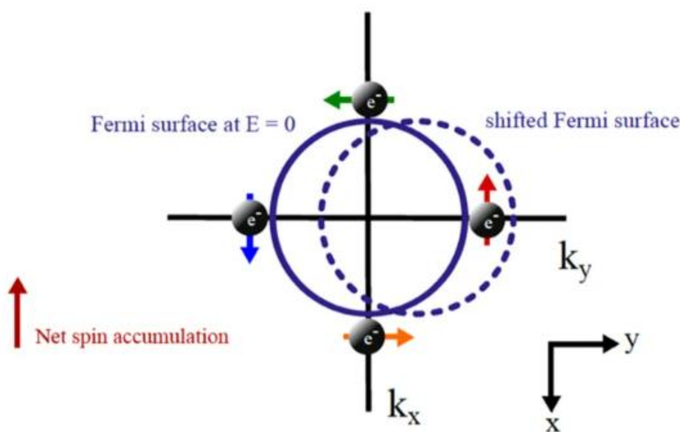

Figure 1.2. Physical principle of topological spin-orbit torque (SOT) [26].

Quantum computing: The unique properties of topological insulators could be used to build quantum computers, which use quantum mechanical phenomena to perform calculations. Recent discoveries in quantum mechanical non-reciprocal transport effects enable controllable rectification, a process normally based on semiconductor diodes [27-31]. Magnetochiral anisotropy (MCA) is an example of non-reciprocal transport effects, in which resistance depends on the direction of an applied magnetic field and the current flow. However, rectification size due to MCA is limited as MCA relies on inversion symmetry breaking that leads to the manifestation of SOC. By artificially breaking the inversion symmetry in heterostructure of topological materials, it is possible to substantially enhance the size of non-reciprocal transport effects. Due to inversion symmetry breaking, topological insulator nanowires could offer large MCAs, which in return results in a maximum rectification coefficient controllable by chemical potential [32]. The giant MCA offers a large spin splitting of the subbands in topological insulator nanowires which is useful for spin filters [33]. Moreover, helical spin polarization and large energy scales in topological insulator nanowires can be useful platform for hosting robust Majorana bound states, that are building block of topological quantum computers in future [34]. The main obstacles for quantum computing are noise and decoherence. Current qubit implementations, such as trapped ions and superconductors, are susceptible to noise and decoherence. In contrast, topological quantum computing employs non-Abelian phase of matter to store quantum information, creating a more resilient qubit. In this approach, information is not encoded in the quasiparticles but in their interaction and braiding, making it topological. As a result, only the macroscopic topological characteristics of the particles' worldlines matter, making topological quantum computing

more resistant to decoherence and noise challenges that affect other qubit implementations [35].

Sensors: Electronic chemical sensors function by converting a surface molecular binding event into and electric signal. The high, fast and reversible response of a materials is desired for sensing applications. TIs could be and potential candidate for sensing applications as the conducting channels of TIs appear on the surface and are exposed to the outside environment [36]. Quantum strain sensor based on a HgTe TI has been proposed based on the transition between TI and trivial insulator around critical thickness [37]. In addition, the surface states of topological insulators are sensitive to magnetic fields, which could be used to detect magnetic fields or other quantities [38, 39].

Thermoelectric materials: Most topological insulators are also excellent thermoelectric materials, and they share similar material features. Bismuth telluride (Bi_2Te_3), antimony telluride (Sb_2Te_3), bismuth selenide (Bi_2Se_3), tin telluride (SnTe) are both topological insulators and thermoelectric materials [17].Topological surface states could serve as excellent conducting channels. Thermoelectric property can be optimised by tuning the position of Fermi level or by introducing disorder [40, 41]. This is because the electronic transport in TI is immune to backscattering by non-magnetic disorders, whereas phonon transport is affected. Careful material engineering could decouple electron and phonon transport, creating a so-called "phonon-glass, electron-crystal" which is useful for improving thermoelectric properties of TIs [42, 43].

Electronics for classical computing: The surface states of topological insulators have high conductivity, making them attractive for electronic devices. These devices could be used in various applications, including high-speed field effect transistors (FET) and computer chips due to the inherent absence of backscattering in the topological surface states. This means, the transport of charge within surface state will not be scattered by impurities that might affect the properties of nanoscale MOSFETs [25]. To investigate the effect of electrical field on the carrier density modulation in TIs, there are some attempts to build FET devices using Bi_2Se_3 [44, 45]. Electrical field gating proved to be an effective way of altering the major carrier type (p vs n), which is essential for CMOS implementation [44, 45]. However, the existence of bulk states due to vacancies are detrimental to the operation of FETs as they offer alternative less-resistive path for current

to flow which diminishes the benefit of TI surface states.

The potential performance of topological materials is driving ongoing experimental and theoretical exploration with the goal of creating fast and low-energy consumption information processing technologies. The Figure 1.3 shows a comparison between topological materials and other existing technologies in terms of their energy consumption per operation and switching speed. Experimental [46] and theoretical [47] data on the performance of topological materials-based FETs is compared with the performance of cutting-edge CMOS [48] and homojunction FETs technologies. The Figure 1.3 indicates that high-performance CMOS transistors consume the most energy but are highly competitive due to their fast-switching speed. The theoretical predictions suggest that topological FETs (TIFET LV and HP) [47] could potentially compete with CMOS technologies with future improvements as TIFET energy consumption is an order of magnitude superior than CMOS.

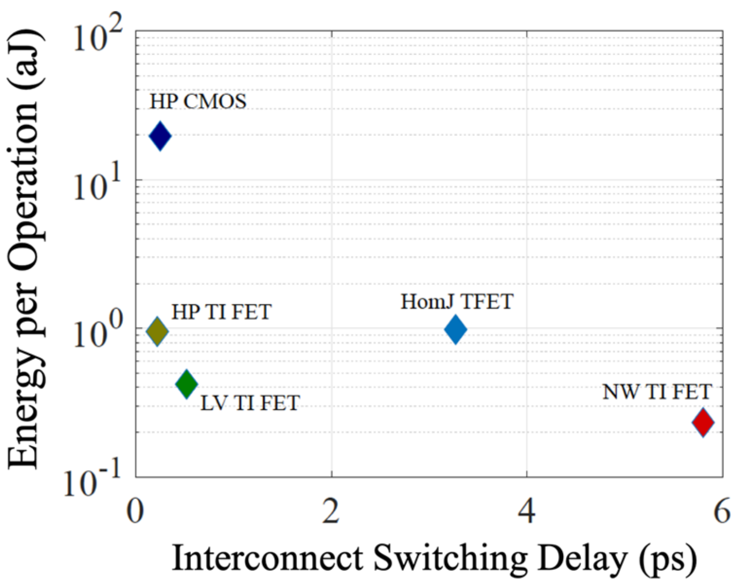

Figure 1.3. Benchmarking topological field effect transistors [25].

1.5 Aims, objectives and hypothesis

TIs are an exciting and rapidly developing area of research, and they hold great promise for developing new technologies and materials. They have potential applications in various fields, including electronics, spintronics, and quantum computing. Although the fundamental physics behind topological insulators has been widely explored in the last two decades, there are still unsolved fundamental questions that have emerged (e.g. the

existence of amorphous topological insulators) and major challenges still exist for practical applications of this new class of materials (e.g. switching time, scalability).

This thesis is centred around the investigation of patterning the surface of Sb_2Te_3 TIs surface using an ion beam. The hypothesis is that the ion-beam irradiation could introduce different levels of disorder which cause a significant change in electronic properties of a material. Hence, precise control of order and disorder in TIs can potentially enable surface engineering. Ion beam techniques have been employed to allow controlled fabrication with non-magnetic and magnetic dopants, and to systematically control the level of disorder at the surface of the TIs, or create alternate forms of surface order (magnetic order). This will be discussed in more details in section 2.13. The resulting electronic properties were studied extensively by a variety of experimental methods, including transport, electron microscopy and X-ray/neutron scattering, Theoretical simulations based on density functional theory and model Hamiltonian calculations assisted in interpreting the data.

References

1. Kibble, T., *Symmetry breaking and defects.* Patterns of Symmetry Breaking, 2003. **127**: p. 3-36.

2. Von Klitzing, K., *25 Years of quantum Hall effect (QHE) a personal view on the discovery, physics and applications of this quantum effect.* progress in mathematical physics, 2005. **45**: p. 1.

3. Thouless, D.J., et al., *Quantized Hall conductance in a two-dimensional periodic potential.* Physical review letters, 1982. **49**(6): p. 405.

4. Wen, X.-G., *Topological orders and edge excitations in fractional quantum Hall states.* Advances in Physics, 1995. **44**(5): p. 405-473.

5. Moore, J.E., *The birth of topological insulators.* Nature, 2010. **464**(7286): p. 194-198.

6. Roy, R., *Topological phases and the quantum spin Hall effect in three dimensions.* Physical Review B, 2009. **79**(19): p. 195322.

7. Fu, L., C.L. Kane, and E.J. Mele, *Topological insulators in three dimensions.* Physical review letters, 2007. **98**(10): p. 106803.

8. Kane, C.L. and E.J. Mele, *Z_2 topological order and the quantum spin Hall effect.* Physical review letters, 2005. **95**(14): p. 146802.

9. Kane, C.L. and E.J. Mele, *Quantum spin Hall effect in graphene.* Physical review letters, 2005. **95**(22): p. 226801.

10. Bernevig, B.A., T.L. Hughes, and S.-C. Zhang, *Quantum spin Hall effect and topological phase transition in HgTe quantum wells.* science, 2006. **314**(5806): p. 1757-1761.

11. König, M., et al., *Quantum spin Hall insulator state in HgTe quantum wells.* Science, 2007. **318**(5851): p. 766-770.

12. Moore, J.E. and L. Balents, *Topological invariants of time-reversal-invariant band structures.* Physical Review B, 2007. **75**(12): p. 121306.

13. Fu, L., C.L. Kane, and E.J. Mele, *Topological insulators in three dimensions.* Physical review letters, 2007. **98**(10): p. 106803.

14. Fu, L. and C.L.J. Kane, *Topological insulators with inversion symmetry.* Physical Review B, 2007. **76**(4): p. 045302.

15. Hsieh, D., et al., *A topological Dirac insulator in a quantum spin Hall phase.* Nature, 2008. **452**(7190): p. 970-974.

16. Xia, Y., et al., *Observation of a large-gap topological-insulator class with a single Dirac cone on the surface.* Nature physics, 2009. **5**(6): p. 398-402.

17. Zhang, H., et al., *Topological insulators in Bi_2Se_3, Bi_2Te_3 and Sb_2Te_3 with a single Dirac cone on the surface.* Nature physics, 2009. **5**(6): p. 438-442.

18. Chen, Y., et al., *Experimental realization of a three-dimensional topological insulator Bi_2Te_3.* Science, 2009. **325**(5937): p. 178-181.

19. Burkov, A., *Topological semimetals.* Nature materials, 2016. **15**(11): p. 1145-1148.

20. Mansha, S. and Y.D. Chong, *Robust edge states in amorphous gyromagnetic photonic lattices.* Physical Review B, 2017. **96**(12): p. 121405.

21. Agarwala, A., *Topological insulators in amorphous systems*, in *Excursions in Ill-Condensed Quantum Matter*. 2019, Springer. p. 61-79.

22. Agarwala, A., V. Juričić, and B. Roy, *Higher-order topological insulators in amorphous solids.* Physical Review Research, 2020. **2**(1): p. 012067.

23. Scanlon, D., et al., *Controlling bulk conductivity in topological insulators: key role of anti‐site defects.* Advanced Materials, 2012. **24**(16): p. 2154-2158.

24. Mitchell, N.P., et al., *Amorphous topological insulators constructed from random point sets.* Nature Physics, 2018. **14**(4): p. 380-385.

25. Gilbert, M.J., *Topological electronics.* Communications Physics, 2021. **4**(1): p. 70.

26. Mellnik, A., et al., *Spin-transfer torque generated by a topological insulator.* Nature, 2014. **511**(7510): p. 449-451.

27. Isobe, H., S.-Y. Xu, and L. Fu, *High-frequency rectification via chiral Bloch electrons.* Science advances, 2020. **6**(13): p. eaay2497.

28. Yasuda, K., et al., *Large unidirectional magnetoresistance in a magnetic topological insulator.* Physical review letters, 2016. **117**(12): p. 127202.

29. Yasuda, K., et al., *Large non-reciprocal charge transport mediated by quantum anomalous Hall edge states.* Nature Nanotechnology, 2020. **15**(10): p. 831-835.

30. Baumgartner, C., et al., *Supercurrent rectification and magnetochiral effects in symmetric Josephson junctions.* Nature nanotechnology, 2022. **17**(1): p. 39-44.

31. He, P., et al., *Bilinear magnetoelectric resistance as a probe of three-dimensional spin texture in topological surface states.* Nature Physics, 2018. **14**(5): p. 495-499.

32. Legg, H.F., et al., *Giant magnetochiral anisotropy from quantum-confined surface states of topological insulator nanowires.* Nature Nanotechnology, 2022. **17**(7): p. 696-700.

33. Braunecker, B., et al., *Spin-selective Peierls transition in interacting one-dimensional conductors with spin-orbit interaction.* Physical Review B, 2010. **82**(4): p. 045127.

34. Legg, H.F., D. Loss, and J. Klinovaja, *Majorana bound states in topological insulators without a vortex.* Physical Review B, 2021. **104**(16): p. 165405.

35. Stern, A. and N.H. Lindner, *Topological quantum computation—from basic concepts to first experiments.* Science, 2013. **339**(6124): p. 1179-1184.

36. Liu, B., et al., *Surrounding Sensitive Electronic Properties of Bi_2Te_3 Nanoplates—Potential Sensing Applications of Topological Insulators.* Scientific Reports, 2014. **4**(1): p. 4639.

37. Korkusinski, M. and P. Hawrylak, *Quantum strain sensor with a topological insulator HgTe quantum dot.* Scientific reports, 2014. **4**(1): p. 4903.

38. Fujita, T., M.B.A. Jalil, and S.G. Tan, *Topological insulator cell for memory and magnetic sensor applications.* Applied Physics Express, 2011. **4**(9): p. 094201.

39. Annunziata, A.J., J.D. Chudow, and D.C. Worledge, *Magnetic field sensor based on topological insulator and insulating coupler materials*. 2018, Google Patents.

40. Liang, J., et al., *Maximizing the thermoelectric performance of topological insulator Bi_2Te_3 films in the few-quintuple layer regime.* Nanoscale, 2016. **8**(16): p. 8855-8862.

41. Xu, Y., Z. Gan, and S.-C. Zhang, *Enhanced thermoelectric performance and anomalous Seebeck effects in topological insulators.* Physical review letters, 2014. **112**(22): p. 226801.

42. Takahashi, R. and S. Murakami, *Thermoelectric transport in topological insulators.* Semiconductor Science and Technology, 2012. **27**(12): p. 124005.

43. Müchler, L., et al., *Topological insulators and thermoelectric materials*. 2013, Wiley Online Library. p. 91-100.

44. Liu, H. and P.D. Ye, *Atomic-layer-deposited Al_2O_3 on Bi_2Te_3 for topological insulator field-effect transistors.* Applied Physics Letters, 2011. **99**(5): p. 052108.

45. Steinberg, H., et al., *Surface state transport and ambipolar electric field effect in Bi_2Se_3 nanodevices.* Nano letters, 2010. **10**(12): p. 5032-5036.

46. Zhu, H., et al., *Topological insulator Bi_2Se_3 nanowire high performance field-effect transistors.* Scientific reports, 2013. **3**(1): p. 1757.

47. Vandenberghe, W.G. and M.V. Fischetti, *Imperfect two-dimensional topological insulator field-effect transistors.* Nature communications, 2017. **8**(1): p. 14184.

48. Nikonov, D.E. and I.A. Young, *Benchmarking of beyond-CMOS exploratory devices for logic integrated circuits.* IEEE Journal on Exploratory Solid-State Computational Devices and Circuits, 2015. **1**: p. 3-11.

Chapter 2. Literature Review

2.1 Order and disorder in solid state physics

Crystalline materials have been the traditional focus of solid-state physics due to their regular structure, which simplifies the formulation of theories for the description of physical properties. An ordering rule relates the property of one object to the same property of another object. In the case of perfect order, the properties of all objects can be derived from knowledge of only one object by repeated application of the ordering rule. If atomic positions are a property in a perfect crystal, then the translational symmetry of the crystal structure is the ordering rule. Most phases differ in their symmetry. Identifying the order parameter or the broken symmetry by looking for the important variables and degrees of freedom has been the key to classifying materials. The degree of freedom that is translational symmetry leads to crystalline ordering, rotational symmetry leads to ferroelectric ordering, a spin state symmetry leads magnetic ordering. The order parameter for superconductors and superfluid He^4 is a complex number φ [1].

However, many practical applications use materials that are weakly or strongly disordered, which poses significant challenges to the traditional approach. It is impossible to predict the positions of atoms from an ordering rule if there exist some randomness in the structure. Nevertheless, partial ordering or degree of disorder can be quantified by an order parameter. Weak disorder involves a perturbation of the perfect crystalline order, which includes defects, vacancies, and dislocations. These types of disorder are frequently observed in real materials. On the other hand, strong disorder signifies a marked departure from crystalline order, and amorphous materials are the most notable examples. These materials do not possess any long-range translational order, and there exists an element of randomness in the atomic positions. The length scales over which order or disorder persists are also of interest. Many materials possess a local order over length scales of a few atoms or molecules but are disordered on larger length scales. Inhomogeneous materials, such as multiphase materials, composites, and porous materials, can be regarded as disordered and homogeneous on sufficiently large length scales, and the inhomogeneities lead to more local strong disorder on mesoscopic (nm-μm) length scales. The concept of disorder is not restricted to structural and chemical

disorder, but it can also be applied to a wide range of materials properties. The structural/topological disorder can be characterised by the lack of long-range order and translational symmetry. The spin exhibits various values at lattice points in the magnetic disorder [2].

The idea of Landau order parameters has been central to physics over the past century, but a major development was the discovery of topological phase, the first being quantum Hall effect (QHE), which are not characterized by a Landau order parameter.

2.2 Quantum Hall effect (QHE)

The Hall effect is a phenomenon where a voltage difference appears across a conductor, transverse to the current and a magnetic field perpendicular to the current. This is due to charge carriers experiencing the Lorentz force. The Quantum Hall effect (QHE) is a quantized version of the Hall effect, which is observed in two-dimensional electron systems at low temperatures and high magnetic fields discovered by von Klitzing in 1980. In the QHE state, the Hall resistance R_{xy} or Hall conductance σ_{xy} can take specific, incredibly precise quantized values, as shown in Figure 2.1, according to the formula below:

$$R_{xy} = \frac{V_{Hall}}{I_{Channel}} = \frac{h}{ve^2} = \frac{25812.80745}{v}\ \Omega \text{ , or } \sigma_{xy} = v\frac{e^2}{h}$$

where h is Planck's constant and e is the elementary charge, whereas v can take on either integer (v=1, 2, 3, …) or fraction values (v =1/3, 2/5, 3/7, …). Depending on whether v is an integer or fraction, the quantum Hall effect is referred to as an integer or fractional quantum Hall effect. What makes this effect incredibly striking is the precision, universality, and resistivity determined by the universe's two fundamental constants (h, e).

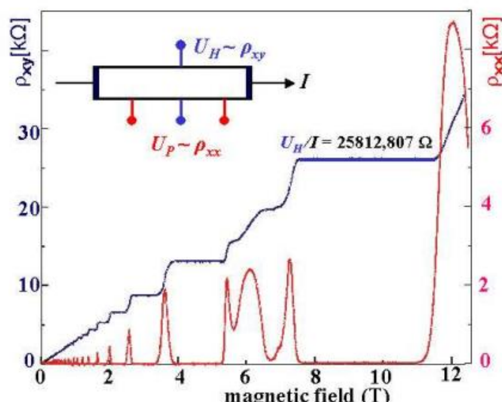

Figure 2.1. Hall and longitudinal resistivity as a function of the magnetic field for GaAs/AlGaAs heterostructures at 1.5 K. [3]

Electrons in such a two-dimensional electron gas (2DEG) system end up with quantized circular orbits having for energies, the famous Landau Levels,

$$E_n = (n + \frac{1}{2})\hbar\omega_c$$

where n is the Landau Level index, $\hbar$ is reduced Planck's constant, ω_c is the cyclotron frequency. One possible scenario is that the N Landau Levels are completely occupied, and the above levels are completely unoccupied. In that case, the Fermi level is located within the energy gap that separates occupied and unoccupied states, resulting in an insulator. However, different from the band insulator, the circular orbits in the 2DEG system drifted in the direction of E x B by the applied electric field perpendicular to the magnetic field. Therefore, metallic edges form at the system's boundaries, which is the observed Hall conductance. When a confining potential is added, it changes slowly in space, at the edges (r_1, r_2) of the samples, as in *Figure 2.2*, the potential must cross the confined harmonic oscillator states to create gapless edge states.

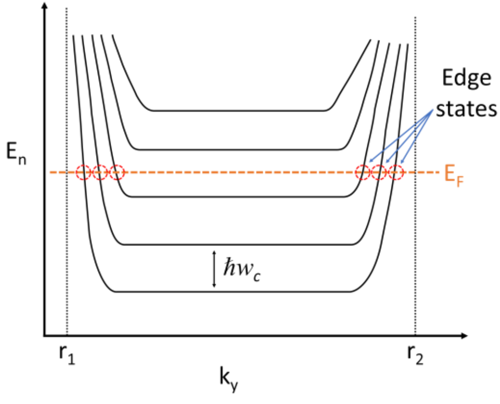

Figure 2.2. Landau level energy separation of a two-dimensional electron gas (2DEG).

Chiral edge modes are obtained with a velocity $v = \frac{1}{\hbar}\frac{\partial E}{\partial k_y}$, and they move in one direction at one edge of the sample and opposite direction at the other edge of the sample (opposite velocity slope). Classically, electrons experience cyclotron motion inside the sample. However, at the two edges of the sample, cyclotron motion cannot be completed and instead the electron is scattered and moves along one direction, whereas electrons on the opposite edge move in the opposite direction. This QHE state, with its distinctive edge modes, was the first example of a topological phase of matter and is the foundation the later discoveries including the Quantum Spin Hall effect and the 3D topological insulator. It is possible to describe such phases using a mathematics, known as a topological invariant, as introduced in the next section.

2.3 Topological band theory

2.3.1 Topology and topological invariant

Topology is a mathematical term that deals with geometrical properties that are not sensitive to small perturbations or smooth deformation. A topological invariant is a property of a topological space that is preserved under continuous deformations, such as stretching, bending, and twisting. To illustrate this idea, as depicted in *Figure 2.3*, each set of objects are topologically identical with each other having the same genus number. The objects within each set can be smoothly transformed into one another without cutting or drilling a hole. This means each pair of objects is, in a topological sense, the same. The solid cylinder in *Figure 2.3* (a) and the hollow cylinder in *Figure 2.3* (b) are distinguished by an integer topological invariant called the genus (g) number, which is the number of holes in the object. Thus, the surfaces with different genus number cannot be smoothly transformed into one another, and they are topologically distinct.

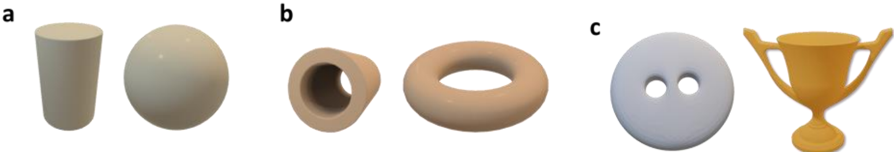

Figure 2.3. Illustrates topologically equivalent objects in (a) g=0, (b) g=1, and (c) g=2 and shows the distinction between each set of objects that are topologically inequivalent. (Topological invariant = number of “holes”, in this case)

Topological invariants are important in mathematics and physics as they provide a method to classify and study the topological structure of different spaces. The majority of the topological invariants used in physics are the result of integrals of some geometric quantity. The Gauss-Bonnet theorem states that the total Gaussian curvature of a closed surface is equal to 2π times the Euler characteristic of the surface, which is useful to link the curvature of a surface to its topology. According to the theorem, the area integral of curvature over a closed surface M is a topological invariant. Here we give an example of calculating the topological invariant of a sphere (2D closed surface). The Gaussian curvature is a measure of the curvature of a surface at a certain point and defined as the product of the principal curvatures ($K=k_1k_2$) at that point, which are the curvatures of the surface along the two principal directions at the point. Gaussian curvature also can be expressed as the inverse of two radii of the curvature, ($K=1/r_1r_2$). For a sphere, the Gaussian curvature is:

$$K = \frac{1}{r^2}$$

$$\iint K \, dA = 2\pi\chi = 2\pi(2 - 2g)$$

where, for a sphere, $g = 0$, K is the Gaussian curvature, A is the surface area, χ is the Euler characteristic number (χ=2 for sphere), and g is genus number.

Although topology classification is easiest to understand when applied to surfaces in normal geometrical space, it can also be applied to any abstract mathematical space including to the quantum Hilbert space that describes the electronic structure of materials. According to the Bloch theorem, the electron wave function in a crystal can be expressed as:

$$\psi_{nk}(r) = e^{ikr} u_{nk}(r)$$

where k is the crystal momentum and u is the periodicity of the crystal lattice. A closed surface M exists by all the k points in the first Brillouin Zone (BZ) of a crystal. To calculate the topological invariant of the electronic band structure, one needs to integrate the Berry curvature, which will be discussed in the next section. Analogous to other topological classifications (e.g., simple shapes), topological insulators and trivial (or normal) insulators are distinct from each other and classified in different topological

classes using the result of the integration. If the Hamiltonian of one insulating state can be continuously transformed into another state without closing the energy gap, then these two states are topologically equivalent. Those classes are described by a topological invariant n, called the Chern number. A detailed mathematical treatment is beyond the scope of this work but is available in Ref. [4].

The basic analogy between topological band-structures and topological shapes is illustrated schematically in Figure 2.4. In both 2D and 3D, topologically non-trivial materials have a variety of unique physical properties, including the existence of conducting surface states, and the potential to exhibit a range of special anomalous Hall conductivity effects, as summarized in *Figure 2.5*.

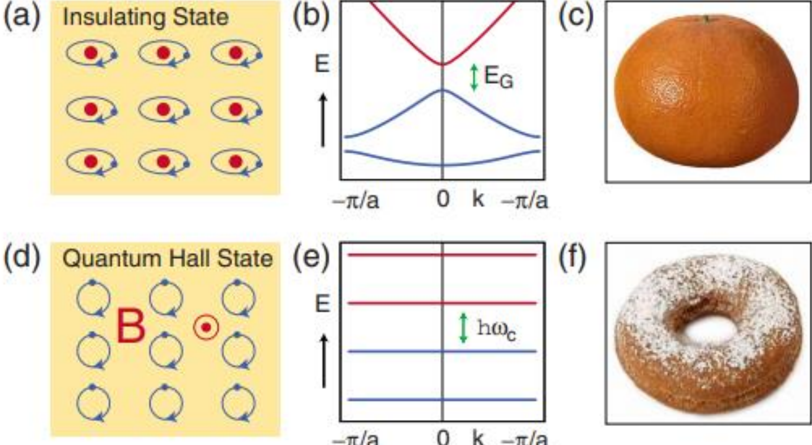

Figure 2.4. An illustration of the analogy between electronic band-structure topology and real-space topology. (a)–(c) The atomic insulating state is a topologically trivial state. The simplest example of a topologically non-trivial state is the Quantum Hall State in (d) which has a band-structure in (e). Like the two surfaces (c and f) which differ in their genus, the band-structures (b) and (e) are also distinguished from one another by a topological invariant, the Chern number, similar to the genus.[5]

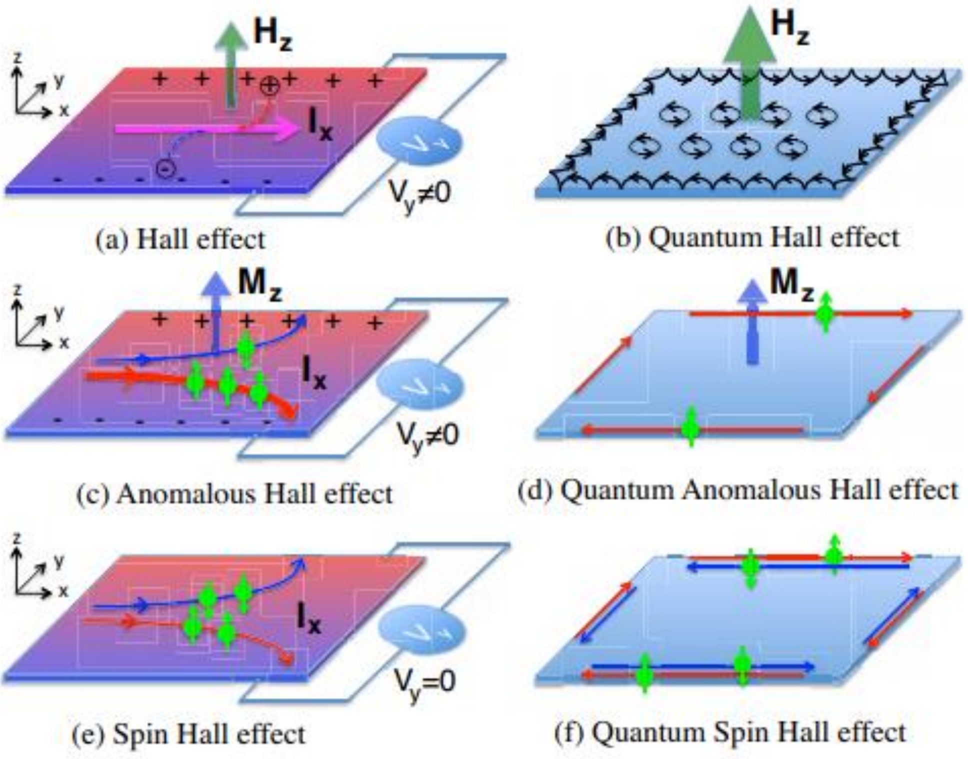

Figure 2.5. Schematic illustrations showing the differences and similarities between various Hall effects. While any semiconductor may exhibit the Hall effect, and any magnetic material may exhibit the Anomalous Hall effect, the Quantum anomalous Hall effect is uniquely realized in topological insulators. Adapted from Ref. [6].

2.3.2 Bulk-boundary correspondence

As discussed in the previous section, the goal of topological band theory is to classify and understand the properties of different electronic phases. This can be by identifying and characterizing the gapless states that occur at interfaces between topologically distinct phases, as illustrated in *Figure* 2.6. Somewhere in between the topological insulator and trivial insulator (vacuum) interface, the energy gap must close, otherwise the two phases would be equivalent. Additionally, there exist low energy electronic states connected to the region where the energy gap crosses zero. In fact, the gapless states at the interface can be topologically classified, according to the so-called bulk-boundary correspondence that relates boundary effects at an interface to the difference in the bulk topological invariants [7]. These states are related to the topological characteristics of the bulk and boundary regions.

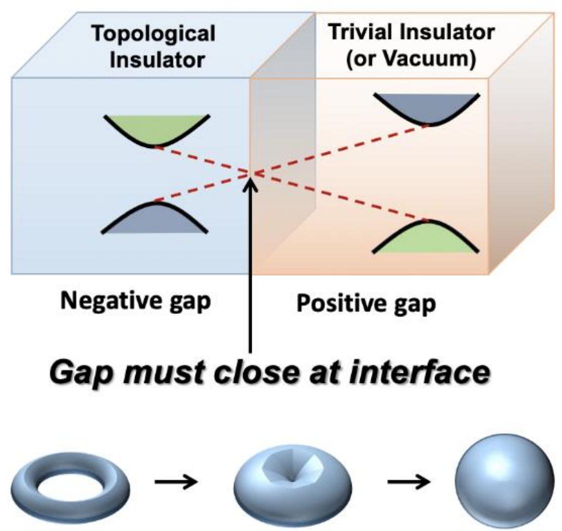

Figure 2.6. Gapless states at the interface of two topologically different phases (Ref. (https://blogs.iu.edu/sciu/2020/11/14/can-you-turn-a-baseball-into-a-donut/))

2.3.3 Berry Phase

The Berry phase is a geometric phase angle between 0-2π, also refers to a phase angle as in complex number $e^{i\phi}$, which describes accumulated global phase evolution of a vector as it traverses around a closed path in a vector space. The Berry phase is named after Michael Berry who explained the concept in his paper [8]. It depends only on the trajectory that the system takes and it is independent of time taken by the system to traverse the path. For example, a similar phase angle appears in parallel transport of vector or parallel translation along the path on a curved surface shown in Figure 2.7. The red vector starts at P moves to A and then continues along the path (green dashed line) shown to B and then finally returns to P (blue vector) while keeping it constant (without any change to its length and direction) .On a curved surface, if a vector travels on a closed loop, the vector has rotated from its initial direction as illustrated in the figure, and additional angle difference between blue and red vectors *v*. The angle of rotation is a geometric phase analogous to Berry phase. In the parallel transport problem, to get the global vector rotation (phase angle), one must keep track of how basis vectors vary along the path. However, in quantum mechanical phase associated with quantum states, one must keep track of how the state $|\psi\rangle$ varies along the path λ. Here, the phase adds up to be $\int\langle\psi(\lambda)|\partial\lambda|\psi(\lambda)\rangle d\lambda$. If λ is a vector with multiple parameters, then ∂λ is a gradient operator with respect to λ, and the integral is a line integral along some trajectory of λ. This line integral is an effective vector potential called the Berry connection. The curl of

that vector potential is some effective magnetic field, called the Berry curvature. Then the line integral above, if it's around some closed path in λ, is equal to the flux of that effective magnetic field through the closed path, and the accumulated Berry phase around that closed path is then analogous to the Aharonov-Bohm phase.

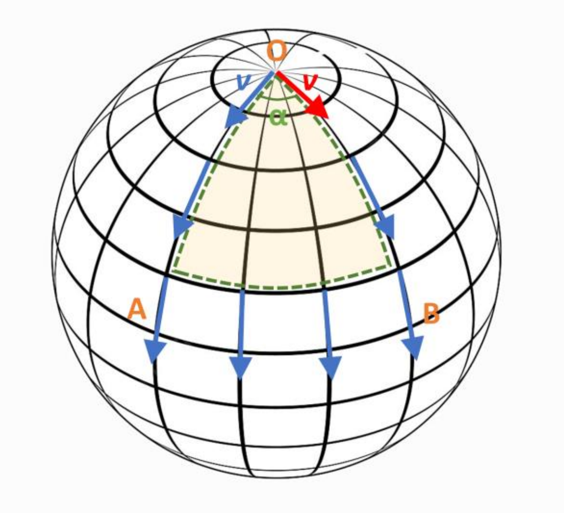

Figure 2.7. Parallel transport of a vector ν around a closed loop (from O to A to B and back to O) on the sphere.

To apply the concept of Berry phase to topological materials, in terms of the standard mathematical language, one can consider the Hamiltonian of a material as it is changed slowly, in the adiabatic limit, so that system remains in time-independent ground states. The wave function evolves as:

$$\psi(t) = \psi_n(\lambda(t))e^{-i\int_0^t dt' \varepsilon_n/\hbar}e^{-i\gamma_n}$$

Where Υ_n is called the Berry phase. As stated previously, the Berry phase doesn't depend on time, it only depends on the geometry of the path.

$$\gamma_n = \oint d\lambda \, \langle \psi_n \left| i\frac{\partial}{\partial \lambda} \right| \psi_n \rangle$$

In crystals, k is equal to the parameter λ. So, the Berry phase is

$$\gamma_n = \oint A(k)\, dk$$

The Berry connection is

$$A(k) = \langle u_{nk} | i\nabla_k | u_{nk} \rangle$$

The Berry connection is gauge dependent and under this change, A(k) changes by the gradient.

$$A(k) \rightarrow A(k) + \nabla_k \chi$$

This is analogous to the vector potential in electrodynamics. In 3D space, Berry's phase resembles the expression for magnetic flux in terms of the vector potential

$$\vec{B} = \nabla \times \vec{A}$$

Analogous to the relationship between magnetic field strength B and its vector potential, we can get the Berry curvature by taking the curl of Berry connection A(k):

$$\Omega(k) = \nabla \times A(k)$$

Using Stokes' theorem, Berry's phase can be expressed as a flux through a surface.

$$\gamma_n \equiv \int_S \vec{B} \cdot \mathrm{d}\vec{a} = \int_S (\nabla \times \vec{A}) \cdot \mathrm{d}\vec{a} = \oint_C \vec{A} \cdot \mathrm{d}\vec{r}$$

In a 2D Brillouin zone, the integral of the Berry curvature over the closed 2D space is equal to 2π times the number of times the unit vector **d**(k) wraps around the sphere as a function of the crystal momentum **k**. This result is known as the "Berry phase" and it is a fundamental concept in the field of condensed matter physics and quantum mechanics. A topological invariant called the Chern number [9], for a closed surface can be expressed as

$$n = \frac{1}{2\pi} \oiint dS \cdot \Omega(k)$$

The Chern number is quantized due to the fact that the surface integral of a loop on a closed surface is a multiple of *2π*. This means that the Berry curvature integrated over the closed surface must be *2πn*. The Table 2.1 shows the analogies of Berry phase for comparison below.

Table 2.1. Analogies of Berry Phase:

Berry Connection: $A(k) = \langle u_{nk} \vert i\nabla_k \vert u_{nk} \rangle$	Vector potential: $\mathrm{A}(r)$
Berry Curvature: $\Omega(k) = \nabla \times A(k)$	Magnetic field: $\mathrm{B}(r)$
Berry phase: $\gamma_n = \oint A(k)\, dk = \iint dS \cdot \Omega(k)$	Aharonov-Bohm phase: $\oint A(r)\, dr = \iint dS \cdot B(r)$
Chern number: $\frac{1}{2\pi} \oiint dS \cdot \Omega(k) = integer$	Dirac monopole: $\oiint dS \cdot B(r) = n\frac{h}{e}$ $(n\ is\ integer)$

In 1982, D. J. Thouless, M. Kohmoto, M. P. Nightingale, and M. den Nijs (TKNN) pointed out that the integer quantum Hall effect in a 2D crystal follows from the integral of Berry curvature, Ω(k).

$$\sigma_H = \frac{ie^2}{2\pi h} \sum \int d^2k \int d^2r \left(\frac{\partial u^*}{\partial k_1} \frac{\partial u}{\partial k_2} - \frac{\partial u^*}{\partial k_2} \frac{\partial u}{\partial k_1} \right) \qquad \left(i\Omega(k) = \left(\frac{\partial u^*}{\partial k_1} \frac{\partial u}{\partial k_2} - \frac{\partial u^*}{\partial k_2} \frac{\partial u}{\partial k_1} \right)\right)$$

$$= \frac{ie^2}{4\pi h} \sum \oint dk_j \int d^2r \left(u^* \frac{\partial u}{\partial k_j} - \frac{\partial u^*}{\partial k_j} u \right) \qquad [10]$$

$$\sigma_H = n\frac{e^2}{h}$$

where n is the TKNN number and is also called the first Chern number.

The Berry phase has significance for approaching the electronic properties of crystalline materials. An electronic wavepacket initially at a specific Bloch state with an initial

crystal momentum of $\hbar$k undergoes propagation, there exist Fermi velocity $\partial E(k)/\partial k$ and can be written **F**=m**a** using electric and magnetic fields. Here, there is the usual phase that adds up from the wavepacket propagating in space (the Fermi velocity piece), but there can be an additional Berry phase which here comes from how the Bloch states vary throughout k-space as discussed earlier. That can be written in terms of an "anomalous velocity" (anomalous because it's not from the usual Fermi velocity picture) and can lead to the anomalous Hall effect.

2.4 $\mathbb{Z}_2$ classification of topological insulators

The $\mathbb{Z}_2$ classification is a way of categorizing insulators, including topological insulators (TIs) to identify their topological properties, and is closely related to the Chern number described above. In this classification system, TIs are divided into two categories: strong topological insulators (STIs) and weak topological insulators (WTIs). Both the STIs and WTIs are TIs that have a topological invariant known as the $\mathbb{Z}_2$ topological index, which is a number that characterizes the topological properties of the material. A 2D system has one $\mathbb{Z}_2$ index with a $\mathbb{Z}_2$=1 index that indicates a topological (nontrivial) state which has an odd number of edge states that cross the energy gap, while a material with a $\mathbb{Z}_2$=0 index is trivial and has an even number of edge states. A 3D topological insulator is characterized by 4-index $\mathbb{Z}_2$ invariants (values either take 0 or 1). These four invariants represent the topological properties of the insulator with respect to time-reversal symmetry, inversion symmetry, and two additional crystalline symmetries. The first two invariants, which correspond to time-reversal and inversion symmetries, are the same as those in the original 2-index $\mathbb{Z}_2$ classification. They indicate whether the material is a strong or weak topological insulator with respect to time-reversal and inversion symmetries. The third and fourth invariants, which correspond to the additional crystalline symmetries, indicate whether the material has topologically protected surface states that are invariant under certain crystal symmetries. These symmetries can include rotational symmetries, mirror symmetries, and other types of symmetries that can be present in crystalline materials. STIs have a fully gapped energy spectrum and surface has an odd number of Dirac points. Non-magnetic disorder on the surface does not affect the electron localization, leading to near-perfect metallic surface states.

WTIs, on the other hand, do not have a fully gapped energy spectrum. They have a small

gap between the valence and conduction bands, but there are also states within this gap that are referred to as "zero-energy states." These zero-energy states are topologically protected and give rise to robust surface states, but they are more susceptible to perturbations than the surface states of STIs. Weak TIs such as Sb_2Se_3 have an even number of Dirac points in their surface Brillouin zone and the presence of strong disorder leads to electron localization on the surface [11].

2.5 Quantum spin Hall (QSH) insulator

The QHE, introduced in Section 2.1, is a topological state of matter. Naturally, questions arise: are there other topological states of matter that do not require two-dimensions and a magnetic field?

The Quantum Spin Hall Effect (QSHE) is a variation of the Hall effect where the total Hall conductance is zero, but the spin Hall conductance is non-zero. It is achieved by combining the spin-up and spin-down versions of the Quantum Hall Effect (QHE) with opposite chirality. Initially, C. L. Kane and E. J. Mele proposed that this can be understood by introducing a spin-orbital interaction/coupling (SOC) term in the system Hamiltonian, similar to Haldane's model [12]. This SOC term creates a periodic magnetic field with no net flux and opens a finite energy gap. At temperatures well below this gap, the double spin Haldane's model leads to a quantized Hall conductance ($\sigma_{xy}=e^2/h$) for each spin, and the edge modes are helical spin modes, where the spin-up and spin-down electrons have opposite momentums. The QSH effect can be understood as a consequence of the interplay between the time-reversal symmetry and the spin-orbit interaction. The time-reversal symmetry enforces a Kramers degeneracy at the time-reversal invariant momenta, which means that the electronic states at these momenta come in pairs with opposite spin. The spin-orbit interaction, on the other hand, breaks the spin degeneracy and opens a gap at the time-reversal invariant momenta. This gap is known as the spin-orbit gap.

The time TRS protects edge modes from non-magnetic impurities and disorder. This is demonstrated in Figure 2.8 b where scattered electrons have a 2π phase difference due to the presence of TRS. In quantum mechanics, this results in the wave function changing

sign when spin -1/2 particles are rotated by 2π, causing two backscattering events to cancel each other out, similar to an anti-reflection coated lens illustrated in Figure 2.8 a. However, the presence of magnetic impurities breaks the TRS and disrupts backscattering-immune transport. The π Berry's phase of TI protects surface states against backscattering from impurities and leads to the weak antilocalization (WAL) effect [13].

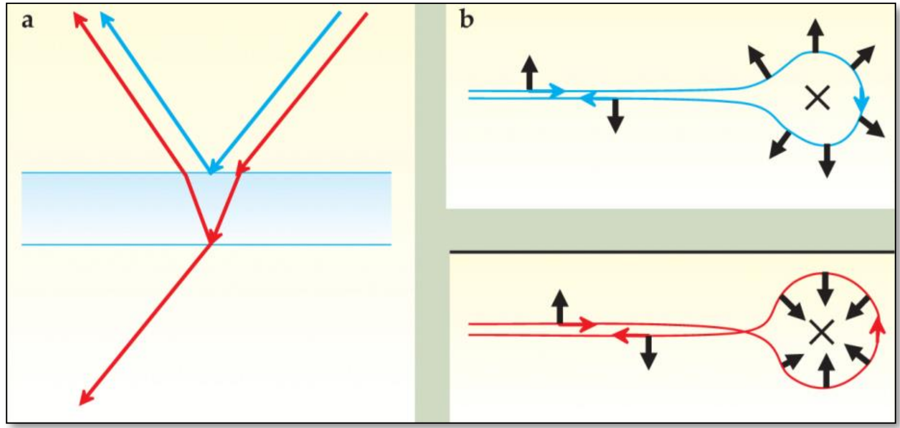

Figure 2.8. (a) On a lens with antireflection coating, light waves reflected by the top (blue line) and the bottom (red line) surfaces interfere destructively, which leads to suppressed reflection. (b) A quantum spin Hall edge state can be scattered in two directions by a nonmagnetic impurity. Going clockwise along the blue curve, the spin rotates by π; counterclockwise along the red curve, by −π. A quantum mechanical phase factor of −1 associated with that difference of 2π leads to destructive interference of the two paths—the backscattering of electrons is suppressed in a way similar to that of photons off the antireflection coating [14].

2.6 Quantum anomalous Hall effect (QAHE) and magnetic TIs

The Hall effect was first discovered in 1879. Later in 1880, E. Hall noticed that, in many ferromagnets, the transverse resistivity gains an additional term independent of magnetic field, which is proportional to the magnetization of the sample. The effect became known as the anomalous Hall effect (AHE). The related quantum version of this phenomenon is called the quantum anomalous Hall effect (QAHE). Unlike the quantum Hall effect, which relies on external magnetic fields, the QAHE arises from the electron orbits and Landau levels present in a ferromagnetic material without an external magnetic field. To achieve a nonzero Hall conductance, time reversal symmetry must be broken. In 1988, F.D.M. Haldane proposed a theoretical model for achieving the QAHE in a spinless

hexagonal lattice using applied periodic magnetic flux [15]. However, experimental realization of this effect was not achieved until many years later in topological systems.

A new state of the quantum anomalous Hall effect (QAHE) was proposed in magnetic doped topological insulator films, such as Bi_2Se_3 [16]. By considering both the exchange field of ferromagnetism and spin-orbit coupling (SOC), a gap can be opened between the bottom of the conduction band and the top of the valence band, as illustrated in Figure 2.9, resulting in a quantum phase transition to the QAHE state. In this state, the Hall conductance is determined by the first Chern number of the occupied bands and must be an integer multiple of e^2/h.

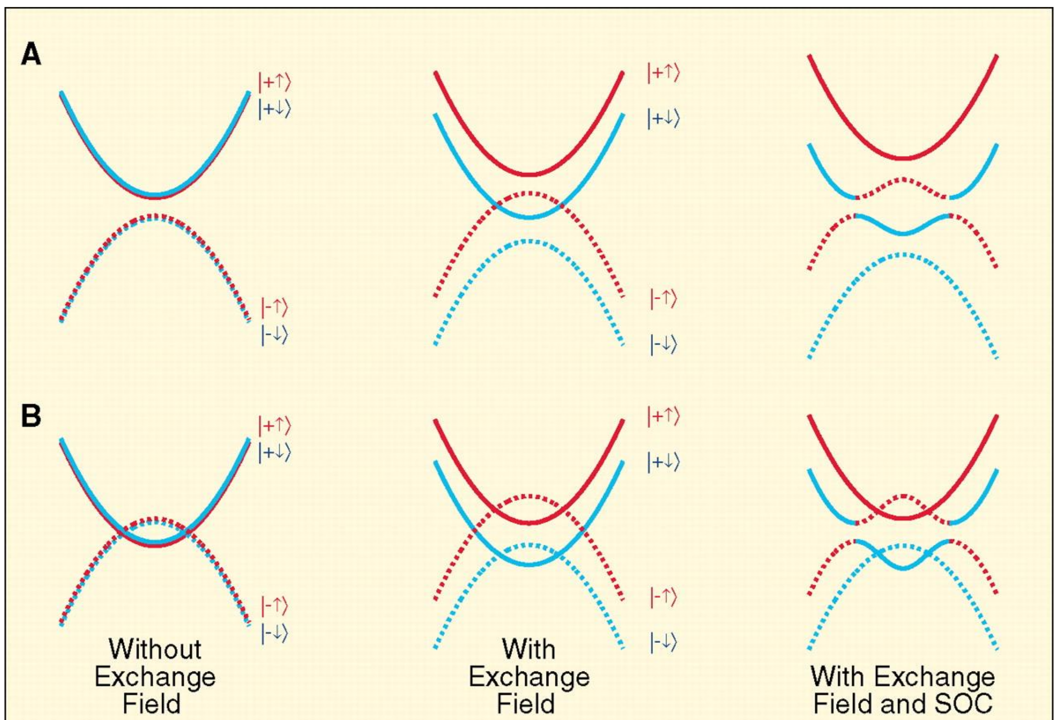

Figure 2.9. Evolution of the subband structure upon increasing the exchange field. The solid lines denote the subbands that have even parity at Γ point, and dashed lines denote subbands with odd parity at Γ point. The blue colour denotes the spin down electrons; red, spin up electrons. (A) The initial subbands are not inverted. When the exchange field is strong enough, a pair of inverted subbands appears (red dashed line and blue solid line). (B) The initial subbands are already inverted. The exchange field releases the band inversion in one pair of subbands (red solid line and blue dashed line) and increases the band inversion in the other pair (red dashed line and blue solid line) [16].

The transport evidence of quantum anomalous Hall states and the QAHE has been experimentally realized in both magnetic chromium and vanadium doped $(Bi,Sb)_2Te_3$ thin

films [17, 18]. These films have been observed to have a quantized Hall resistance of h/e^2 and a decrease in longitudinal resistance. However, the onset temperature of these states is low, and it is believed that in-gap features introduced by the transition metal dopants can negatively impact performance. Therefore, research is ongoing to study other magnetic dopants in TIs, such as V-, Cr- and Mn-Sb_2Te_3, Fe- and Mn-doped single crystals of Bi_2Te_3, and Cr- and Mn-doped Bi_2Se_3, in order to determine the optimal set of dopants, magnetic order, and transport properties in thin films and single crystals.

The quantized anomalous Hall effect (QAHE) has the potential to lead to a new generation of low-energy devices that can work at zero fields. To achieve this important quantum state, a wide-band topological insulator with a Dirac point near the Fermi energy is needed. This can be achieved by doping the topological insulator with a ferromagnetic element or sandwiching the TI between ferromagnetic layers. One of the signature of QAHE is that with decreasing temperature, ρ_{xy} develops a hysteresis loop induced by the ferromagnetic order in the system [19]. To make this effect more practical, it is important to raise the critical temperature at which QAHE can be observed by ensuring the survival of topological surface states at high temperatures and maintaining ferromagnetic ordering. The first experimentally realised QAHE in the $Cr0_{.15}(Bi_{0.1}Sb_{0.9})_{1.85}Te_3$ film was observed at 30 mK [17].

2.7 Two-dimensional (2D) to three-dimensional (3D) topological insulators

The earliest discovery and research on topological insulators mainly focused on the quantum well 2D systems [15, 20-23]. This trend continued until the first theoretical calculations by Zhang’s group using first-principle calculations proposed the 3D TIs based on chalcogenides containing elements of Sb, Bi, Te, and Se [24]. Their calculations predicted that Sb_2Te_3, Bi_2Te_3, and Bi_2Se_3 are topological insulators whereas Sb_2Se_3 is an ordinary, trivial insulator. These calculations were supported by the ARPES experiments and scanning tunnelling microscopy (STM) measurements showing the dispersion of metallic surface states together with a bulk insulating gap with a single Dirac cone [11, 25-27]. The Sb_2Te_3, Bi_2Se_3, and Bi_2Te_3 chalcogenide family of TIs is now the most experimentally explored TIs. Sb_2Te_3 is one of the most important topological insulators with a layered structure and it is also used for as a phase change memory material [28,

29]. Each quintuple layer consists of 2 sheets of Sb and 3 sheets of Te in the order of Te-Sb-Te-Sb-Te. Bi_2Te_3 is a well-studied topological insulator and also is an efficient thermoelectric material [25, 30-33]. Bi_2Te_3 has a rhombohedral crystal structure with the space group R$\overline{3}$m, and quintuple layers (Te (A) - Bi (B) - Te (C) - Bi (B) -Te(A)) stacked along the rhombohedral [111] direction as depicted in Figure 2.10 (a). The high symmetry points in the Brillouin zone are depicted in Figure 2.10 (b).

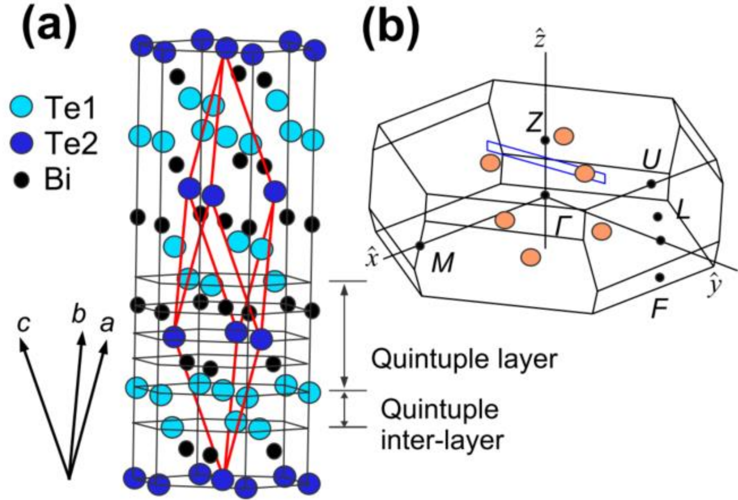

Figure 2.10. (a) Bi_2Te_3 crystal structure and corresponding (b) rhombohedral Brillouin zone. [34]

In the same family, Bi_2Se_3 is a well-known and one of most representative examples of 3D topological insulators with a theoretically predicted energy gap of 0.3 eV [24] which agrees well with the experimentally measured energy gap of 0.2-0.3 eV [35, 36]. Below Figure 2.11 shows the band structure of Bi_2Se_3 (a) without consideration of spin-orbit coupling (SOC), and (b) with spin-orbit coupling. By comparison, it can be clearly seen that an anti-crossing feature has been introduced around the Γ point and thus the inversion between the conduction band and valence band s-p states occurs due to the SOC effect. By calculating the product of the parities of the Bloch wavefunction at Γ, F, L, Z in the Brillouin zone, it has been confirmed that only at the Γ point, the parity changes owing to the SOC effect and the parity remains the same at other momenta F, L, Z points. This indicates that Bi_2Se_3 is a topological insulator.

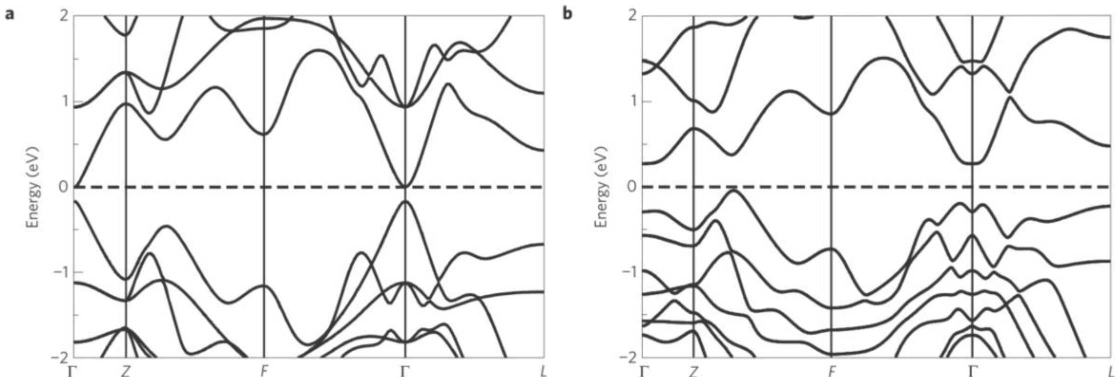

Figure 2.11. Bulk band structure of Bi_2Se_3 (a) without consideration of spin-orbit coupling (SOC), and (b) with spin-orbit coupling. [24]

The existence of topological surface states is one of the key signatures of the topological insulators. The *ab initio* calculation is a powerful tool to calculate the surface states to see the topological features of different systems. Figure 2.12 shows the dispersion of the local density of states (LDOS) based on an *ab initio* calculation of Sb_2Se_3, Sb_2Te_3, Bi_2Se_3, and Bi_2Te_3 systems. It can be clearly seen that the surface states (red lines in the figures) are dispersed in the bulk band gap of Sb_2Te_3, Bi_2Se_3, and Bi_2Te_3 systems around the Γ point as a single Dirac cone. In contrast, there is no surface state for Sb_2Se_3, therefore it is a trivial insulator rather than a topological insulator.

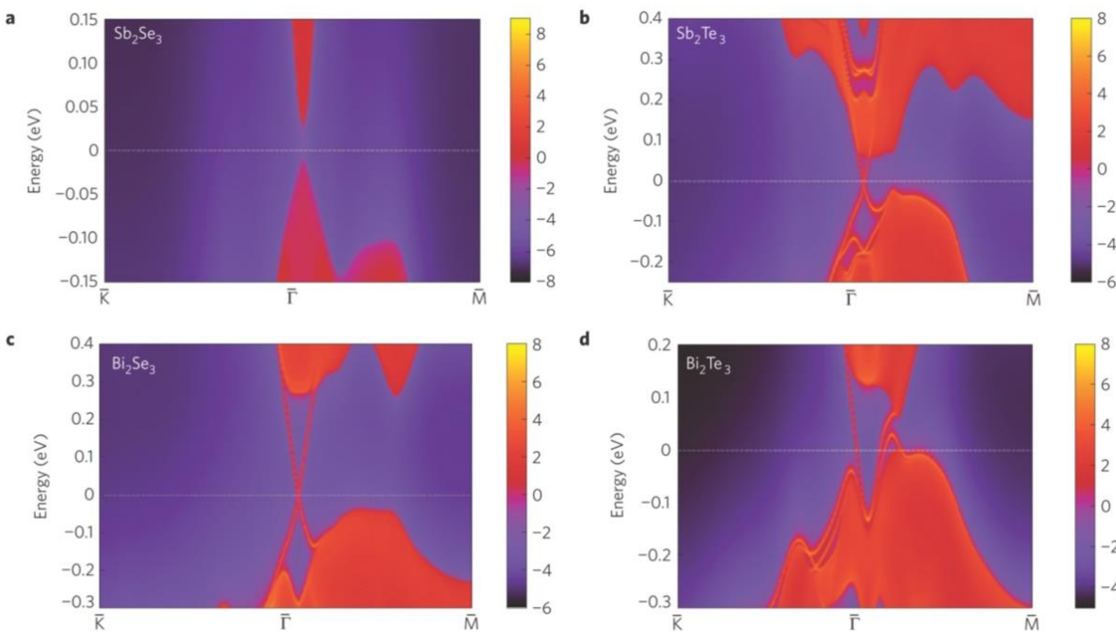

Figure 2.12. The surface local density of states (LDOS) on the (111) plane for (a) Sb_2Se_3, (b) Sb_2Te_3, (c) Bi_2Se_3, and (d) Bi_2Te_3 systems. [24]

2.8 Overview of available methods for topological insulator electronic structure

There are several experimental probes that are commonly used to study the properties of topological insulators (TIs). For comprehending the literature on topological insulators, it is critical that any reader is familiar with these common widespread techniques, although not all of these were used in the current thesis. The specific techniques used in this thesis was magnetotransport, and the specific technical details are discussed in Chapter 3. Here we just provide a literature of a wider range of common techniques in the field for the sake completeness/comparison, providing an overview of the basic information that these techniques provide. These probes include:

ARPES: This optical/X-ray technique provides a direct measurement to probe the allowed energies and momenta of the electrons in a material. It is based on the photoelectron effect, whereby photoelectrons are emitted from a sample irradiated with photons. In ARPES measurements, the photon beam incidence angle determines the momentum transfer to the sample. By sweeping the angle of incidence of the photon beam while keeping the energy fixed, and analysing the energy and momentum of the out-going electrons, one can gain insights into the electronic band structure and electronic interactions, in the system [37]. ARPES can map the electronic band structure and Fermi surfaces, and dispersion of the surface states by direct measurement of kinetic energy and the emission angle distribution of emitted photoelectrons. Thus, ARPES is well suited for detecting the topological surface states. By using modulated photon energy and conducting high-resolution ARPES, it is possible to clearly differentiate between the surface states and the bulk 3D band structure. This is because the surface states do not disperse in a direction perpendicular to the surface, whereas the bulk states do. ARPES measurement on Bi_2Se_3 [36], Bi_2Te_3, and Sb_2Te_3 has directly confirmed the topological nature of those materials.

STM: STM is a great example of using a quantum mechanical process (electron tunnelling) in a real-world practical application. The STM technique uses a fine conductive probe to scan the surface of a material and measure the local density of states (LDOS). When the STEM probe tip is extremely close to the surface (usually <1 nm), the electron cloud of the first atom of the probe tip and surface begin to overlap. It can be

used to study the spatial distribution of the surface states and to observe local phenomena such as the formation of bound states [38]. Applying a bias between the probe tip and the surface generates a current as electrons are driven to tunnel through the potential barrier from the tip to the surface. This tunnelling current is very sensitive to the gap between the probe tip and specimen surface. When the probe tip scans the surface of a conductive specimen, the intensity of the tunnelling current maps the sample's electronic density of states. The STM has two operating modes. Using the "constant height mode", the probe tip scans across a specimen and measures the changes in the intensity of tunnelling current. Under this mode, the applied voltage to the tip is varied at each pixel point as the tip scans over the sample. This allows the probing of electronic density of states of the sample surface, defects, frontier molecular orbitals [38]. Another popular mode is "constant current mode", in which tunnelling current is constant by adjusting distance (between probe tip and surface). Under this mode, surface roughness, defects, and the size and conformation of molecules on the surface can be constructed [38].

Magnetotransport measurements: These measurements involve applying a magnetic field to a material and measuring the response of the material's electrical transport properties at various temperatures. In this thesis, magnetotransport is the main technique used to characterize the electronic properties of topological insulators. The Figure 2.13 shows the typical configuration for transport measurements, where R_{xx}/ρ_{xx} is calculated through measuring voltage drop along the current flow direction (magnetoconductivity is $\sigma_{xx} = 1/\rho_{xx}$). Then, magnetoresistance (MR) can be calculated with the below formula:

$$MR(\%) = \frac{\rho(H) - \rho(0)}{\rho(0)} \times 100$$

where, ρ(H) is the resistivity at a certain magnetic field, ρ(0) is the resistivity at zero magnetic field. Hall resistance/resistivity (R_{xy}/ρ_{xy}) is calculated through measuring the Hall voltage (V_H) created by an applied magnetic field. Hall measurements are also used for the calculation of the Hall coefficient, carrier concentration (and determination of carrier type) and the carrier mobility of the measured sample.

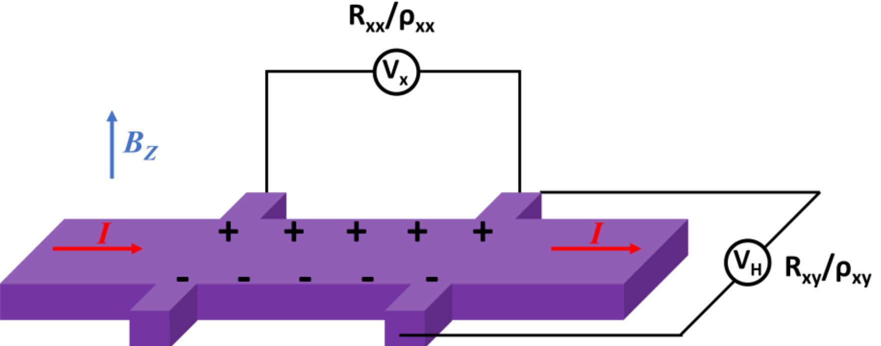

Figure 2.13. Standard transport measurement configuration where a sample's resistance and Hall resistance are measured at different temperatures and magnetic fields.

Transport measurements are bulk measurements that provide average behaviour of the electrons over a large scale as compared to ARPES and STM. ARPES and STM are surface sensitive techniques, which require delicate sample preparation and handling, and moreover generally mainly provide information about the electronic properties of the near-surface regions, whereas sample preparation for transport measurements is easy and can be performed on various material types.

Topological insulators provide numerous signatures in the magnetotransport, including distinctive quantum oscillations, weak antilocalization and Landau quantization. Transport measurements are a powerful technique for gaining insight into a material's fundamental physics and potential applications. These are discussed in detail in the next section (2.9).

2.9 Magnetotransport of topological insulators and surface states

2.9.1 Quantum oscillations

When a large magnetic field is applied, owing to Landau quantization of energy states, the density of states (DOS) is modulated by the magnetic field. This leads to the occurrence of quantum oscillations in conductivity or resistivity, known as Shubnikov de Hass (SdH) oscillations. The SdH oscillation follows

$$\Delta(1/B) = \frac{e}{hF_S} \qquad 2.1)$$

$$\mathrm{f} = \frac{1}{\Delta(1/B)} = \frac{hF_S}{e} \quad 2.2)$$

where B is magnetic flux density, F_S is area of the Fermi surface, e is the electron charge, f is oscillation frequency, and h is the Plank constant. The SdH oscillation frequency (period) is proportional to the inverse of the magnetic field (1/B), Δ(1/B) is the change in inverse magnetic field needed to cause oscillation. By getting the oscillation frequencies, one can study the extremal cross-sectional area of the Fermi surface perpendicular to the magnetic field. In magnetotransport of 3D TIs, SdH oscillations are used to distinguish and evaluate the 2D metallic surface states, which exist alongside the 3D bulk states. By analysing the oscillation, the position of the Fermi level, the Berry phase, and the concentration of the 2D surface state carriers etc. parameters related to the surface states can be determined.

2.9.2 Weak antilocalization and weak localization

In Figure 2.8 (section 2.5), it was mentioned that π Berry phase associated with the TI surface carriers leads to the WAL effect. WAL was first derived by Hikami, Larkin, and Nagaoka, which is related to the strong SOC [39]. In the quantum diffusion regime (system size ~ phase coherence length >> mean free path), the phase coherence of an electron is unchanged even after it is scattered many times [40]. This results in an enhancement of the classical electronic conductivity due to the destructive quantum interference that suppresses back-scattering leading to WAL [41]. Destructive interference tends to break when applying a magnetic field, leading to a negative magnetoconductivity (MC), a typical signature of WAL.

Hikami-Larkin-Nagaoka (HLN) theory is frequently applied for weak magnetic field conductivity variation in 2D electron systems within the limit of strong spin-orbit interaction [42].

$$\Delta\sigma = \frac{ae^2}{2\pi^2\hbar}\left[\ln\left(\frac{\hbar}{4eBl_\emptyset^2}\right) - \psi\left(\frac{1}{2} + \frac{\hbar}{4eBl_\emptyset^2}\right)\right] \quad 2.3)$$

where ψ is the digamma function, and the prefactor α=1/2 if topological surface carriers have a π Berry phase. Multiple independent bands with WAL in weak interband coupling limit, add up to result in bigger α (e.g.,1, 1.5). Whereas weak localization (WL) is the

result of the gap opening at the Dirac point, and gives ρ_{xx} with a linear dependence on field (at low field), magnetic scattering or a hybridized gap can lead the MC from WAL to parabolic dependence on the magnetic field (B^2). Increasing the energy gap (Δ)/ Fermi energy (E_F) ratio can drive the MC to the opposite weak localization (WL) regime. The cross-over from WAL to WL can occur by tuning the TRS-breaking energy gap or the position of Fermi level. The relationship between the Berry phase, the gap and E_F can be expressed as:

$$\emptyset = \pi(1 - \frac{\Delta}{2E_F})$$

$\phi = \pi$ for WAL when $\Delta/2E_F = 0$ and $\phi = 0$ for WL when $\Delta = 2E_F$.

2.9.3 Landau level quantization

Landau level quantisation occurs when a charged particle travels in a magnetic field perpendicular to its motion. Due to a Lorentz force, a charged particle moves in a circular trajectory and this is quantised, known as a Landau level. They can be used to study the topological nature of the surface states through Landau level quantization of energy states by large magnetic fields. Quantization occurs as follows:

$$E_{\pm}(N) = \pm\sqrt{(2e\hbar v_F^2 B/c)N}$$

where N = 0, 1, 2, …. The formula indicates that the 0th Landau level with N=0 is located at the Dirac point. In a Dirac fermions system, Landau level spacing is not a constant unlike ordinary metals in which Landau level spacing is $\hbar w_c$ and is independent of the Fermi level. This means, the Landau quantization of massless Dirac fermions is distinguished by the existence of zero energy and the occurrence of $\sqrt{N}$ states on the positive and negative energy sides of the Dirac point. SdH oscillations are a quantum oscillatory behaviour of electrical conductivity of a 2DEG due to Landau quantisation in the magnetic field. Landau level quantisation is related to topological properties such as QHE.

2.10 Types of disorder (magnetic and non-magnetic)

Defects and disorder occur in a variety of forms in a crystalline material. **0 D defects or point defects:** could be a single atom or ion, such as vacancies, interstitials, and substitutional impurities. **1D defects or line defects:** could be a line of missing atoms in a crystal such as dislocations and stacking faults. **2D defects or planar defects:** could be a plane of missing atoms or different composition as compared to parent crystal such as grain boundaries and twin boundaries. **3D defects or volumetric defects:** could be significant volume of crystal with a different composition or crystal structure such as secondary phase or precipitates and voids. Defects and disorder can change materials properties significantly, the following section will discuss their effect on the electronic properties of TIs.

The most convenient starting point to study 3D topological insulators is to consider perfect, periodic crystals without defects. In this case, the idealized situation illustrated in Figure 2.14 a and b may be achieved, in which the Fermi level lies in the bulk band-gap, and crosses the surface-states, giving idealized surface-dominated transport. However, in reality point defects such as vacancies, anti-site defects and dopants in crystals modify this picture considerably. In particular, point defects with a magnetic spin are thought to alter the state of TIs significantly, as shown in Figure 2.14 c and d, in which gap opens in 3D Dirac like surface states. Furthermore, extended 1D defects such as surface features (terraces) and 2D defects (grain boundaries, dislocations) also modify the situation.

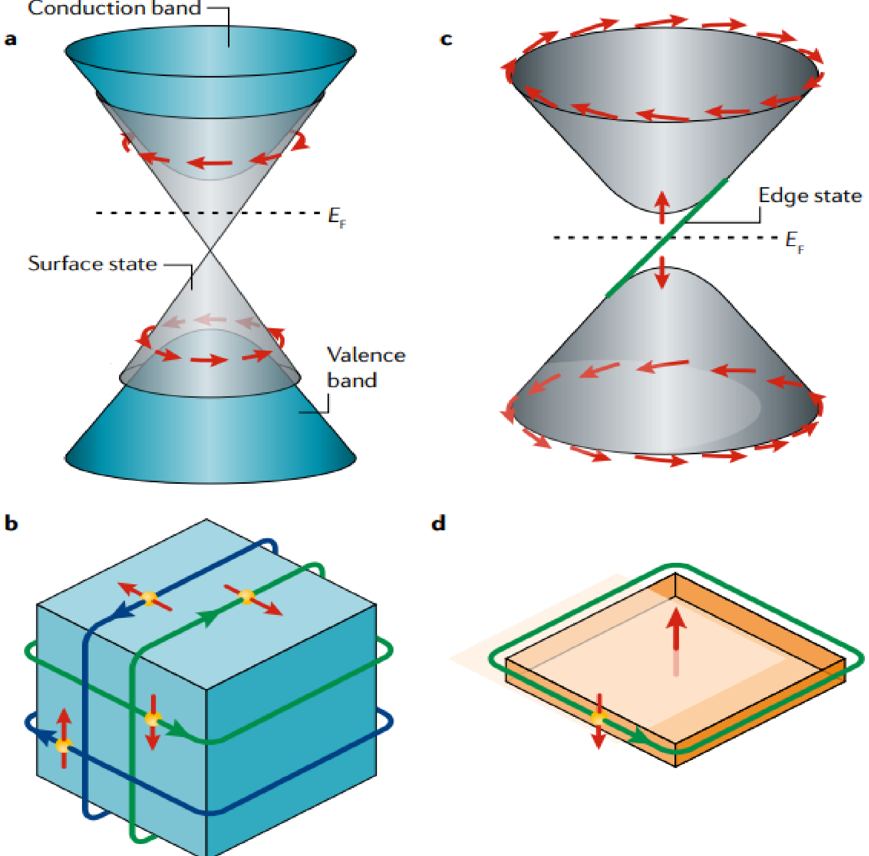

Figure 2.14. The electronic structure of a topological insulator and of a magnetic topological insulator. a. The massless Dirac-like dispersion of the surface state with spin–momentum locking in a 3D topological insulator. b. Real-space picture of the surface state in a 3D topological insulator. Electrons with spins pointing up and down (red arrows) move in opposite directions. c. The gapped Dirac-like dispersion of the surface state in a magnetic topological insulator. d. The chiral edge mode that appears in a magnetic topological insulator when the Fermi level, E_F, is located in the mass gap induced by the magnetic exchange interaction.[43]

Broadly these different types of defects can be grouped into two main types of disorder that can occur in materials: magnetic disorder and non-magnetic (charge) disorder. Non-magnetic disorder could be the defects and disorder of any type mentioned above that do not create any magnetic order in the system or do not create unpaired spins and local magnetic moments, with or without order. This can occur in amorphous materials, where the atoms are randomly arranged, or in crystalline materials that have defects such as vacancies or impurities. Non-magnetic disorder can also have a significant impact on the electronic properties of a TI, such as its electrical conductivity. Although TIs are said to be immune to 180 degrees backscattering from non-magnetic defects, however in the presence of other forms of scattering, such as small angle scattering are still allowed, and

do effect transport properties of TIs [44].

Magnetic disorder breaks time reversal symmetry, so that 180 degrees backscattering is allowed for TI states. Thus, even a small number of (disordered) paramagnetic spins can affect TI magnetotransport. Magnetic disorder occurs when the magnetic moments in a material are disordered or randomly oriented. Here in the thesis, magnetic disorder refers to the local magnetic order introduced at random points (e.g. ferromagnetic clusters) embedded in the TI. Surface states of TIs TRS protected and insensitive to disorder or impurities. However, magnetic disorder/impurities can break TRS that is critical for the existence of surface states. The interaction between the magnetic moments of magnetic impurities and the electrons in TI could lead to a spin-split surface state (can be regarded as gap opening). If the magnetic moments are sufficiently ordered, the spin-splitting of surface states could lead to a new phase known as a magnetic topological insulator, Chern insulator, Axion Insulator or Quantum Anomalous Hall Insulator, depending on the magnetic orientation vector and the nature of magnetic order[43]. For example, QAHE has been achieved by opening a magnetic mass gap either intrinsic magnetic order [45, 46] or magnetic impurities [17, 47] in the Dirac cone as shown in Figure 2.14 c.

2.11 Disorder effects in topological insulators: Anderson localisation and the fate of surface states under strong disorder

Initially the surface states of TIs were thought to be immune to various forms of disorder owing to the adiabatically protected nature of the Dirac spectrum, and absence of back-scattering. However, detailed work later revealed that, while this may be true if the Dirac nature is treated in a 2D continuum Dirac model with a small electronic disorder potential, for very strong disorder (e.g. lattice disorder at an energy scale larger than the Dirac spectrum), the 2D continuum Dirac model breaks down and Anderson localization is possible [48]. Anderson localization describes the decrease in mobility of an electronic system in a disordered lattice [49]. When the disorder is weak and the defects are spread over a large region of space (disorder), the electronic wave function will be distorted due to the scattering effect of the random potential over long length-scale although the planewave character will remain when viewed at shorter length scales. However, with stronger and more closely-packed defects and disorder, plane waves descriptions break down and long range transport of plane waves becomes impossible due to the interference

of multiple electron scattering points by random impurities and defects [48] [50].

Most of the work systematically exploring the effects of disorder in TI materials or existence of amorphous TIs has been purely theoretical work [51-53] V. Sacksteder et. al have numerically demonstrated a practical way of systematically manipulating the topological transport property of a 3D TI by introducing strong disorder in a layer (with controlled depth) near the surface [52]. Figure 2.15 shows the topological states under different levels of disorder. This is a very useful study in sense that it shows that topological states are insensitive to small or weak disorder (W), however beyond certain critical disorder level, the topological states vanish. As can be seen from the figure, there is also a special point where $W \approx W_c$, the topological states depin from surface resulting in conduction which is topological and sensitive to disorder depth.

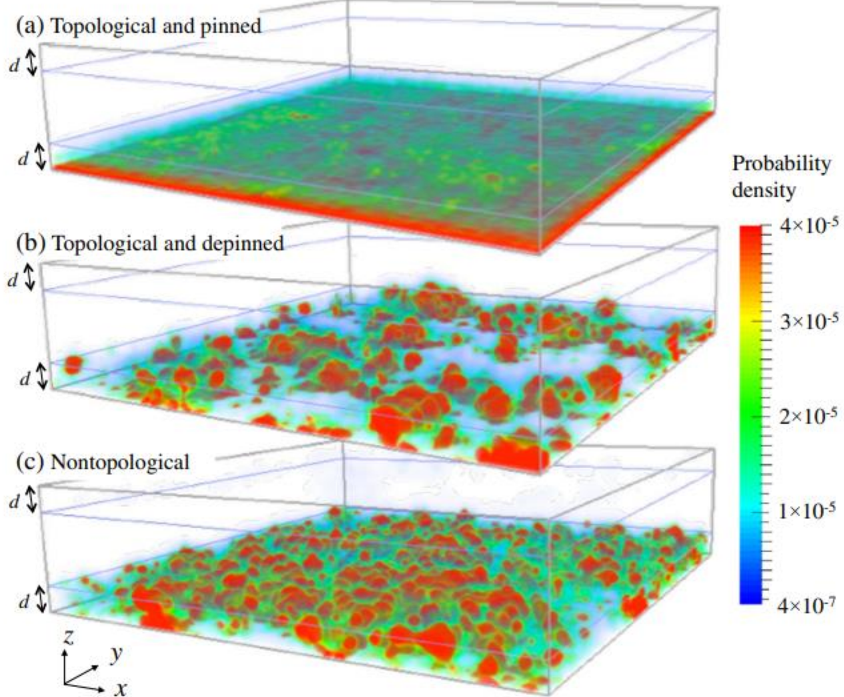

Figure 2.15. Disorder depth-dependent transport illustrated in a disordered surface layer of depth d=5. (a) W=4.5, topological state pinned to bottom surface. (b) W=7.5 near W_c, fully depinned from bottom surface. (c) W=9, under strong disorder, the disorder region is no longer topological. [52]

One interesting prediction was given by Li and Guo et. al who, from their theoretical calculations, found the formation of new topological phases when strong electronic disorder is introduced into the ordinary insulator. This new phase was termed a

"topological Anderson insulator" [54, 55].

Although, there are several previous theoretical calculations showing topological states can only survive under certain limits of disorder, very recent studies claim existence of topological states in amorphous topological insulators [56, 57]. The claim is that amorphization quenches the topological band gap, but does not close it. Survival of the QSH state through the amorphization process was predicted to depend on the SOC strength of the material and the size of the bulk band gap [58]. The following section describes in detail the recent predictions of amorphous topological insulators.

2.12 Amorphous topological insulators?

In condensed matter physics, a phase of matter is usually classified by the way it spontaneously breaks certain types of symmetry. However, the discovery of the quantum spin Hall effect and realization of topological insulators in 2D and 3D systems, has introduced a new way of classifying the quantum phases of matter, which is topology. The advance in classification of matter according to topology, has led to theoretical prediction and experimental discovery of many TIs in the last decade. An important set of discoveries was the realization that certain systems, which lack crystalline symmetry, may still give rise to topological effects [59].

Agarwala A. et al. have constructed hopping models on random lattices and show that their gapped ground states possess nontrivial topological nature, which manifests as quantized conductances in systems with a boundary. This adds a new dimension to the search for topological systems beyond crystalline solids and points to promising possibilities in amorphous solids and other engineered random systems [60]. Mitchell N. P. [61]reported that amorphous Chern insulators can be constructed from arbitrary underlying structures, including hyperuniform, jammed, quasi-crystalline, and uniformly random point sets. They focus on networks of interacting gyroscopes as a model system and demonstrate that local decorations control the topology of the vibrational spectrum, endowing amorphous structures with protected edge modes with a chirality of choice. Using a real-space generalization of the Chern number, the authors investigated the topology of their structures numerically and analytically that enables the topological

design and self-assembly of non-crystalline topological metamaterials on the micro and macro scale. Costa M. [62] discussed the topological properties of two-dimensional amorphous bismuthene systems using *ab initio* calculations. Their study of electronic and transport study shows that amorphous materials can display topological insulator properties, characterized by the topological index $Z_2=1$ and bulk-edge duality. The linear conductance of these systems is quantized for Fermi energies within the topological gap, $G=2e^2/h$. The results open the path to the experimental and theoretical investigation of amorphous topological insulator materials. This finding was also confirmed by the Focassio B. et al. [58], who performed investigations into two-dimensional amorphous bismuthene structures, in which their calculations also show a $2e^2/h$ conductance plateau within the topological gap. Amorphous H-bismuthene quantum spin Hall insulators may be the key to the experimental realization of QSHI-based devices at room temperature due to the robustness of such systems displaying the gapless helical edge state and also hindering the bulk transport response [58]. In summary, several theoretical studies described above suggest that amorphous topological insulators can exist, however, the experimental realisation and characterisation of these materials is still lacking and challenging.

Amorphous materials cannot be represented by Bloch states due to the lack of translational symmetry. Recent experimental work by Barton A. T. et al., have investigated the He^+ sputtering and inductively coupled plasma Cl_2 etching effect on the Molecular beam epitaxy (MBE) grown Bi_2Se_3. ARPES measurements show that the topologically protected surface states remain even after inducing significant surface disorder and chemical changes, demonstrating that topological insulators are quite promising for defect-tolerant electronics. However, that work did not present rigorous microstructural characterisation of the crystalline structure using TEM/STEM, which would be needed to clarify the level of disorder induced. Another study by P. Corbae et al. [57] explored whether topological states necessarily rely on a periodic crystal lattice, and whether they can be detected in amorphous materials of Bi_2Se_3. Their experimental results on amorphous Bi_2Se_3 indicates the existence of 2D surface states, as confirmed by the ARPES spectra of the amorphous Bi_2Se_3 [57], which is unique to topological surface states [58, 61, 63-65]. However, here, I provide a critical assessment on the latter work on the existence of topological surface states in amorphous Bi_2Se_3. The microstructural analysis using TEM/STEM and fluctuating electron microscopy (FEM) analysis

presented in the latter work, should have been done on the same samples which were later analysed by ARPES or transport rather than on a 10-nm-thick Bi_2Se_3 films deposited on a 10-nm-thick SiN window. Decapping process of Se layer on Bi_2Se_3 is not discussed in detail, even a small amount of heating, required to remove the Se cap could lead to accidental or partial recrystallization. Therefore, additional experimental measurements are still required to study amorphous Bi_2Se_3, and related compounds such as Bi_2Te_3 and Sb_2Te_3.

If the realization of amorphous materials with topological properties comes true, no doubt, this will provide another classification scheme beyond what is available so far, and open a new door for exploring a diverse range of amorphous topological insulators.

2.13 Hypothesis: Methods to control order and disorder in TIs with ion beam techniques will enable surface engineering

In the literature, there are numerous ways to introduce disorder in TIs surfaces, such as dopants, mechanical surface abrasion, and even by atmospheric exposure to gases [32-36]. A capping layer is thought to be effective in protecting the surface, thus selective etching of TIs surface while masking seems to be a promising technique to enable control over which regions of the surface experience disorder [37].

Past work has shown that ion beam irradiation with transition metal ions can form amorphous layers in Sb_2Te_3 surfaces [66]. For similar reasons, this thesis proposes the hypothesis that single-step gallium focused-ion beam (Ga-FIB) irradiation of Sb_2Te_3 single crystals is a viable strategy to create an amorphise material by knocking out Sb and Te atoms from their chemically ordered crystalline sites and creating a localised modified electronic structure. Amorphous Sb_2Te_3 is then locally generated in the disordered regions due to the ion induced atomic displacements. It was hypothesized that this method can be used for tailoring the electronic properties of the crystalline structures. If so, then a Ga-FIB may potentially provide an easy way to enable direct "writing" of guided electronic paths on the surface states of topological insulators. Ion beam energy and ion doses should be carefully chosen, so that the disorder depth can be more precisely controlled in the ion beam process. By utilizing this phenomena, one can potentially engineer and pattern

topological states to meet specific device requirements. Moreover, if TIs are irradiated with magnetic ion beams (such as Mn, V, and Cr), it may introduce magnetic order in TIs. The magnetic moment in TIs could break TRS and provide a promising way to achieve QAHE. This thesis will explore how ion beams can be used to engineer the surfaces of TIs, to control the level of charge and magnetic order/disorder. Further, it will explore magnetic ion beam patterning of TIs for future device functionalities.

References

1. Sethna, J.P., *Statistical mechanics: entropy, order parameters, and complexity*. Vol. 14. 2021: Oxford University Press, USA.

2. Coleman, S. and A. Zichichi, *Introduction to spontaneous symmetry breakdown and gauge fields*. 1975, Harvard Univ., Cambridge, MA.

3. Von Klitzing, K., *25 Years of quantum Hall effect (QHE) a personal view on the discovery, physics and applications of this quantum effect.* progress in mathematical physics, 2005. **45**: p. 1.

4. Bernevig, B.A., *Topological insulators and topological superconductors*. 2013: Princeton university press.

5. Hasan, M.Z. and C.L. Kane, *Colloquium: topological insulators.* Reviews of modern physics, 2010. **82**(4): p. 3045.

6. Weng, H., X. Dai, and Z. Fang, *From Anomalous Hall Effect to the Quantum Anomalous Hall Effect.* arXiv preprint arXiv:1509.05507, 2015.

7. Kane, C.L., *Topological band theory and the $\mathbb{Z}_2$ invariant*, in *Contemporary Concepts of Condensed Matter Science*. 2013, Elsevier. p. 3-34.

8. Berry, M.V., *Quantal phase factors accompanying adiabatic changes.* Proceedings of the Royal Society of London. A. Mathematical and Physical Sciences, 1984. **392**(1802): p. 45-57.

9. Nakahara, M., *Geometry, topology and physics*. 2018: CRC press.

10. Thouless, D.J., et al., *Quantized Hall conductance in a two-dimensional periodic potential.* Physical review letters, 1982. **49**(6): p. 405.

11. Hsieh, D., et al., *A tunable topological insulator in the spin helical Dirac transport regime.* Nature, 2009. **460**(7259): p. 1101-1105.

12. Kane, C.L. and E.J. Mele, *Quantum spin Hall effect in graphene.* Physical review letters, 2005. **95**(22): p. 226801.

13. Ando, T., T. Nakanishi, and R. Saito, *Berry's phase and absence of back scattering in carbon nanotubes.* Journal of the Physical Society of Japan, 1998. **67**(8): p. 2857-2862.

14. Qi, X.-L. and S.-C. Zhang, *The quantum spin Hall effect and topological insulators.* arXiv preprint arXiv:1001.1602, 2010.

15. Haldane, F.D.M., *Model for a quantum Hall effect without Landau levels: Condensed-matter realization of the" parity anomaly".* Physical review letters, 1988. **61**(18): p. 2015.

16. Yu, R., et al., *Quantized anomalous Hall effect in magnetic topological insulators.* science, 2010. **329**(5987): p. 61-64.

17. Chang, C.-Z., et al., *Experimental observation of the quantum anomalous Hall effect in a magnetic topological insulator.* Science, 2013. **340**(6129): p. 167-170.

18. Chang, C.-Z., et al., *High-precision realization of robust quantum anomalous Hall state in a hard ferromagnetic topological insulator.* Nature materials, 2015. **14**(5): p. 473-477.

19. Nagaosa, N., et al., *Anomalous Hall Effect.* Reviews of modern physics, 2010. **82**(2): p. 1539.

20. Klitzing, K.v., G. Dorda, and M. Pepper, *New method for high-accuracy determination of the fine-*

structure constant based on quantized Hall resistance. Physical review letters, 1980. **45**(6): p. 494.

21. Cage, M.E., et al., *The quantum Hall effect*. 2012: Springer Science & Business Media.
22. Bernevig, B.A. and S.-C. Zhang, *Quantum spin Hall effect.* Physical review letters, 2006. **96**(10): p. 106802.
23. König, M., et al., *Quantum spin Hall insulator state in HgTe quantum wells.* Science, 2007. **318**(5851): p. 766-770.
24. Zhang, H., et al., *Topological insulators in Bi_2Se_3, Bi_2Te_3 and Sb_2Te_3 with a single Dirac cone on the surface.* Nature physics, 2009. **5**(6): p. 438-442.
25. Chen, Y., et al., *Experimental realization of a three-dimensional topological insulator Bi_2Te_3.* science, 2009. **325**(5937): p. 178-181.
26. Alpichshev, Z., et al., *STM imaging of electronic waves on the surface of Bi_2Te_3: topologically protected surface states and hexagonal warping effects.* Physical review letters, 2010. **104**(1): p. 016401.
27. Hsieh, D., et al., *A topological Dirac insulator in a quantum spin Hall phase.* Nature, 2008. **452**(7190): p. 970-974.
28. Liu, B., et al., *Y-Doped Sb_2Te_3 Phase-Change Materials: Toward a Universal Memory.* ACS applied materials & interfaces, 2020. **12**(18): p. 20672-20679.
29. Sultana, R., et al., *Crystal growth and characterization of bulk Sb_2Te_3 topological insulator.* Materials Research Express, 2018. **5**(4): p. 046107.
30. Zhu, X.-G., et al., *Electronic structures of topological insulator Bi_2Te_3 surfaces with non-conventional terminations.* New Journal of Physics, 2016. **18**(9): p. 093015.
31. Osterhage, H., et al., *Thermoelectric properties of topological insulator Bi_2Te_3, Sb_2Te_3, and Bi_2Se_3 thin film quantum wells.* Applied Physics Letters, 2014. **105**(12): p. 123117.
32. Qu, D.-X., et al., *Quantum oscillations and Hall anomaly of surface states in the topological insulator Bi_2Te_3.* Science, 2010. **329**(5993): p. 821-824.
33. Hajlaoui, M., et al., *Ultrafast surface carrier dynamics in the topological insulator Bi_2Te_3.* Nano letters, 2012. **12**(7): p. 3532-3536.
34. Noh, H.-J., et al., *Spin-orbit interaction effect in the electronic structure of Bi_2Te_3 observed by angle-resolved photoemission spectroscopy.* EPL (Europhysics Letters), 2008. **81**(5): p. 57006.
35. Orlita, M., et al., *Magneto-optics of massive Dirac fermions in bulk Bi_2Se_3.* Physical review letters, 2015. **114**(18): p. 186401.
36. Xia, Y., et al., *Observation of a large-gap topological-insulator class with a single Dirac cone on the surface.* Nature physics, 2009. **5**(6): p. 398-402.
37. Damascelli, A., *Probing the electronic structure of complex systems by ARPES.* Physica Scripta, 2004. **2004**(T109): p. 61.
38. Chen, C.J., *Introduction to Scanning Tunneling Microscopy Third Edition*. Vol. 69. 2021: Oxford University Press, USA.
39. Hikami, S., A.I. Larkin, and Y. Nagaoka, *Spin-orbit interaction and magnetoresistance in the two dimensional random system.* Progress of Theoretical Physics, 1980. **63**(2): p. 707-710.
40. Lu, H.-Z., J. Shi, and S.-Q. Shen, *Competition between weak localization and antilocalization in*

topological surface states. Physical review letters, 2011. **107**(7): p. 076801.

41. Bergmann, G., *Weak localization in thin films: a time-of-flight experiment with conduction electrons.* Physics Reports, 1984. **107**(1): p. 1-58.

42. Kou, X., et al., *Scale-invariant quantum anomalous Hall effect in magnetic topological insulators beyond the two-dimensional limit.* Physical review letters, 2014. **113**(13): p. 137201.

43. Tokura, Y., K. Yasuda, and A. Tsukazaki, *Magnetic topological insulators.* Nature Reviews Physics, 2019. **1**(2): p. 126-143.

44. Brahlek, M., et al., *Transport properties of topological insulators: Band bending, bulk metal-to-insulator transition, and weak anti-localization.* Solid State Communications, 2015. **215**: p. 54-62.

45. Otrokov, M.M., et al., *Prediction and observation of an antiferromagnetic topological insulator.* Nature, 2019. **576**(7787): p. 416-422.

46. Deng, Y., et al., *Quantum anomalous Hall effect in intrinsic magnetic topological insulator* $MnBi_2Te_4$. Science, 2020. **367**(6480): p. 895-900.

47. Checkelsky, J., et al., *Trajectory of the anomalous Hall effect towards the quantized state in a ferromagnetic topological insulator.* Nature Physics, 2014. **10**(10): p. 731-736.

48. Schubert, G., et al., *Fate of topological-insulator surface states under strong disorder.* Physical Review B, 2012. **85**(20): p. 201105.

49. Anderson, P.W., *Absence of diffusion in certain random lattices.* Physical review, 1958. **109**(5): p. 1492.

50. Lee, P.A. and T. Ramakrishnan, *Disordered electronic systems.* Reviews of Modern Physics, 1985. **57**(2): p. 287.

51. Kobayashi, K., T. Ohtsuki, and K.-I. Imura, *Disordered weak and strong topological insulators.* Physical review letters, 2013. **110**(23): p. 236803.

52. Sacksteder, V., T. Ohtsuki, and K. Kobayashi, *Modification and control of topological insulator surface states using surface disorder.* Physical Review Applied, 2015. **3**(6): p. 064006.

53. Wang, J.-H., et al., *Structural Disorder Induced Second-order Topological Insulators in Three Dimensions.* 2020.

54. Guo, H.-M., et al., *Topological Anderson insulator in three dimensions.* Physical review letters, 2010. **105**(21): p. 216601.

55. Li, J., et al., *Topological anderson insulator.* Physical review letters, 2009. **102**(13): p. 136806.

56. Jiang, Y., et al., *Landau quantization and the thickness limit of topological insulator thin films of* Sb_2Te_3. Physical review letters, 2012. **108**(1): p. 016401.

57. Corbae, P., et al., *Observation of spin-momentum locked surface states in amorphous* Bi_2Se_3. Nature Materials, 2023: p. 1-7.

58. Focassio, B., et al., *Structural and electronic properties of realistic two-dimensional amorphous topological insulators.* 2D Materials, 2021.

59. Halperin, B.I., *Quantized Hall conductance, current-carrying edge states, and the existence of extended states in a two-dimensional disordered potential.* Physical Review B, 1982. **25**(4): p. 2185.

60. Agarwala, A., *Topological insulators in amorphous systems.* Physical Review Letters, 2017. **118**: p. 236402.

61. Mitchell, N.P., et al., *Amorphous topological insulators constructed from random point sets.* Nature Physics, 2018. **14**(4): p. 380-385.

62. Costa, M., et al., *Toward Realistic Amorphous Topological Insulators.* Nano Letters, 2019. **19**(12): p. 8941-8946.

63. Agarwala, A., *Topological insulators in amorphous systems*, in *Excursions in Ill-Condensed Quantum Matter*. 2019, Springer. p. 61-79.

64. Agarwala, A., V. Juričić, and B. Roy, *Higher-order topological insulators in amorphous solids.* Physical Review Research, 2020. **2**(1): p. 012067.

65. Zhou, P., et al., *Photonic amorphous topological insulator.* Light: Science & Applications, 2020. **9**(1): p. 1-8.

66. Cortie, D., et al., *Creating thin magnetic layers at the surface of Sb_2Te_3 topological insulators using a low-energy chromium ion beam.* Applied Physics Letters, 2020. **116**(19): p. 192410.

Chapter 3. Methodology and Characterization techniques

3.1 Materials structure characterisation

3.1.1 Scanning electron microscopy imaging

Scanning electron microscopy (SEM) is a very useful and readily available characterisation tool for imaging and analysis [1]. Electrons may be elastically scattered from the surface of the sample by the interaction of the primary electron beam with the atomic nuclei in the sample, known as back-scatter electrons (BSE). The contrast obtained from BSE data depend on the atomic number, density and, (as will be discussed in detail later) the incident/exit trajectory of crystallographic planes of the sample. Higher atomic number elements and higher densities result in stronger backscattering. Hence, BSE provide contrast based on differences in atomic number and density of the sample. Conversely, inelastically scattered electrons which derive from secondary scattering events (such as core ejection ionisation as a part of X-ray generation process), are termed secondary electrons (SE), and are much more sensitive to surface topology. While SE’s are generated throughout the interaction volume, their low energy and correspondingly shallow escape depth leads to a correlation between the exposed surface that sections the interaction volume (where large exposed surfaces – such as with glancing angles) and as such provides topography information because the intensity of the signal is proportional to the surface features of the sample. Hence, SE images reveals surface morphology, texture, and roughness of the sample [2].

In this thesis, the JEOL JSM-6490LV SEM Figure 3.1 a) and FEI HELIOS G3 FIB-SEM Figure 3.1 b were used for regular SEM imaging and energy dispersive spectroscopy (EDS) analysis. EBSD analysis, FIB lamella and transport device fabrication was conducted on FEI HELIOS G3 FIB-SEM Figure 3.1 b. Both of these microscopes are based at the Electron Microscopy Centre (EMC) at the University of Wollongong.

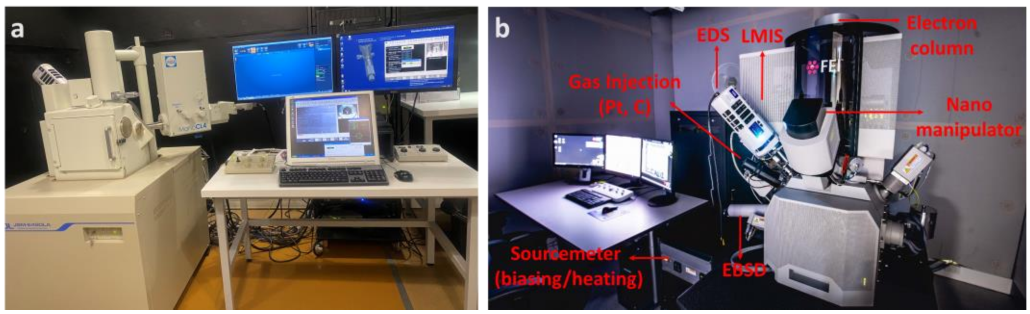

Figure 3.1. Electron microscopes used in the thesis for the characterization. a. JEOL JSM-6490LV SEM used for regular imaging and EDS analysis. b. FEI Helios G3 FIB-SEM used for imaging, EDS and EBSD analysis, FIB lamella and transport device fabrication.

3.1.2 Electron back-scattering diffraction (EBSD)

EBSD was used for performing the quantitative microstructural analysis (crystal structure and orientation) in the FEI HELIOS G3 microscope equipped with an EBSD detector. Electron back-scattering patterns (EBSP) typically originate from electrons scattered 20-200 nm below the surface of a specimen. Usually, the specimen surface must be smooth and free of contaminants and any mechanical damage layers removed before performing EBSD. The electron beam is incident on the surface specimen, which is tilted to approximately 70° relative to normal position as shown in Figure 3.2 (a). This is to bias the electrons and specimen interaction volume close to the surface, which increases the backscattered electron yield and affords a collection geometry in which the scattered electrons can be projected onto an imaging plane where their intensity compared to their scattering angle at the point of origin can be determined. Generally, most EBSD analyses are performed between 10-30kV. As such in this thesis work, an accelerating voltage of 20 kV and current of 2.8 nA was used in all EBSD scans on the FEI HELIOS G3 microscope [3]. When the electron beam is incident upon the surface of a crystalline sample, electrons scatter in all directions within the interaction volume, during this process they interact strongly with the crystal lattice and thus undergo diffraction obeying Bragg's equation, $n\lambda=2d \sin\theta$, where, λ is electron beam wavelength, d is crystal lattice spacing and θ is the Bragg angle.

For each set of lattice planes that satisfies the Bragg equation, diffracted electrons spread in all directions in the form of a cone as shown in Figure 3.2 b. The central axis of the diffracted cone is normal to the diffracting lattice plane. There exist two diffracted cones at the front and back of each set of lattice planes, as illustrated in Figure 3.2 c, forming a

bright band with two dark lines at the border on intersecting phosphor screen (which are generally called Kikuchi bands) [4]. Various oriented sets of lattice planes produce various projected Kikuchi bands, as in Figure 3.2 d, that are collectively called a Kikuchi pattern. The distance between the two dark lines in a Kikuchi band is inversely proportional to the d-spacing of that diffracting plane family. The Angle between two Kikuchi bands is equal to the angle between two corresponding diffracting family of planes.

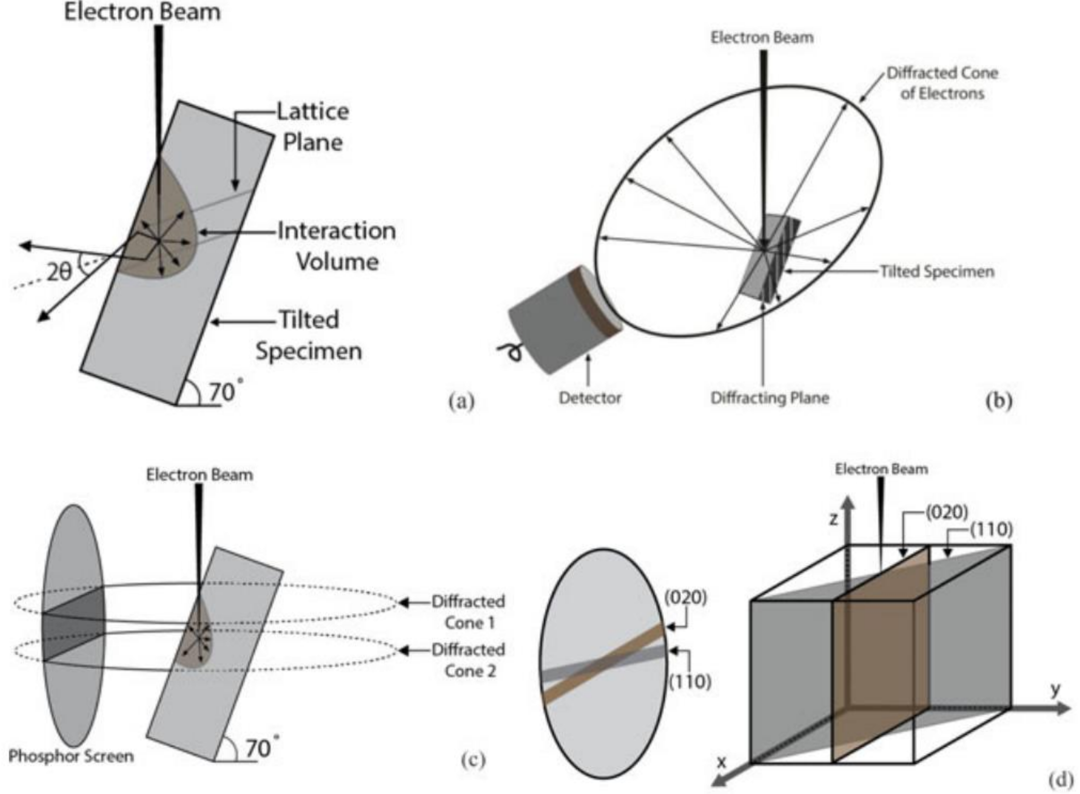

Figure 3.2. (a, b) Electron scattering acts as a divergent source of electrons within a specimen. These electrons are incident upon a lattice plane satisfying Bragg's equation. The resulting diffraction forms a pair of cones at the front and back end of the plane. (c) Diffracted rays are formed along the surface of cones and strike the phosphor screen resulting in a pair of lines for each set of lattice planes. (d) Schematic illustration of electron beam interaction with the lattice planes giving rise to Kikuchi bands on a phosphor screen [1].

In this thesis, EBSD has been used for identifying the crystallographic orientation, surface crystallinity and recrystallisation of Sb_2Te_3. Oxford Instrument's AZtec software was used for indexing Kikuchi patterns and analysing the EBSD maps.

3.1.3 X-ray analysis/ Energy dispersive spectroscopy

X-rays are generated in a SEM through electron beam-sample interactions. When the electron beam interacts with the atoms in the specimen, inelastic scattering occurs, with the primary electron beam knocking off inner-shell electrons and leading to ionization or excitation of the atoms. An electron can then move from the outer higher-energy to the inner lower-energy shell of the atoms, the energy difference can be released as a characteristic X-ray. These X-rays are detected by an X-ray detector, providing elemental composition and distribution.

Monte Carlo simulations of the electron trajectories via the (CASINO) software [3], can be used to calculate the low-energy electron beam interaction in a solid, including the electron interaction volume, backscattered electron coefficient, and X-ray production. It is worth to note that for samples with complex surface composition, or samples that have inhomogeneity on the length-scale of the beam interaction volume, EDS analysis (in the absence of suitable standards) provides only qualitative information. Computer simulations are especially useful for guiding experiments such as the analysis of ion-beam doped Sb_2Te_3 (such as Mn-doped Sb_2Te_3 presented in Chapter 7) where the dopant ions are implanted in the top 50-60 nm region, and tilting the specimen in SEM and selecting appropriate lower beam energies is helpful. This elongation of the x-ray generation volume along the surface increases the overlap with the dopant implanted region and slightly increases x-ray intensity as shown in Figure 3.3. This method has been utilised during characterisation to facilitate detection of low dose implanted elements in a specimen or thin films (of few nanometres) at the top surface of a substrate for qualitative confirmation of presence of the dopant.

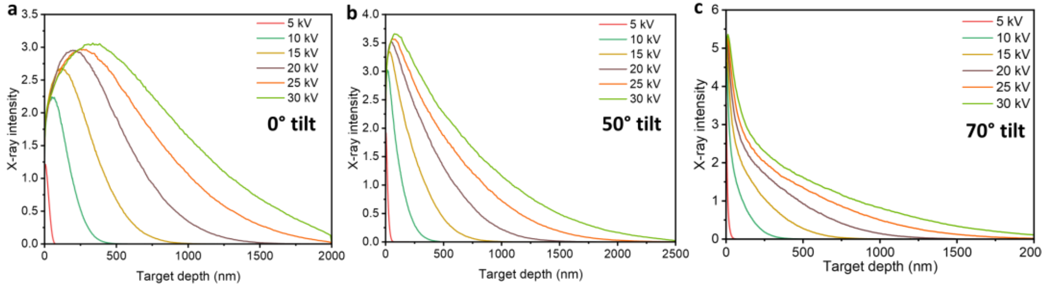

Figure 3.3. Monte Carlo simulation of X-ray generation intensity and depth in Sb_2Te_3 under at the beam energy range of 5-30 kV. X-ray generation depth and intensity at a. 0° specimen tilt, b. 50° specimen tilt, c. 70° specimen tilt, show that by tilting specimen x-ray generation could be brought to near surface of specimen.

Apart from Monte Carlo simulation with CASINO, Castaing's formula is also used to estimate the analytical volume of the X-rays generated within the sample:

$$Z_m = 0.033(E_0^{1.7} - E_C^{1.7})\frac{A}{\rho Z} \qquad 3.1$$

where Z_m is the X-ray analytical depth, E_0 is the accelerating voltage (kV), E_C is the minimum emission voltage (keV), A is atomic mass, ρ is density (g/cm^3) and Z is atomic number. Ideally the accelerating voltage (E_0) is set at 2-5 times the critical ionization/excitation energy (E_C) of the elements of interest. The critical excitation energy of the elements can be estimated by the formula below:

$$\begin{aligned} E_{c(K)} = E_{K\alpha} + E_{c(L)} &= E_{K\alpha} + E_{L\alpha} + E_{c(M)} \\ &= E_{K\alpha} + E_{L\alpha} + E_{M\alpha} + E_{c(N)} \qquad 3.2 \\ &\approx E_{K\alpha} + E_{L\alpha} + E_{M\alpha} \end{aligned}$$

where, $E_{C(K)}$ is the critical excitation energy of the shell, $E_{K\alpha}$, $E_{L\alpha}$, $E_{M\alpha}$ are characteristic X-ray energies. According to equations 3.1 and 3.2, and the simulations shown in Figure 3.3, the following conditions were used during EDS analysis in this thesis: the accelerating voltage (E_0) was in the range of 10-20 KV, the angles of incidence ranged from 0-60 degrees and a sufficient beam current was selected for acquiring reasonable enough X-ray counts. For the Sb_2Te_3 crystals, according to Castaing's formula, a 10-20 kV beam energy has the analytical volume in the range of 0.2-1.2 μm. When, performing EDS analysis for the magnetic ion doped Sb_2Te_3 crystals, a reduced beam energy of 10 kV was used, and the sample stage was tilted up to 50-60 degrees in order to bring the X-ray analytical volume more towards the surface. This could increase the X-ray signals from the magnetic ions (such as V, Cr, and Mn) doped within the top 50 nm range from the surface (i.e when the ion-beam implantation energy ≤ 40 kV), as shown in Figure 3.3.

EDS analysis can identify chemical composition of materials but fails to differentiate materials with same composition but having different crystal structures. The limitation in the EDS analysis can be overcome by EBSD analysis, which will be introduced in the following section.

3.1.4 Transmission electron microscope (TEM)/ Scanning transmission electron microscope (STEM)

In TEM, a relatively broad beam of parallel electrons are transmitted through the sample

with the thickness of (ideally) less than 100 nm to form the image or diffraction pattern. Whereas, in the related technique of STEM, the electron beam is focused by electron optics to form a small probe which is then raster-scanned across a sample. The transmitted electrons are then collected by various specialized detectors for creating the image of the sample. There are several types of TEM techniques, including bright-field TEM, annular dark-field (ADF) TEM, and high-resolution TEM. Each of these techniques detects a different portion of transmitted electrons (e.g., diffracted or non-diffracted electrons), and they are used to study different aspects of the sample. In this thesis, all of the TEM and STEM imaging and EDS analysis utilized the JEOL JEM-F200 and JEOL JEM-ARM200F, as shown in the Figure 3.4, located at the Electron Microscopy Centre (EMC) at the University of Wollongong.

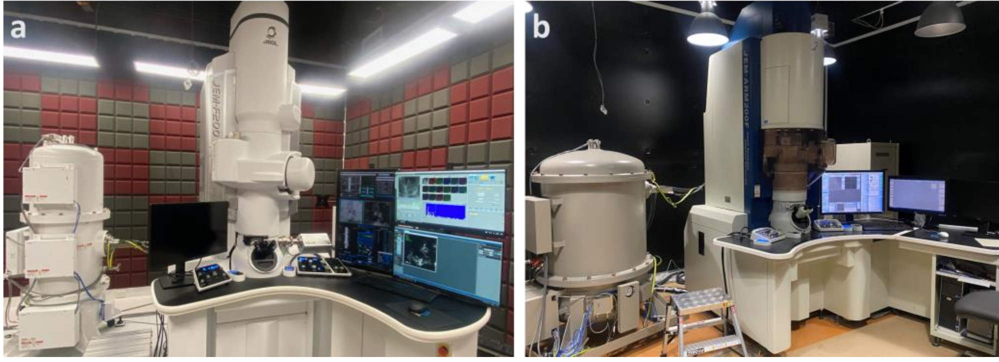

Figure 3.4. TEM/STEM models used for characterisation in the thesis (a) JEOL JEM-F200 TEM/STEM and (b) JEOL JEM-ARM200F aberration-corrected TEM/STEM.

STEM ADF/HAADF imaging mode uses electrons that are elastically scattered at a high angle, and it provides incoherent imaging and has become arguably the most ubiquitous imaging mode. ADF images are incoherent in nature and relatively insensitive to focusing errors, this makes it easy to interpret observed compositional changes from atomic contrast. In theory, as the scattering angle increases to those used in ADF, the scattered intensity from an atom approaches Z^2 dependence. However, in practice, the scattered intensity would not reach this limit and typically is around $Z^{1.7}$ due to the screening effect of the atomic core electrons [5]. In contrast, conventional TEM cannot obtain incoherent imaging, as diffraction contrast is always present.

3.1.5 X-ray diffraction (XRD)

For quantum waves, including electromagnetic radiation or neutrons, to be diffracted, the atomic spacing should be of the same order as the wavelength. In a crystal, the typical interatomic spacing is a few angstroms (Å), hence neutrons, electrons, and x-rays all can be used for diffraction studies of a material's crystal structure. X-ray diffraction (XRD) is a most common technique used to study the crystal structure of materials including minerals, metals, and polymers. It is based on the fact that when an X-ray beam is shone on a crystal, the atoms in the crystal scatter the X-rays in a predictable pattern. By measuring the angles and intensities of the scattered X-rays, it is possible to determine the arrangement of atoms in the crystal. It is also used to identify unknown materials, measure the purity of a sample, and study the effects of processing on the crystal structure of a material. In XRD patterns, the diffraction peak position is determined by the interplanar spacing according to Bragg's law

$$n\lambda = 2d_{hkl}\sin\theta$$

There are several types of XRD instruments, including powder X-ray diffractometers and single crystal X-ray diffractometers. Powder X-ray diffractometers are used to study polycrystalline materials, while single crystal X-ray diffractometers are used to study the structure of single crystals. A polycrystalline sample usually contains tens of thousands of crystallites in a random orientation, which produce all possible diffraction peaks for a given crystal structure. Many powder x-ray diffractometers use the Bragg-Brentano geometry, as illustrated in Figure 3.5, in which the diffraction vector (s) is always normal to the surface of the sample. Here, the diffraction vector is bisecting the angle between the incident and diffracted beam. When a single crystal specimen is placed under Bragg-Brentano geometry on a single crystal diffractometer, it will produce only a family of peaks (e.g. (L00)) in the XRD pattern (i.e those where the scatter vector direction is aligned along the respective crystal axis).

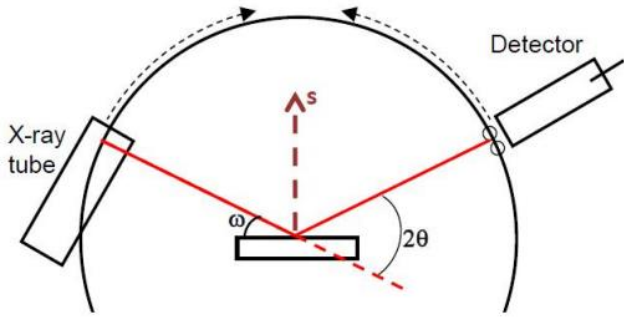

Figure 3.5. Bragg-Brentano geometry, as used in many powder x-ray diffractometers.

3.1.6 X-ray reflectometry (XRR)

X-ray reflectometry (XRR) is a non-destructive technique used to study the surface and interface structure of thin films and multilayer materials, including coatings, semiconductor devices, and biological samples. It probes the electron density contrast with depth resolution, typically sensitive to film features from 0.5 – 500 nm. Hence, it provides information on the surface or interface roughness, density and thickness of the sample. Figure 3.6 summarizes the effect of film density, thickness, surface and interface roughness on the XRR curve of a thin film. As the periodical oscillation of intensity is related to the thickness of a layer, the thickness of a layer can be obtained by Fourier transformation. However, no information can be extracted about the density, surface/interface roughness using direct Fourier transforms. Those values can, however, be obtained by solving the inverse problem and fitting the curve in software such as refnx, Simulreflec, GlobalFit, and GenX etc. which use a non-linear least-squares fitting method. Such software can simulate a reflectivity curve based on the multilayer structure model.

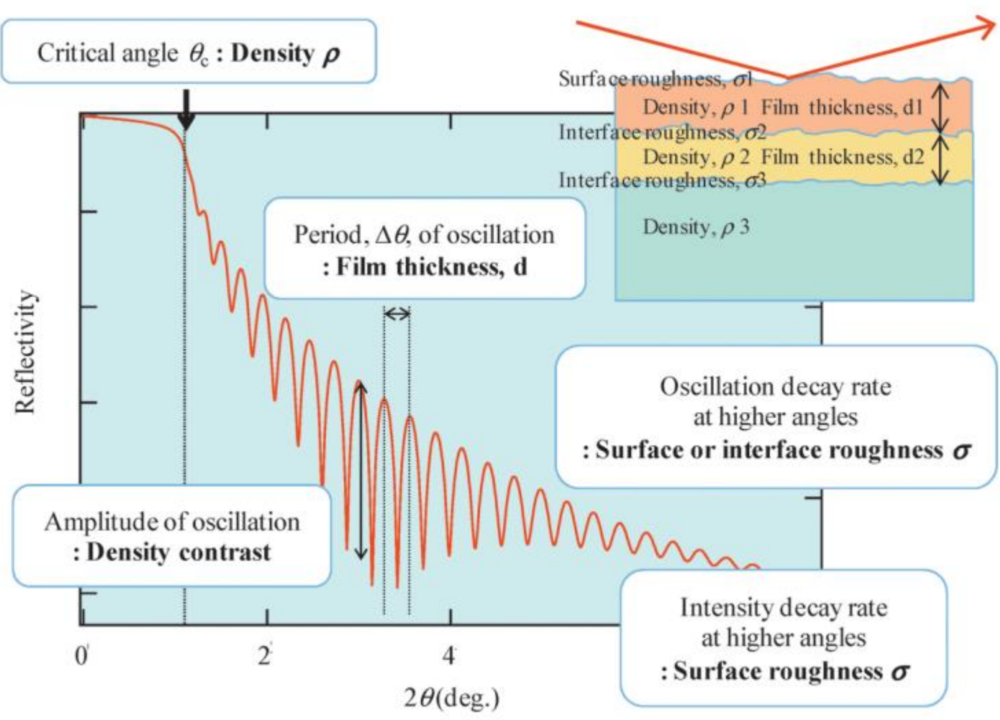

Figure 3.6. Information provided by a X-ray reflectometry profile [6].

3.1.7 X-ray photoelectron spectroscopy (XPS)

X-ray photoelectron spectroscopy is a surface-sensitive and non-destructive technique used to analyse the elemental composition of materials and the chemical state of elements. XPS provides information about the electronic structure of atoms and molecules on the surface of a sample (~ 10 nm). In XPS, a specimen is irradiated with focused monochromatic X-rays in an ultrahigh vacuum system, as illustrated in Figure 3.7. The X-rays interact with the electrons in the sample, causing them to be ejected from their respective energy levels as photoelectrons. These ejected photoelectrons carry information about the binding energy and identity of the atoms they originated from. The photoelectrons are collected by an electron energy analyser, which is used to discriminate among the energies of the photoelectrons. By measuring the kinetic energies of the photoelectrons, the binding energies of the electrons in the specimen can be determined and used to identify the elements present and to analyse the chemical bonding and electronic structure.

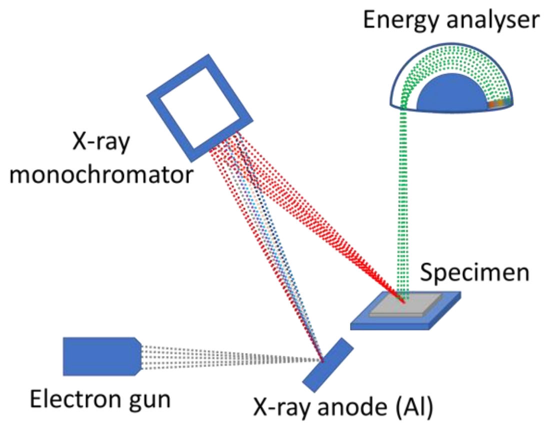

Figure 3.7. A simple schematic shows the XPS instrument's main components and working principle.

XPS can provide quantitative information about the elemental composition of a specimen by measuring the intensity of the photoelectron peaks relative to different elements. It can also provide information about the chemical environment of the atoms, such as oxidation states and chemical bonding. Thus, XPS is beneficial for characterizing the surfaces of various materials.

3.1.8 Polarized neutron reflectometry (PNR)

Polarised neutron reflectometry (PNR) is a powerful technique for studying the structure of thin films and multilayer systems. The technique can be used to study a wide range of material systems, including magnetic and superconducting thin films, multilayers, and surfaces with complex structures. One of the main advantages of PNR is its ability to probe the magnetic structure of a material with high sensitivity and spatial resolution which offers the option to resolve magnetization as a function of sample depth. This allows for the creation of a magnetic depth profile, which can provide information about inhomogeneous magnetization distributions, the magnitude and direction of moments, and mechanisms such as magnetic domain formation and magnetization vector rotation. Additionally, PNR has a similar sensitivity to both light and heavy elements, unlike electron/X-ray scattering techniques where heavier elements generally scatter much more strongly. This makes it a powerful tool for studying the chemical properties of thin films, multilayers, and surfaces with complex structures involving light elements (e.g H or O). Figure 3.8 shows the PNR experimental setup, working principles, and application in characterising various materials. A polarizing supermirror allows only one neutron spin-state, either spin up (+) or spin down (-), to pass through it. An alternate neutron spin-

state can be selected using a spin flipper if required. The spin-polarized beam is reflected by a thin film or heterostructure, and the outgoing spin-state is analysed using an analysing supermirror. A complete reflectivity pattern of the sample is obtained by performing the measurement at various angles (ω) and/or neutron wavelengths [7].

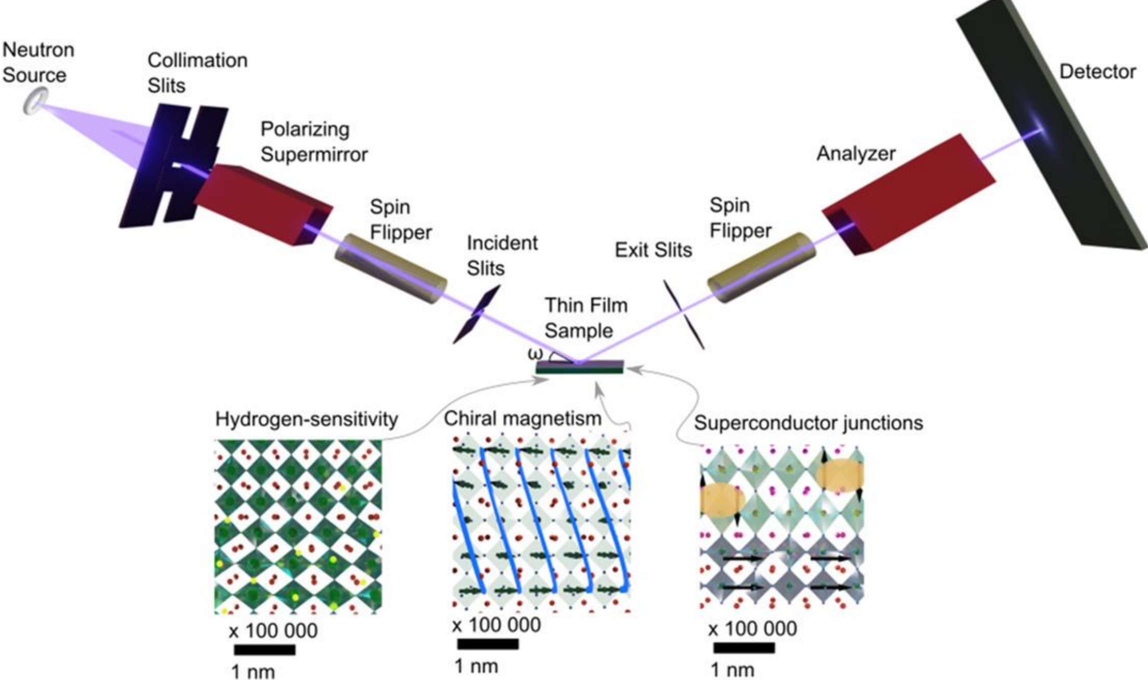

Figure 3.8. Schematic of the PNR setup shows the working principles and application in various materials systems [7].

From the PNR curve, it is possible to determine the thickness and roughness of the sample, as well as magnetisation in the material. However, specular PNR is only sensitive to in-plane magnetizations, as neutron scattering does not resolve magnetization components parallel to the wave vector transfer Q [8]. In PNR and XRR, the reflected wave intensity is usually expressed as a function of the wave vector transfer:

$$Q_Z = \frac{4\pi}{\lambda} sin\theta$$

The Figure 3.9 shows an example of a reflectivity curve which is simulated for a 40-nm-thick nickel film on a silicon substrate with a 0.6 μB per Ni atom in-plane magnetization rotated by 45° with respect to the applied measurement field [8]. The top two curves (R^{++} and R^{--}) provide information about the sample composition, layer thickness, and magnetization parallel to the field. The location of the intensity oscillations (or Kiessig

fringes) results from the Ni layer thickness. In this single-layer case, the fringe amplitude is related to the scattering contrast between the film and the substrate. As the scattering vector is inversely proportional to the real-space separation of interfaces, thicker layers will result in more tightly packed fringes with lower Q spacing between the maxima. The bottom curve (R^{+-} and R^{-+}, spin flip reflected signal) is related to the component of the magnetization perpendicular to the applied field and is identical for most cases of magnetization profiles. The difference in SLD between the parallel (R++) and antiparallel (R--) alignment of the neutron spin-states with respect to the sample magnetization results in a difference in reflectivity for each spin channel. This difference is known as the spin asymmetry (SA). (+/- sign represents the incident neutrons being spin polarized parallel (+) and antiparallel (-) to the sample magnetization).

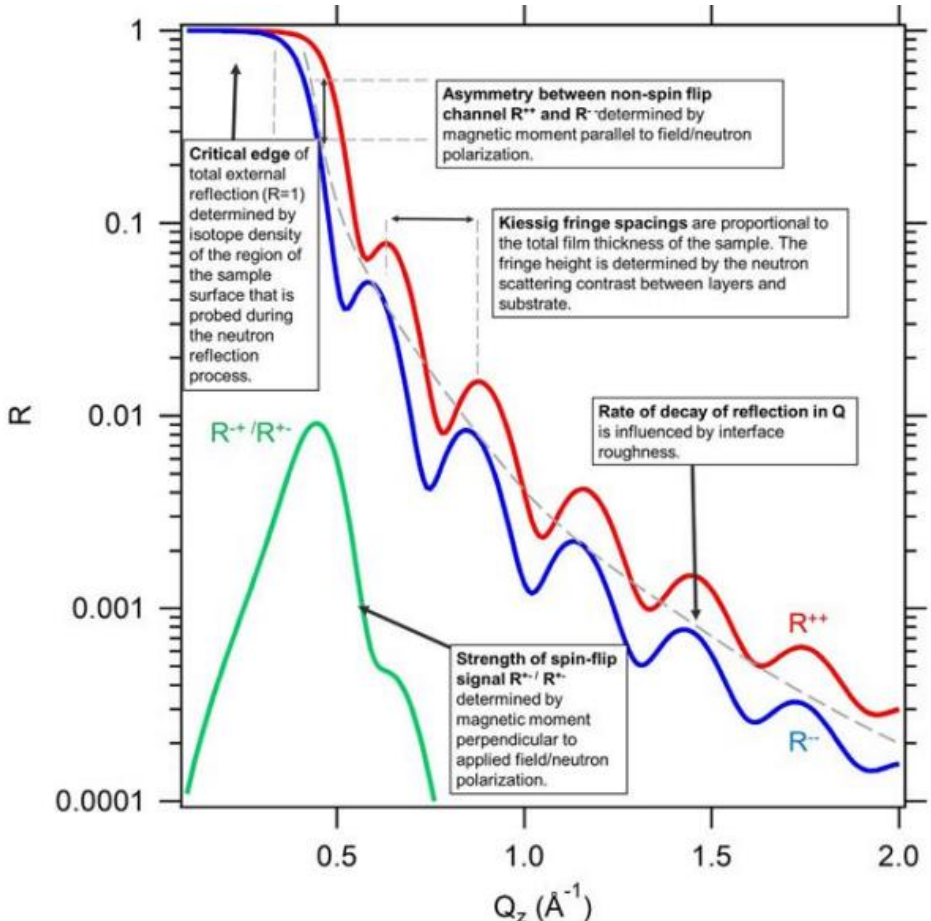

Figure 3.9. Information provided by a typical neutron reflectometry profile showing how layer thickness, chemical composition and magnetization can affect the observed signal [8].

Quantitative information from the reflectivity curve is obtained by modelling it using a scattering length density (SLD) profile that corresponds to the sample's structure. The model is refined by using different fitting algorithms that align the calculated reflectivity

from the SLD profile to the observed reflectivity. The SLD profile serves as a representation of the thin film composition and in-plane magnetization as a function of depth. In unpolarized neutron reflectometry (NR), magnetic contributions to the SLD are not distinguished and the fitted profiles only depend on the chemical composition and density of each layer. Profiles across interfaces from one layer to the next are resolved in the form of a laterally averaged roughness with sub nm resolution, depending on the nuclear contrast.

In this thesis, measurements were performed on the neutron reflectometry instruments SPATZ and PLATYPUS located at Australian Centre for Neutron Scattering (ACNS) at ANSTO.

3.2 Ion beam modification

3.2.1 FIB lamellar preparation methods

For bulk samples, before the characterisation with TEM/STEM, there is a critical lamella preparation process to obtain a lamella with thickness less than 100 nm. For most metallic, ceramic, single crystal, and their thin film samples a general method of FIB lamella fabrication procedure is suitable to fabricate high quality lamella. However, the general FIB lamella methods are not suitable for ion-beam sensitive crystals and their thin films as ion-beam sensitive specimens tend to become amorphized at the relatively low ion-beam dose. Figure 3.10 a shows an illustrated procedure composed of four main steps in FIB lamella preparation. Applying a thick protective layer prior to ion-beam exposure, as shown in Figure 3.10 b and milling at reduced ion-beam energies could be very helpful in reducing ion-beam damage. Figure 3.10 c shows a FIB lamella with enough protecting coating (Pt and C) even after final polishing. Sb_2Te_3 crystals are very sensitive to ion beams, this creates challenges for FIB lamella preparation and subsequent atomic resolution imaging. In this thesis, a new procedure was developed for preparing high quality FIB lamella suitable for atomic resolution imaging with STEM which is detailed in chapter 4 or can be accessed from the ref. [9].

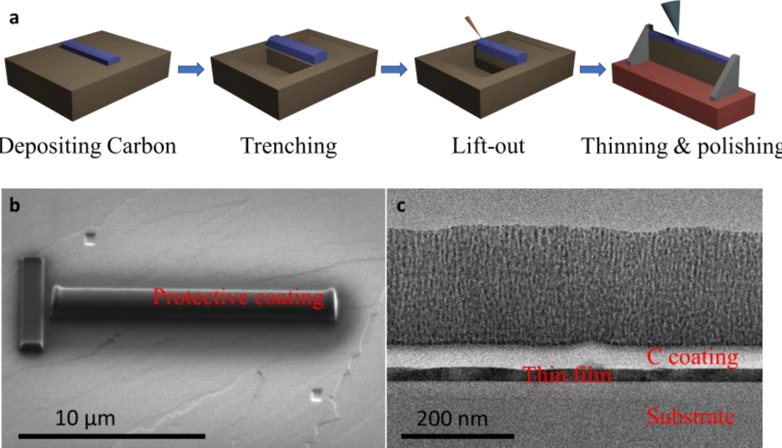

Figure 3.10. FIB lamella preparation process. (a) Schematic illustration shows a summarised procedure for FIB lamella preparation. (b) An SEM image shows a thick protecting layer deposited on to sample before trenching. (c) Low-magnification TEM image shows the remaining~300 nm protecting coating.

3.2.2 Magnetic ion implantation (Broad-beam accelerator based ion mplantation)

Magnetic ion implantation has been conducted on the Low Energy Ion Implanter (LEII), which can implant various ions of elements at the energy range of few kV up to 50 kV. Figure 3.11 shows the LEII located at Centre of Accelerator Science (CAS) at the Australian Nuclear Science and Technology Organisation (ANSTO). Various species of ions can be achieved by changing the target materials in the Penning ion source. Generated ions from target materials are accelerated through the electric field and the bending magnet strength can be tuned to select desired ion/isotope species to irradiate samples.

Ion implantation is a process in which an energetic ion beam interacts with a solid material. During this interaction, ions penetrate the material and lose energy due to electronic and nuclear interactions. Historically, ion beam implantation was primarily used to modify, etch, dope and amorphise the surface of bulk semiconductors (eg. Si or Ge) and create p-type or n-type semiconductors. However, recent studies have demonstrated that ion implantation can be used to selectively alter the properties of a wide range of materials, including 2D vdW materials, thin films, nanostructure materials, and biocompatible materials, for specific applications [10-13]. The properties of the materials can be controlled by carefully selecting the ion species, ion energy, substrate temperature, and ion fluence. Currently, low-energy ion implanters are being used to change the physical, chemical, electrical, or magnetic properties of thin films and nanostructure

materials by introducing dopant atoms or creating defects. This technique is particularly useful for synthesizing doped nanostructure materials that are difficult to produce through chemical methods.

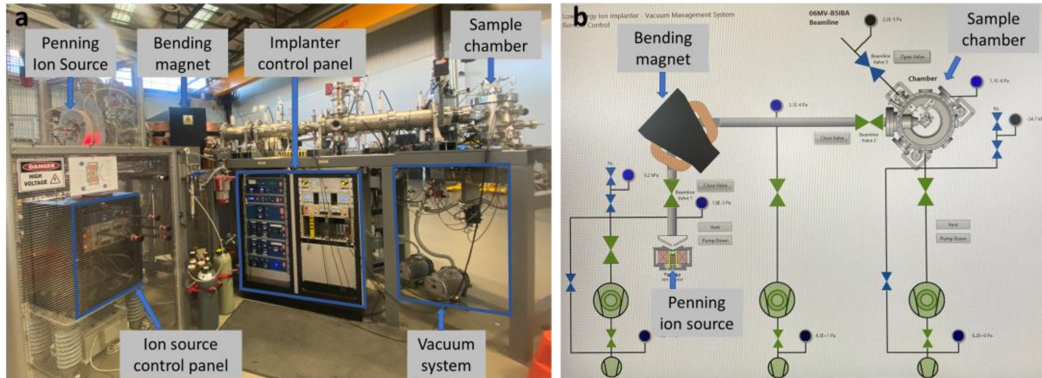

Figure 3.11. (a) Low energy ion implanter (LEII), and corresponding (b) vacuum management and control system showing the simplified schematic of LEII based at CAS, ANSTO.

In this thesis, the Stopping and Range of Ions in Matter (SRIM) [14] software was used to simulate the magnetic ions (such as Cr, Mn, V) penetration depth in the Sb_2Te_3. The software can be used to calculate and predict the transport of ions in various types of materials. Typical applications include predicting the ion stopping range in a given target, ion implantation, and sputtering etc. However, the model does not take into account any crystallinity and low dose impanation simulation maybe less accurate as ion channelling can occur in real crystalline materials. Other models/software exist to predict channelling effects due to crystallinity, for example, see the work of Gerhard Hobler at TU Wien (need a ref).

3.3 Electronic and magnetic characterisation

3.3.1 Transport measurements using PPMS

Single crystal and thin films transport measurements were performed on a Quantum Design Physical Property Measurement System (PPMS) equipped with a 14 Tesla superconducting magnet and Quantum Design DynaCool 9T PPMS (shown in Figure 3.12). The crystal or thin films samples can be wired in four probe and Hall configurations, as shown in Figure 2.13 to measure MR and Hall at various temperatures and magnetic fields.

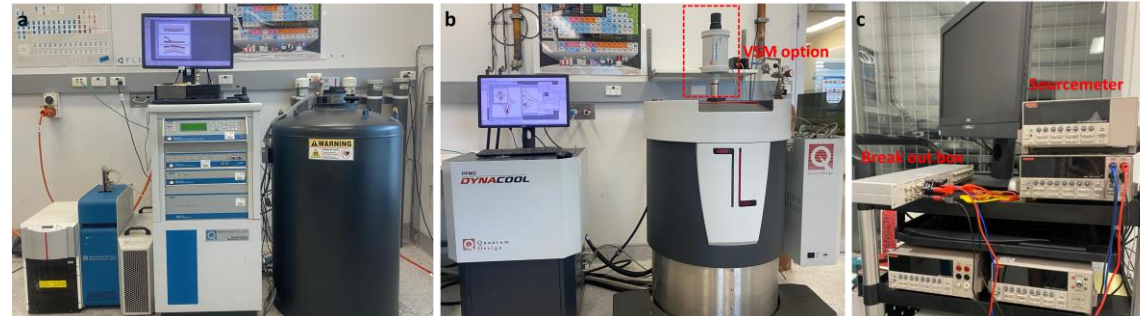

Figure 3.12. Physical properties measurements system used for transport measurements a. 14 T PPMS, and b. DynaCool 9T PPMS showing the VSM option attached. c. Sourcemeter and break out box apparatus used for high resistance measurements.

As the standard PPMS system could not measure very high resistance samples, this thesis work implemented an external measurement setup that can measure high resistance samples (such as amorphous Sb_2Te_3). Figure 3.12 shows two different models of PPMS used for transport measurement. Figure 3.13 shows two types of commercially available chips used for transport and in-situ heating measurements in our study. Transport measurements of larger, square-shaped thin films were conducted with van der Pauw contact layout.

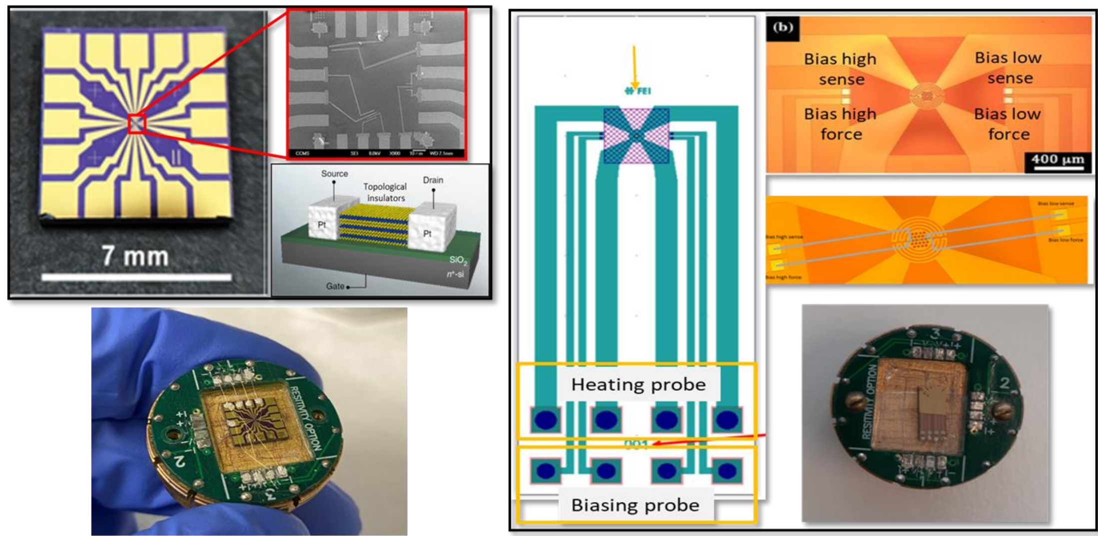

Figure 3.13. Commercially available chips used for transport measurement device fabrication. Left chip (FEI MEMS chip can be used to conduct in-situ biasing and heating in a FEI Helios G3 microscope).

3.3.2 Vibrating sample magnetometry measurements

Magnetic measurement of samples was performed on Quantum Design DynaCool 9T PPMS, as shown in Figure 3.12 b (in section 3.6), with vibrating sample magnetometry

(VSM) option attached. Low background quartz rod sample holder used for all VSM measurement. VSM working principles based on Faraday's law of induction. During the measurements, a sample is placed in a magnetic field, as shown in Figure 3.14 a, and if it is magnetic, it will align its magnetization with the external field. The magnetic dipole moment of the sample produces a magnetic field that varies with time as the sample moves up and down (vibrates). The alternating magnetic field generates an electric field in the pickup coils of the VSM. The current produced is proportional to the magnetization of the sample, larger induced current indicating higher magnetization. Figure 3.14 b shows two common sample holder-geometry for VSM measurements which are mainly performed for pure in-plane or out-of-plane directions.

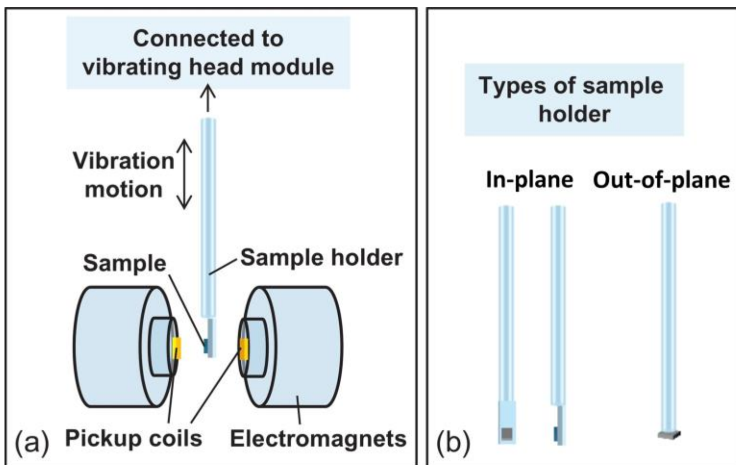

Figure 3.14. Schematic diagram of a. VSM measurement setup and b. types of sample holders used in VSM showing in-plane and out-of-plane configurations. [15]

3.4 Transport measurement device fabrication with a focused ion-beam

The results in this Section 3.6 below form a part of a draft manuscript that will be submitted for publication.

3.4.1 Overview

In order to carry out transport measurements on micro/nano scale crystals, this section provides a detailed description of 2 main strategies provided for fabricating transport measurement devices. There are a couple of advantages of fabricating transport devices with FIB. These include (1) Relatively high precision fabrication of micro and nanoscale

devices. (2) Being able to lift out from single phase crystal region and along certain crystallographic orientations with the help of EBSD. (3) Crystal transport properties can be measured along various crystallographic orientations at the micro-nano scale and correlated with the device performance and/or quantum oscillations/magnetoresistance. (4) Device can be bespoke, and it is easy to incorporate subtle changes from device to device. (5) It is possible to further modify devices after measurement. (6) FIB only needs to access a small amount to construct a viable device, suitable for samples are either very small or in limited supply.

Nevertheless, fabricating devices in the FIB poses several challenges, and a great deal of the current thesis work was directed at making this process more reliable and reproducible. Figure 3.15 shows some of the custom-designed electrical contacts and failures during an early stage of device fabrication due to various reasons, such as over-heating, applying high currents, accidental collision/manipulation of the device etc. A significant improvement in device fabrication and optimizing testing parameters eventually resulted in the successful fabrication of device and transport measurements, which will be discussed in a later section.

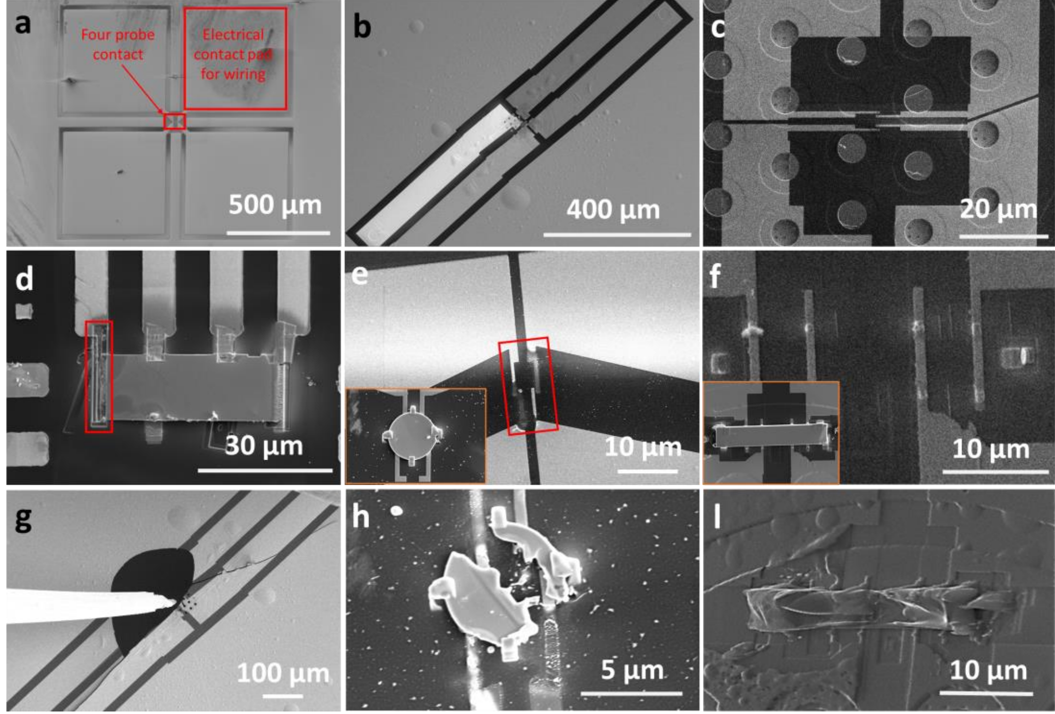

Figure 3.15. (a-c) A few custom-designed gold electrical contacts for four-probe measurements (d) Pt deposition at higher currents and voltages also induces significant milling damage on a rectangular geometry device, (e) Burnt electrical legs and disk geometry in the inset image. (f) Electrical contacts were fabricated for four-probe measurements and Sb_2Te_3 rectangular geometry

was placed on the pre-fabricated contacts. (g) Broken chip due to the fast approaching of the manipulator during placing the lift-out geometry on the contacts. (h) Damaged device due to high current during testing. (i) Overheated device due to high current.

3.4.2 Introduction

Due to unique and novel physical properties, functional nanostructures and devices are of great significance for a range of applications, such as photonics[16], optoelectronics[17] and micro/nano electromechanical systems (MEMS/NEMS) [18]. A broad range of nano/micro engineering techniques have been developed over the past years, including electron beam lithography, self-assembly, laser nano patterning, 3D printing etc. [19-21]. However, those techniques are rarely capable of engineering 3D structures and devices with high precision and arbitrary geometry. In the case of micro nano electronics, interesting device proposals and emerging physical phenomena requires precise control of the nanostructure shape and size [22].

Focused ion beam (FIB) has been playing a critical role in the semiconductor industry for mask repairing, device modification, and integrated circuit debugging and is increasingly being used to fabricate nanostructured devices. FIB nanofabrication (also called direct writing) transfers patterns by direct impingement of spots onto substrate surfaces. Projection printing or ion projection lithography (IPL) originated from the semiconductor industry, which uses a collimated ion beam that passes through a stencil mask to form a pattern that is projected and printed onto substrate surfaces.

Liquid-metal ion sources (LIMS) are the most common source for FIB and Ga is the most widely used ion species in FIBs due to its low melting point [23]. FIB milling is a process including sputtering, material redeposition, and amorphization. Sputtering is the main mechanism responsible for material removal during milling which is generally represented by sputter yield defined as the number of atoms knocked out from the target surface per incident ion. The Stopping and Range of Ions in Matter (SRIM) [24] software packages calculate many features of the transport of ions in matter. It has been widely used for the prediction of stopping powers, range and straggling distributions for any ion at any energy in any elemental target including targets with complex multi-layer configurations. Moreover, SRIM is also used for predicting ion implantation and associated kinetic effects, phonon production, sputtering, and ion transmission.

Generally, sputtering yield increases with ion energy and levels off or decreases at higher ion energies where implantation dominates as ions penetrate deeper into the target and are trapped inside the target lattice. In general, sputtering yield increases with the ion beam incident angle and reaches a maximum near 80° then decreases rapidly to zero as the incident angle further increases and approaches 90° [25]. Redeposition is the consequence of sputtered atoms in the gas phase when these condense back to the solid phase upon collision with any solid surface nearby. Thus, ejected atoms have the possibility of bumping into the sputtered surface and redepositing on it. Thus, FIB milling is a destructive method to create patterns and nano structures. Hence, the method requires a careful milling strategy depending on the geometry/ shape of nanostructures and consideration of materials-related issues, such as amorphization, redeposition and swelling. Multiple studies confirm that nanoscale channel milling with a single pass has an inherent 'V-shaped cross-section similar to hole milling[26, 27]. Redeposition can be greatly avoided by applying multiple passes instead of a single pass milling with the same amount of ions [28]. The ion beam irradiation at low ion energy and fluence tends to amorphise crystalline samples and induce swelling. In the case of crystalline silicon, ion fluences in the range of 10^{13} ions/cm^2 to 10^{15} ions/cm^2 causes pronounced swelling due to amorphisation, while the effective sputtering dose should be two orders of magnitude higher than the amorphisation dose. [29]

A FIB can also be used as a deposition tool associated with a gas injection needle to allow the injection of a variety of organometallic precursor gases on target surfaces. The ion beam can decompose the organometallic molecules adsorbed onto the surface of the target and lead to the release of metal atoms. The following precursor gases $C_{10}H_8$ (Naphthalene), WF_6 (or $W(CO)_6$), $C_7H_7F_6O_2Au$, $(CH_3)_3NAlH_3$, $C_9H_{16}Pt$, and TMOS+O_2 (TMOS=tetramethyloxysilane) have been used to deposit C, W, Au, Al, Pt, and SiO_2, respectively [30]. FIB deposits contain significant amounts of carbon due to the usage of organometallic compounds used for metal deposition. Selection of proper beam size, current, and energy of a FIB is critical for removing or adding a certain amount of materials at the nanometre level from a certain location in a controlled manner. The in-situ capability of FIB to deposit various metals and micro/nano machining made it a powerful tool for fabricating various structures for testing materials properties at the micro/nano scale. FIB is also widely used for preparing and thinning specimens for transmission electron microscopy (TEM) [9]. Samples for in-situ micro mechanical tests

have been performed on FIB-fabricated micro pillars to investigate length-scale effects on deformation and strength [31]. FIB has been also a key tool for rapid nano structuring of metallic, semiconducting and dielectric materials and devices with ion-beam etching [32-34]. More recently, thanks to high-resolution imaging, 3D reconstructed images/ slice views obtained from FIB tomography are becoming increasingly popular in biological samples [35]. Modern FIB systems enable high-precision localised milling and deposition as a versatile maskless lithography technique. Thus, it has been utilised in developing prototypes of electrical and optical devices from microcrystallites where their size and shape are challenging for traditional lithographic or manual contact fabrication techniques [36]. P. Wang et al. used FIB to fabricate tapered cantilever specimens and T-shaped specimens from the multilayered Bi_2Te_3 and precisely measured the interlaminar fracture toughness (IFT) [37]. Their method is well-suited for assessing IFTs of multilayered van deer Walls materials. W. Xu et al. fabricated a Te nanotube photodetector assisted by the FIB technique that simply uses a W nanomanipulator to pick up a Te nanotube and transfer it on to the Au electrodes to build two terminal devices [38]. Some of the experiments are limited by the size and shape of available crystals, especially newly discovered and crystal growths not yet fully developed to grow large-size compounds [39]. A method derived from traditional lamella creation has demonstrated the fabrication of standard four-probe microstructures for anisotropic transport measurements which could provide anisotropic or interlayer transport properties of layered materials both parallel and perpendicular to the c-axis [40-42]. Alternatively, to measure the interlayer transport properties of single crystals, some strategies have borrowed from the fabrication of Josephson stacks [43]. This idea has been utilised to fabricate an s-shaped device from single crystal $PrFeAsO_{0.7}$, and study the transport properties along the c-axis and ab plane [43, 44].

The device fabrication methods in the literature are based on the adopted FIB lamella preparation method, hence all surfaces are exposed to ion beam milling while fabricating desired nano/microstructures. Even milling at reduced ion beam energies still introduces a few nanometres of the amorphous damaged layer. The surface damaged layer might not represent the true transport behaviour of some chalcogenide vdW layer materials, where surface layers play an important role in the electronic properties. For example, topological materials have fascinating transport properties originating from the surface. It is critical to maintain the surface crystal structure of a device fabricated from topological materials.

In this study, we describe two novel approaches for the device fabrication and transport characterization of topological insulator antimony telluride (Sb_2Te_3) and another similar van der Waals structure layered materials. The main advantages of the methods described in this section are that they are suitable for vdW layered materials and the in-situ vacuum fracturing/exfoliation could be helpful for vdW materials that are not stable in air. Most importantly, in both methods, the front and back surfaces of the devices are kept pristine and unexposed from ion beam irradiation. This could be very important for studying the transport properties of some materials where their surfaces have significant contributions to the electronic properties.

3.4.3 Results and discussions

Before fabricating a device from a site-specific region on a crystal using a FIB, it is helpful to identify the phase and crystal structure of materials. Using energy dispersive spectroscopy (EDS) combined with electron backscattered diffraction (EBSD) maps, the correct elemental composition and phase of single crystal Sb_2Te_3 can be identified. It is also possible to align the crystalline samples to certain crystallographic orientations to study anisotropic properties. Figure 3.16 a shows the image of a Sb_2Te_3 crystal, where different phases are present. A further EDS mapping in Figure 3.16 b and EBSD mapping in Figure 3.16 c to Figure 3.16 e show that the crystal piece is not from a pure Sb_2Te_3 single crystal but rather intermixed phases of Sb_2Te_3 and Te single crystals. The EDS overlayer image in Figure 3.16 b shows the distribution of Te element (in green colour), and Sb elements (in red colour) on the crystal surface. Figure 3.16 c shows the band contrast image, in which brighter regions indicate well-indexed crystallinity as opposed to darker regions which indicate poorly indexed crystallinity. Sb_2Te_3 phases scattered as islands in Te phases, as shown in Figure 3.16 d EBSD phase colour image, which combined with EDS mapping, composition and the crystal phases can be identified. The Euler colour image in Figure 3.16 e indicates the Te phase has a single crystallographic orientation while the Sb_2Te_3 phase has multiple crystallographic orientations (see pole figure in Figure 3.16 l). A further point analysis in Figure 3.16 f and Figure 3.16 g shows the typical Kikuchi patterns for the Sb_2Te_3 phase and Te phase, respectively. In comparison, Figure 3.16 h shows the SE image of a freshly cleaved pure Sb_2Te_3 single crystal, and EBSD mapping in Figure 3.16 i to Figure 3.16 l confirms the single crystallinity and (c-axis) normal to the 001 planes.

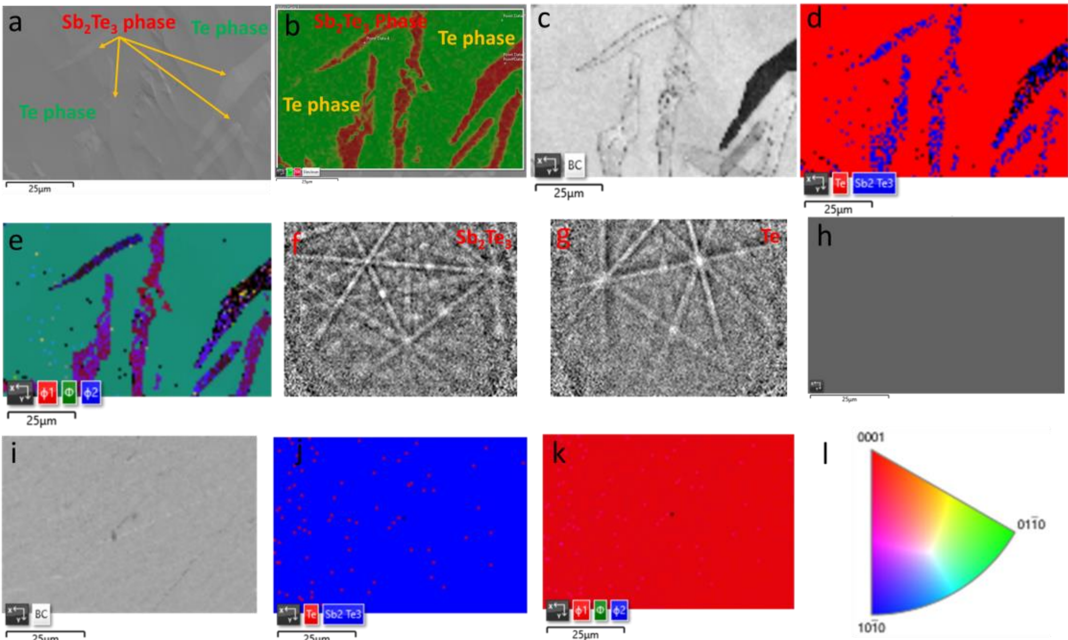

Figure 3.16. Using EDS and EBSD to identify composition and crystal phase. Poor quality single crystals showing the formation of Sb_2Te_3 and Te single crystal phase in a piece of crystal (a) SE image, (b) EDS overlayer image, (c) Band contrast image, (d) Phase colour image, (e) Euler colour image collectively showing Sb_2Te_3 and Te crystal phases present in the crystal pieces being analysed. (f) and (g) are Kikuchi patterns for Sb_2Te_3 and Te single crystals. In contrast, (b) SE image of a high-quality single crystal Sb_2Te_3 and corresponding (i) Band contrast image, (j) Phase colour image, (k) Euler colour, and (l) Pole figure from EBSD mapping indicates the pure single crystalline phase of Sb_2Te_3.

After identifying the correct composition and phase of Sb_2Te_3, a design-specified geometry can be milled and lifted out for subsequent device fabrication. The Figure 3.17 shows the main 4 steps (a-d) involved in the device fabrication by a controlled fracturing method. Figure 3.17 a1 shows disk shape geometry milling and Figure 3.17 a2 shows rectangular geometry milling, while Figure 3.17 a3 shows the schematic illustration of the various milling process recreated with a 3D model to view the lateral dimension. Geometry milling using FIB is a maskless process, this makes it possible to pattern curved and irregular surfaces. However, the role beam focus becomes particularly important when milling precise micro nanoscale structures. Here, the geometry milling process is usually performed at higher beam energy (>15 kV) and relatively smaller current (< 1 nA) to focus the ion beam as best as possible to create a sharp milling periphery. After milling desired geometry and creating a trench around it, a controlled fracturing of the disk shape and rectangular shape geometry can be performed with a manipulator, as shown in the Figure 3.17 b1 and Figure 3.17 b2, respectively. The Figure 3.17 b3 shows

the schematic illustration of the controlled fracturing procedure, in which specific shaping of the manipulator tip is essential. The enlarged regions in Figure 3.17 b3 shows a sharp (and wide) tip of the manipular penetrates Sb_2Te_3 to laminate and then lift the disk-shape geometry. Importantly, the bottom half part of the disk is left unexfoliated so as to obtain a pristine cleave surface, free of ion beam damage. For slightly thicker geometry, blunt (and wide) shaped manipulator tips can also push from the side to dislocate and liberate geometry from the parent specimen, however, this process has a much lower less success rate. For successful “push-offs”, the manipulator tip can then be welded to the half-exfoliated/liberated geometry to be lifted off from the parent specimen. The third step includes approaching and placing the geometry welded on the manipulator to the prefabricated contacts or chip as shown in Figure 3.17 c1 and Figure 3.17 c2. The geometry transferring on a chip is illustrated in the Figure 3.17 c3. The last step is electrical contact fabrication using FIB-assisted Pt deposition. Figure 3.17 d1 and Figure 3.17 d2 show four-probe/Hall contact fabricated on a disk and rectangular shape geometries, respectively. Figure 3.17 d3 shows an illustration of the four-probe/Hall contact fabrication and the enlarged region in Figure 3.17 d3 shows typical contact fabrication for all the subsequent transport measurements in this work.

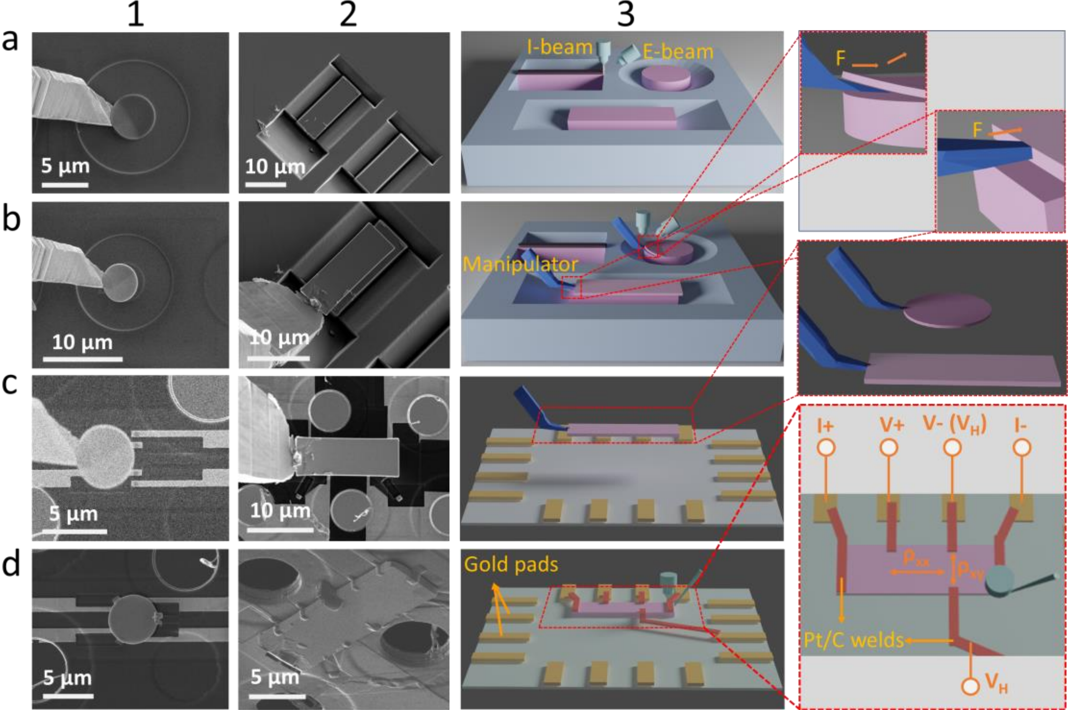

Figure 3.17. Device fabrication through controlled fracturing, (a) A geometry milling, (b) Controlled fracturing, (c) Transferring on a chip, and (d) Electrical contact fabrication. Column 2 shows the controlled fracturing of the rectangular geometry process, and column 3 shows the illustration of each step.

Ion-beam induced damage could significantly change the transport properties of crystalline materials. Important consideration should be given to minimise ion-beam induced damage during geometry milling and ion-beam imaging. Ion-beam imaging also induces damage, which can be significantly minimised by adopting lower ion-beam energies (≤ 8 kV) and currents (40 pA), which are the usual ion-beam imaging parameters in this work. Due to the Gaussian distribution of ion density, some ions from the beam skirt still irradiate the surface of geometry, which causes ion beam damage, especially for ion-beam sensitive materials, such as Sb_2Te_3 [9]. Figure 3.18 a shows EDS and EBSD mapping of the Sb_2Te_3 surface before milling a geometry, which indicates the single crystallinity of Sb_2Te_3. When the ion beam starts trenching around the 5 μm diameter disk shape geometry, EBSD mapping in Figure 3.18 b indicates that not only trenched region but also the disk shape gradually loses crystallinity at the top surface. As ion-beam continues to mill a doughnut shape trench, ion-beam induced damage gradually spreads as evidenced by the EBSD mapping in Figure 3.18 c and Figure 3.18 d. One way to avoid a surface damaged layer is to exfoliate/fracture a certain thickness of geometry, as shown in the Figure 3.17 as the first step of device fabrication. This process is able to expose the fresh exfoliated crystalline surface of Sb_2Te_3, which then again following the controlled fracturing method to obtain a desired crystalline geometry free of ion-beam damage. During transferring the geometry on a chip and subsequent Pt deposition, a snapshot was used rather than continue viewing with the ion-beam imaging to minimise ion-beam irradiation of the geometry surface as much as possible. The device fabrication with the controlled fracturing method described above is possible, and some of the results were reported in the past publication [45]. However, this method can be time-consuming due to the nature of the process being skill and experience demanding.

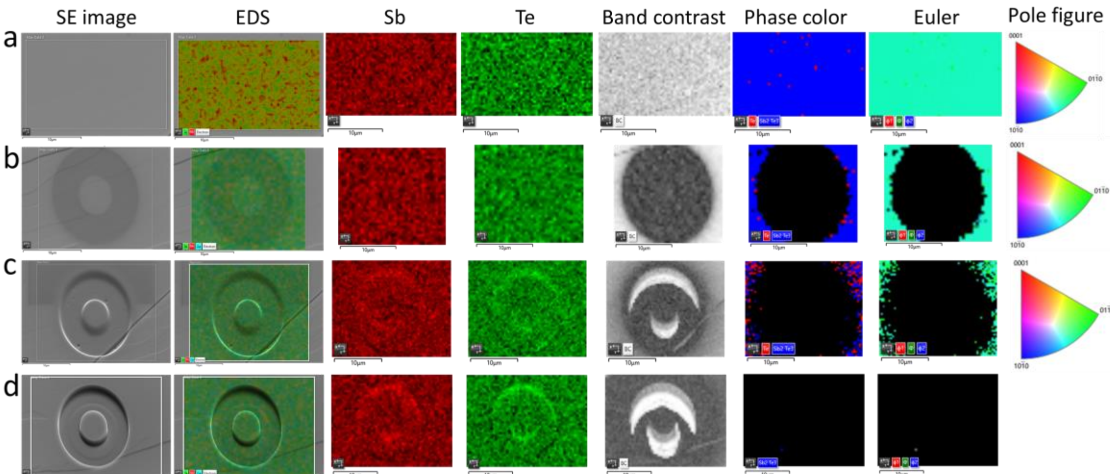

Figure 3.18. EBSD mapping shows the degree of amorphisation of Sb_2Te_3 single crystal surfaces as ion beam milling continues. (a)-(b) EDS and EBSD mapping at intervals during the different levels of trenching.

An alternate and easier method is ex-situ exfoliation combined with FIB milling. Figure 3.19 below summarises the major four steps (1-4) in transport device fabrication using a combination of ex-situ exfoliation to create flaky surfaces for vdW layered crystal followed by cutting a desired geometry. This method involves a process of ex-situ exfoliation to create flaky surfaces as shown in Figure 3.19 a1 and Figure 3.19 b1. Then, fresh exfoliated Sb_2Te_3 crystals were placed in the FIB chamber, followed by identifying a flake with desired thickness under electron imaging mode (i.e. no ions involved). One end of the rectangular geometry was welded to the manipulator before cutting the geometry completely, as shown in Figure 3.19 a2 and Figure 3.19 b2. Cutting the desired geometry from the flakes can be done blindly to further reduce beam damage from ion-bam imaging (or snapshotting) with the help of well-aligned and linked electron image and ion-beam image. The lift-out welded on the manipulator was transferred onto a chip for contact fabrication, as shown in Figure 3.19 a3 and Figure 3.19 b3. Then this was followed by the final step of electrical contact fabrication using Pt deposition, as shown in Figure 3.19 a4 and Figure 3.19 b4. The ion beam milling and imaging (snapshotting) parameters were similar as described in the previous methods. A complimentary EBSD characterisation is helpful to check the surface crystallinity of the device after fabrication is completed. EBSD mapping of a device on a chip was reported in our past publication [45].

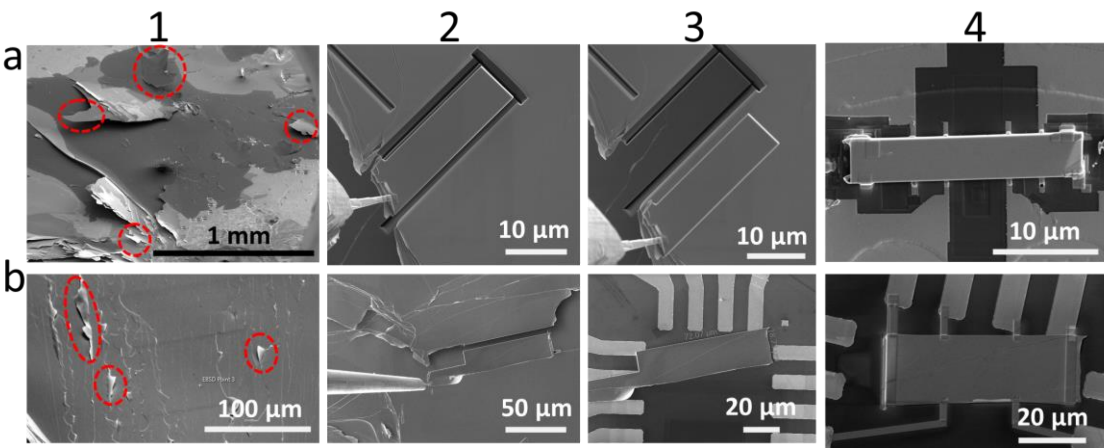

Figure 3.19. Four -probe and Hall measurement device fabrication process using a combination of ex-situ exfoliation and FIB milling. (a) and (b) Rectangular transport device contacted on custom-made electrical contacts and commercial chip.

As Sb_2Te_3 single crystal is a topological insulator, maintaining surface crystallinity during transport device fabrication is critical for subsequent transport measurements. Figure 3.20 shows the transport behaviour of an early, low quality device whose surface is amorphised during fabrication. In comparison, Figure 3.21 shows the transport measurement of a high quality, Sb_2Te_3 device where the process has been optimised to maintained surface crystallinity after device fabrication and transport measurements. The Figure 3.20a shows a Sb_2Te_3 device (with a thin surface amorphous layer) has metallic resistance versus temperature response, whereas in some cases, with surfaces deliberately amorphised to form thick layers, it shows semiconducting resistance versus temperature response. The magnetoresistance (MR) curve in Figure 3.20b shows a lack of Shubnikov-de Haas (SdH) oscillation possibly due to the collapse of surface states when ion-beam amorphises the surface of Sb_2Te_3 single crystals [45]. The data in Figure 3.20b is not smoothed to show large measurement fluctuation at low temperatures as compared to higher temperatures under the same excitation current. Figure 3.20c shows the Hall measurement, p-type semiconductor nature of Sb_2Te_3 single crystals.

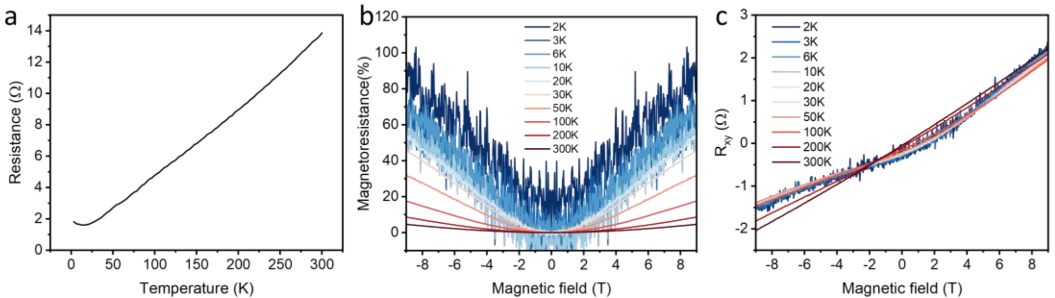

Figure 3.20. Transport of a surface amorphized Sb_2Te_3 of the device during fabrication. (a) Resistance versus temperature curve, (b) Magnetoresistance at various temperatures, (c) Hall measurement at various temperatures.

Figure 3.21a again shows metallic resistance versus temperature response. More interestingly, SdH oscillations, a key feature of Sb_2Te_3 crystal, can be seen from the MR in Figure 3.21b, which can be used to map the Fermi surface of the material and evaluate the contribution of surface states. Upon subtracting the background, an SdH oscillation pattern can be obtained, as shown in Figure 3.21c. The amplitude of SdH oscillation shows a major oscillation frequency accompanied by satellite oscillation frequency (indicating multiple pockets exist near the Fermi surface) and decreases at a higher temperature, as shown in Figure 3.21d. The oscillation magnitudes provide information about the electronic structure of materials, such as the effective mass and carrier mobility. The Hall measurement in Figure 3.21e shows the p-type semiconductor nature of Sb_2Te_3 single crystals. SdH oscillations provide an effective way to study the surface states in 3D TIs. The angular dependence of the SdH oscillations is useful to isolate surface state contribution. Figure 3.21f shows the angle dependent SdH oscillation of the Sb_2Te_3 device, and Figure 3.21g shows the SdH oscillation pattern after subtracting the background. The SdH oscillation amplitude in Figure 3.21h shows a frequency shift with the change in angle. This may indicate that the oscillation component is due to the contribution of 2D electrons that might originate from surface states. However, the intrinsic ellipsoidal shape of the bulk Sb_2Te_3 surface may also lead to a shift.

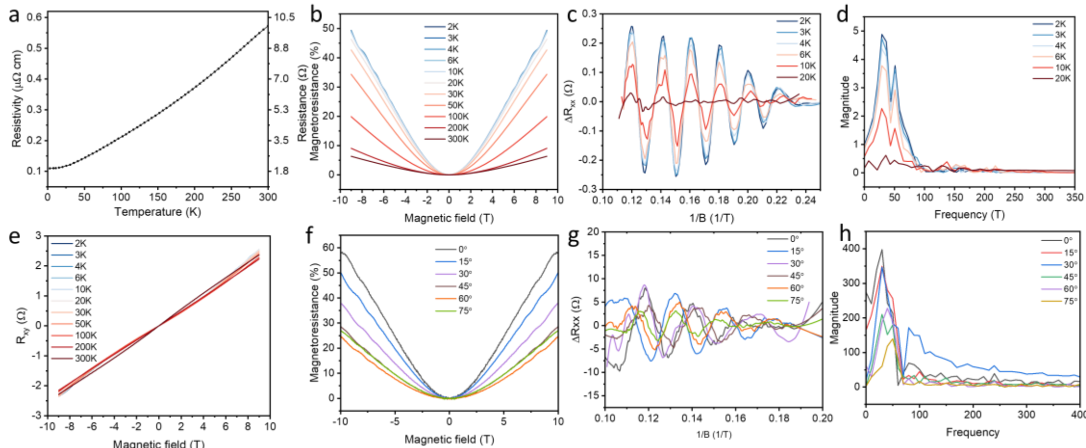

Figure 3.21. Transport of the Sb_2Te_3 device with the surface crystallinity preserved during fabrication. (a) Resistance versus temperature curve, (b) Magnetoresistance at various temperatures, (c) SdH oscillation pattern after background subtraction, (d) Oscillation frequency versus magnitude after performing Fast Fourier transform (FFT) on (c), and (c) Hall measurement at various temperatures. (f) Angle-dependent magnetoresistance at various temperatures, (g) SdH oscillation pattern after background subtraction, (h) Oscillation frequency versus magnitude after performing Fast Fourier transform (FFT) on (g).

These device fabrication methods are beneficial for studying the transport properties of vdW layered crystals that are not yet been grown in large sizes. Moreover, with the help of EBSD, it is possible to cut certain geometry with specific crystallographic orientation in FIB to study their anisotropic properties. Fabrication of nano micro transport devices using FIB holds great promise as it helps observe enhanced physical properties of crystals [42].

3.4.4 Conclusions

FIB-assisted device fabrication opens a viable venue for exploring new physical phenomena and observing enhanced physical properties of newly discovered materials. Especially, the crystals that cannot be grown in large sizes could benefit from FIB-assisted device fabrication. Device fabrication using FIB is skill demanding task, and ion-beam induced damage could dramatically change the transport properties of the crystalline materials. Especially for topological insulator, where interesting transport phenomena originate from the surface states of materials. Thus, protecting the surface of crystalline materials from ion-beam induced damage is critical for successful transport device fabrication. Nevertheless, this work provides two different methods, mainly in-

situ controlled fracturing and ex-situ exfoliation-based transport device fabrication. The work provides multiple strategies to minimise ion-beam damage and shows the importance of surface crystallinity in transport measurements.

Our work has successfully presented two different methods to fabricate transport devices based on in-situ controlled fracturing and ex-situ exfoliation. Moreover, the work provided a few strategies to minimise ion-beam damage, during device fabrication, which could affect the transport properties significantly. Two different device fabrication methods reported in this work are generally suitable for vdW layered materials which take advantage of easy exfoliation. As compared to the device fabrication method modified from FIB lamella preparation, the controlled fracturing and exfoliation-based methods could significantly reduce ion-beam irradiation of the surfaces of lift-out geometry. As a 3D TI Sb_2Te_3 example, we showed the possibility of fabricating a transport device with surface crystallinity maintained, which is critical for the transport properties.

References

1. Ul-Hamid, A., *A beginners' guide to scanning electron microscopy*. Vol. 1. 2018: Springer.

2. Goldstein, J.I., et al., *Scanning electron microscopy and X-ray microanalysis*. 2017: Springer.

3. de Oliveira Jr, O.N., et al., *Nanocharacterization techniques*. 2017: William Andrew.

4. Nishikawa, S. and S. Kikuchi, *Diffraction of cathode rays by calcite.* Nature, 1928. **122**(3080): p. 726-726.

5. Nellist, P.D., *Scanning transmission electron microscopy*, in *Springer Handbook of Microscopy*. 2019, Springer. p. 49-99.

6. Yasaka, M., *X-ray thin-film measurement techniques.* The Rigaku Journal, 2010. **26**(2): p. 1-9.

7. Causer, G.L., et al., *Topical review of quantum materials and heterostructures studied by polarized neutron reflectometry.* physica status solidi (RRL)–Rapid Research Letters.

8. Callori, S.J., et al., *Using polarized neutron reflectometry to resolve effects of light elements and ion exposure on magnetization*, in *Solid State Physics*. 2020, Elsevier. p. 73-116.

9. Bake, A., et al., *Lamellae preparation for atomic-resolution STEM imaging from ion-beam-sensitive topological insulator crystals.* Journal of Vacuum Science & Technology A: Vacuum, Surfaces, and Films, 2022. **40**(3): p. 033203.

10. Ishaq, A., L. Yan, and D. Zhu, *The electrical conductivity of carbon nanotube sheets by ion beam irradiation.* Nuclear Instruments and Methods in Physics Research Section B: Beam Interactions with Materials and Atoms, 2009. **267**(10): p. 1779-1782.

11. Tsuji, H., et al., *Nerve-cell attachment properties of polystyrene and silicone rubber modified by carbon negative-ion implantation.* Surface and Coatings Technology, 2007. **201**(19-20): p. 8123-8126.

12. Husnain, G., et al., *Structural and magnetic impact of Cr implantation into GaN thin film.* Solid state sciences, 2012. **14**(6): p. 735-738.

13. Cortie, D., et al., *Creating thin magnetic layers at the surface of Sb_2Te_3 topological insulators using a low-energy chromium ion beam.* Applied Physics Letters, 2020. **116**(19): p. 192410.

14. Ziegler, J.F., M.D. Ziegler, and J. Biersack, *SRIM–The stopping and range of ions in matter (2010).* Nuclear Instruments Methods in Physics Research Section B: Beam Interactions with Materials Atoms, 2010. **268**(11-12): p. 1818-1823.

15. Adeyeye, A. and G. Shimon, *Growth and characterization of magnetic thin film and nanostructures*, in *Handbook of Surface Science*. 2015, Elsevier. p. 1-41.

16. Chen, F., *Micro‐and submicrometric waveguiding structures in optical crystals produced by ion beams for photonic applications.* Laser & Photonics Reviews, 2012. **6**(5): p. 622-640.

17. Zhang, Y., et al., *A large-area 15 nm graphene nanoribbon array patterned by a focused ion beam.* Nanotechnology, 2014. **25**(13): p. 135301.

18. Nagase, M. and H. Namatsu, *A method for assembling nano-electromechanical devices on microcantilevers using focused ion beam technology.* Japanese journal of applied physics, 2004. **43**(7S): p. 4624.

19. Shahrubudin, N., T.C. Lee, and R. Ramlan, *An overview on 3D printing technology: Technological,*

materials, and applications. Procedia Manufacturing, 2019. **35**: p. 1286-1296.

20. Li, L., et al., *Laser nano-manufacturing–state of the art and challenges.* CIRP annals, 2011. **60**(2): p. 735-755.

21. Chen, Y., *Nanofabrication by electron beam lithography and its applications: A review.* Microelectronic Engineering, 2015. **135**: p. 57-72.

22. Mehlin, A., et al., *Stabilized skyrmion phase detected in MnSi nanowires by dynamic cantilever magnetometry.* Nano letters, 2015. **15**(7): p. 4839-4844.

23. Orloff, J., et al., *Physics of liquid metal ion sources.* High Resolution Focused Ion Beams: FIB and its Applications: The Physics of Liquid Metal Ion Sources and Ion Optics and Their Application to Focused Ion Beam Technology, 2003: p. 21-77.

24. Ziegler, J.F., M.D. Ziegler, and J.P. Biersack, *SRIM–The stopping and range of ions in matter (2010).* Nuclear Instruments and Methods in Physics Research Section B: Beam Interactions with Materials and Atoms, 2010. **268**(11-12): p. 1818-1823.

25. Tseng, A.A., *Recent developments in nanofabrication using focused ion beams.* Small, 2005. **1**(10): p. 924-939.

26. Frey, L., C. Lehrer, and H. Ryssel, *Nanoscale effects in focused ion beam processing.* Applied physics A, 2003. **76**(7): p. 1017-1023.

27. Li, H.-W., et al., *Focused ion beam fabrication of silicon print masters.* Nanotechnology, 2003. **14**(2): p. 220.

28. Tseng, A.A., *Recent developments in micromilling using focused ion beam technology.* Journal of micromechanics and microengineering, 2004. **14**(4): p. R15.

29. Lugstein, A., et al., *FIB processing of silicon in the nanoscale regime.* Applied Physics A, 2003. **76**(4): p. 545-548.

30. Melngailis, J., *Applications of ion microbeams lithography and direct processing*, in *Handbook of VLSI Microlithography*. 2001, Elsevier. p. 790-855.

31. Uchic, M.D., et al., *Sample dimensions influence strength and crystal plasticity.* Science, 2004. **305**(5686): p. 986-989.

32. Nagel, J., et al., *Resistively shunted YBa2Cu3O7 grain boundary junctions and low-noise SQUIDs patterned by a focused ion beam down to 80 nm linewidth.* Superconductor Science and Technology, 2010. **24**(1): p. 015015.

33. Kadowaki, K., et al., *Dynamical properties of Josephson vortices in mesoscopic intrinsic Josephson junctions in single crystalline Bi2Sr2CaCu2O8+ δ.* Physica C: Superconductivity and its applications, 2006. **437**: p. 111-117.

34. Lobo, D.E., et al., *Miniaturized supercapacitors: focused ion beam reduced graphene oxide supercapacitors with enhanced performance metrics.* Advanced Energy Materials, 2015. **5**(19): p. 1500665.

35. Narayan, K. and S. Subramaniam, *Focused ion beams in biology.* Nature methods, 2015. **12**(11): p. 1021-1031.

36. Pisoni, A., et al., *Single crystals of superconducting SmFeAsO H x: Structure and properties.* Physical Review B, 2016. **94**(2): p. 024525.

37. Wang, P., et al., *Interlaminar Fracture Toughness Measurement of Multilayered 2D Thermoelectric Materials Bi2Te3 by a Tapered Cantilever Bending Experiment.* Experimental Mechanics, 2022.

62(1): p. 165-180.

38. Xu, W., et al., *FIB-assisted fabrication of single tellurium nanotube based high performance photodetector.* Micromachines, 2021. **13**(1): p. 11.

39. Jaroszynski, J., et al., *Upper critical fields and thermally-activated transport of NdFeAsO 0.7 F 0.3 single crystal.* Physical Review B, 2008. **78**(17): p. 174523.

40. Moll, P.J., et al., *High magnetic-field scales and critical currents in SmFeAs (O, F) crystals.* Nature materials, 2010. **9**(8): p. 628-633.

41. Pisoni, A., et al., *Upper critical field, pressure-dependent superconductivity and electronic anisotropy of Sm4Fe2As2Te1− xO4− yFy.* Journal of Physics: Condensed Matter, 2016. **28**(11): p. 115701.

42. Moll, P.J., et al., *Field-induced density wave in the heavy-fermion compound CeRhIn5.* Nature Communications, 2015. **6**(1): p. 6663.

43. Shirai, K., et al., *Local transport properties of PrFeAsO0. 7 using FIB micro-fabrication technique.* Physica C: Superconductivity and its applications, 2010. **470**(20): p. 1473-1476.

44. Kashiwaya, H., et al., *C-axis critical current of a PrFeAsO 0.7 single crystal.* Applied Physics Letters, 2010. **96**(20): p. 202504.

45. Bake, A., et al., *Top-down patterning of topological surface and edge states using a focused ion beam.* Nature Communications, 2023. **14**(1): p. 1693.

Chapter 4. Lamellae preparation for atomic-resolution imaging from topological insulator crystals

This results in this chapter were originally published in the article [1], and selected as an Editors Highlight (link: https://pubs.aip.org/avs/jva/article/40/3/033203/2842927, title: Lamellae preparation for atomic-resolution STEM imaging from ion-beam-sensitive topological insulator crystals, and DOI: 10.1116/6.0001771). In the sections below an adapted version of the article is presented, which has been modified slightly for stylish consistency and to highlight connections with the other results presented in this thesis.

4.1 Overview

As discussed in the earlier chapters, ion-beam irradiation induces disorder and damage to materials' crystal structure. However, ion beam-induced damage should be minimised during FIB lamella preparation to obtain high-resolution imaging in TEM/STEM. Atomic-resolution imaging with scanning transmission electron microscopy (STEM) is an important technique for determining the level of order and disorder at the surface of topological insulators. Good specimen quality is a key factor in achieving STEM analysis. Thin and damage-free specimens are prerequisites for obtaining atomic-resolution imaging. Topological insulator single crystals and thin films in the chalcogenide family such as Sb_2Te_3 are sensitive to electron and ion beams. It is therefore challenging to prepare a lamella suitable for high-resolution imaging from these topological insulator materials using standard focused ion beam instruments. This thesis project developed a modified method to fabricate thin TEM lamellae with minimal ion-beam damage and artifacts. The technique described in the current study enables the reliable preparation of high-quality TEM lamellae, necessary for studying ultra-thin surface regions. This thesis project has successfully demonstrated that the careful selection of FIB milling parameters at each stage minimises the damage layer without the need for post-treatment. These methods were key to obtaining the results presented in the later Chapters 5, 6, and 7.

4.2 Introduction

Topological insulators have attracted great attention since their discovery due to their fascinating physical properties. The existence of unique conducting electronic surface states which are topologically protected makes them promising materials for future quantum devices [2-5]. This led to renewed interest in the tetradymite family Sb, Bi chalcogenides such as Sb_2Te_3, Bi_2Te_3, and Bi_2Se_3 etc. [6, 7]. These have a layered structure similar to transition metal chalcogenides, graphene, and other two-dimensional materials. However, in the Sb, Bi-chalcogenides, each tetradymite layer consists of five atomically thick quintuple layers. At the heart of uncovering new physical properties of topological insulators is the application of high-precision methods with which to probe their atomic structures, interfaces, and defects. Analytical scanning transmission electron microscopy (STEM) is an ideal technique for the identification and characterization of the surface structure, and defects, in Bi, Sb-chalcogenides [8-11], which are critical for emerging technologies based on their exotic properties [9].

While the characterisation instruments are constantly being improved, there has been limited progress in high-quality sample preparation techniques for these materials. In the case of atomic-resolution STEM imaging for cross-sectional studies of surface regions, specimen quality is becoming the primary factor limiting the success of STEM characterisation. The quality and resolution of the STEM images depend on the thickness and the extent of surface modification/contamination of the FIB lamellae. Thinner specimens, free of ion beam milling artifacts, enable lower voltage TEM imaging with higher resolution. Gallium focused ion beam (FIB) preparation is widely used in site-specific specimen preparation, and several specialised instruments offer a standard configuration for this task. However, it is challenging to prepare sufficiently thin electron-transparent specimens as ion milling always produces layers of damage (defect generation/amorphisation/redeposition) near the free surfaces. This damaged layer can compromise atomic resolution STEM imaging and introduce ambiguity by disrupting the original crystal structure of the specimen. This issue is particularly common in delicate van der Waals crystal structures such as chalcogenides. One method that has been employed in some materials is wet chemical polishing after FIB milling to remove the damaged layer [12]. However, this method has limited use for complex multiphase or

multilayered TEM specimens due to material dependency. Further, low-energy Ar ion milling treatment methods have been utilised to overcome the disadvantages of FIB milling [12, 13]. Past studies revealed that lamellae of a GaN thin film which were exposed to 1.6 keV of focused Ar ion milling have only a ~2.2 nm amorphous layer covering the crystalline part of the specimen. The surface amorphous layer can be further reduced to less than 0.5 nm with an Ar ion milling energy of 200 V [14]. However, at very low voltages, a broad ion beam causes the redeposition of material from the TEM grid support. This could be disadvantageous for imaging and investigations of the chemical composition. For this reason, for most of the high-quality FIB lamellae requirements, a modern Ga-FIB is a fast way to prepare very thin lamellae with minimum damage. Post-processing of FIB lamellae is not usually needed or desirable. There is no doubt that efforts to produce thinner FIB lamellae with less surface damage will result in a significant improvement in image quality for STEM imaging in van-der Waals materials. However, ion beam damage is the major barrier.

Extensive ion beam damage is very common during specimen preparation unless special care is taken during the process. The mechanism of the beam damage is complex and depends on the material [15-18]. Knock-on damage and heating effects are the major mechanisms for beam-induced damage [19-21]. Minimising the beam damage can be achieved by gas-assisted etching [17, 19]. The use of cryo-FIB reduces the heating damage to some extent. An alternative and the more general solution is to use low ion energies and currents for thinning the lamella before significant damage occurs. The shorter penetration depth associated with lower energy ions significantly reduces the depth of the knock-on damage layer.

This work focuses on FIB lamella preparation of bulk single crystalline Sb_2Te_3 using a Ga FIB employing a reduced ion beam energy. Our results show that general FIB lamella preparation practices failed to produce high-quality FIB lamella from ion beam-sensitive single crystals and thin films. STEM imaging shows that, unless careful FIB preparation methods were used, the original crystalline structure was damaged making it hard to obtain atomic resolution imaging. However, with proper protective coatings, reduced ion beam energies at each thinning step, and longer milling times at very low ion beam energies during the final thinning, ion-beam-induced damage and artifacts can be minimised. This enables the preparation of high-quality TEM lamellae for atomic

resolution imaging (and similar principles can be applied to the FIB-based device fabrication discussed in Chapters 5 and 6). The modified FIB preparation method does not require additional low-energy Ar ion polishing or other post-treatment of the lamellae. STEM imaging shows lamellae specimen surfaces prepared with this method are relatively free from surface damage and are well suited for atomic resolution STEM imaging. Our results showing the reduced damage layer are supported by Monte Carlo calculations from the Stopping and Range of Ions in Matter (SRIM) software [22].

4.3 Experimental

The standard FIB cross-section lift-out method using an FEI HELIOS G3 dual beam microscope was employed for focused ion beam lamellae preparation. A summary of the different schemes for FIB lamella preparation for general materials and ion-beam-sensitive crystals is shown in Figure 4.1. In this experimental work, for ion-beam sensitive topological insulator Sb_2Te_3 bulk crystals, there was no need to coat the surface with 50 nm of Cu in a sputter coater as standard carbon protective layers are sufficient to protect the underlying surface from ion beam damage. FIB lamella preparation can directly proceed provided that the C protective layer is initially deposited using a low-energy electron beam, rather than the ion beam at the first step. Deposition of the C protective layer from an organic gas precursor must be performed first before exposing the surface to any ion beam irradiation since even minor ion irradiation can induce damage. After deposition of a sufficiently thick C-protecting layer (≥ 1000 nm) (using the E-beam), the layer can then be augmented by ion-beam-induced carbon deposition. Ion beam-driven carbon deposition (and also C/Pt used later) is much faster than electron beam-induced deposition and permits rapid build-up of an additional thicker protective layer. However, for ultra-thin films (<10 nm thick) or heterostructures on a substrate, 50nm of Cu was used, but for bulk samples, it was not needed. Subsequently, specimens were carefully prepared for lift-out with an ion-beam voltage of 16 kV (rather than the more typical 30 kV) and a current of 11 nA for cross-section trenching. To minimise the ion beam damage, it is crucial to keep the sides of the trench cuts sufficiently distant (2 μm) from the region protected by the carbon layer. A cleaning cross-section can be performed two or more times using an ion beam voltage of 16 kV and a significantly reduced current of approximately 1 nA. The lamellae can then be lifted out and welded on to the

nanomanipulator and then transferred on to a TEM grid for thinning. During these processing steps, exposure to the ion beam for imaging/micromanipulator alignment etc. should be minimised as far as possible, and where necessary, the lowest beam currents and shortest exposures practicable should be used.

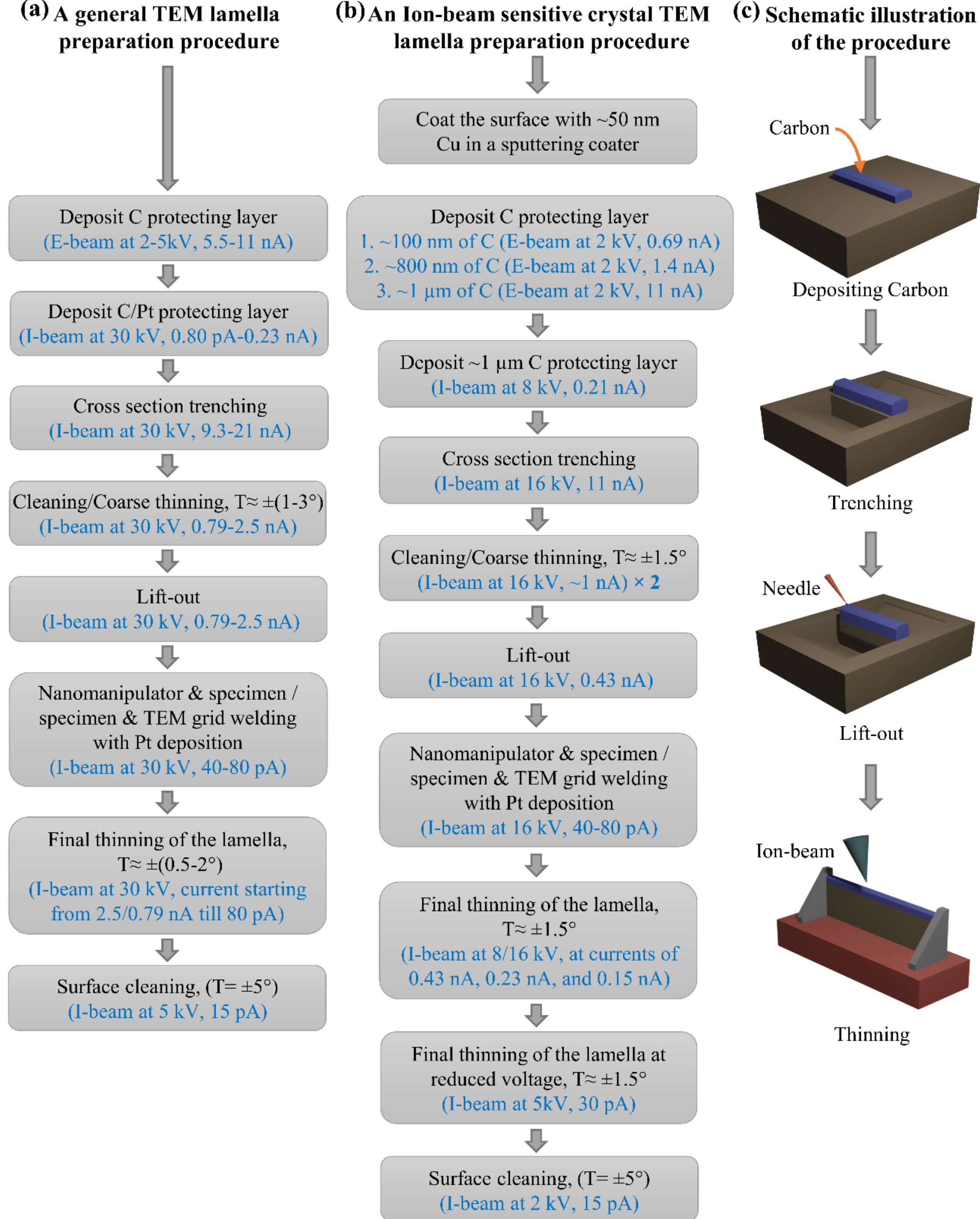

Figure 4.1. (a) and (b) Comparison of a general FIB lamella preparation procedure and the modified procedure for ion-beam-sensitive crystals used in this work. (c) Schematic illustration of the key steps for the preparation of an electron-transparent specimen including the deposition of the protective carbon layer, trenching, lift out and thinning steps.

Figure 4.2 (a) shows the SEM image of a FIB lamella from a Sb_2Te_3 single-crystal welded on a Cu TEM grid. The inset image shows that it has a sufficiently thick protective coating layer (~500 nm) for subsequent final thinning. Final thinning of the lamella was carried out at in three stages using16 kV ions and beam currents of 0.43 nA, 0.22 nA, and finally 0.15 nA. An optional final low voltage ion polishing step can be carried out at 8kV (in three stages with currents of 0.43, 0.22, and 0.15 nA) for extremely ion-beam sensitive specimens. The use of low voltage/low current milling is not without its challenges. The lateral focus on the ion beam is reduced at lower ion-beam voltages, and slower milling rates are achieved at lower ion-beam currents. Depending on the types of samples, beam voltages and currents will need to be optimised in order to produce a FIB lamella that retains the original atomic structure. During the final thinning stages, it is a sensible precaution to subdivide the lamella into several panels and then thinned these to various thicknesses as shown in Figure 4.2 (b). This helps to ensure that at least one of the panels is likely to be close to optimum electron transparency, even if other panels may be insufficiently thinned, or over milled/damaged. The final thinning stage involves milling to electron transparency using extended milling of both surfaces of a panel using 5 kV beam voltage and a 30 pA beam current. During this step, the ion beam and specimen surface were inclined at approximately 1.5° from parallel. Milling of each side of the panel takes approximately 3-4 minutes. This step can be repeated several times to ensure that the lamella reaches the desired thickness before final cleaning. This last cleaning step is designed to remove the ion-beam induced artefacts and amorphous layer from the surface. We have carried out the surface cleaning at an ion beam voltage of 2 kV and a current of 15 pA with the specimen inclined at 5° from the beam. Improving the ion-beam image focusing and inclining the lamellae to slightly higher angles can help to see the profile of a lamella at very low voltages. The low-magnification STEM image in Figure 4.2 (b) shows that Sb_2Te_3 surface regions still retain a thick protective carbon coating layer after FIB thinning. After Ga-FIB preparation, some past work has explored further treating the TEM lamellae with low-energy Ar ion milling with ion energies of less than 2 keV at the currents of 45 pA or 110 pA at an angle of 10° [14]. However, post surface treatment processes substantially increase the time and cost of preparing a lamella. Moreover, these require a secondary ion beam source for cleaning the surface. Our modified FIB lamella preparation method is advantageous in that the initial lamella did not require any further surface treatment, allowing all of the work to be done under vacuum in a single instrument.

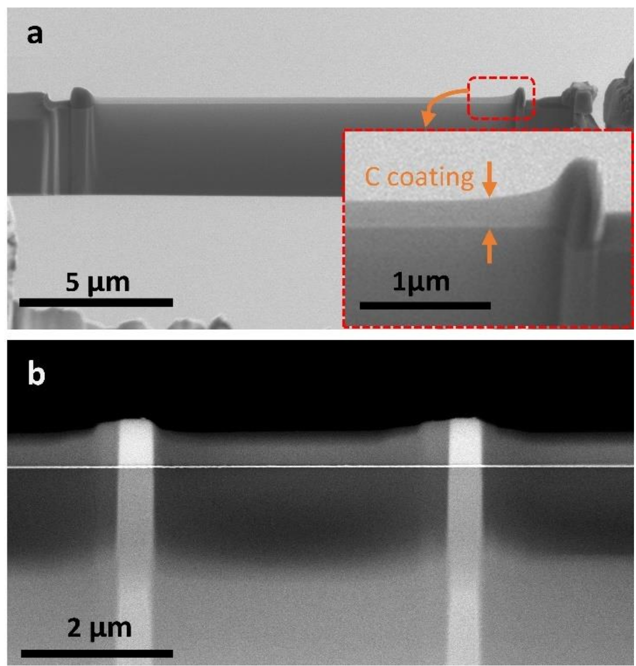

Figure 4.2. (a) Cross-sectional SEM image of a FIB lamella from a Sb_2Te_3 single crystal welded onto a Cu TEM grid and inset shows the ~ 500 nm protective C layer (appearing lighter grey) is intact at the last step of surface polishing. (b) Cross-sectional STEM image showing subdivided panels in a FIB lamella.

4.4 Results and discussion

4.4.1 SRIM calculations

During the milling process, Ga ions penetrate into the material, and may damage the crystalline structure as the ions lose kinetic energy by electronic and nuclear interactions, ultimately forming an amorphous layer at the surface. It is also unavoidable that some fraction of the Ga ions will be implanted within the ion-beam affected layer. The amorphisation threshold of materials depends on the nature/type of structure and the chemical bonds present. For metallic materials, FIB-induced surface amorphisation is negligible as their crystallinity is retained because metallic bonds will reform in the lattice after FIB milling even at the maximum FIB voltage of 30 keV. However, semiconductor and electronic ceramic materials can be amorphised during FIB milling [18]. Chalcogenide topological insulators are particularly vulnerable to amorphization, and this is discussed below.

Careful tuning of the ion-beam parameters at each lamella processing step, enables the

damage in the finished lamella to be minimised to a negligible level. Ion/matter interaction can be understood by Monte-Carlo simulations using the SRIM software [22]. As past experimental work has revealed that gallium ions can readily amorphise Bi_2Se_3 [23], which is a closely related chalcogenide, it is valuable to simulate the damage mechanism and penetration depth for different beam conditions for the specific target materials, in our case Sb_2Te_3. The milling process of selected specimens in the Ga-FIB was simulated using the ion-beam parameters detailed above. In all calculations, a fluence of 10^5 ions was used with full damage cascades. We have simulated the distribution of vacancies generated per impinging ion as a function of specimen depth for the Sb_2Te_3 and Bi_2Te_3 crystals for comparison, finding similar results in both cases.

Figure 4.3 (a and b) shows the vacancy depth distribution in Sb_2Te_3 and Bi_2Te_3 as a function of incident Ga ion energies respectively. At lower accelerating voltages, the Ga ions produce less damage, and it is increasingly localised to the near-surface. The number of vacancies generated in Bi_2Te_3 is slightly higher than that in Sb_2Te_3 for a given Ga ion energy. Another critical parameter affecting the lamella quality is the ion-beam angle of incidence during milling. From Figure 4.3 (c), we can see that as the angle of incidence is reduced both the cumulative damage and the depth of the damage decrease. The vacancy distributions for different incident angles in Figure 4.3 (c) indicate that milling at very small incidence angles, preferably between 0.5-2°, will result in the least damage. It was noted above that low ion beam voltages and low currents also favour minimal damage. However, to achieve a reasonable milling rate, it is normally not practical to reduce the ion beam energy and current too significantly during the milling process. Therefore, the best option to minimise ion-beam damage is by keeping the ion-beam incidence angle as small as possible. An exception to this is that ion beam energy and currents can be reduced significantly at the very last stage of lamella cleaning/polishing, as detailed in our modified lamella preparation method. Here the low removal rates are beneficial as the aim is to strip away only a very thin (2-10 nm) of damaged material, rather than large scale milling. This allows us to slightly increase the tilting angle of lamellae (or angle between the lamella side surface and ion-beam, preferably less than 5-10°) to clean up the surfaces of the lamellae uniformly.

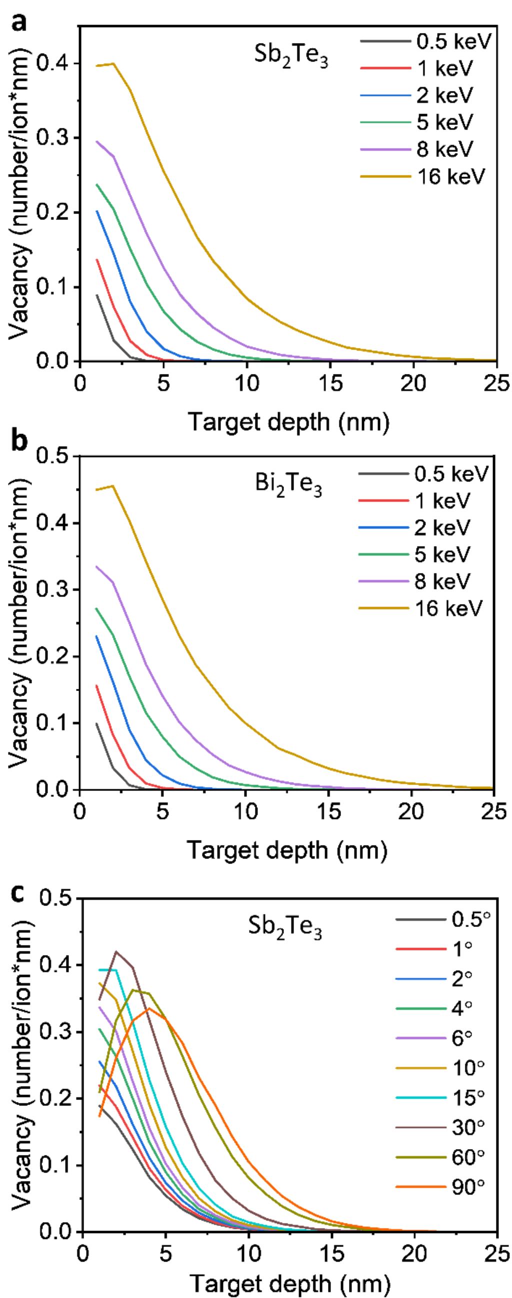

Figure 4.3. Vacancy versus target depth at Ga ion beam energies from 0.5 - 16 keV for (a) Sb_2Te_3, (b) Bi_2Te_3. (Angle between the ion beam and lamella side surface is 5° for 0.5-2keV and 1.5° for 5-16 keV) (c) Vacancy versus target depth in Sb_2Te_3 for different Ga ions incident angles. (At 90°, the ion beam is perpendicular to the specimen surface.)

4.4.2 STEM imaging

To illustrate the effectiveness of the revised preparation method, we have compared intentionally amorphized Sb_2Te_3 with the pristine crystalline structure. This has been done in the same STEM image by deliberately failing to deposit protective layers in some

regions. We irradiated an Sb_2Te_3 single crystal along a line using 8 keV, 16 keV, and 30 keV Ga ion beam energies (with the ion beam perpendicular to the specimen surface) to the same ion dose of 3.5×10-12 C/μm2 (inset image in Figure 4.4 (b)). A carbon protective layer was deposited (along the horizontal direction in Figure 4.4 (b) inset) using first an electron beam and then an ion beam to cover all the irradiated lines. Finally, we applied the modified FIB lamella preparation procedure as described above to prepare a FIB lamella from the bulk Sb_2Te_3 single crystal. The interface between the irradiated region and the unirradiated crystal was investigated.

Figure 4.4 (a), (c), and (d) show that the regions on the Sb_2Te_3 single crystal irradiated with Ga ion-beam energies of 30, 16, and 8 keV are all amorphised. Amorphisation occurs as deep as 60 nm if an area on the Sb_2Te_3 crystal directly irradiated with a 30 keV Ga ion-beam (at 90° incident angle), whereas the amorphisation depth reaches 35 nm and 20 nm for Ga ion-beam energies of 16 keV and 8keV respectively. The SRIM calculations show that the majority of Ga-ions can penetrate approximately up to 60-65 nm depth at 30 KeV energy, and reduced to approximately 38-42 nm at 16 keV energy, and further reduced to approximately 20-23 nm at 8 keV enegy. The penetration depth of the ion-beam is slightly larger than the amorphization depth as there is certain threshold of ion fluence required to amorphise the Sb2Te3. That being said, there are very small number of ions still can penetrate further deeper than the amorphization depth shown in STEM images (Figure 4.4 (a), (c), (d)), yet not enough to cause amorphization. At the same time, the protected region immediately adjacent to the amorphised area is highly crystalline and the structure has not been compromised by the FIB lamella preparation procedure. This confirmed the effectiveness of the protective layers chosen which cover those areas. It shows that by avoiding direct exposure to higher ion beam energies at high angles of incidence (which penetrates deeper in the Sb_2Te_3 single crystal), amorphisation can be avoided. By following the modified TEM lamella preparation procedure, the protected region of the Sb_2Te_3 single crystal maintained its perfect lattice structure. Figure 4.4 (a) inset image (from unirradiated region of Figure 4.4 (a)) and Figure 4.4 (b) show atomic-resolution images of Sb_2Te_3. Thes region is from a protected region and clearly shows the typical five atomic sheets layered structure held together by weak van der Waals forces. In contrast, Figure 4.4 (e) and (f) show STEM HAADF images of Sb_2Te_3 where we followed the unrefined, conventional lamella preparation method. Figure 4.4 (e) shows the over milled lamella and Figure 4.4 (f) image and inset show the ion damaged Sb_2Te_3. Thus,

the quintuple layers are not observable as compared to the Figure 4.4 (b) image.

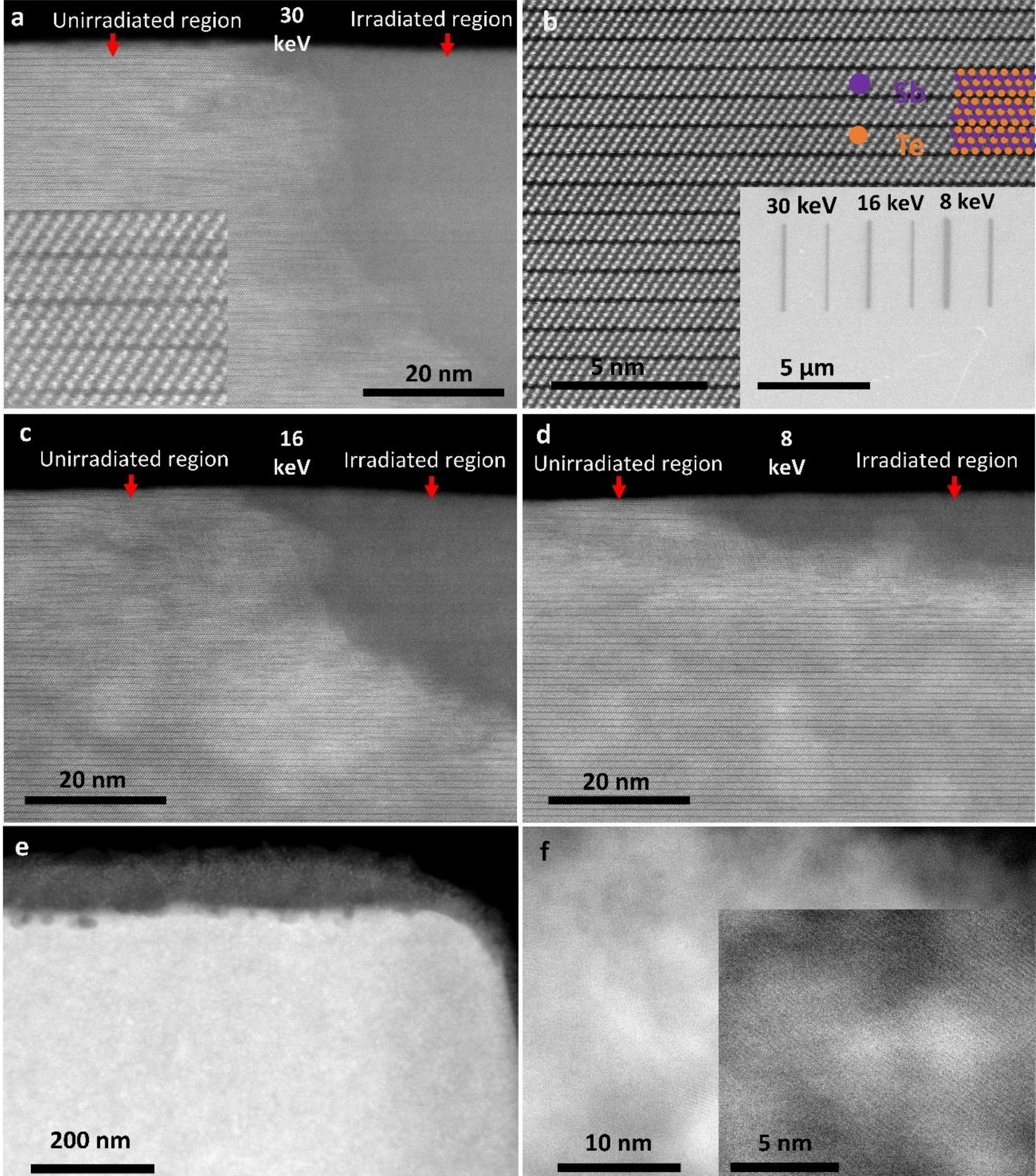

Figure 4.4. STEM HAADF images of a Sb_2Te_3 single crystal taken at the edge of stripes irradiated with Ga ion of various energies (shown inset Figure 4.4 b). The unirradiated region (left) shows the original crystalline structure while the irradiated region (right) is amorphous:(a) A region irradiated with 30 keV ion beam energy where certain areas were protected from irradiation by the additional protective coating and inset image from unirradiated region, and (b) high-resolution STEM image taken from the unirradiated region of (a). (c) and (d) are STEM HAADF images irradiated with 16 keV and 8 keV, respectively. In contrast, (e) and (f) shows STEM HAADF images of FIB lamella prepared by the standard, unrefined method showing a case of beam damage at the surface from over milling.

4.5 Summary and conclusions

Ion beam modification is a key vacuum-technology, used not only in TEM sample preparation but also in chemical modification of materials, including topological insulators for electronics [23, 24]. Focused ion beam milling requires much higher fluences than traditional chemical doping, however, the principles of the ion-solid interaction are identical. Therefore, many of the lessons and process-improvements we have outlined in this article could be relevant to traditional ion beam implantation for electronics. We have demonstrated that by carefully optimising the FIB milling parameters at different stages, a modern Ga FIB is capable of preparing a high-quality cross-sectional lamella of chalcogenide topological insulators (Sb_2Te_3) for STEM analysis. These materials are extremely susceptible to amorphization even at a relatively low fluence of Ga ion beam irradiation. Guided by the SRIM calculations and past experience, we developed a preparation recipe for Sb_2Te_3 lamellae and provided the details for reference. Our modified method is also suitable for the preparation in related materials, and has been used for ultra-thin Bi_2Te_3 thin films (not discussed in detail here for the sake of brevity). The improved TEM lamella preparation method should assist future researchers working on topological crystals and ultra-thin films by enabling accurate STEM analysis.

References

1. Bake, A., et al., *Lamellae preparation for atomic-resolution STEM imaging from ion-beam-sensitive topological insulator crystals.* Journal of Vacuum Science & Technology A: Vacuum, Surfaces, and Films, 2022. **40**(3): p. 033203.

2. Moore, J.E., *The birth of topological insulators.* Nature, 2010. **464**(7286): p. 194-198.

3. Kane, C.L. and E.J. Mele, *Z_2 topological order and the quantum spin Hall effect.* Physical review letters, 2005. **95**(14): p. 146802.

4. Hasan, M.Z. and C.L. Kane, *Colloquium: topological insulators.* Reviews of modern physics, 2010. **82**(4): p. 3045.

5. Bernevig, B.A., T.L. Hughes, and S.-C. Zhang, *Quantum spin Hall effect and topological phase transition in HgTe quantum wells.* science, 2006. **314**(5806): p. 1757-1761.

6. Zhang, H., et al., *Topological insulators in Bi_2Se_3, Bi_2Te_3 and Sb_2Te_3 with a single Dirac cone on the surface.* Nature physics, 2009. **5**(6): p. 438-442.

7. Chen, Y., et al., *Experimental realization of a three-dimensional topological insulator Bi_2Te_3.* Science, 2009. **325**(5937): p. 178-181.

8. Jiang, Y., et al., *Direct atom-by-atom chemical identification of nanostructures and defects of topological insulators.* Nano letters, 2013. **13**(6): p. 2851-2856.

9. Reifsnyder Hickey, D. and K.A. Mkhoyan, *Atomic-resolution analytical scanning transmission electron microscopy of topological insulators with a layered tetradymite structure.* APL Materials, 2020. **8**(7): p. 070902.

10. Cortie, D., et al., *Creating thin magnetic layers at the surface of Sb_2Te_3 topological insulators using a low-energy chromium ion beam.* Applied Physics Letters, 2020. **116**(19): p. 192410.

11. Zhu, T., et al., *Synthesis, Magnetic Properties, and Electronic Structure of Magnetic Topological Insulator $MnBi_2Se_4$.* Nano Letters, 2021.

12. Mehrtens, T., et al., *Optimization of the preparation of GaN-based specimens with low-energy ion milling for (S) TEM.* Micron, 2012. **43**(8): p. 902-909.

13. Miyajima, N., et al., *Combining FIB milling and conventional Argon ion milling techniques to prepare high‐quality site‐specific TEM samples for quantitative EELS analysis of oxygen in molten iron.* Journal of microscopy, 2010. **238**(3): p. 200-209.

14. Lotnyk, A., et al., *Focused high-and low-energy ion milling for TEM specimen preparation.* Microelectronics reliability, 2015. **55**(9-10): p. 2119-2125.

15. Barber, D.J., *Radiation damage in ion-milled specimens: characteristics, effects and methods of damage limitation.* Ultramicroscopy, 1993. **52**(1): p. 101-125.

16. Barna, A., B. Pécz, and M. Menyhard, *Amorphisation and surface morphology development at low-energy ion milling.* Ultramicroscopy, 1998. **70**(3): p. 161-171.

17. Yu, J., et al., *TEM investigation of FIB induced damages in preparation of metal material TEM specimens by FIB.* Materials Letters, 2006. **60**(2): p. 206-209.

18. Huh, Y., K.J. Hong, and K.S. Shin, *Amorphization induced by focused ion beam milling in metallic and electronic materials.* Microscopy Microanalysis, 2013. **19**(S5): p. 33-37.

19. Yamaguchi, A. and T. Nishikawa, *Low‐damage specimen preparation technique for transmission electron microscopy using iodine gas‐assisted focused ion beam milling.* Journal of Vacuum Science Technology B: Microelectronics Nanometer Structures Processing, Measurement, Phenomena, 1995. **13**(3): p. 962-966.

20. Susi, T., et al., *Atomistic description of electron beam damage in nitrogen-doped graphene and single-walled carbon nanotubes.* ACS nano, 2012. **6**(10): p. 8837-8846.

21. Egerton, R., *Mechanisms of radiation damage in beam‐sensitive specimens, for TEM accelerating voltages between 10 and 300 kV.* Microscopy research technique, 2012. **75**(11): p. 1550-1556.

22. Ziegler, J.F., M.D. Ziegler, and J. Biersack, *SRIM–The stopping and range of ions in matter (2010).* Nuclear Instruments Methods in Physics Research Section B: Beam Interactions with Materials Atoms, 2010. **268**(11-12): p. 1818-1823.

23. Friedensen, S., J.T. Mlack, and M. Drndić, *Materials analysis and focused ion beam nanofabrication of topological insulator Bi_2Se_3.* Scientific Reports, 2017. **7**(1): p. 13466.

24. Sharma, P.A., et al., *Ion beam modification of topological insulator bismuth selenide.* Applied Physics Letters, 2014. **105**(24): p. 242106.

Chapter 5. Feasibility for controlled patterning of Sb_2Te_3 surfaces

The results in this chapter were originally published as a supplementary information for the article [1] (link: https://www.nature.com/articles/s41467-023-37102-x, title: Top-down patterning of topological surface and edge states using a focused ion beam, and DOI: 10.1038/s41467-023-37102-x). In the sections below an adapted version of the supplementary information (theoretical calculations excluded) is presented, which has been modified slightly for stylish consistency and to highlight connections with the other results presented in Chapter 6 of this thesis.

5.1 Overview

The previous chapter demonstrated clearly evidence showing the ion beam sensitivity of the Sb_2Te_3 crystal structure, which is prone to amorphization. The natural question is how this affects electronic properties. Does the topological insulating surface state survive upon amorphisation? Is an amorphous Anderson topological insulator generated? This chapter provides a systematic set of experiments studying the effects of amorphization. Based on ion-beam induced amorphization (phase change), it explores the feasibility of precise ion-beam surface patterning of Sb_2Te_3.

5.2 Monte Carlo calculations

The results in Chapter 5 and Chapter 7 show experimentally how irradiation with Ga ions modifies the atomic structure and electronic properties of a Sb_2Te_3 surface. This section presents complementary Monte Carlo (MC) calculations to clarify the nature of the ion-beam/matter interaction, and radiation damage, for Ga implanted into Sb_2Te_3.

The Stopping and Range of Ions in Matter (SRIM)[2] software was used to simulate the characteristics of Ga^+ ions implanted into a Sb_2Te_3 surface. Figure 5.1 (a) shows that the collisions taking place within the energy range of 8-40 keV (as in the experiment) are dominated by nuclear energy loss (i.e., via phonons and ionic displacements rather than via electronic excitations). This is a characteristic of low-energy ions and is quite distinct from the energy loss of high-energy ions in the MeV range, where electronic loss is the

primary mechanism. Ultimately, the low-energy Ga^+ ions penetrate only several nanometers before losing sufficient kinetic energy to become stationary. Figure 5.1 (b) shows the projected ion range as a function of the initial kinetic energy. Incident ions with 8–40 keV have a mean penetration depth of 7–23 nm. Figure 5.1 (c) shows that the longitudinal and lateral straggle is comparable in the 5–20 nm range. For an ideal parallel-collimated ion beam and infinitely sharp mask, the lateral implant profile would be slightly tighter than the vertical spread. However, in a focused ion beam microscope, the beam spot is varied very largely with species, energy, and beam defining aperture (or condenser settings, e.g., beam current) with a 3D Gaussian profile (see 5.3). Thus, in practice, for the experiments performed in this work, the actual interaction volume of the ion beam is larger in the lateral dimension than in the vertical dimension.

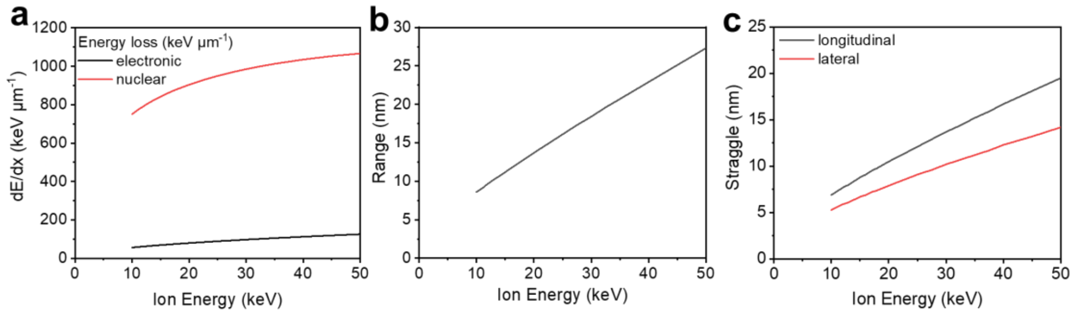

Figure 5.1. Ga^+ ions stopping range and energy loss in Sb_2Te_3. (a) The energy loss for various incident ion energies. (b) The projected ion range as a function of the incident ion energy. (c) The longitudinal and lateral straggle.

To evaluate the effect of ion-beam damage introduced by the incident Ga^+ ions, the damage-per-atom (DPA) profiles were calculated for the Sb_2Te_3 using the Equation (1), as in past work [3]:

$$DPA = \frac{N_d F M}{\rho N_A} \qquad \text{Equation (1)}$$

where N_d is the number of Sb/Te displacements per ion calculated by the SRIM software (where this quantity varies as a function of depth), F is the Ga ion fluence, M is the molar mass, ρ is the mass density of the target material (Sb_2Te_3) and N_A is the Avogadro number. In general, as shown in Figure 5.2 (a)-(d), the total damage in the Sb_2Te_3 crystal increases with the Ga ion fluence, with Sb and Te atoms being displaced between 1–60 times per incident Ga ion for fluences between 1×10^{15} and 1×10^{16} ions/cm^2. Apart from the ion species and fluence, the angle of incidence and energy are other important factors governing the damage depth and sputter rate. In the present work, the Sb_2Te_3 crystals were always irradiated with the beam perpendicular to the surface. The total damage

increases with the ion beam energy for the same ion fluence in Figure 5.2 (a)-(d), given the additional nuclear energy loss required. The sputtering rate is determined by the nuclear stopping collisions and by the surface binding energy of the Sb and Te atoms which are removed by the sputtering process. Due to the low sputtering yield for Ga:Sb_2Te_3, sputtering only becomes significant at higher fluences and implantation is the dominant process at lower fluences [4]. For the regime where sputtering is negligible, Figure 5.2 (e)-(h) shows the predicted Ga concentration profile (in atomic percent) as a function of the depth (from the top surface of the crystal) superimposed on the DPA profile calculated for the Ga ion dose at $10^{15}/cm^2$ for energies in the range of 8–40 keV. According to the Ga concentrations calculated from SRIM (Figure 5.2) and the experimental EDS analysis in the later section (Figure 5.3), the typical amount of Ga in the amorphous regions of the sample is 0.5–2 atomic percent for the fluences used in this work.

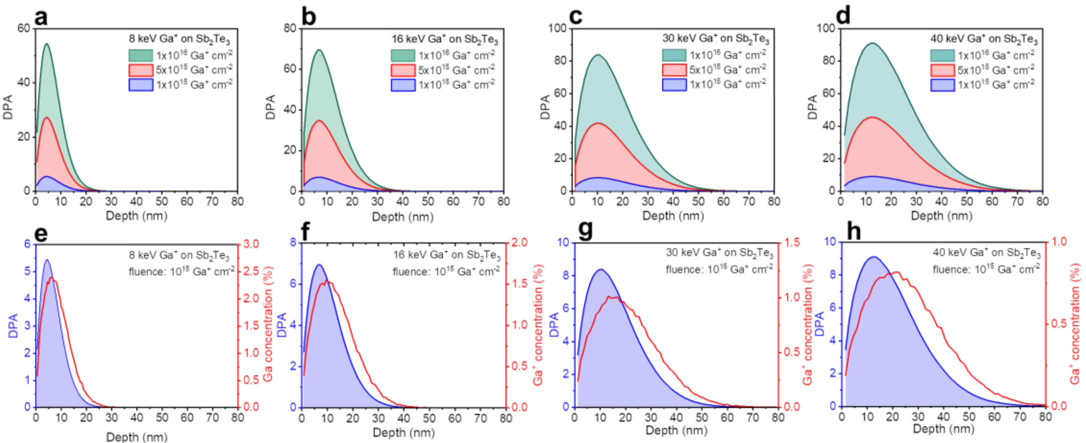

Figure 5.2. Monte Carlo calculations of the ion-beam irradiation process in Sb_2Te_3 showing the Ga concentration and total damage profiles. (a)-(d) Accumulated damage profiles for Ga ion beam energies between 8–40 keV for the selected fluences of 10^{15}, 5×10^{15}, and 10^{16} ions/cm^2, respectively. (e)-(h) The variation of the Ga concentration in Sb_2Te_3 at Ga ion beam energies between 8–40 keV for the selected fluence of $10^{15}/cm^2$.

5.2.1 Validation of the ion beam stopping depth calculations against STEM images

In this section, scanning transmission electron microscopy (STEM) was used to experimentally study a Sb_2Te_3 crystal surface exposed to an 8 keV Ga ion beam with 2.18×10^{15} ions/cm^2 (3.5×10^{-12} C/μm^2) fluence. The procedure for high-quality FIB lamella preparation from Sb_2Te_3 single crystals can be found in our publication[5]. The

STEM characterizations were performed on cross-sections of the surface to study the depth-dependency of the damage profile. These datasets were combined with complementary electron back-scattering diffraction measurements in a scanning electron microscope (SEM) to determine the lateral feature dimensions. These measurements enable a comparison with the damage depths obtained from Monte Carlo calculations described in section 5.2.

Figure 5.3 (a)-(c) shows that the 8 keV beam penetrated to an approximate depth of 20–30 nm below the surface and caused amorphization. The maximum penetration depth is in good agreement with the earlier Monte Carlo theory calculations (Figure 5.2 a, e). Several images at various magnifications are presented to survey the region where the Ga beam impacted the surface. At high magnifications, as in Figure 5.3 (a), clear lattice fringes from the quintuple layers of Sb_2Te_3 can be observed in the STEM images in the unirradiated regions, confirming that the surface was initially crystalline. The images are taken in high-angle annular darkfield (HAADF) mode so that the intensity originates from atomic contrast, and secondary diffraction effects are minimal. A lower magnification image of the region impacted by the beam is shown in Figure 5.3 (b). In both images, the amorphous region appears as a featureless dark grey area. A remarkably sharp interface is formed between the amorphous and single-crystalline Sb_2Te_3 below the central irradiated region (Figure 5.3 (a)), directly below the point where the amorphization depth is greatest. In contrast, the STEM images in Figure 5.3 (g) and (h) are taken at the lateral edges of the irradiated region (as indicated in Figure 5.3 (c)). These show that the amorphous/crystalline interface on the lateral borders of the beam spot is not as sharp. This is attributed to the Gaussian spread of the focused ion beam spot (laterally), which causes an intensity gradient on the edges of the beam spot.
To enable a side-by-side comparison of theory and experiment in the vertical dimension, Figure 5.3 (f) shows the DPA and Ga atomic percentage profiles in Sb_2Te_3 for the Ga^+ ions with 8 keV energy and the fluence of 10^{15} ions/cm^2 calculated from SRIM. This can be compared with the experimental EDS profile (Figure 5.3 (e)). The Ga atomic percentage variation in Figure 5.3 (e) is very low in the irradiated regions, below 2±1.5 atomic %, in agreement with the MC predictions. Indeed, the Ga concentration is low enough to be near the detection limit with the EDS technique, and there is considerable uncertainty in the experimental measurement. Although the final concentration of Ga is low, the main effect of Ga irradiation is to cause displacements of Sb/Te atoms (up to 60

displacements per Ga atom). Thus, the STEM images clearly show the after-effects of the irradiation (Figure 5.3 g/h), where the amorphous phase is formed by the beam damage, precisely in the region accessed by the Ga ions during the irradiation. In addition, a faint elemental signal is also visible in the two-dimensional EDS elemental mapping in Figure 5.3 (d) (which probes the same region of interest shown in Figure 5.3 (c)). The depth of the damaged region and the region enriched with Ga agree well with the profile predicted by the Monte Carlo calculations (Figure 5.3 (f)).

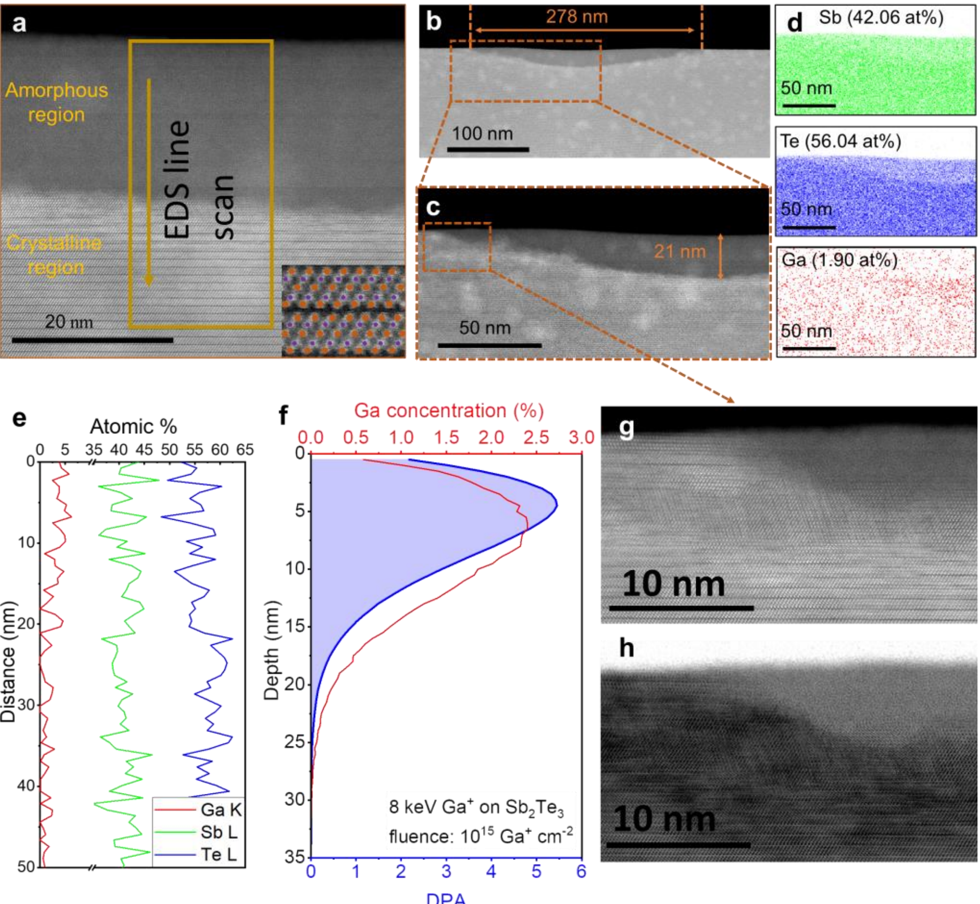

Figure 5.3. (a) STEM HAADF image showing distinct amorphous and crystalline regions. The inset shows an enlarged image of the quintuple atomic layered structure of Sb_2Te_3 superimposed with Sb and Te atoms. (b) Low magnification image surveying the cross-section of the Ga-irradiated region of the Sb_2Te_3 surface. The ion beam energy was 8 keV, and the fluence was 2.18×10^{15} ions/cm^2. (c) Detail of the boxed region in b) showing the lateral and depth scale of the amorphous region near the edge of the irradiated area. (d) EDS elemental maps of (c). (e) Ga, Sb, and Te line profiles are taken along the line shown in (a). (f) Monte Carlo calculations of the displacement per atom and Ga atomic concentration within Sb_2Te_3 for 8 keV Ga^+ ions at a fluence of 10^{15} ions/cm^2. (g) HAADF image showing a detail of the boxed region in (c). (h) Bright-field image of (g) showing strong diffraction contrast (dark) from the crystalline regions, which were not exposed to the Ga ion beam.

5.2.2 Lateral feature size from the ion beam writing process

The damaged region takes the form of a 3D Gaussian as determined by the lateral beam shape and horizontal straggle, together with the vertical penetration depth. To illustrate this point, Figure 5.4 (a) shows the 3D distribution profile of Ga^+ ions and the intrinsic horizontal straggle predicted by the Monte Carlo calculations for an infinitely sharp beam. In the experimental case, the horizontal dimension deviates from the theoretical calculations because the ion beam is Gaussian with a width of ~ 100 nm. To assess the lateral sharpness of the pattern in the horizontal dimension, Figure 5.4 (b) shows a secondary electron image of the Sb_2Te_3 single crystal surface after irradiation with a Ga focused ion beam to form a series of parallel lines. The nominal widths of these irradiated regions specified in the input pattern were 20, 50, and 100 nm. The corresponding EBSD band contrast image of Figure 5.4 (c) shows the ion beam-induced amorphization as indicated by dark lines on the image. From further analysis of the gray values on the band contrast image, we have calculated the approximate width of the Ga ion beam. Gaussian peak fitting was used to obtain the FWHM of each peak of 166, 184, and 220 nm, respectively, as shown in Figure 5.4 (d).

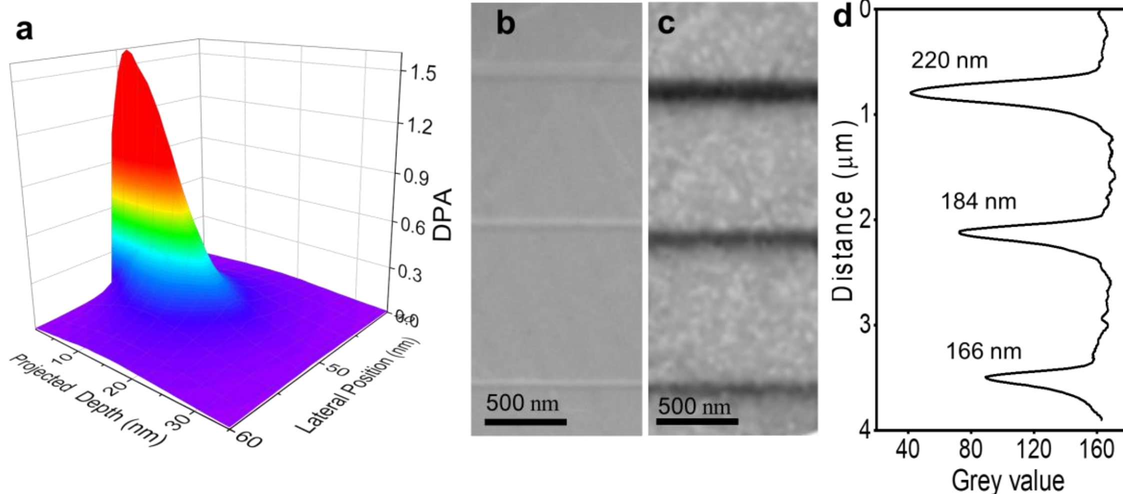

Figure 5.4. (a) 3D distribution of the Damage-Per-Atom profile in a Sb_2Te_3 crystal for a Ga beam with energy 8 keV, as calculated from the Monte Carlo calculations. (b) Secondary electron image showing Ga ion beam irradiated lines of various widths (top to bottom, input pattern width of 100, 50 and 20 nm and z depth set to 110 pm at beam energy of 30 kV and current of 1.1 pA) and (c) corresponding EBSD band contrast image. (d) Vertical intensity profile through the band contrast image measures the actual width of the amorphized regions as (top to bottom), 200, 184 and 166 nm.

5.2.3 The crystallinity of the underlying Sb_2Te_3 crystal after ion implantation

To confirm the orientation and crystallinity of the Sb_2Te_3 pieces used for FIB fabrication, X-ray diffraction (XRD) was conducted with a Rigaku XRD SmartLab using a Cu K_α source. The crystal was mounted with the (00L) direction along the scattering vector in Bragg-Brentano geometry. A 2D detector was used to collect the pattern, and the central region of the detector was integrated to yield the 1D pattern shown in Figure 5.5. The observed peaks obey the selection rule (00L) where L=3n and n is an integer, consistent with the R-3c space group for Sb_2Te_3, and the peaks have been indexed using the Inorganic Crystal Structure Database (ICSD Entry #192780). As the X-ray penetrates many micrometers into the sample, the XRD in this geometry is dominated by the crystalline region underneath the nanometer-scale implanted region at the surface. In Section 5.5.6, complementary data is given using low-angle (reflectometry) measurements for thin films to probe the implanted region directly.

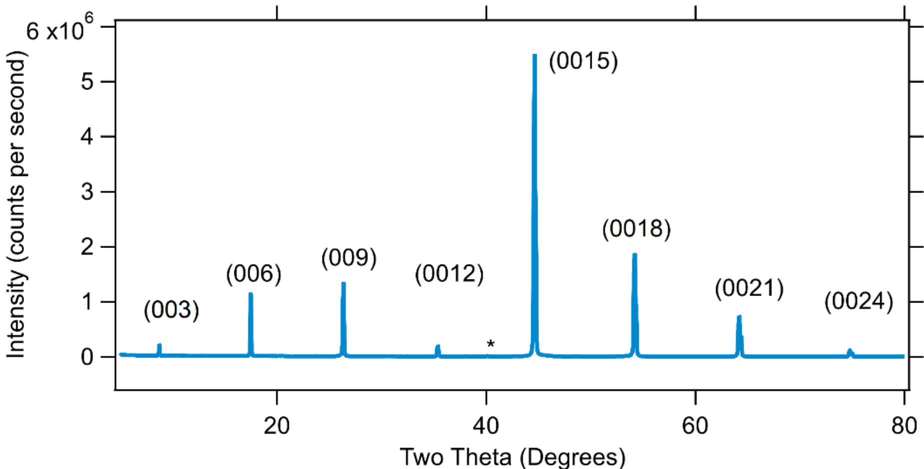

Figure 5.5. The XRD diffraction pattern of a c-axis orientated Sb_2Te_3 crystal was irradiated with $1x10^{17}$ /cm^2 Ga ions at 40 keV. The strong (00L) diffraction peaks show that the crystallinity is preserved below the nanometer-scale implanted region. The much smaller peak marked with a* is from Cu K_β.

5.3 Additional data for the effect of irradiation fluences and geometries

5.3.1 High fluence irradiation leading to sputtering

This section presents additional electron back-scattering diffraction (EBSD) and AFM measurements of Sb_2Te_3 surfaces. The data is presented for a wider variety of ion-beam fluences compared to the datasets in the main text, which focused only on a subset. These show the additional effects of the ion beam on laterally patterned surface regions via

amorphization and forming trenches/valleys (i.e. sputtering at higher fluences).

The patterns in Figure 5.6 (a) were formed using a single ion beam energy of 8 keV and a constant current of 1.9 pA. The irradiation time was varied in each square to modify the overall fluence. The ion fluence of each region (R1-R9) is provided in Table *5.1*. The higher fluences in regions R7, R8, and R9 produce clear shallow trenches, which indicates the onset of material removal by the sputtering process (Figure 5.6 (a)) and quantified using atomic force microscopy (Figure 5.6 (b)). The trenches are very shallow in this fluence regime (<10 nm). For lower fluences, the Sb_2Te_3 crystals experience slight swelling due to Ga implantation giving a nanometer-scale increase in surface height. This transition from swelling to sputtering occurs around 10^{15} ions/cm^2 for the 8 keV beam, and a similar transition was reported for Ga irradiation in silicon[4].

EBSD scans were performed for the region of interest using an electron beam voltage of 20 keV and a current of 2.8 nA. In Figure 5.6 (c), the band contrast image is constructed from all EBSD patterns. Dark areas in the images indicate regions without an observable Kikuchi pattern (i.e., these could not be indexed to the Sb_2Te_3 crystal structure), and bright gray regions show where the clear crystalline pattern was detected. Gray and black regions, therefore, indicate the crystalline and amorphous states, respectively. All of the irradiated surfaces in this regime of fluences were amorphous. The phase identification from the EBSD mapping is shown in Figure 5.6 (d), where crystalline regions of Sb_2Te_3 appear as blue. The complementary AFM and EDS images show that surface amorphization occurs well before the onset of sputtering.

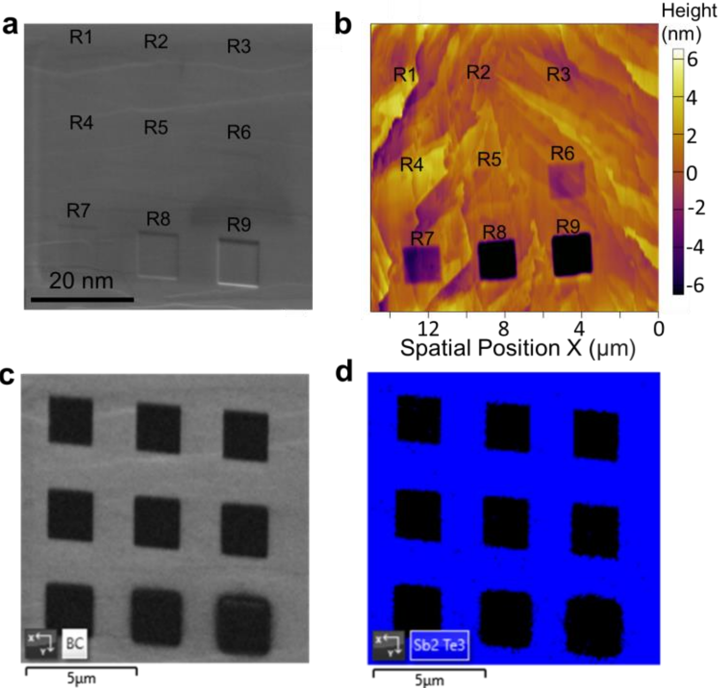

Figure 5.6. (a) Secondary electron image of the 3×3 grid of irradiated regions labelled R1 – R9. Only the higher fluence regions (R7-R9) show topography due to sputtering effects. (b) AFM topography image labelled with the matching pattern ID (Note: the scan direction and imaging angle is different in the SEM/AFM images, as EBSD measurements require using an inclined surface). (c) Band contrast image obtained through an EBSD scan on the same region of interest, where amorphous regions appear black. (d) Phase color image showing the crystalline Sb_2Te_3 in blue and the non-indexable regions (amorphous) as black.

Table 5.1. Identity of irradiated regions in Figure 5.6, with corresponding ion fluences irradiated within the microscope at 8 keV (C/µm^2) and conversion to the standard unit (ions/cm^2).

ID	C/µm^2	ions/cm^2
R1	6×10^{-14}	3.74×10^{13}
R2	1.2×10^{-13}	7.49×10^{13}
R3	3×10^{-13}	1.87×10^{14}
R4	6×10^{-13}	3.74×10^{14}
R5	1.1×10^{-12}	6.87×10^{14}
R6	2.3×10^{-12}	1.44×10^{15}
R7	3.6×10^{-12}	2.25×10^{15}
R8	9×10^{-12}	5.62×10^{15}
R9	1.8×10^{-11}	1.12×10^{16}

5.3.2 Patterning of circular and dot geometries

Systematic investigations were carried out to further investigate disorder profiles close to the crystal-to-amorphous phase transition and the prospects for geometric patterning of non-trivial shapes. Sb_2Te_3 surfaces were irradiated using a series of lower ion beam fluences in different geometries. The table below (Table 2) reports the pattern sizes and corresponding ion fluence received for each pattern.

Table 5.2. Pattern ID and size with corresponding ion fluence irradiated within the FIB microscope (C/μm^2) at 8 keV and conversion to the standard unit (ions/cm^2).

Pattern ID	R1	R2	R3	R4	R5	R6	R7	R8	R9
500 × 500 nm	■	■	■	■	■	■	■	■	■
r_1 =500 nm	●	●	●	●	●	●	●	●	●
r_1 =500 nm r_2 =1000 nm	○	○	○	○	○	○	○	○	○
Dose (C/um^2)	1x10^{15}	5x10^{15}	1x10^{14}	2x10^{14}	5x10^{14}	1x10^{13}	2x10^{13}	5x10^{13}	1x10^{12}
Dose Ions/cm^2	6.24x10^{11}	3.12x10^{12}	6.24x10^{12}	1.25x10^{13}	3.12x10^{13}	6.24x10^{13}	1.25x10^{14}	3.12x10^{14}	6.24x10^{14}

Figure 5.7 (a) shows the electron image for the Sb_2Te_3 surface irradiated with the ion beam patterns described in the Table 2. Figure 5.7 (b) and (c) show the matching band contrast and phase color images. This indicates that the crystalline-amorphous transition of the Sb_2Te_3 surface begins to appear for patterns in column R5 (i.e. the critical fluence is ~ 3.12×10^{13} ions/cm^2 for 8 keV Ga^+). Figure 5.7 (d) and (e) show the band contrast and phase color images of high-magnification EBSD scans for rectangular patterns R2-R5. Figure 5.7 (f) shows the corresponding Kikuchi patterns of R3-R5. The Kikuchi bands start to disappear for the pattern R5, which is a signature of the amorphous transition. A further high magnification EBSD scan for ring-shaped patterns R6-R9 is shown in Figure 5.7 (g) and (h) and indicate that any pattern which received Ga^+ ion fluence greater 3.12×10^{13} ions/cm^2 (5×10^{-14} C/μm^2) was amorphized, for the 8 keV beam. Clear circular, crystalline dots can be formed, surrounded by an amorphous boundary with this patterning method. For much higher fluences, it is clear the damage spreads out further and the amorphous region gradually expands as shown by comparing the ring structures in R8 and R9 (Figure 5.7 (g-h)). This study not only helps determine the critical fluence required to amorphize Sb_2Te_3 crystals; it also illustrates the possibilities for precisely "writing" lithographic patterns on the Sb_2Te_3 surface at lower doses.

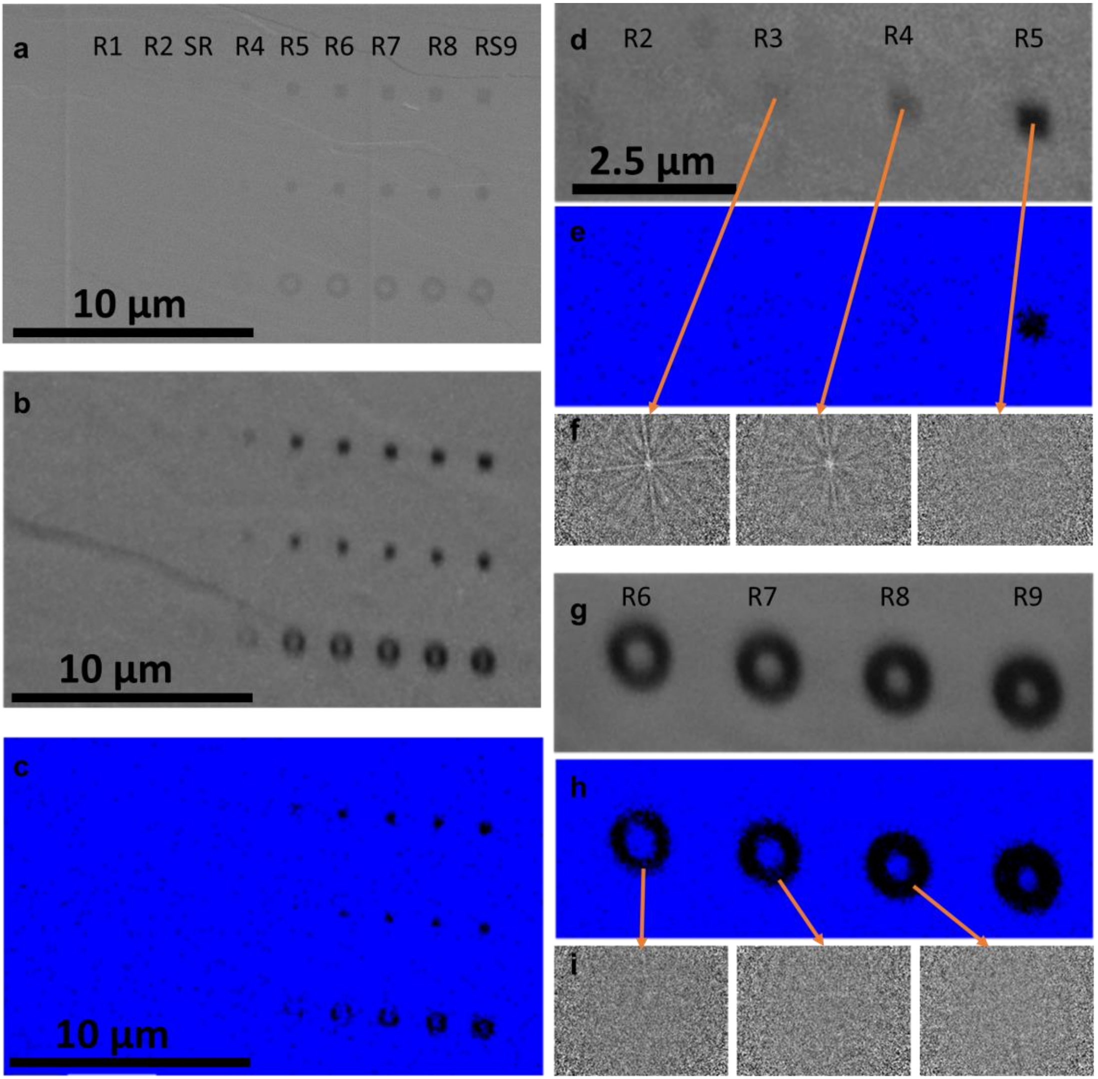

Figure 5.7. (a) Scanning electron image with each pattern ID labelled on it, and (b) Band contrast image from EBSD scan. (c) Phase color image. (d) High-magnification band contrast image. (e) Corresponding phase color image. (f) Kikuchi patterns taken at R3, R4, and R5. (g) High-magnification band contrast image of the patterns with higher Ga irradiation dose. (h) Corresponding phase color image. (i) Kikuchi patterns within patterns R6, R7, and R8.

5.4 Additional CAFM characterization

This section presents additional IV and line-profile measurements performed using a conductive atomic force microscopy (CAFM). Electrical characterization of ion-beam patterns was performed by a conductive atomic force microscopy using a commercial scanning probe microscope (Cyper S, Asylum Research, US). Conductive probes with Pt coating were used for both current mapping and current-voltage (I-V) measurements under a contact mode.

5.4.1 Line profiles through a region patterned using high Ga fluences

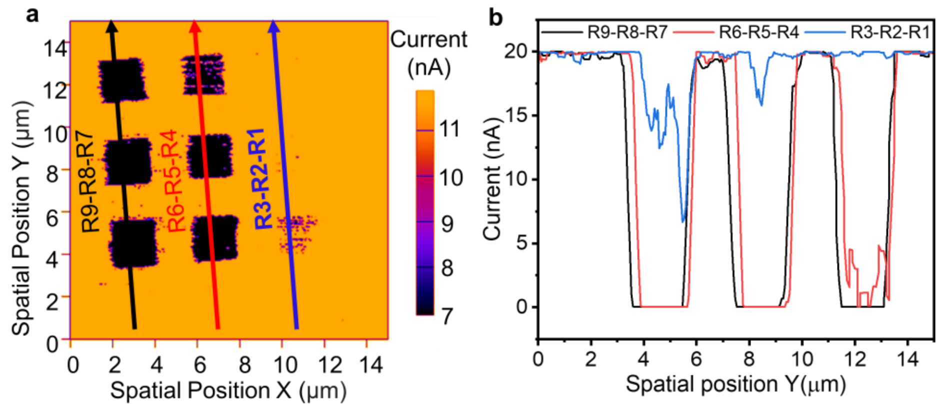

Figure 5.8. (a) Line profiles through the array of irradiated grid squares (see Figure 5.6 (a) and Table 5.1 for details) for cAFM measurement at a scanning bias of 1V. (b) Current response along the line profile scans in (a) showing that the current decreases to zero within the most heavily irradiated grid squares (R4 – R9).

5.4.2 I-V characterization

Figure *5.9* (a) shows the I-V characteristics of several patterned regions, similar to the region shown in (b). The areas exposed to Ga have a significantly different I-V from the boundary and the unirradiated regions. Figure *5.9* (b) CAFM image shows representative points where I-V scans were performed. We note that, while all of the scans over sufficiently irradiated regions show a large, consistent decrease in the current at the centre of A-V 2D boundaries from nanoamps to picoamps, the currents of the “edge” states at the A-C boundary only give contrast at specific bias voltages, and the current contrast is small (in the 50-100 picoamp range). This is near the sensitivity limits of the instrument. Concerning the anisotropic effect on the pattern edge conductivity for the “1D” C-A boundaries: this is due to the nature of conductive atomic force microscopy (CAFM), where the conductive tip was scanned along the X-axis (leftwards and rightwards). At the edges of the pattern where there are stages/steps, the contact area of the tip with the sample may vary slightly (with a higher or lower contact area depending on the surface condition). This causes observed anisotropy around the pattern. To demonstrate this, in Section 5.4.4, the samples were rotated, and scans were performed in various directions. Furthermore, to confirm the observed high edge conductivity from CAFM is real, we have also performed multiple point I-V measurements on several different irradiated areas and

boundaries and compared these with neighboring crystalline areas. The results in Figure *5.9* (c)-(e) confirm that the high conductivity from edges is reproducible, and the central amorphous areas of the pattern (at A-V surfaces) show a much lower current than both A-C edges and C-V substrate boundaries.

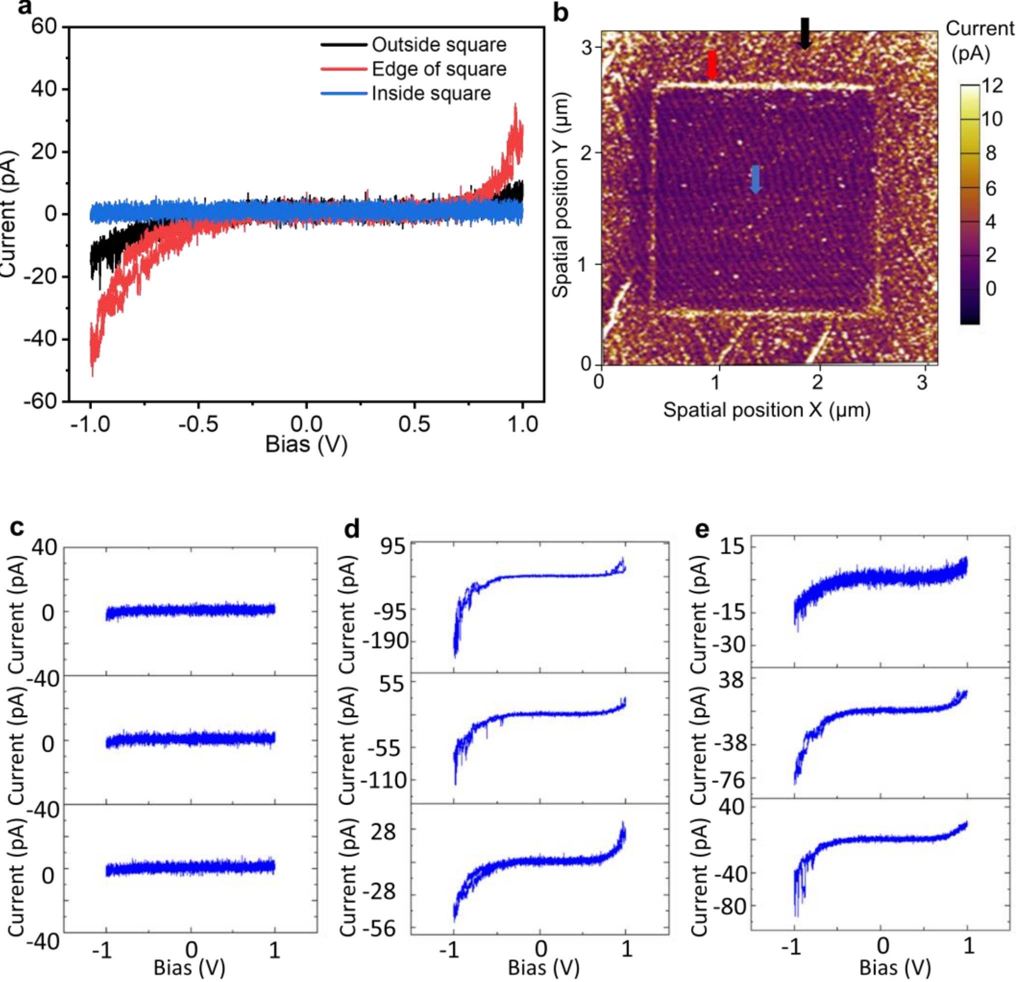

Figure 5.9. I-V characteristics. (a) Comparison of an ion-beam irradiated area (inside the midpoint of the square for an A-V boundary), with the A-C boundary (edges of the square), and unirradiated area at the crystallinity C-V boundary (outside the square). (b) CAFM image with colored arrow labels indicate the irradiated area, boundary, and crystalline area where I-V scans have been performed. (c-e) A series of repeated I-V scans at multiple patterned areas, edges, and crystalline regions to confirm the reliability of the measurements.

5.4.3 Line profile showing edge conductivity

A line scan profile on the CAFM image in Figure *5.10* shows a clear current spike at both boundaries and terraces of the crystal, indicating that the high conductivity possibly originates from edge states. The similar high conductivity possibly originated from edge

states present on natural cleavage terraces on crystal surface (also see Figure 5.11 and Figure 5.12).

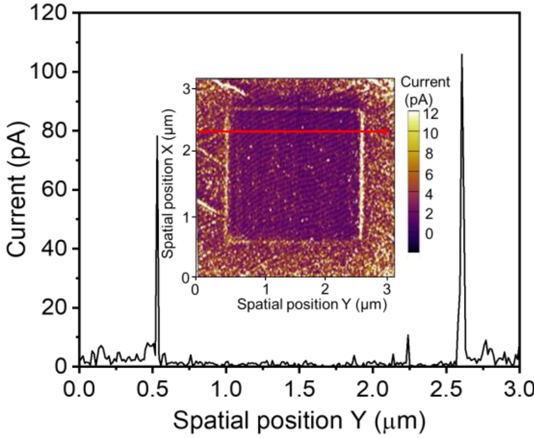

Figure 5.10. The current line scan profile shows the high conductivity at the edges at the boundary between ion-beam irradiated and unirradiated areas. (Note: the CAFM image is rotated so that the line profile direction matches the x-axis of the figure.)

5.4.4 Characterizing the anisotropy in the CAFM scans

Figure *5.11* (a) and (b) CAFM images are collected from the same pattern, but the scanning angle has been deliberately rotated by 90 degrees (as indicated by the tip position and the arrows showing the fast/slow scanning directions). The numbers inside the figures label the same edges before and after the rotation. For either scan, the edges of the pattern show higher conductivity and irradiated areas show relatively lower conductivity. Figure *5.11* (a), edges 1 and 3 show relatively higher current than edges 2 and 4; however, in Figure *5.11* (b), edge 1 and 4 both show higher conductivity. Please note the scale of the current value is quite small (within 15 pA) and probe-sample contact issues (as mentioned above) explain the observed anisotropy in the edges; however, the existence of the edge currents is well-supported by the data.

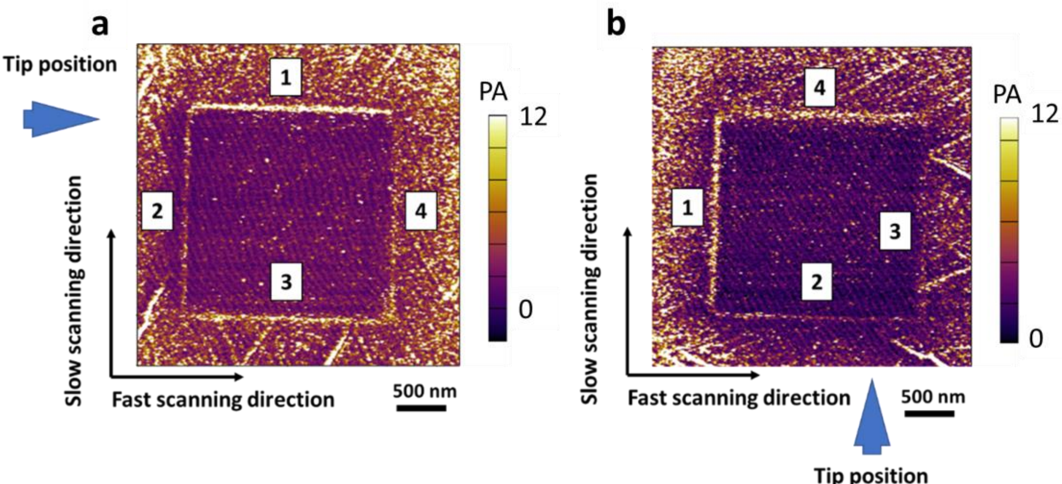

Figure 5.11. Current mapping using 1V DC bias for an individual irradiated box. (a) CAFM scans with a fast-scanning direction parallel to the probe. (b) CAFM scans with a fast scanning direction perpendicular to the probe.

Figure *5.12* shows a triangular-shaped logo that includes several edge lines at different angles to the scan direction. All the edges show an observable, higher conductivity (including the small circles inside the pattern), while the central parts of the irradiated pattern show lower conductivity. Our CAFM results collectively confirm the high conductivity at the boundary, although future work is needed to provide quantitative measurements.

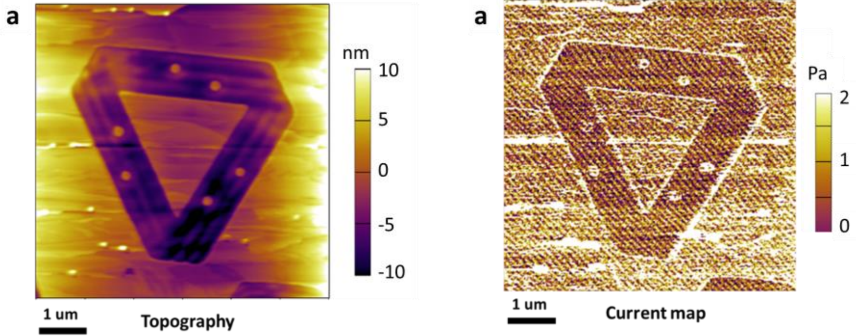

Figure 5.12. CAFM images of a patterned logo with edges at different angles to the scan direction. (a) Topography. (b) Current mapping of an individual irradiated FLEET logo pattern.

5.5 Details of transport measurements for the FIB devices and thin films

5.5.1 Details on the focused-ion beam device preparation methodology

To enable four-probe resistivity measurements on crystalline devices, a method was developed to prepare devices with minimal exposure to the focused ion beam, taking advantage of the van-der Waals (flaky) nature of Sb_2Te_3, and using the nanomanipulator. Figure 13 illustrates the main steps. The details are summarized below:

1. First, we exfoliate the Sb_2Te_3 single-crystal surface with adhesive tape to liberate thin flakes on the surface. Under SEM imaging mode, we search for the flakes of desired thickness.
2. At low ion-beam voltage and current (8-16 KeV, <80 pA), we cut the desired size of lift-out, having welded a nano manipulator to one end of Sb_2Te_3 rectangular lift out. The process aims to avoid, as much as possible, exposing the surface of the lift-out to the ion-beam. Imaging of the procedure involves taking low current snapshots in ion-beam imaging mode at 8 KeV, <25 pA. Thus, the majority of surface of the flake lift out is unirradiated although one edge is slightly irradiated by a negligible amount of the Ga ion beam.
3. The rectangular lift-out is carefully placed on a set of pre-made contacts on a commercial chip. If any ion beam imaging is performed, this is done at very low voltage and current for a short time (<=8 keV, =<25 pa) to ensure the surface of the lift-out remains crystalline.
4. Pt deposition in the FIB is used to fabricate four-probe and Hall measurement contacts which link the gold pads on the chip to the surface of the crystal.
5. The crystallinity of the main areas of the device is confirmed using electron back-scatter diffraction (see Figure 14).

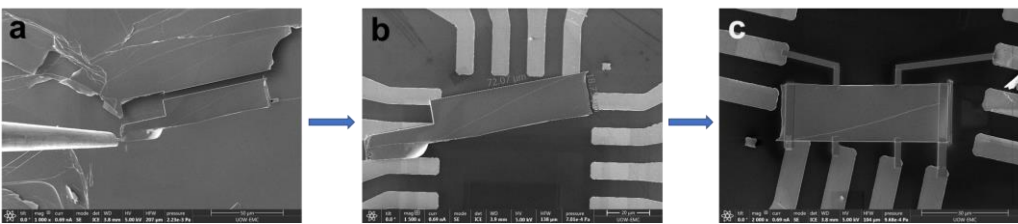

Figure 5.13. Device fabrication procedure for crystalline FIB devices. (a) A thin exfoliated flake region is selected, and a single cut is made to remove a bar-like section and weld it to a nanomanipulator. (b) The flake is placed on prefabricated gold contacts. (c) Platinum contacts are deposited, linking the gold contacts to the surface of the Sb_2Te_3 bar (thickness=500-600 nm).

5.5.2 Crystallinity of an as-prepared device

The Figure 5.14 a shows the electron image with superimposed EDS mapping after the fabrication of four-probe and Hall resistivity contacts. Figure 5.14 b shows the EDS mapping (together with an electron image in the top panel) of the Sb, Te, Si, Pt, and Ga elements. The Si X-ray signals arise from the underlying Si chip, which supports the rectangular topological insulator device. The rectangular device thickness is in the range of 500-600 nm, and X-ray spectra originate not only from the Sb_2Te_3 device, but also from the micron deep regions from the underlying Si chip. Contacts were fabricated with ion-beam deposited Pt. Figure 5.14 c shows the EBSD map (the band contrast image is at the top) and Figure 5.14 e is an inverse pole figure coloring key for the EBSD map. Figure 5.15 b and c show the electron backscattered Kikuchi patterns (EBSP) and corresponding simulated solutions in the Aztec software taken from the points B and C respectively on Figure 5.15 a. The presence of clear Kikuchi patterns indicates that the detectable surface of the Sb_2Te_3 rectangular device is still crystalline after the contact fabrication steps. Figure 5.15 d shows the 3D phase view of the hexagonal crystal structure of Sb_2Te_3, which is generated in the Aztec software.

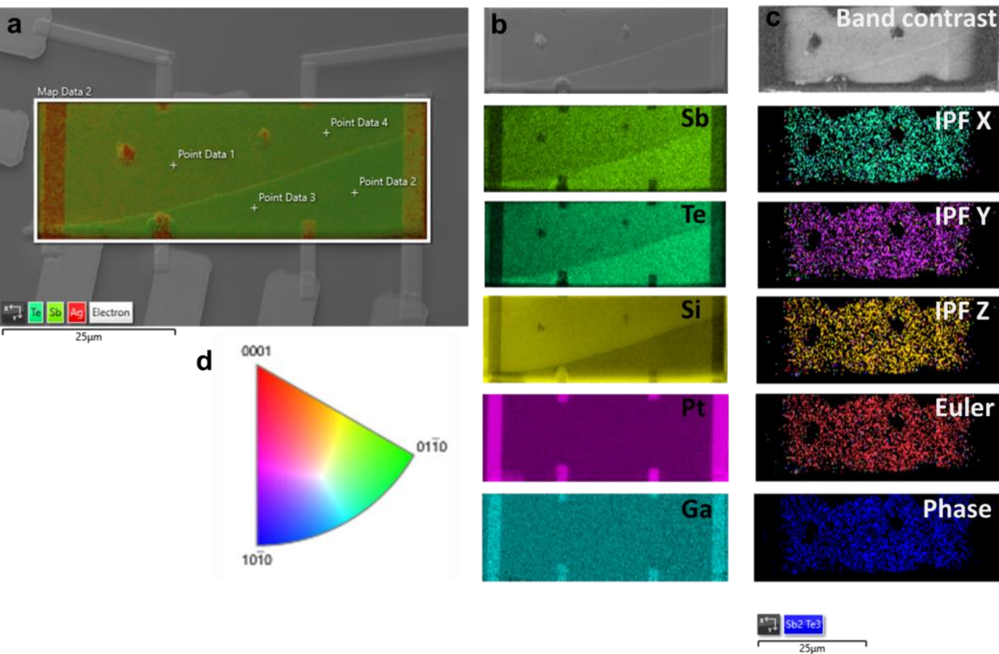

Figure 5.14. EDS and EBSD characterization of the rectangular lift-out on a chip shows that the device is crystalline. (a) EDS layered image. (b) EDS elemental map taken from the white box in (a) (SE image at the top), and corresponding (c) EBSD and crystal orientation map with (d) inverse pole figure (IPF) coloring key.

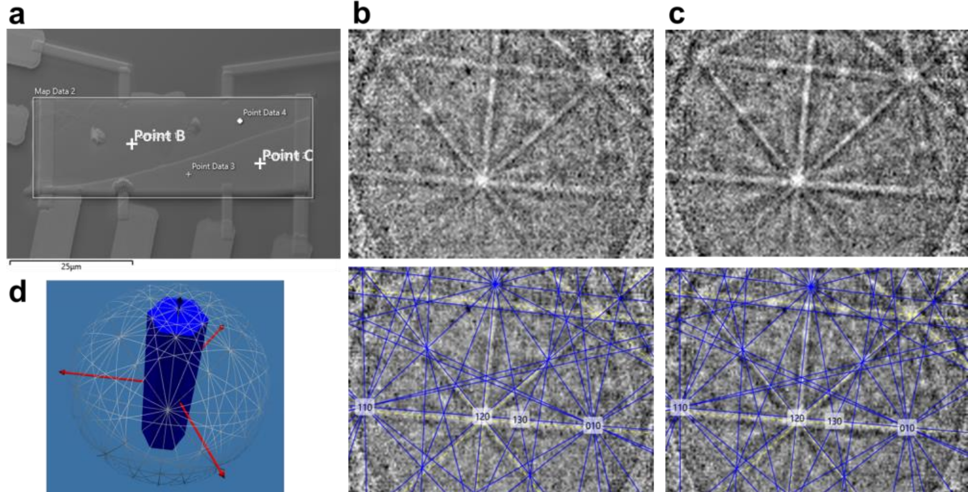

Figure 5.15. Representative Kikuchi patterns for sections of the device showing it to be crystalline. (b) and (c) Electron back-scattered Kikuchi Patterns (EBSD) (with simulated solutions generated within the Aztec software) from point B and point C on the SE image in (a). (d) The 3D phase view of the unit cell shows the orientation is identical for points B and C, indexed to the hexagonal crystal structure of Sb_2Te_3.

5.5.3 Shubnikov-de-Haas oscillations of the as-prepared crystalline device

To confirm that the device exhibits the quantum oscillations, characteristic of the bulk crystalline Sb_2Te_3 Fermi surface, magneto-transport experiments were performed on the device shown in Figure 5.15. The temperature-dependent resistivity of the device is shown in Figure 5.16 a, indicating a metallic-like resistance characteristic of Sb_2Te_3 where the Fermi level is positioned in the bulk valence band. The magnetoresistance measurements are shown in Figure 5.16 b, from which the oscillatory component is extracted in Figure 16 c. The Fourier transforms of the oscillations shows that the main component is very similar to past reports for crystalline Sb_2Te_3 [6].

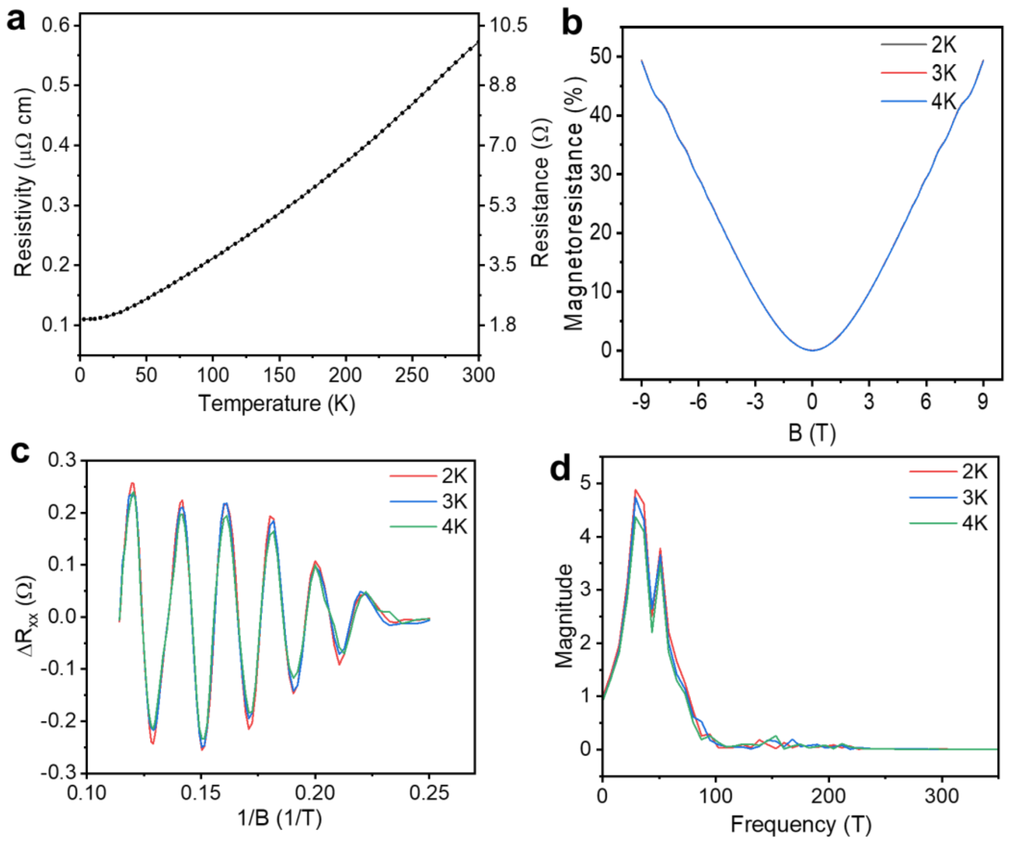

Figure 5.16. Transport measurement of the FIB fabricated device. (a) RT measurement. (b) Magnetoresistance at 2, 3, and 4 K. (c) Shubnikov-de Hass (SdH) oscillation extracted by subtracting the background from the magnetoresistance measurement. (d) Fast Fourier transform (FFT) magnitude of the SdH oscillations measured at 2−4K.

5.5.4 Effect of irradiation and post-annealing in the FIB-fabricated device

To investigate whether the amorphous transition can be reversed, an in-situ heating experiment was conducted as shown in Figure 5.17. First, a bar similar in dimension to the devices was prepared on a heating element. The EBSD Euler map in Figure 5.17 a shows that the bar is initially crystalline as it can be indexed to Sb_2Te_3. The elemental maps of each component are also illustrated in the EDS maps. To selectively amorphize a region of this bar, a high dose of 7 pA Ga beam, at 30 keV (z depth set to 10 nm) was used to irradiate an area of 5x3 μm in the center of the bar. The EBSD band contrast and Euler maps in Figure 5.17 b show that this region becomes amorphous. The sample was then heated to 400°C and held for 0.5 hour in-situ. After heating, Figure 5.17 c shows the amorphous region recrystallized, evident from the re-appearance of the electron back-

scattering diffraction (Kikuchi) pattern shown in the band-contrast image. Ga EDS map (after recrystallization) in Figure 5.17 c shows a slight increase in Ga as compared to Figure 5.17 b Ga EDS map (before recrystallization). This might be caused by the Ga diffusion to the surface. There might be very less trance for Ga to be retained in between Sb_2Te_3 layers when recrystallized, as this might cause significant lattice distortion, which would change the EBSD pattern and indexing. Whereas EBSD pattern and indexing after recrystallization could confirm that Ga may not remain in between layers after recrystallization.

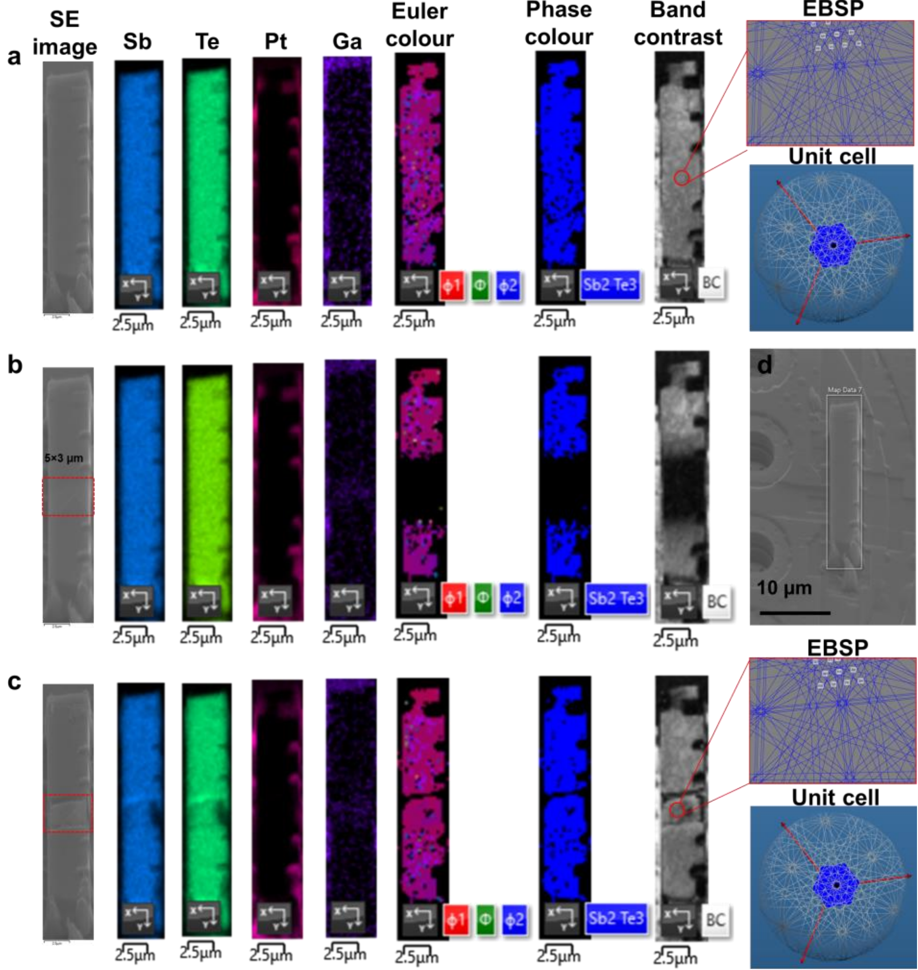

Figure 5.17. In-situ characterization of a Sb_2Te_3 bar before irradiation, post-irradiation and post-heating. (a) EDS and EBSD scan of a rectangular lift-out section welded on an FEI heating chip before irradiation. The EBSD and unit cell image indicate the lift-out surface's crystalline nature. (b) EDS and EBSD scan after the 5x3 μm area (indicated in the red box on the SE image) was irradiated with a Ga ion beam. The EBSD scan highlights the amorphous nature of the irradiated area. (c) After in-situ heat treatment at 400 °C for 30 minutes, the EBSD images show the recrystallization of the Sb_2Te_3 region via the disappearance of the dark amorphous region in the band contrast images. Images were generated within the Aztec software.

5.5.5 Lumped-element model for the FIB fabricated devices

When intentionally irradiating the rectangular lift-out device with Ga ions at 30 KeV, a surface amorphous layer of approximately ts=50 nm thick is formed. For lower incident energies (8 keV), the amorphous layer is approximately 20 nm thick (see Figure 5.2). Based on the four-probe measurement configuration and a scenario where a FIB device has an amorphous surface layer, and a crystalline underlayer, we created a lumped element model as in Figure 5.18. This introduces two parallel conduction channels for the amorphous surface layer (modelled by a resistor RS) and the crystalline underlayer (RB). As the contacts are made to the surface layer, any current which passes through the bulk must first pass through a series resistor that models the surface leakage resistance (RL). The total (net) resistance of the device can be approximately calculated with the Equation (2) below:

$$R_T = \frac{R_S\,(2R_L+R_B)}{R_S+R_B+2R_L} \qquad \text{Equation (2)}$$

where R_T is the total resistance, R_S is the surface resistance, R_B is the bulk resistance, and R_L is the leakage resistance. Based on the device measurements (see main manuscript Figure 2 (f)), the total room-temperature resistance of the device when the surface is crystalline is $R_T = 22.23\ \Omega$. After surface amorphization, $R'_T = 89\ \Omega$. From
Figure 5.19, we estimate the leakage resistivity of the amorphous Sb_2Te_3 is in the range of 1×10^6 Ω-µm to 1×10^7 Ω-µm. Using the device dimensions with l = 50 µm, w = 15 µm, t = 0.5 µm and t_s=50 nm, the value of R_S is $6.67 \times 10^8\ \Omega$, and assuming that leakage occurs through the entire surface area (l×w) over length t_s, R_L=67-667 Ω. This gives the total resistance of the amorphized device of approximately 170–1370 Ω, which is in the same order as observed experimentally (88 Ω). We infer that pinholes and imperfections in the nanoscale amorphous layer substantially decrease the leakage resistance. R_L is reduced to 26 Ω, to account for the observed total resistance of 88 Ω observed experimentally.

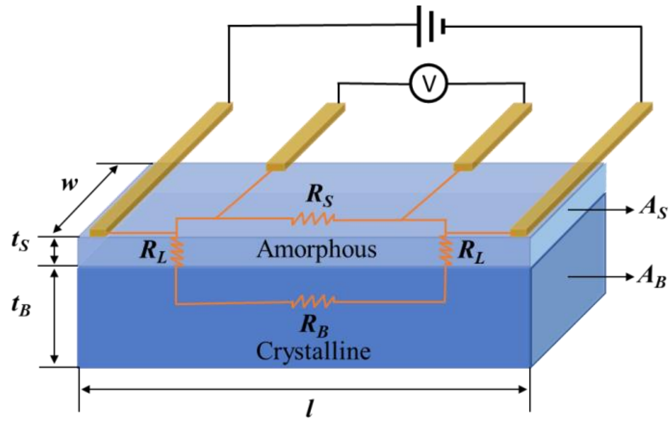

Figure 5.18. Schematic illustration showing the configuration for the four-probe contact measurements and the corresponding lumped element model of a Ga-FIB device with an amorphous surface layer, and a parallel bulk conducting channel.

Table 5.3. Total resistance calculation of the FIB device based on the lumped element model.

	Resistivity, ρ (Ω.μm)	Area, A (μm^2)	Surface area	Resistance, R (Ω)
Bulk (R_B)	5	6.75	$A_B = w \times t_B$	37
Surface (R_S)	1×10^7	0.75	$A_S = w \times t_S$	6.67×10^8
Leakage (R_L)	1×10^6 -1×10^7	750	$A_L = w \times l_{CONTACT}$	67-667
Total resistance (FIB device R_T = 22.23 Ω, R_T'(Amorphous surface) = 89.45 Ω)				170 -1370

5.5.6 Complementary thin film devices

The FIB devices shown in the previous section have an amorphous surface and a crystalline bulk region. This introduces parallel conduction as illustrated by the lumped element model described in section 5.5.5. In order to eliminate the bulk crystalline conduction channel and measure the intrinsic response of the amorphous Sb_2Te_3 itself, subsequent experiments utilized thin film Sb_2Te_3 which can be fully amorphized at the available Ga-ion beam energies. This allows for a clearer study of the intrinsic resistance of the amorphous phase, and the behavior of the A-V boundary.

Thin films were grown by molecular beam epitaxy on single crystal Al_2O_3 (001)-

orientated substrates, with a total thickness between 5–30 nanometers. The lateral area of the samples was 10 × 10 mm^2. The crystallinity was confirmed by their RHEED patterns, and XRD (see later). The resistivity of a crystalline film is shown in Figure 5.19 a, exhibiting a metallic resistance with an upturn at low temperatures. This entire film was then amorphized using a broad-beam low-energy ion beam accelerator, with Ga ions at 30 keV and a fluence of 1×10^{15} ions/cm^2. This fluence was selected as it is above the Ga ion-beam amorphization threshold of crystalline Sb_2Te_3.

After irradiation, the resistance of the film increased by almost six orders of magnitude, as shown by Figure 5.19 b, as compared to the resistance of the crystalline counterpart as shown in Figure 5.19 a. Furthermore, the resistivity exhibited an exponential increase with decreasing temperature – a hallmark of a good insulator. Unfortunately, low-temperature measurements could not be performed because the resistance became too high to measure accurately with the available equipment. This is attributed to the excellent insulating properties of the Sb_2Te_3 amorphous phase, and the complete suppression of any surface conducting channels. The transition between the crystalline as-grown film to the amorphous-irradiated film was confirmed using cross-sectional TEM images as shown by Figure 5.19 c and d.

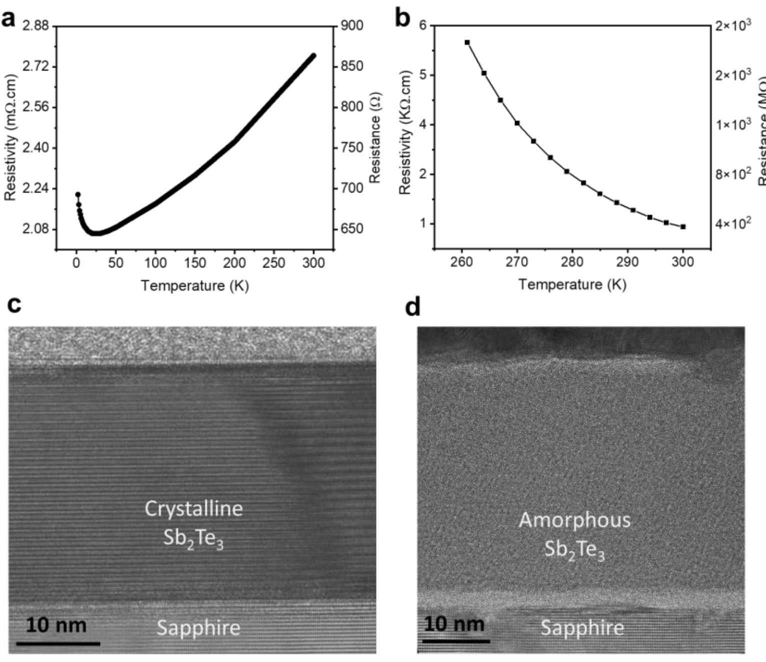

Figure 5.19. Temperature-dependent resistivity of (a) the as-grown crystalline and (b) amorphized Sb_2Te_3 thin film grown by molecular beam epitaxy. (c) Cross-sectional TEM images of the starting film illustrating the clear lattice fringes from the crystalline order. D) Image of the same film after Ga-ion irradiation using a broad beam Low Energy Ion Implanter.

To further understand this transition, and provide accurate measurements of the film morphology, low angle X-ray diffraction, X-ray reflectometry, neutron reflectometry and polarised neutron reflectometry were performed on the film before and after irradiation. Measurements were performed on the Rigaku Smart Lab X-ray instrument, the SPATZ neutron reflectometer, and the PLATYPUS reflectometer at the Australian Centre for Neutron Scattering (ACNS) at ANSTO. The X-ray data are shown in Figure 5.20. The disappearance of the (003) Bragg peak shows that the entire film was transformed to the amorphous state by the irradiation step. The noticeable shift in the low-angle Kiessig fringes shows that the film thickness slightly increased by several nanometers after irradiation due to swelling. A similar conclusion is reached using the neutron reflectometry data in Figure 5.21. These data were quantitively fitted to a model constructed using the REFNX software package to obtain the 1D scattering length density profiles. The larger Q-range in the X-ray data allows for a higher resolution structural solution, where the modulations from the Sb_2Te_3 quintuple layers can be resolved (giving rise to the Bragg peaks at ~0.6 $Å^{-1}$). The neutron dataset probed a lower Q-range and was fitted to the continuum model. Both datasets show that the film swelled from an initial thickness of 28nm to 30 nm after irradiation. This is attributed to the lower mass density of the amorphous phase, which is also consistent with the lower scattering length density (SLD) values observed in the irradiated phases. From the neutron and X-ray contrast, the mass density of the amorphous phase can be uniquely calculated as: 6.1 g/cm^{3,} which is reduced relative to the crystalline phase (6.5 g/cm^3).

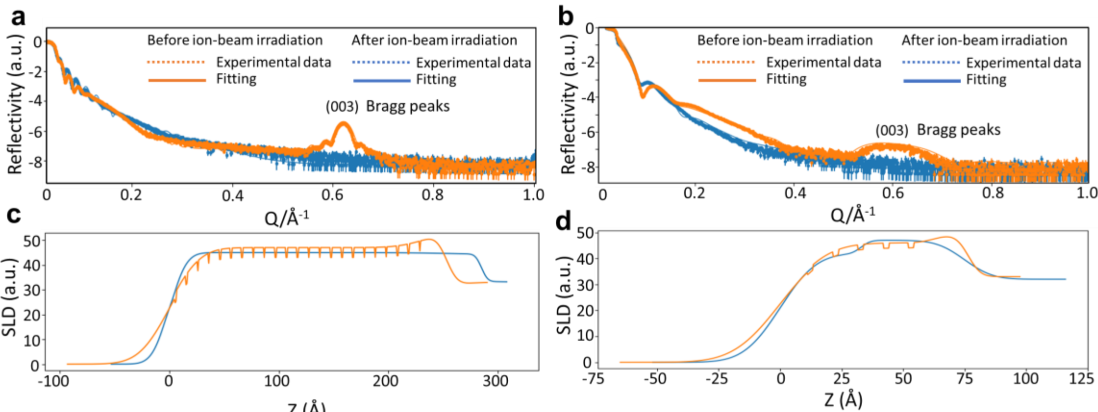

Figure 5.20. X-ray reflectometry of (a) MBE-grown Sb_2Te_3 film before and after ion-beam irradiation. (a) ~28 nm thick film before irradiation (b) MBE-grown Sb_2Te_3 film (~10 nm) before and after ion-beam irradiation. (c) and (d) SLD profiles for (a) and (b), respectively.

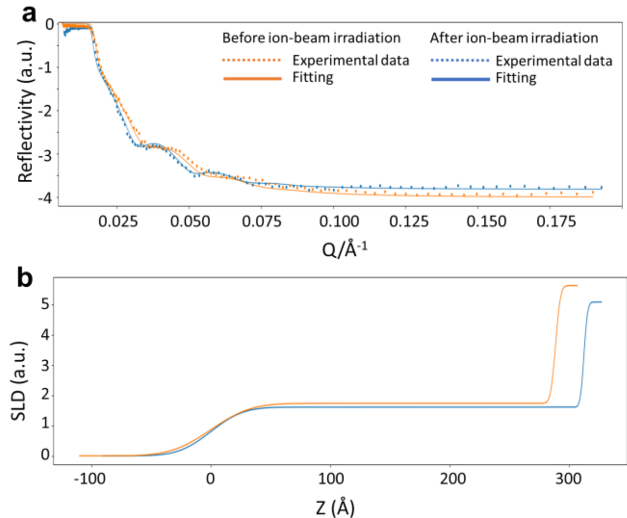

Figure 5.21. (a) Neutron reflectometry of MBE-grown Sb_2Te_3 film (~30 nm) before and after ion-beam irradiation (b) Corresponding SLD profiles.

A recent work by I. Korzhovska reported a robust magnetic signal from disordered materials. They observed that the magnetic signal crucially depends on the level of disorder and reported an effective magnetic moment per atom of up to 0.17 μB in Sb_2Te_3 [7]. To clarify whether there is a detectable magnetic signal from the amorphous Sb_2Te_3 film, a polarized neutron reflectometry (PNR) measurements were carried out on ~10 nm Sb_2Te_3 thin films amorphized by a Ga ion beam. The lack of a Bragg peak (in Fig. 5.20b) indicates the amorphous nature of the Sb_2Te_3 films after Ga ion beam irradiation. Meanwhile, our PNR measurements in Fig. 1 show a barely detectable magnetic signal. If the magnetic moment per atom is more than 0.16 μB in amorphous Sb_2Te_3 films, then the corresponding spin asymmetry should lie within the yellow shaded region, as shown in Fig. 1b. From the best fit to the PNR data, we conclude that amorphous Sb_2Te_3 shows negligible magnetic signal.

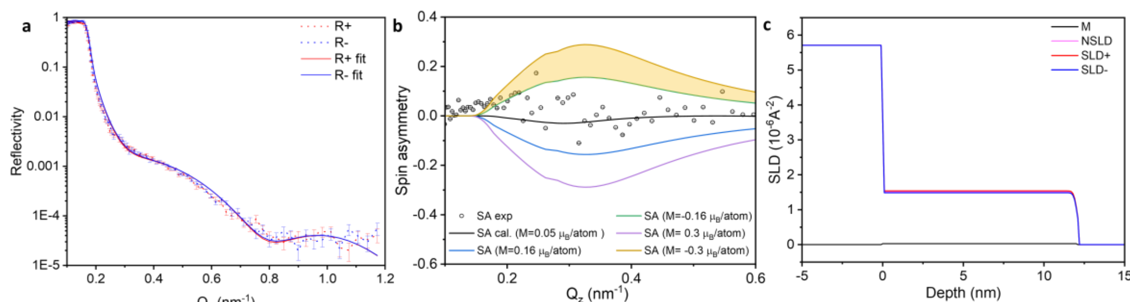

Figure 5.22. a) Polarised neutron reflectometry pattern for 10 nm Sb_2Te_3 thin films at 5 K in a field of 0.1 T. b) The neutron spin asymmetry, and best fit to the data. c) The best fit SLD model to the neutron data at 5 K.

References

1. Bake, A., et al., *Top-down patterning of topological surface and edge states using a focused ion beam.* Nature Communications, 2023. **14**(1): p. 1693.

2. Ziegler, J.F., M.D. Ziegler, and J. Biersack, *SRIM–The stopping and range of ions in matter.* Nuclear Instruments and Methods in Physics Research Section B: Beam Interactions with Materials and Atoms, 2010. **268**(11-12): p. 1818-1823.

3. Hengstler-Eger, R., et al., *Heavy ion irradiation induced dislocation loops in AREVA's M5® alloy.* J. Nuclear Mater., 2012. **423**(1-3): p. 170-182.

4. Frey, L., C. Lehrer, and H. Ryssel, *Nanoscale effects in focused ion beam processing.* J. Appl. Phys. A, 2003. **76**(7): p. 1017-1023.

5. Bake, A., et al., *Lamellae preparation for atomic-resolution STEM imaging from ion-beam-sensitive topological insulator crystals.* Journal of Vacuum Science & Technology A: Vacuum, Surfaces, and Films, 2022. **40**(3): p. 033203.

6. Zhao, W., et al., *Quantum oscillations in iron-doped single crystals of the topological insulator* Sb_2Te_3. Physical Review B, 2019. **99**(16): p. 165133.

7. Korzhovska, I., et al., *Spin memory of the topological material under strong disorder.* npj Quantum Materials, 2020. **5**(1): p. 39.

Chapter 6. Top-Down Patterning of Topological Surface and Edge States using an Ion Beam

The results in this chapter were originally published in Nature Communications [1].(article link: https://www.nature.com/articles/s41467-023-37102-x, title: Top-down patterning of topological surface and edge states using a focused ion beam, and DOI: 10.1038/s41467-023-37102-x). In the sections below, an adapted version of the article is presented, which has been modified slightly for phase consistency of style and to highlight connections with the other results presented in this thesis.

6.1 Overview

The conducting boundary states of topological insulators appear at an interface where the characteristic invariant $\mathbb{Z}_2$ switches from 1 to 0. These states offer prospects for quantum electronics; however, a method is needed to spatially-control $\mathbb{Z}_2$ to pattern conducting channels. It is shown that modifying Sb_2Te_3 single-crystal surfaces with an ion beam switches the topological insulator into an amorphous state exhibiting negligible bulk and surface conductivity. This is attributed to a transition from $\mathbb{Z}_2 = 1 \rightarrow \mathbb{Z}_2 = 0$ at a threshold disorder strength. This observation is supported by density functional theory and model Hamiltonian calculations. Here we show that this ion-beam treatment allows for inverse lithography to pattern arrays of topological surfaces, edges and corners which are the building blocks of topological electronics.

6.2 Introduction

The sub-classes of quantum insulators can be distinguished using invariants (e.g., $\mathbb{Z}_2$) — simple groups of integers related to the Berry curvature — which also encode information on their distinctive physical properties [2-9]. A special case is the 3D strong topological insulator (TI) having one “strong” index $\mathbb{Z}_{2s}$=1*. The non-zero strong index is the criterion for the existence of zero-gap spin-helical Dirac surface states which appear within the bulk electronic bandgap, as observed experimentally [10-18]. These states offer the prospect of dissipationless transport for nanoelectronics, enabling topological transistors

to potentially evade the so-called "Boltzmann's tyranny" of conventional semiconductors [19], together with enticing prospects for topological qubits based on Majorana zero modes [20]. Although dissipationless channels have already been observed at the natural edges of TI crystals [21], a missing step is a precise top-down method to spatially engineer nanoscale arrays of conducting channels for scalable integrated circuitry, which would require regions of both $\mathbb{Z}_{2s}$=1 and $\mathbb{Z}_{2s}$=0. Adopting the surface engineering paradigm from silicon technology, an effective way to do this would be to define the channels using lithography of monolithic crystal surfaces enabled by ion beams [22, 23],[24]. So far there has been no demonstration of this technique, which is well-known in other microelectronics, to pattern the position of topological edge states. Here we demonstrate the ability to perform top-down nanopatterning of topological surface and edge states at the Sb_2Te_3 surface using an ion beam to induce atomic displacements that pin the edge states at the boundary with local amorphous regions. We find that, with ion beam processing, we can study and control three types of interfaces in a topological insulator, each with distinctive electronic properties. The nomenclature used here to describe these three interfaces is: A-V for amorphous-vacuum, C-V for crystalline-vacuum and A-C for amorphous-crystal boundaries. Furthermore, we observe modified conductivity from 2D topological "surface states" and 1D "edge" regions.

Determining if amorphous "glassy" states at an A-V 2D surface are topological or trivial is currently of great interest [25],[26, 27], and here we first focus on this question experimentally. This question is the main unknown, and is of key importance to surface engineering, as it determines whether disordered regions behave as a "topological vacuum". Initial theories predicted that, while the TI Dirac band-structure is resilient against low energy charge disorder, strong disorder from lattice defects can introduce an electronic gap and transform the amorphous system into a trivial Anderson insulator, with $\mathbb{Z}_{2s}$=0 (i.e. equivalent to that of vacuum) [28]. More recent theories, in contrast, predict that the collapse of the topological state in the glass is not guaranteed, and instead, solid-state amorphous topological insulators do exist in special cases, at least in numerical simulations [29],[26, 30], and model photonic/mechanical metastructures [31],[32, 33]. This is expected to be non-universal as the emergence of topological edge states requires very special interactions in the semi-random glass, and for example, Voronoi-type amorphous networks of interconnected points are predicted to be topological insulators, whereas those formed from triangulation are not [26]. In practice, it is unclear which

conditions apply in real solids. Recent theories are divided on this point for the prototypical chalcogenide family of TIs [34],[35] where experimental information on the glassy state is also limited [36],[37]. This motivated a detailed systematic experimental study of the electronic properties of Sb_2Te_3 as it transforms from the crystalline state into a glass.

Crystalline Sb_2Te_3 is a textbook example of a $\mathbb{Z}_2$ 3D TI described by the space-group (SG) $R\bar{3}c$ #166 (illustrated in Figure 6.1 a), which possesses inversion symmetry. As a good example of a strong TI, as designated in the topological materials database (TMD) [16], it hosts a single Dirac cone in its surface electronic band structure, with a bulk-band gap of 0.2-0.3 eV, as detected by angle resolved photoemission spectroscopy (ARPES) and magneto-transport experiments.[10-18] However, the related high-pressure Sb_2Te_3 compound of the C2/m space-group (SG #12, Figure 6.1 b) has disordered Sb/Te sites and is completely topologically trivial with $\mathbb{Z}_{2s}$=0 and $\mathbb{Z}ws$=0 (TMD #187539), therefore having an absence of topologically-protected surface states. The topology of amorphous Sb_2Te_3 (Figure 6.1 c) is unknown, however, in this work, we will show that being structurally similar to the C2/m phase, it behaves as a trivial insulator, and hosts no detectable surface states. This intuition is supported by the past literature, where the insulating properties of amorphous Sb_2Te_3, both in the bulk and surface, have been established as a key property in its role as a phase change memory (PCM) material [38],[39],[40]. The collapse of the topological state has also recently been inferred in disordered Sb_2Te_3 thin films [35, 37], although the growth-induced disorder makes it difficult to achieve top-down patterning in that case.

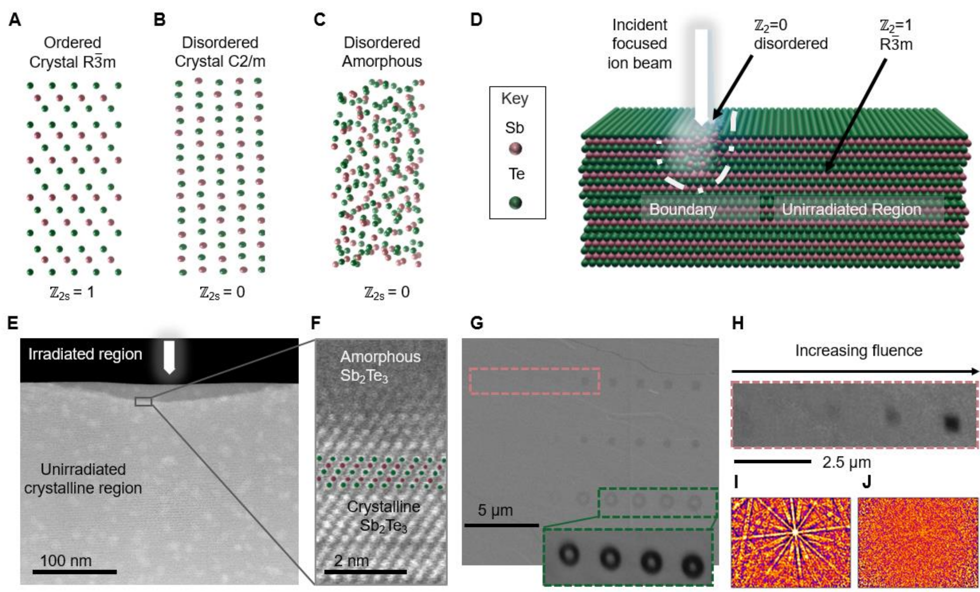

Figure 6.1. The crystalline state of the topological insulator Sb_2Te_3 can be modified using a focused-ion beam. (a) Illustration of the ordered crystalline $R\bar{3}m$ phase of Sb_2Te_3 which has $\mathbb{Z}_{2s}$ =1. (b) The disordered C2/m phase has random Sb/Te sites and has $\mathbb{Z}_{2s} = 0$. (c) Amorphous Sb_2Te_3 shares similarities with the disordered crystalline phase. (d) Schematic illustration of the ion-beam assisted amorphization process. (e) Cross-sectional scanning transmission image in HAADF mode of the irradiated region at the surface of the crystal. (f) High-resolution HAADF image showing the amorphous and crystalline regions where the irradiation used was 2.2×10^{15} ions/ cm^2 at 8 keV. (g) Secondary electron image of a plane view of the surface showing the ion-beam irradiated patterns (inset image shows the EBSD band contrast image of a selected region). (h) EBSD band contrast image from a region in (g) (pink dashed line). Electron backscattered diffraction patterns (i) from lightly irradiated pattern and (j) from the highly irradiated pattern in (h), showing the transition from order to disorder as the ion fluence is increased. (see Table 5.2 and Figure 5.7 in Chapter 5).

6.3 Results

To parametrize the level of surface disorder experimentally, Sb_2Te_3 single crystals were grown and polished and the surface exfoliated to present (001) planes with flat regions interspaced by terraces. The smooth regions of the crystalline surfaces were then exposed to a focused-ion beam at low energy (5–30 keV) using a systematic set of ion beam fluences (1×10^{11} to 5×10^{16} ions per cm^2) (see Figure *5.1* to Figure *5.15* Chapter 5). The initial crystals are typical of Sb_2Te_3, showing well-defined Shubnikov-de Haas oscillations, a non-trivial Berry phase, high mobility and residual bulk conductivity, as

reported previously [41] (see also Figure 5.16 Chapter 5). The incident ions modify the first few nanometers of the surface, as shown schematically in Fig. 1 d, primarily by displacing Sb and Te from their chemically-ordered crystalline sites, (see Monte Carlo simulations in Figure 5.2 in Chapter 5), in turn modifying the electronic structure. Low-energy gallium ion beams were found to be effective for modifying the surface, as they cause a large amount of lattice displacement, with a sharply-defined stopping depth, and do not lead to porosity or flaking. The small residual Ga^{3+} impurity is also isovalent with the Sb^{3+}, minimizing electronic doping.

Using this method, the Sb2Te3 surface can be tailored with high precision so that the top 20 nanometers of the irradiated surface where the ion beam is focused becomes amorphous, as shown by the cross-sectional scanning transmission electron microscope (STEM) image (Figure 6.1 e), whereas unirradiated regions remain crystalline. The transition from the crystalline to the amorphous phase occurs over a small spatial scale of 2-4 nm (Figure 6.1 f). Lateral patterns can be formed by raster scanning the beam across the surface, or using a mask, and the resulting modification depends on the ion fluence. A plane view scanning electron microscopy (SEM) image is shown of a surface irradiated to form various geometric patterns with fluences systematically ranging from 1×10^{12} to 1×10^{15} ions/cm^2 (Figure 6.1 g). Three distinct regimes are observed. At low fluences (left), there is no detectable change in the surface. At high fluences (right), the ion beam ablates the surface, resulting in microscale trenches (e.g. a physical vacuum). The most interesting situation occurs at intermediate fluences where there is a clear change in electron contrast, but the surface is flat down to the nanoscale (see atomic force microscopy later). In this regime, the ion irradiation introduces lattice disorder and mixes atomic Sb/Te sites leading to a situation similar to Figure 6.1 b/c. The change in the atomic structure leads to modified contrast in the electron backscattering diffraction (EBSD) maps (Figure 6.1 h), which probe the surface crystal structure from the exit beam Kikuchi diffraction patterns within the first few nanometers near the surface [42-44]. The irradiated regions become amorphous as shown by the lack of Kikuchi patterns, whereas the unirradiated surface is crystalline (Figure 6.1 i and j). The pattern for the unirradiated points can be indexed to the crystalline unit cell of $R\bar{3}c$ ordered Sb_2Te_3 (the Figure *5.14* in Chapter 5 contains a full EBDS band map, Euler orientation and elemental map). In contrast, the highly irradiated region shows a featureless pattern (Figure 6.1 j) characteristic of a non-crystalline structure. The disappearance of Kikuchi bands, together

with the loss of lattice fringes in the STEM imaging (Figure 6.1b) shows the system transitions to the amorphous state only where it has been impacted by the ion beam irradiation. This demonstrates that it is possible to precisely engineer an amorphous phase transition in a local surface region whilst preserving the surrounding crystallinity which is a prerequisite for well-controlled lithographic patterning.

The ion-beam patterned regions show strongly modified electronic properties, as detected using conductive atomic force microscopy (cAFM) and standard transport measurements (see below). cAFM has the advantage of mapping the local conductivity, which can be also correlated with the physical topography (height). For this purpose, a grid of squares was patterned on the Sb2Te3 using fluences near the amorphization threshold (Figure 6.2 a). The fluence applied to each of the grid points was varied systematically. The squares irradiated with higher fluences show significantly lower conductivity (Figure 6.2 b) and the observed currents are vanishingly small (pA, at the instrumentation limit). These insulating regions appear dark on the current map. In contrast, unirradiated or lightly irradiated regions (fluence < 6.24×10^{13} ions/cm) exhibit currents which are 2-3 orders of magnitude larger (nA) for the same scanning bias (1-2.2 V), indicating a highly conductive surface. The current map shows a clear step function in behavior with Ga ion fluence. Grids irradiated with fluences above 1.87×10^{14} ions/cm^2 (8 keV incident energy), show a dramatic decrease in conductivity. This step function behavior is attributed to the point where the amorphous layer, observed by the EBSD and STEM in Figure 6.1, becomes sufficiently thick to disrupt the electronic transport through the surface regions. Importantly, the remarkably large change in the surface conductivity occurs in the room temperature data in Figure 6.2 f which implies a radical change in the electronic structure, rather than a minor doping effect. As a consequence of the cAFM measurement geometry, any observed current must flow both through the bulk and surface regions of the crystal, and both in-plane and out-of-plane currents may contribute, depending on the position of the tip relative to the pattern. We therefore conclude that both the surface and the bulk of the amorphous Sb_2Te_3 irradiated regions become highly insulating, consistent with the collapse of the topological bulk state into a trivial insulator. To provide complementary insights into the electronic properties, simple four-probe devices were made by extracting a small and thin (640 nm-thick) rectangular region from the crystalline Sb_2Te_3 surface using a nanomanipulator. A custom FIB-lift out procedure was developed to transfer crystalline Sb_2Te_3 chips to a premade set of contacts (inset in Figure 6.2 f) whilst

preserving the crystallinity of the surfaces (i.e., the top and bottom surfaces are virgin, unexposed to an ion beam). At these thicknesses, the surface-region transport is expected to account for a substantial fraction of the overall conductivity. The chip was transferred to a cryostat and measurements of resistivity shows the nearly metallic behavior commonly found in crystalline Sb_2Te_3 (Figure 6.2 f). The chip was subsequently transferred back to the focused ion-beam mill and the entire top surface was exposed to a high Ga dose, before remeasuring the resistance. The same device after ion beam amorphization had a resistance that was two orders of magnitude higher than in the unirradiated state at 3 K. Moreover, in contrast to crystalline Sb_2Te_3, the resistance of amorphous Sb_2Te_3 increased with decreasing temperature. This is a signature of a trivial insulator ($\mathbb{Z}_2$=0), since topological states would be expected to introduce a resistivity plateau. As the FIB devices have a parallel bulk conduction channel from the residual crystalline region (see *Figure 5.18*Chapter 5), we also reproduced these findings for MBE-grown ultra-thin Sb2Te3 films on insulating alumina finding that, in the absence of the bulk channel there is an even more impressive increase in resistance (see

Figure 5.19 Chapter 5). Similar high-resistance states have been reported in the literature for Sb_2Te_3 thin films in phase change memory devices [38],[39],[40]. Together with the cAFM observation, the direct transport measurements strongly suggest the irradiated amorphous regions at the A-V boundaries become trivial insulators and therefore form a topological vacuum ($\mathbb{Z}_2$=0) [45].

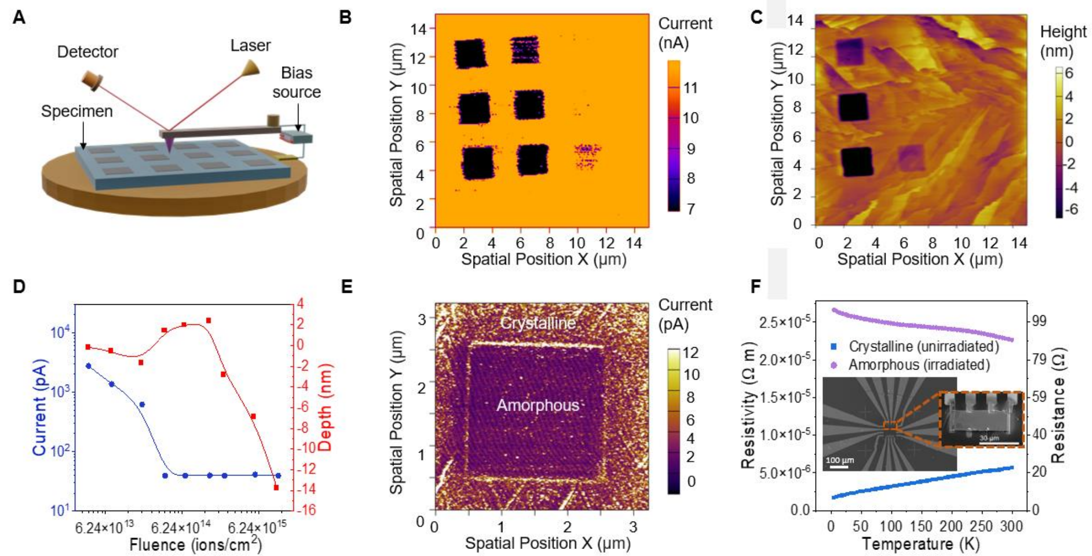

Figure 6.2. The disordered regions modified by the ion beam have a suppressed surface conductivity. (a) Schematic of the AFM configuration showing how current and topography is measured over a patterned region. (b) Mapping of surface currents of a Sb_2Te_3 single

crystal showing that the 3×3 rectangular grid sections, which were modified by the ion beam, are less conducting. Each square received a sequentially increasing ion beam dose. The measurement bias was 2.5 V. (c) Height map over the same region as in (b) showing that topography is modified for higher fluences. (d) Integrated current and height of each Sb_2Te_3 grid point irradiated with increasing dose of Ga^+ ions, measured using cAFM with a scanning bias of 2.2 V. (e) Current mapping using a 1V DC bias for an individual irradiated box (see *Figure 5.9* in Chapter 5 for IV characterization) showing additional conductivity at the edges of the pattern, and on surface terraces. (f) Four-probe temperature-dependent resistance of a Sb_2Te_3 device before and after amorphization, showing the increase resistance. The inset shows the measurement configuration.

The experimental evidence for the insulating 2D A-V boundaries is extremely robust, and it is also supported by the density functional theory (described in a later section) which explains this this on the basis of a topological transition to $\mathbb{Z}_2$=0. The observation of the highly insulating A-V 2D region is the main claim of our work as it appears consistently in all patterned regions above the critical fluence level. There are, however, also interesting secondary effects that occur at many of the 1D A-C boundaries which warrant discussion. Consistent with the $\mathbb{Z}_2$=0 characteristic of the A region and the $\mathbb{Z}_2$=1 region of the C region, the A-C boundary hosts additional edge conductivity as observed in the cAFM image (Figure 6.2 e). This only appears at specific low scanning voltages, (Figure 6.2 e and Figure *5.8* Chapter 5) and is experimentally challenging to detect. We excluded a geometric measurement artifact because the scans were repeated over various regions and in various directions. The additional boundary currents only appeared at low voltages and were electronic in origin as they responded to IV cycling. It is tempting to assign these as quasi-1D edge at the A-C boundary predicted by topological theory. Indeed similar conductivity enhancement was observed at the edges of the terraces of Bi2Se3 where a physical vacuum ($\mathbb{Z}_2$=0) is present[46]. We add the disclaimer that, while the experiment is robust for the A-V boundaries, a great deal more experimental work is required to investigate the A-C boundaries to determine whether the "edge" 1D/2D conductivity is topological. This is because complex geometric, chemical and crystallographic defects at the A-C boundary may potentially introduce trivial electronic states. Nevertheless, from a theoretical perspective, the existence of topological states at the A-C boundary is well-grounded, although we note these states may not be purely 1D, and may also contain a contribution from 2D TI states that wrap around the A-C boundary

and appear as quasi-1D when viewed at the surface. Below we present theoretical modelling that supports the main experimental findings above for the A-V boundary, and also the secondary feature of 1D/2D states at A-C boundaries.

To develop a theory of the topological transition, and model the A-V and A-C interfaces, two approaches were used: density functional theory (DFT) and by solving a model Hamiltonian. Firstly, ab initio molecular dynamics (AIMD) simulations were conducted based on DFT to model the crystalline and amorphous components separately, and the transition between states. DFT is a powerful tool, capable of performing the dual role of modelling glassy structures, and also topological Dirac states in crystals without empirical parameters. Although bulk chalcogenide glasses have been studied using similar methods [47],[48], the past calculations did not include the spin-orbit interaction or surface slab models, so the question of the topological surface states remained unresolved. To directly compare the crystalline and non-crystalline surface/vacuum interface, the starting point was a large Sb_2Te_3 supercell (Figure 6.3 a). High-temperature AIMD was applied to generate a molten state at 1600 K which was quenched to 100 K into the "frozen" glass (for the details see Methods). The resulting structure of the glass compares very well with previously published pair-distribution functions and the model also correctly describes the finite-temperature vibrational density of states, implying a high level of realism in the model. To model the 2D surface states at the A-V and A-C interfaces, an open boundary condition (OBC) was introduced in the z-direction by including a 15 Å vacuum region, and periodic boundary conditions (PBC) were applied in-plane. Using this calculation approach, the electronic density of states (DOS) for the glassy slab structure has a clear bandgap (Fig. 3 a). In contrast, the crystalline starting cell shows in-gap states (Figure 6.3 b) attributed to the Dirac bands, as evident in the full band structure calculated (Figure 6.3 c). It is therefore valid, by induction, to conclude that the Dirac bands present in the crystalline state (Figure 6.3 c) must vanish after amorphization in order to result in the gap observed (Fig. 3 a). This is expected if the system becomes a trivial insulator with $\mathbb{Z}_2=0$. This glassy-electronic transition is intrinsic (as it only required Sb-Te displacements and does not require impurities).

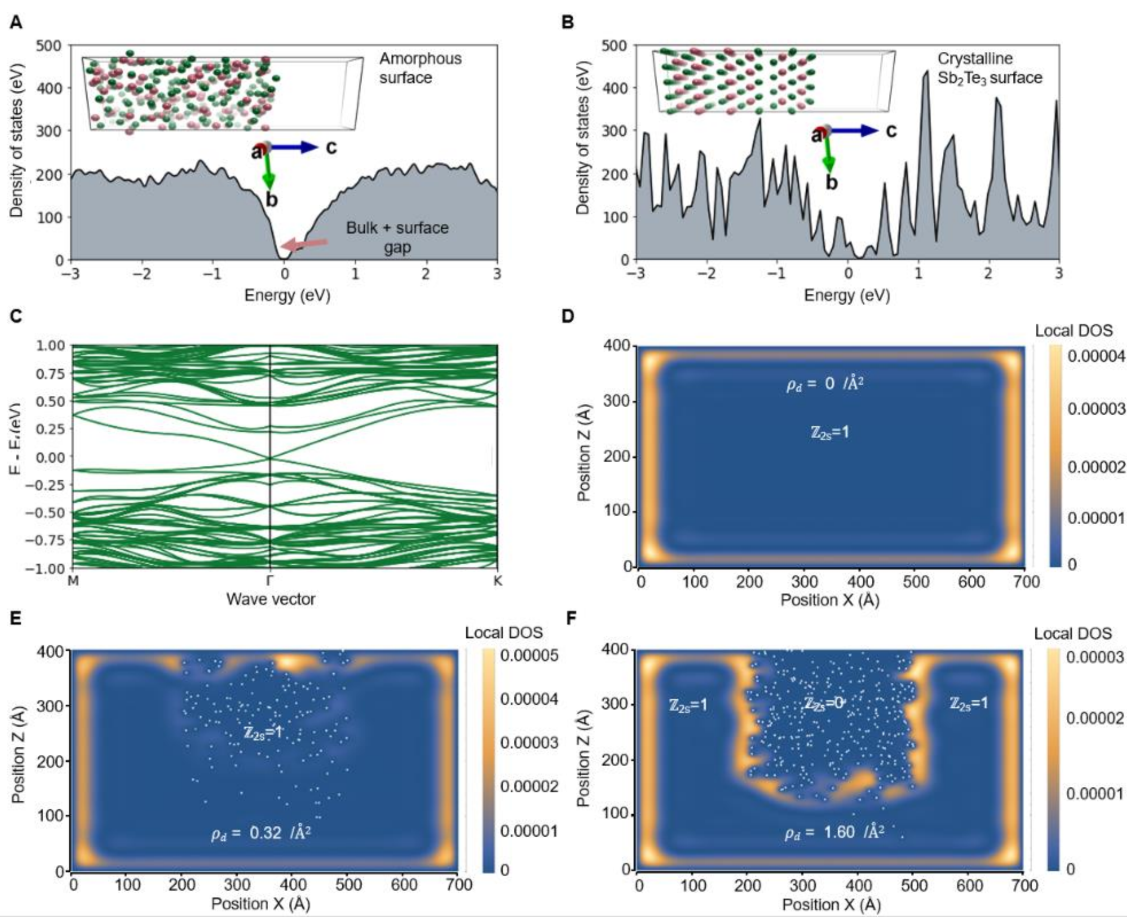

Figure 6.3. Theoretical calculations show that while crystalline Sb_2Te_3 hosts Dirac surface states, the amorphous version does not, consistent with the $\mathbb{Z}_2 = 1 \rightarrow \mathbb{Z}_2 = 0$ transition (a) The electronic density of states of an amorphous Sb_2Te_3 surface exhibits a bandgap with no states crossing the Fermi level. The inset shows the atomic model of the amorphous Sb_2Te_3 surface slab generated from the molecular dynamics quench, used to calculate the electronic structure with a 15 Å vacuum boundary in the c-direction. (b) The electronic density of states of the crystalline Sb_2Te_3 surface has states crossing the Fermi level. The inset shows the crystalline surface slab used to calculate the electronic structure. (c) The band structure of the crystalline surface shows the characteristic Dirac surface states crossing the Fermi level. (d) The real-space image of the defect-free crystal shows the electron density calculated with the model Hamiltonian, and exhibits surface states at the crystal-vacuum interface. (e) A moderate level of defects does not remove the surface state position. Each white dot represents a defect in the system. (f) At a critical threshold of disorder, the disordered region becomes non-topological ($\mathbb{Z}_2$=0) as the surface states then reposition to wrap around the new topological vacuum region.

Additionally, by applying a minimal description of a TI using a model Hamiltonian, it is

possible to show that, if a region becomes topologically trivial due to strong disorder, this will not only remove 2D states at the A-V boundary, but also introduce new 1D/2D states at the A-C n ordered-disordered interfaces resembling some of the features observed experimentally (Figure 6.3 e). To describe the amorphous-crystalline boundary theoretically, a model Hamiltonian was introduced, starting from the accepted standard model of a fully crystalline TI [4], [49].

$$H_{TI} = \begin{bmatrix} m(k) & Bk_z & 0 & A\,k_- \\ Bk_z & -m(k) & Ak_- & 0 \\ 0 & Ak_+ & m(k) & -Bk_z \\ Ak_+ & 0 & -Bk_z & -m(k) \end{bmatrix} \tag{1}$$

where $m(k) = m_0 + m_1 k_z^2 + m_2\left(k_x^2 + k_y^2\right)$. The k.p parameters are taken from Ref. [50]. To solve the eigenproblem, a multi-band envelope function and finite-element method was used. For a pristine, defect free TI crystal surrounded by physical vacuum, this model produces the well-known surface states as shown in Fig. 3 d. Non-magnetic disorder was then introduced to this Hamiltonian to model the impact of the ion beam using a disorder potential:

$$V_{im}(r_i) = \sum_{i=1,N} v_i f(r - r_i) \tag{2}$$

where v_i is the local potential which is assumed to be much larger than the bulk bandgap [28], and $f(r)$ is a range function (for simplicity assumed to be a cubic box potential, width of 3-5 Å). The total Hamiltonian was thus given by:

$$H = H_{TI} + V_{im} \tag{3}$$

To model irradiation-induced damage similar to the experiment, we assume an ensemble of defects, with a probabilistic distribution in space according to a Gaussian in the vertical z −direction with a peak at 20 nm and width of 10 nm, approximating the experimental depth and Monte Carlo simulations for the Ga implantation. The resulting calculations show that the location of the surface state depends closely on the distribution of the defects, and the defect density ρd. For zero defects, the surface state only exists around the edges of the virtual crystal (Figure 6.3 d) at the physical crystal-vacuum boundary. A small percentage of defects does not modify this, and the surface state at the disordered region is still mostly intact and localized near the physical crystal-vacuum boundary (Figure 6.3 e). For high defect densities (Figure 6.3 f), however, the disordered region undergoes a quantum transition into an (Anderson) insulating layer. This converts the

defective area into a "topological vacuum" such that the surface state now is shifted away from the physical vacuum, and instead traces the boundaries of the new effective vacuum region. Notably, the surface state is not destroyed, instead, new states are formed underneath at the effective surface spanning the $\mathbb{Z}2=1|0$ boundary. Importantly as these new states trace the outline of the disordered region, they will yield additional conductivity along the edge of an ion beam-patterned region. The new states at the A-C boundary include the standard 2D surface state, but can also contain additional 1D states that form at the edge of the pattern, depending on the depth of the disordered region, thereby introducing a new source of conductivity not present in the unpatterned surface. This is qualitatively consistent with the cAFM measurements.

6.4 Discussion

Both experiment and theory provide a strong argument that a $\mathbb{Z}_{2s}=1 \rightarrow \mathbb{Z}_{2s}=0$ transition occurs when crystalline Sb_2Te_3 is amorphized. The 2D topological surface states, which are present at the planar C-V boundary are destroyed by the non-periodic disorder which converts the region to an A-V boundary via ion beam processing. Thus our finding appears to be the first experimental proof that directly verifies earlier predictions concerning the level of topological protection against non-periodic non-magnetic disorder, namely that strong bulk disorder can lead to a quantum transition into a non-topological state [28]. Additionally, as a secondary point, there is some preliminary evidence for the existence of new "quasi-1D" states at the lateral A-C interfaces. Based on the theory, it is likely that these states contain a topological contribution, however future work is needed to establish whether chemical and crystallographic effects introduce trivial electronic states. Even if these 1D A-C states are topological, they are a byproduct of the crystalline nature of one side of the interface, and thus do not modify our central claim about the non-topological nature of the 2D A-V interface. In terms of technological implications, ion beams were theoretically proposed as a promising method to engineer the topological conductivity [22], and our work shows how this is implemented in practice. Aside from lateral patterning, the ability to create vertical A-C boundaries with ion beam irradiation could potentially open a way to control buried topological states to yield functionality that is fundamentally different from junctions in traditional electronics. While electron irradiation has also been recently explored in Tis [51], there is a

compelling reason to use ions rather than electrons for lateral and vertical patterning: the relative difference in inelastic scattering cross-sections makes it possible to create a much greater impact in a much smaller volume with ions to allow finer feature size and controlled amorphization. Feature size is a key goal for CMOS-compatible fabrication, where ion beams remain an "industry standard" tool [52, 53]. Our initial work has mostly used a focused ion beam to implement patterning, as FIBs are readily available at most laboratories worldwide and enable rapid prototyping to test new principles in topological electronics. To this end, past work has established that FIBS can be used to achieve a variety of geometries and device functionalities in other topological materials [54],[55], however our work appears to be the first systematic study on the electronic effects of ion-beam amorphization in topological insulators. However, in practice, it is not practical to use a FIB to pattern a large (wafer-sized) area. For large (cm^2) scale irradiation, it is better to use standard accelerator-based broad ion beams in combination with lithography. In the section 5.5.6 in Chapter 5, we have demonstrated that cm2-sized films can be amorphized using a 40 keV accelerator-based broad ion beam, showing that the underlying mechanism is identical to that in the FIB. This controlled functionality offers great opportunities for engineering the surface of TIs. In conventional silicon technology, the challenge is combining ion beams with photolithography to approach the 3-10 nm feature size. Our process was the first attempt and is far from optimized, but the cross-sectional TEM and Monte Carlo calculations show that we can already experimentally achieve vertical dimensions smaller than 20 nm, so with advanced lithography, this technique could foreseeably grant access to the sub-10 nm regime.

6.5 Methods

Crystal growth: The Sb_2Te_3 single crystal growth method is described in reference[41]. X-ray diffraction patterns confirmed the single-phase nature of Sb_2Te_3 possessing a rhombohedral crystal structure. The single crystal Sb_2Te_3 was cleaved using adhesive tape to expose a fresh and visually flat c-plane. Subsequent exfoliations for devices were done in the vacuum environment of the FEI HELIOS G3 microscope.

Focused ion beam irradiation: The surface of Sb_2Te_3 was irradiated with a gallium focused ion-beam generated within a FEI HELIOS G3 CX microscope at an energy of 8-

30 kV using an ion fluence ranging from 3.74×10^{13} ions/cm^2 to 1.12×10^{16} ions/cm^2. After the Sb_2Te_3 surface was irradiated with a Ga ion beam, electron backscattered diffraction images were obtained using a detector built into the microscope to confirm the amorphous nature of the Sb_2Te_3 surface. EBSD and general SEM imaging were performed on the same instrument. EBSD was conducted at 20 kV and 2.8 nA electron beam current.

Conductive atomic force microscopy: The exfoliated sheet of Sb_2Te_3 was fixed to the chip and transferred onto a magnetic atomic force microscopy holder in air for topography and local electrical characterizations using a commercial scanning probe microscopy (SPM) system (Cypher S, Asylum Research, US). Pt/Cr coated conductive probes (ElectriMulti 75G, BudgetSensors, Bulgaria) with a radius of < 25 nm were used for all the SPM measurements. The current mapping and local I-V measurements were performed under conductive atomic force microscopy (cAFM) mode. The current mapping was acquired by scanning the probe across the selected areas with a DC bias between 2 V and 2.5 V. During I-V measurement, the probe was first engaged at a selected point on the film surface, followed by applying the sweeping bias function of 0V to 1V to -1V to 0V. Additional scans were performed up to 2.5 V.

Computer simulations: Structural simulations and band-structure calculations were performed using density functional theory (DFT) in the Vienna Ab Initio Simulation Package (VASP) version 5.4.452. The calculations used the generalized gradient approximation (GGA) to the exchange-correlation energy as implemented by Perdew et al. (GGA-PBE) [56]. The projector augmented-wave method was used [57-59] and the number of electrons treated as valence was 5 for Sb and 6 for Te. The cutoff energy for the plane-wave basis was 400 eV. The final structures were relaxed until forces converged to better than 0.02 eV/Å and the total energy convergence threshold was 10^{-6} eV. To describe the dispersion forces, the D3 Grimme method with zero damping was found to yield the best agreement with the experimental lattice parameters. For the crystalline models, we used a dense k-point grid equivalent to $x \times x \times n$ in the unit cell, where x ranges from 1-16 k points and n = 16 for 3D models and n=1 for surface models. We found the Dirac surface states were already predicted using a single point in the crystalline models (n=1, x=1). Consequently, the amorphous model calculations were performed as single Γ-point calculations. For the surface models, a 15 Å vacuum slab was introduced to break the periodic boundary conditions in one direction, and slab layers were formed

by cleaving at the van-der Waals gap of the bulk crystal structure which occurs at a specific (001) plane. For molecular dynamics, calculations were performed using ionic relaxation using the same convergence criteria outlined above, except with a single K-point at Γ. Large Sb_2Te_3 supercells ranging from 3×3×2 to 4×4×1 hexagonal cells were constructed using the crystalline starting model. These were heated to 1600 K in the simulation. The temperature was controlled by a Nose-isostat method to model the coupling to the heat bath. Melting occurred over the course of 3 picoseconds. The molten structures were then quenched to 100 K over the course of 12 picoseconds, using a time step of 2 femtoseconds. The mean-squared displacements and vibrational density of states of the DFT model were calculated by analyzing the trajectory using the nMoldyn software. This confirmed that the vibrational density of states accurately reproduced experimental measurements, and the ions did not diffuse at 100 K in the amorphous state. To generate fully optimized structures, additional 0 K relaxation with a higher convergence criterion was applied at the final step using a conjugate gradient method. The spin-orbit interaction was included when calculating the density of states and electronic band structure. Calculations were performed on the GADI supercomputer, which is part of the Australian National Computer Infrastructure.

References

1. Bake, A., et al., *Top-down patterning of topological surface and edge states using a focused ion beam.* Nature Communications, 2023. **14**(1): p. 1693.

2. Hasan, M.Z. and C.L. Kane, *Colloquium: topological insulators.* Reviews of Modern Physics, 2010. **82**(4): p. 3045.

3. Kane, C.L. and E.J. Mele, *Quantum spin Hall effect in graphene.* Physical Review Letters, 2005. **95**(22): p. 226801.

4. Zhang, H., et al., *Topological insulators in Bi_2Se_3, Bi_2Te_3 and Sb_2Te_3 with a single Dirac cone on the surface.* Nature Physics, 2009. **5**(6): p. 438-442.

5. Chadov, S., et al., *Tunable multifunctional topological insulators in ternary Heusler compounds.* Nature Materials, 2010. **9**(7): p. 541-545.

6. Slager, R.-J., et al., *The space group classification of topological band-insulators.* Nature Physics, 2013. **9**(2): p. 98-102.

7. Otrokov, M.M., et al., *Prediction and observation of an antiferromagnetic topological insulator.* Nature, 2019. **576**(7787): p. 416-422.

8. Cornfeld, E. and S. Carmeli, *Tenfold topology of crystals: Unified classification of crystalline topological insulators and superconductors.* Physical Review Research, 2021. **3**(1): p. 013052.

9. Narang, P., C.A. Garcia, and C. Felser, *The topology of electronic band structures.* Nature Materials, 2021. **20**(3): p. 293-300.

10. Kane, C.L. and E.J. Mele, *Z_2 topological order and the quantum spin Hall effect.* Physical Review Letters, 2005. **95**(14): p. 146802.

11. Fu, L. and C.L. Kane, *Topological insulators with inversion symmetry.* Physical Review B, 2007. **76**(4): p. 045302.

12. Fu, L., C.L. Kane, and E.J. Mele, *Topological insulators in three dimensions.* Physical Review Letters, 2007. **98**(10): p. 106803.

13. Shiozaki, K., M. Sato, and K. Gomi, *Topology of nonsymmorphic crystalline insulators and superconductors.* Physical Review B, 2016. **93**(19): p. 195413.

14. Khalaf, E., et al., *Symmetry indicators and anomalous surface states of topological crystalline insulators.* Physical Review X, 2018. **8**(3): p. 031070.

15. Bradlyn, B., et al., *Topological quantum chemistry.* Nature, 2017. **547**(7663): p. 298-305.

16. Vergniory, M., et al., *A complete catalogue of high-quality topological materials.* Nature, 2019. **566**(7745): p. 480-485.

17. Vergniory, M.G., et al., *All Topological Bands of All Stoichiometric Materials.* Science, 2022.

18. Aroyo, M.I., et al., *Bilbao Crystallographic Server: I. Databases and crystallographic computing programs.* 2006. **221**(1): p. 15-27.

19. Nadeem, M., et al., *Overcoming Boltzmann's Tyranny in a Transistor via the Topological Quantum Field Effect.* Nano Letters, 2021. **21**(7): p. 3155-3161.

20. Breunig, O. and Y. Ando, *Opportunities in topological insulator devices.* Nature Reviews Physics,

2021: p. 1-10.

21. Xu, Y., I. Miotkowski, and Y.P. Chen, *Quantum transport of two-species Dirac fermions in dual-gated three-dimensional topological insulators.* Nature Communications, 2016. **7**(1): p. 11434.

22. Sacksteder, V., T. Ohtsuki, and K. Kobayashi, *Modification and control of topological insulator surface states using surface disorder.* Physical Review Applied, 2015. **3**(6): p. 064006.

23. Lee, W.J., et al., *Possible permanent Dirac-to Weyl-semimetal phase transition by ion implantation.* NPG Asia Materials, 2022. **14**(1): p. 1-8.

24. Cortie, D., et al., *Creating thin magnetic layers at the surface of Sb2Te3 topological insulators using a low-energy chromium ion beam.* Applied Physics Letters, 2020. **116**(19): p. 192410.

25. Agarwala, A., *Topological insulators in amorphous systems.* Physical Review Letters, 2017. **118**: p. 236402.

26. Mitchell, N.P., et al., *Amorphous topological insulators constructed from random point sets.* Nature Physics, 2018. **14**(4): p. 380-385.

27. Wang, C., et al., *Structural Amorphization-Induced Topological Order.* Physical Review Letters, 2022. **128**(5): p. 056401.

28. Schubert, G., et al., *Fate of topological-insulator surface states under strong disorder.* Physical Review B, 2012. **85**(20): p. 201105.

29. Agarwala, A., *Topological insulators in amorphous systems*, in *Excursions in Ill-Condensed Quantum Matter*. 2019, Springer. p. 61-79.

30. Costa, M., et al., *Toward realistic amorphous topological insulators.* Nano letters, 2019. **19**(12): p. 8941-8946.

31. Mansha, S. and Y.D. Chong, *Robust edge states in amorphous gyromagnetic photonic lattices.* Physical Review B, 2017. **96**(12): p. 121405.

32. Zhou, P., et al., *Observation of photonic antichiral edge states.* Physical Review Letters, 2020. **125**(26): p. 263603.

33. Biesenthal, T., et al., *Fractal photonic topological insulators.* Science, 2022: p. eabm2842.

34. Focassio, B., et al., *Amorphous Bi_2Se_3 structural, electronic, and topological nature from first principles.* Physical Review B, 2021. **104**(21): p. 214206.

35. Corbae, P., et al., *Evidence for topological surface states in amorphous Bi_2Se_3.* arXiv preprint arXiv:1910.13412, 2019.

36. Barton, A.T., et al., *Impact of etch processes on the chemistry and surface states of the topological insulator Bi_2Se_3.* ACS Applied Materials & Interfaces, 2019. **11**(35): p. 32144-32150.

37. Korzhovska, I., et al., *Spin memory of the topological material under strong disorder.* npj Quantum Materials, 2020. **5**(1): p. 39.

38. Jacobs-Gedrim, R.B., et al., *Reversible phase-change behavior in two-dimensional antimony telluride (Sb_2Te_3) nanosheets.* Applied Physics Letters, 2018. **112**(13): p. 133101.

39. Ding, K., et al., *Recipe for ultrafast and persistent phase-change memory materials.* NPG Asia Materials, 2020. **12**(1): p. 63.

40. Li, Z., et al., *Yttrium-Doped Sb_2Te_3: A Promising Material for Phase-Change Memory.* ACS Applied Materials & Interfaces, 2016. **8**(39): p. 26126-26134.

41. Zhao, W., et al., *Quantum oscillations in iron-doped single crystals of the topological insulator Sb_2Te_3.* Physical Review B, 2019. **99**(16): p. 165133.

42. Rice, K.P., R.R. Keller, and M.P. Stoykovich, *Beam Broadening in Transmission EBSD.* Microscopy Today, 2015. **23**(2): p. 32-37.

43. Sneddon, G.C., P.W. Trimby, and J.M. Cairney, *Transmission Kikuchi diffraction in a scanning electron microscope: A review.* Materials Science and Engineering: R: Reports, 2016. **110**: p. 1-12.

44. Wilkinson, A.J. and T.B. Britton, *Strains, planes, and EBSD in materials science.* Materials Today, 2012. **15**(9): p. 366-376.

45. Liu, B., et al., *Y-doped Sb_2Te_3 phase-change materials: toward a universal memory.* ACS Applied Materials Interfaces, 2020. **12**(18): p. 20672-20679.

46. Macedo, R.J., et al., *Nanoscale probing of local electrical characteristics on MBE-grown Bi_2Te_3 surfaces under ambient conditions.* Nano Letters, 2015. **15**(7): p. 4241-4247.

47. Caravati, S., M. Bernasconi, and M. Parrinello, *First-principles study of liquid and amorphous Sb_2Te_3.* Physical Review B, 2010. **81**(1): p. 014201.

48. Guo, Y.R., et al., *Structural signature and transition dynamics of Sb_2Te_3 melt upon fast cooling.* Physical Chemistry Chemical Physics, 2018. **20**(17): p. 11768-11775.

49. Liu, C.-X., et al., *Model Hamiltonian for topological insulators.* Physical Review B, 2010. **82**(4): p. 045122.

50. Nechaev, I.A. and E.E. Krasovskii, *Relativistic k.p Hamiltonians for centrosymmetric topological insulators from ab initio wave functions.* Physical Review B, 2016. **94**(20): p. 201410.

51. Friedensen, S.E., et al., *Transmission Electron Microscope Nanosculpting of Topological Insulator Bismuth Selenide.* ACS Nano, 2018. **12**(7): p. 6949-6955.

52. Hamm, R.W., *Industrial Accelerators and Their Applications*. 2012: World Scientific 436.

53. Lian, Y., *Semiconductor Microchips and Fabrication: A Practical Guide to Theory and Manufacturing*. 2022: Wiley / IEEE Press.

54. Moll, P.J.W., et al., *Transport evidence for Fermi-arc-mediated chirality transfer in the Dirac semimetal Cd3As2.* Nature, 2016. **535**(7611): p. 266-270.

55. Friedensen, S., J.T. Mlack, and M. Drndić, *Materials analysis and focused ion beam nanofabrication of topological insulator Bi_2Se_3.* Scientific Reports, 2017. **7**(1): p. 13466.

56. Perdew, J.P., K. Burke, and M. Ernzerhof, *Generalized gradient approximation made simple.* Physical Review Letters, 1996. **77**(18): p. 3865.

57. Kresse, G. and J. Furthmüller, *Efficient iterative schemes for ab initio total-energy calculations using a plane-wave basis set.* Physical Review B, 1996. **54**(16): p. 11169.

58. Kresse, G. and J. Furthmüller, *Efficiency of ab-initio total energy calculations for metals and semiconductors using a plane-wave basis set.* Computational Materials Science, 1996. **6**(1): p. 15-50.

59. Kresse, G., *Ab initio molecular dynamics for liquid metals.* Journal of Non-Crystalline Solids, 1995. **192**: p. 222-229.

Chapter 7. High temperature magnetic order and superparamagnetism in Mn-doped Sb_2Te_3 topological insulators

The results in this chapter will form a part of a manuscript that is under preparation to be submitted to a journal.

7.1 Overview

Order and disorder have essential effects on the electronic properties of TIs, including disrupting the topological protection and leading to the emergence of localized states. In the previous chapters, we have discussed the effect of strong disorder that can collapse the topological states. In this chapter, contrary to introducing disorder using Ga-ions, we design an ion beam implantation scheme to introduce magnetic order on the surface of Sb_2Te_3 single crystal TIs through controlled Mn ion implantation. Mn ion fluences in the range of 1×10^{15} to 5×10^{16} ions/cm^2 were selected and implanted at the energy of 40 kV which has an implantation depth around 65 nm in Sb_2Te_3. The microstructure and magnetic properties were systematically studied, and magnetometry was used to characterize Sb_2Te_3 from 5 - 300 K. Creating a new form of magnetic order through ion implantation at the surface of TIs is promising as it provides an avenue for the surface order-disorder engineering based TIs application.

7.2 Introduction

The interaction between magnetism and TIs surface states has become an important subject as it may provide a unique way for manipulation of surface electronic transport. Although, TIs said to be immune to certain level of non-magnetic disordering and impurities, the effect of strong disorder is under debate [1-3], and currently less is known about magnetic dopants. Magnetic impurities can break TRS and lead to a gap opening in the surface states due to local magnetic ordering that causes backscattering of surface states. Depending on the strength and type of magnetic order/ disorder introduced into a TI, the TI system can undergo a quantum transition into new state such as an axion insulator, Quantum Anomalous Hall insulator, Chern insulator or a magnetic topological

insulator [4, 5]. However, the chiral symmetry still protects the surface states even in the presence of magnetic impurities which does not completely suppress the surface states in TIs. Furthermore, the surface states in magnetic TIs can exhibit interesting magnetic and transport properties due to the coupling between the magnetic ordering and the surface electrons. This can lead to the emergence of new phenomena such as the quantum anomalous Hall effect (QAHE). Currently all known doping schemes lead to very low magnetic transition temperatures in the TI, making them unsuited for room-temperature applications.

In magnetic tetradymite-type TI materials, the development of a strong out-of-plane magnetization is possible due to the inherent large Van Vleck spin susceptibility of the host TI materials. This robust magnetization can be achieved without the need for itinerant carriers to mediate the magnetic properties [6-8]. Magnetic ordering introduced by doping of transition metal can play the same role as the external magnetic field. In this regard, there are several attempts to study the effects of magnetic doping in Tis [9]. The precise control of the ratio of the multiple elements and Fermi level position in chromium-doped $(Bi,Sb)_2Te_3$ materials system have led to experimental observation of the QAHE [7, 10-12]. Zhang J. et al. theoretically investigated the magnetic properties of V, Cr, Mn, and Fe doped TIs Bi_2Se_3, Bi_2Te_3, and Sb_2Te_3 [13]. Mn doping of TIs could lead to ferromagnetism and opens new doors for study the interplay between magnetism and surface states [14]. Ferromagnetism in $MnSb_2Te_4$ is triggered by the exchange interaction induced by Mn–Sb site exchange in combination with a slight in-plane contraction. The excess Mn on Sb sites enhance the ferromagnetic interactions, leading to an increase of the Curie temperature. Moreover, the spin-orbit interaction in $MnSb_2Te_4$ compared to $MnBi_2Te_4$ is sufficiently large to maintain both the band inversion and the perpendicular magnetic anisotropy. This makes $MnSb_2Te_4$ highly favorable for the QAHE and other topology-based device applications as the critical temperature is twice as large as for $MnBi_2Te_4$ and the Dirac point is close to Fermi Energy (E_F) [15]. A study by Vergniory M. G. et al have shown that the magnetic interaction is long-range and mediated out of plane by double exchange mechanism in transition metal doped Bi_2Se_3, Bi_2Te_3 and Sb_2Te_3 [16].

Nevertheless, there is currently no unanimous agreement regarding the specific magnetic order exhibited by similar materials system, with some studies suggesting

ferromagnetism [17], while others report its absence [18], and yet others indicate the presence of diamagnetism [19]. The discrepancies could be due to complex interactions among magnetic atoms within the 3D TIs bulk and their surroundings, which could contain various defects at different lattice positions. In this study, we present a systematic ion beam doped Mn into the surface of Sb_2Te_3 with the Mn fluence in the range of 1×10^{15} to 5×10^{16} ions/cm^2 at 40 kV ion beam energy. Ion beam induced damage is characterised by scanning transmission electron microscopy (STEM). A systematic investigation in the magnetic properties reveal that the existence of a complex magnetic order up to room temperature. We also show that the direct or implantation through mask can be used for engineering order and disorder at the surface of TIs. Through our study, we show that ion implantation is a promising way for building new types of devices designs and lateral/vertical heterostructures through design of implantation masks.

7.3 Synthesis and structural characterisation

High quality crystals were grown in our lab with a method described in Ref. [20]. Mn ions were implanted into the surface of Sb_2Te_3 using a low energy ion beam implanter (LEII) at room temperature conditions with implantation energy of 40 keV and the fluence of 1×10^{15},5×10^{15},1×10^{16}, 2×10^{16}, and 5×10^{16} ions/cm^2, respectively. First, energy dispersive spectroscopy analysis in a scanning electron microscopy (JEOL JEM-9400LV) was used to confirm the successful implantation of Mn ions. Figure 7.1 a-d show a representative uniform Mn doping in EDS analysis of $2\text{x}10^{16}$ ions/cm^2 Mn-Sb_2Te_3, whereas all 5 samples did not show any surface chipping or detectable Mn implant agglomeration at the Sb_2Te_3 surface. Here, the purpose of EDS analysis is to qualitatively confirm the successful and uniform implantation of Mn in Sb_2Te_3 without a capping or buffering layer. Figure 7.1 e clearly shows the Mn Kα peaks around 5.9 keV and 0.8 at% Mn detected for 2×1016 ions/cm^2 Mn-Sb_2Te_3. All three Mn-Sb_2Te_3 samples with Mn fluence of 1×10^{16}, 2×10^{16}, and 5×10^{16} ions/cm^2 show convincing Mn Kα peaks to confirm Mn implant. Whereas two samples with lowest Mn fluence of 1×10^{15}, 5×10^{15} show no detectable Mn even in samples tilted to 50° due to very low concentration of Mn. Here Mn at% from EDS is a qualitative method for confirming the presence of the Mn-implanted layer, however the quantitative atomic percentages are only an estimate, because the Mn ions only implant within the region of up to 60 nm deep, while X-ray generation depth can be up to 400 nm in Sb_2Te_3 at the electron beam energy of 10 kV, as

shown in Figure 7.1 f. Selecting a reasonable electron beam energy is important during EDS analysis to detect the characteristic X-ray. Figure 7.1 f shows that tilting the specimen to a higher angle at the specific electron beam energy brings the X-ray generation depth much closer to the surface (with a significant increase in X-ray intensity). Table *7.1.* shows the Mn at% comparison at the specimen tilt of 0° and 50°. As expected, at higher specimen tilt of 50°, Mn at% increase due to peak X-ray intensity generation depth within the 100 nm region.

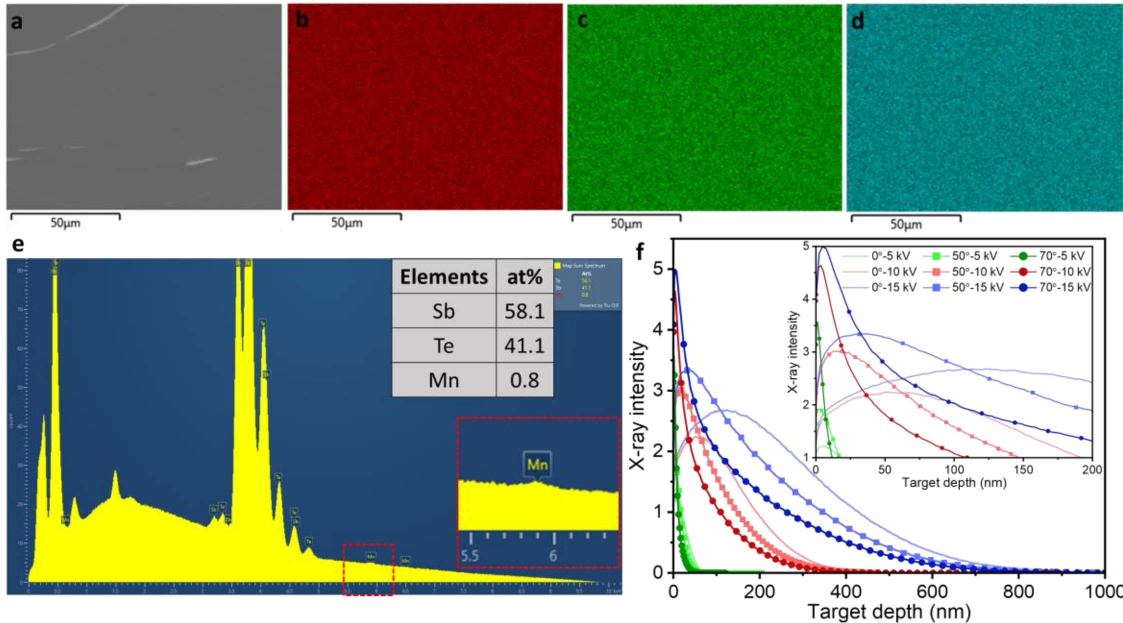

Figure 7.1. EDS analysis of the 2×10^{16} Ions/cm^2 Mn doped Sb_2Te_3 at 0° tilt. a. SE image displays the region analysed by EDS. b-d. EDS elemental mapping for Sb, Te, Mn, respectively. e. EDS spectroscopy clearly shows the Mn K_α peak. f. X-ray intensity and generation depth in Sb_2Te_3 for different beam energy at various specimen tilt.

Table 7.1. Mn atomic percentage (at%) and elemental composition of Mn-Sb_2Te_3.

Specimen tilt	**at% at 0° specimen tilt**			**at% at 50° specimen tilt**		
Mn dose (ions/cm^2)	**Sb**	**Te**	**Mn**	**Sb**	**Te**	**Mn**
$5x10^{16}$	56.9	40.9	2.2	56.3	40.6	3.1
$2x10^{16}$	58.1	41.1	0.8	58.2	40.8	1.1
$1x10^{16}$	58.6	41.1	0.3	58.5	40.8	0.7

The EDS analysis presented above therefore demonstrates that Mn ions can be successfully implanted into the surface of Sb_2Te_3. Figure *7.2* further shows that magnetic patterning of TIs surfaces can be achieved through a specially designed mask, which is a

promising way to introduce order at the desired region in TIs. Figure *7.2* a shows a Cu grid used as a mask before implanting Mn onto the surface of Sb_2Te_3. The secondary electron (SE) image, after the gird has been removed, in Figure 2 b shows the surface of Sb_2Te_3 after being implanted with an Mn ion beam at the energy of 40 kV, and ion fluence of 3×10^{16} ions/cm^2. The inset SE image in Figure *7.2* b and the SE image in Figure *7.2* c show a clear contrast between the Mn implanted region (darker) and the unimplanted region (brighter). EDS mapping is from the area shown in Figure *7.2* c, and elemental mapping Mn, Sb and Te are shown in Figure *7.2* d,e, and f, respectively. Mn elemental mapping in Figure *7.2* d confirms that Mn is implanted within the specific area and there is no detectable diffusion of Mn throughout the surface. The implementation of magnetic ion beam implantation offers the potential for custom fabrication of device functionalities that can be controlled by a magnetic field.

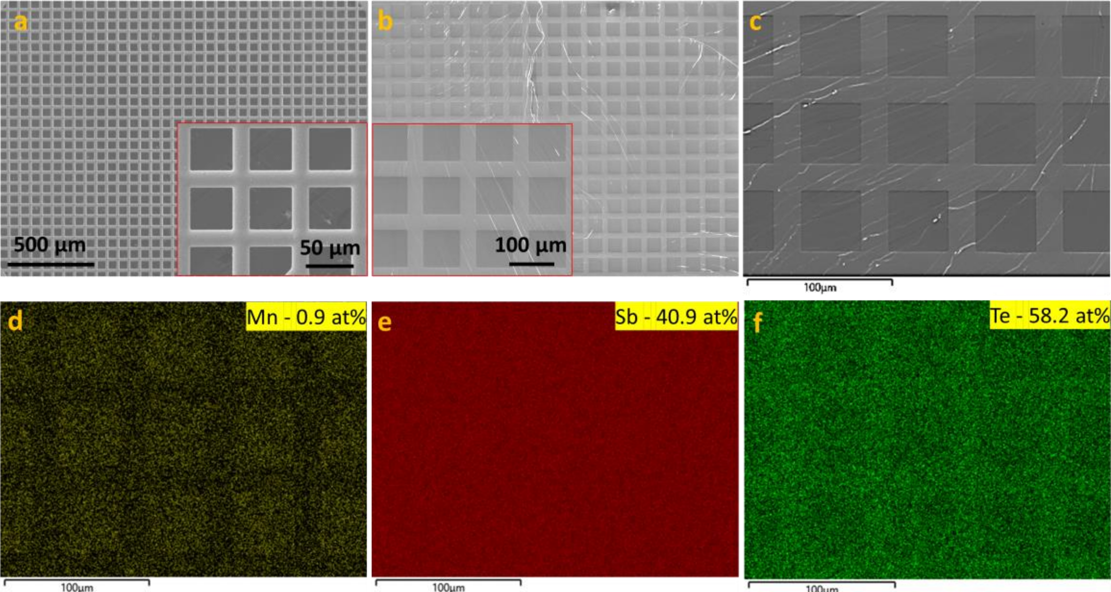

Figure 7.2. Magnetic patterning of Sb_2Te_3 surfaces. a. SEM image of a Cu grid used for implanting Mn through the Cu grid. b. SEM image of Sb_2Te_3 surface patterned through the Cu grid with Mn implantation at energy of 40 kV, and fluence of 3×10^{16} ions/cm^2. c. SEM image of the region where EDS mapping was acquired. d-f. EDS elemental mapping for Mn, Sb, and Te, respectively.

Figure *7.3* a shows the XPS survey scan for all five Mn-Sb_2Te_3 samples. Figure *7.3* b shows the characteristic Mn 2p core level binding energy spectra. The Mn-Sb_2Te_3 sample with the lowest Mn fluence (1×10^{15} ions/cm^2) shows no clear formation of the peak for Mn 2P scan. However, as Mn implantation fluence is increased in the other samples, the peaks from Mn 2P are more prominent. The asymmetric and broad peaks imply the presence of multiple oxidation states of Mn near the Sb_2Te_3 surface. 5x10^{16} ions/cm^2 Mn-doped Sb_2Te_3 sample Mn 2P scan spectra were selected for fitting the data, as shown in

Figure *7.3* c. Based on the peak fitting results and comparing values reported in the literature, Gaussian fitting for Mn 2p3/2 spectral peaks, we obtain binding energies of 641.80 and 640.55 eV, corresponding to the oxidation state of Mn^{4+}, Mn^{3+} and the other minor peak observed at a higher energy of 645.85 eV, which originates from the MnO satellite peak (shake-up peak) Mn^{2+}. Another major peak for Mn 2p1/2 at 653.28 eV, corresponds to oxidation states of Mn^{2+}. Therefore, the core level binding energy spectra of Mn 2p confirm the presence of Mn^{2+}, Mn^{3+} and Mn^{4+}oxidation states in the near-surface area of Mn-doped Sb_2Te_3 [21]

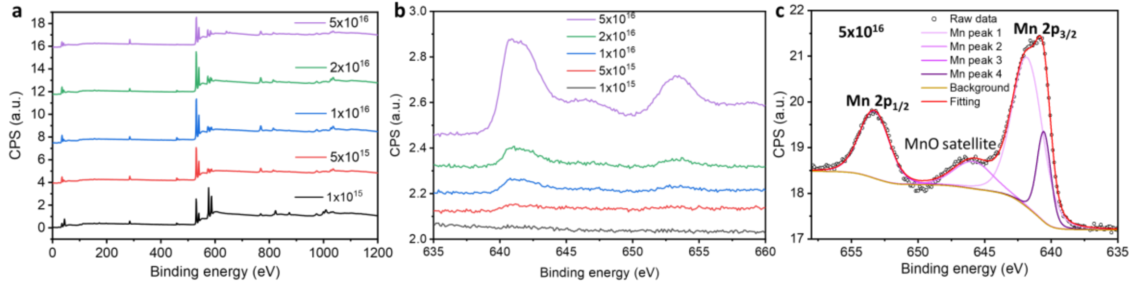

Figure 7.3. X-ray photoelectron spectroscopy analysis of Mn-Sb_2Te_3. a. XPS survey scan for all five Mn-Sb_2Te_3 samples, b. Mn 2p spectra, and c. fitting of Mn 2p spectrum of the Mn-Sb_2Te_3 with Mn implantation fluence of 5×10^{16} ions/cm^2.

A FIB lamella was carefully prepared from the 2×10^{16} ions/cm^2 Mn-Sb_2Te_3 sample following the lamella preparation method developed for ion-beam sensitive crystals to avoid introducing structural ion-beam damage [22]. The FIB lamella TEM imaging and EDS analysis were performed using a JEOL F200 TEM. Figure *7.4* a and c show that an approximately 65 nm deep region from the surface of Sb_2Te_3 has been amorphised. At the same time, some fragments of crystallinity remains in a few scattered regions in top 65 nm amorphous region, as shown in Figure *7.4* b. HRTEM image taken beneath the Mn implanted region shows a quintuple layered (5 atomic layers) structure in Figure *7.4* d. Figure *7.4* f Mn element mapping shows that Mn is primarily implanted in the depth up to 50-60 nm which is clear from the Mn at% concentration change from the line scan in Figure *7.4*i. The Monte Carlo SRIM calculation performed for 10^5 Mn ions confirms that the majority of Mn ions are within the region of 60 nm depth, as illustrated by Figure *7.4* j. In fact, some Mn ions could penetrate slightly deeper than 65 nm in Sb_2Te_3 (Figure *7.4* j); however, the number of Mn ions is insufficient to further below 65 nm to amorphise the region, as only a small fraction penetrates so deeply. Past experimental work has also demonstrated that ion beam implantation could cause disorder or amorphization, hence a

limiting factor on achieving magnetic order with ion beams are the possible formation of amorphous layer.

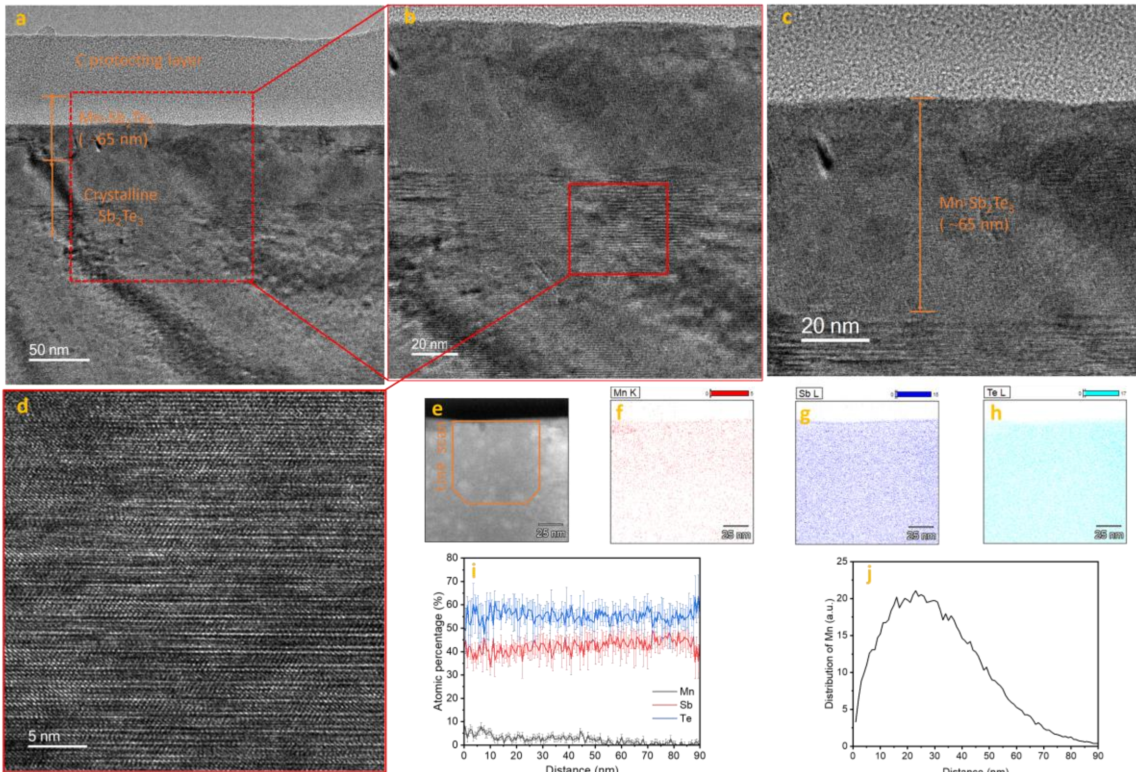

Figure 7.4. TEM imaging and EDS analysis performed on a 2×10^{16} ions/cm^2 Mn-Sb_2Te_3 sample. a-c. TEM images from different regions on the lamella. d. The HRTEM image taken from the region shown in b shows the quintuple layered structure of Sb_2Te_3. f-h. EDS mapping analysis from the region shown in e. i. EDS line scan as shown in e. SRIM calculation showing Mn distribution in Sb_2Te_3 calculated for 10^5 Mn ions.

7.4 Magnetic properties

Systematic vibrating sample magnetometry measurements (on a DynaCool 9T PPMS) have been performed for all five samples doped with Mn fluence ranging from 1×10^{15} to $1\text{x}10^{16}$ ions/cm^2. Only the sample with the lowest Mn implantation dose (1×10^{15} ions/cm^2) showed no magnetic feature or negligible magnetization, only exhibiting the strong diamagnetic signal negatively sloped linear response characteristics which is intrinsic to undoped Sb_2Te_3. Whereas all four samples with Mn implantation fluences in the range of 5×10^{15} to 5×10^{16} ions/cm^2 show a small positive non-linear signal superimposed on the diamagnetic response, as shown in top left inset figures (axis labels same as Figure *7.5*) in Figure *7.5* a-d before diamagnetic background subtraction. Figure

7.5 a-d show the possible ferromagnetic/superparamagnetic behaviour of Mn-Sb_2Te_3 samples after diamagnetic background subtraction. Diamagnetic background determined via fitting high field slope at 300 K and has been subtracted from data measured at all temperatures. Observable magnetic coercive-field formation at low temperatures (⩽100 K) might imply ferromagnetic ordering. The inset figures in the bottom left (axis labels same as Figure *7.5* with x-axis in Oe) in Figure *7.5* a-d show the enlarged area for the magnetic hysteresis loop for 5 and 300 K.

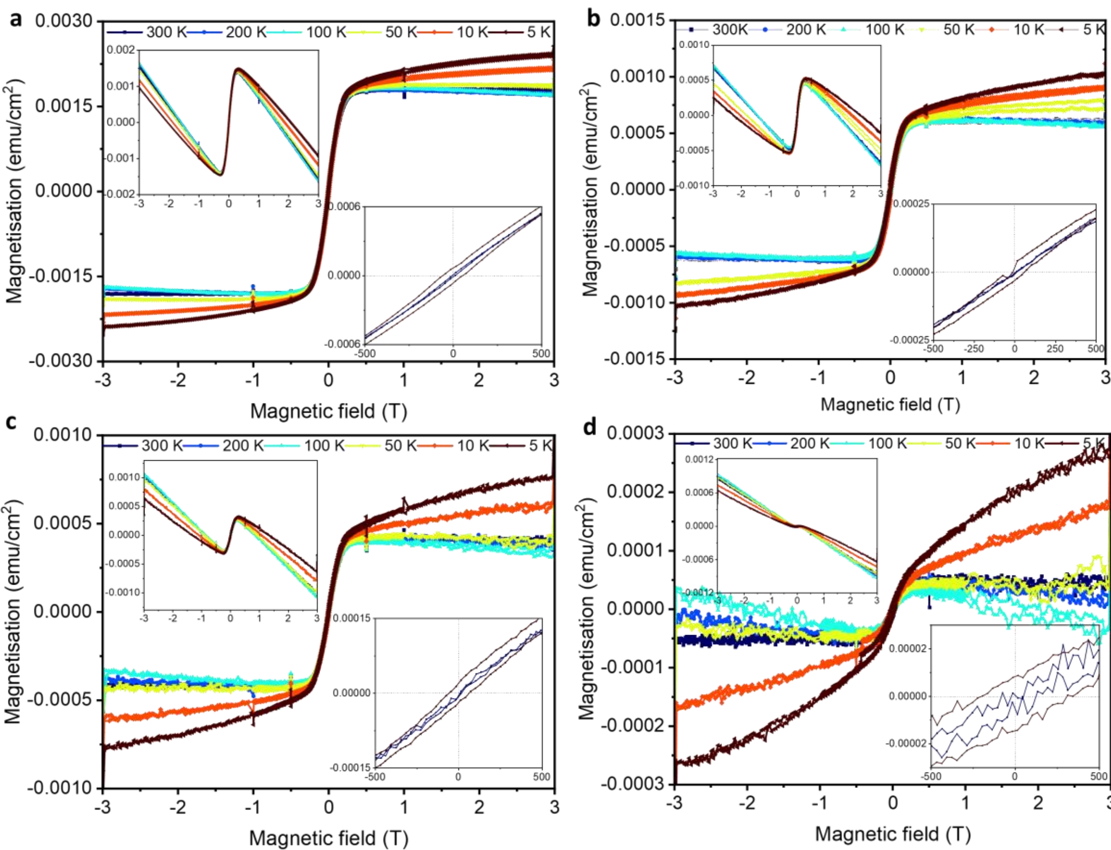

Figure 7.5. Magnetisation versus magnetic field (MH) measurements of the Mn-Sb_2Te_3 samples with Mn fluence of a. 5×10^{16} ions/cm², b. 2×10^{16} ions/cm², c. 1×10^{16} ions/cm², d. 5×10^{15} ions/cm². The inset figures at the top left corners show without background correction and inset figures in the bottom right corners show an enlarged region of hysteresis loop after the diamagnetic correction (only for the temperature of 5, 300K).

There is an observable coercive field for all four samples (Mn fluence of 5×10^{15} - 6×10^{16} ions/cm²). The relationship between the coercive field and the Mn implantation fluence is shown in Figure 7.6 a. The existence of a coercive field demonstrates that Mn-Sb_2Te_3 samples may exhibit weakly ferromagnetic behaviour at low temperatures. Moreover, there is a systematic increase in the magnetisation of Mn-Sb_2Te_3 samples with the

increase in Mn implantation fluence, as shown in Figure 7.6 b.

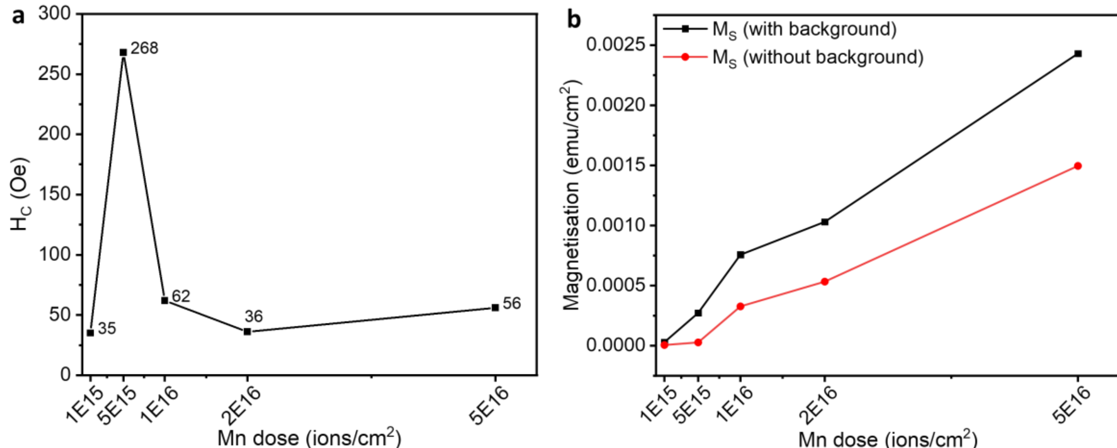

Figure 7.6. a. Coercive field with respect to Mn implantation fluence for Mn-Sb_2Te_3 samples measured at 5 K. b. Saturation magnetisation (with and without diamagnetic background subtraction) with respect to Mn fluence for Mn-Sb_2Te_3 samples measured at 5K.

Figure 7.7 a and b show the magnetisation response with respect to temperature for the Mn-Sb_2Te_3 samples with Mn implantation fluence of 5×10^{16} and 5×10^{15} ions/cm^2, respectively. Underlying crystal diamagnetism is dominating at high fields. With the decrease in temperature, the magnetisation increases for all four samples with Mn fluence at or above 5×10^{15} ions/cm^2. We only showed the magnetisation curve for the highest and lowest Mn implanted Sb_2Te_3, as all four samples show similar magnetisation responses. Field-cooled and zero-field-cooled curves in Figure 7.7 c and d for the Mn-Sb_2Te_3 samples with Mn implantation fluence of 5×10^{16} and 5×10^{15} ions/cm^2 show a transition temperature of around 126 K. (similarly, the remaining two samples with intermediate Mn implantation fluences show similar trend). However, it is worth mentioning that we have observed a very high transition temperature of 126 K compared to previous reports showing ferromagnetism with Tc ≈ 10 K [17, 23, 24]. At or below 100 K, all samples showed a hysteresis loop which is a signature of a ferromagnetic component.

In contrast, there is no hysteresis loop opening for temperatures of 200 or 300 K. Thus, the MH curves in Figure 7.5 might imply superparamagnetism at higher temperatures, while possible existence of ferromagnetism at lower temperatures. The superparamagnetic/paramagnetic behaviour of the Mn-Sb_2Te_3 could indicate the formation of Mn clusters that could play a role. However, ZFC/FC magnetisation curves of Mn-Sb_2Te_3 in Figure 7.7 c and d might indicate there could be a) the Curie temperature, b) the blocking temperature, c) an antiferromagnetic (AF) to paramagnetic (PM)

transition, or d) a spin glass / frustration temperature at T=126 K, which is close to the antiferromagnetic order in MnO nanoparticles [25]. MnSb is soft ferromagnetic material and T_C can be tuned from 293 K to 595 K with the Mn content in Mn_xSb compounds [26]. Hexagonal manganese telluride (MnTe) is antiferromagnetic and has a relatively high Néel temperature (T_N) of 310 K [27]. Due to complex oxidation states of Mn, it is hard to specify the exact origin of magnetism in Mn-Sb_2Te_3, however, the existence of high magnetization at relatively high temperature of 126 – 300 K is promising.

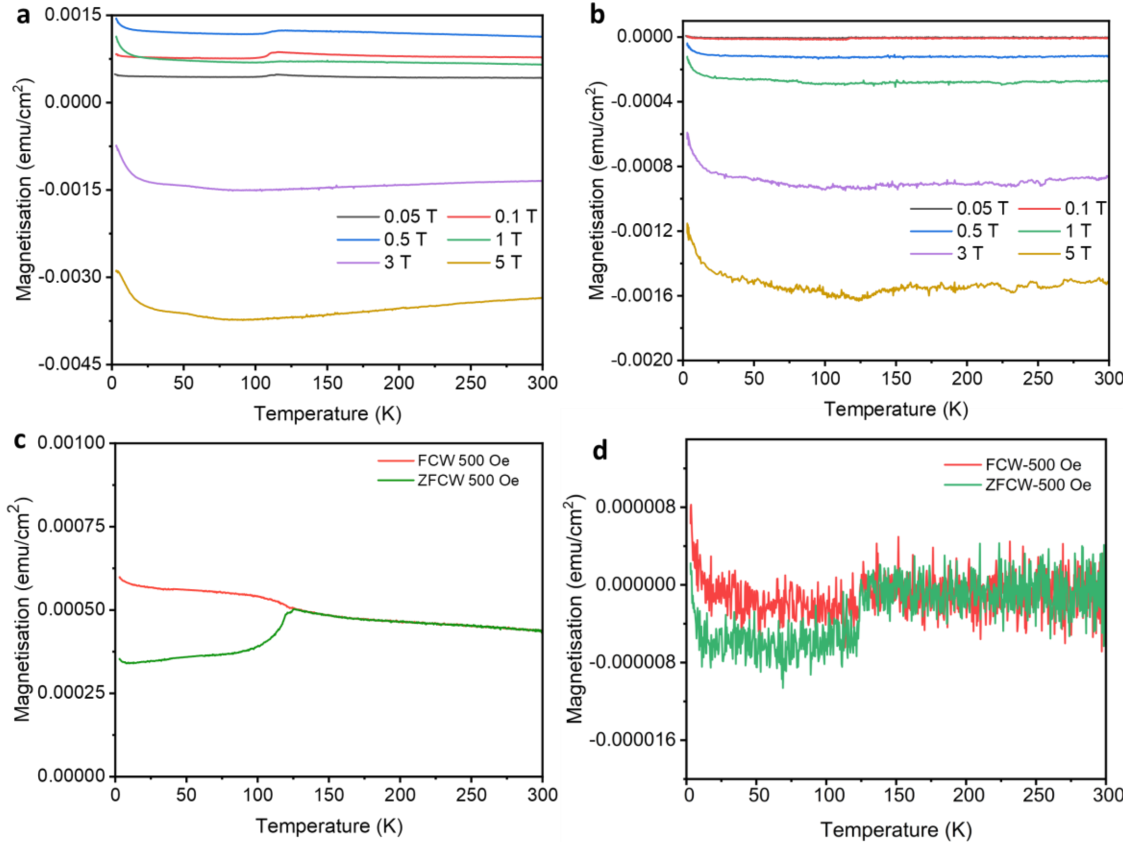

Figure 7.7. Magnetisation versus temperature for a. 5×10^{16} ions/cm^2 Mn-Sb_2Te_3, and b. 5×10^{15} ions/cm^2 Mn-Sb_2Te_3. Corresponding field cooled zero field cooled (FC ZFC) magnetisation curves for c. 5×10^{16} ions/cm^2 Mn-Sb_2Te_3, and d. 5×10^{15} ions/cm^2 Mn-Sb_2Te_3.

7.5 Conclusion

Ion beam implantation is a widely used technique in the semiconductor industry for modifying semiconductor materials' physical and electrical properties. Here, the use of a low-energy ion beam to introduce Mn dopant atoms at the surface of Sb_2Te_3 was explored. It was found that the Mn-doped Sb_2Te_3 system has achieved a form of magnetic order, at least partial, evidence from the strong magnetic response. However, there is also clearly

some disorder associated with the ion-beam irradiation, as the Mn-doped region of Sb_2Te_3 is amorphous. The superparamagnetic/paramagnetic behaviour of the Mn-Sb_2Te_3 indicates the formation of Mn clusters that could play a role. More work is required with post-heat treatment to achieve perfect magnetic order, excluding the effect of disorder. Nevertheless, our work has demonstrated the possibility of engineering surface order and disorder magnetic transitions using the ion-beam implantation technique. The interaction of magnetism and topological states promises a fascinating phenomenon, such as the QAHE. Introducing magnetic order at the surface of TIs through ion-beam patterning seems to be a viable route to fabricating devices and tailor-made heterostructure interfaces.

References

1. Schubert, G., et al., *Fate of topological-insulator surface states under strong disorder.* Physical Review B, 2012. **85**(20): p. 201105.

2. Corbae, P., et al., *Observation of spin-momentum locked surface states in amorphous Bi_2Se_3.* Nature Materials, 2023: p. 1-7.

3. Bake, A., et al., *Top-down patterning of topological surface and edge states using a focused ion beam.* Nature Communications, 2023. **14**(1): p. 1693.

4. Liu, C., et al., *Robust axion insulator and Chern insulator phases in a two-dimensional antiferromagnetic topological insulator.* Nature materials, 2020. **19**(5): p. 522-527.

5. Bernevig, B.A., C. Felser, and H. Beidenkopf, *Progress and prospects in magnetic topological materials.* Nature, 2022. **603**(7899): p. 41-51.

6. Kou, X., et al., *Interplay between different magnetisms in Cr-doped topological insulators.* ACS nano, 2013. **7**(10): p. 9205-9212.

7. Chang, C.-Z., et al., *Experimental observation of the quantum anomalous Hall effect in a magnetic topological insulator.* Science, 2013. **340**(6129): p. 167-170.

8. Chu, R.-L., J. Shi, and S.-Q. Shen, *Surface edge state and half-quantized Hall conductance in topological insulators.* Physical Review B, 2011. **84**(8): p. 085312.

9. Cortie, D., et al., *Creating thin magnetic layers at the surface of Sb_2Te_3 topological insulators using a low-energy chromium ion beam.* Applied Physics Letters, 2020. **116**(19): p. 192410.

10. Checkelsky, J., et al., *Trajectory of the anomalous Hall effect towards the quantized state in a ferromagnetic topological insulator.* Nature Physics, 2014. **10**(10): p. 731-736.

11. Kou, X., et al., *Scale-invariant quantum anomalous Hall effect in magnetic topological insulators beyond the two-dimensional limit.* Physical review letters, 2014. **113**(13): p. 137201.

12. Bestwick, A., et al., *Precise quantization of the anomalous Hall effect near zero magnetic field.* Physical review letters, 2015. **114**(18): p. 187201.

13. Zhang, J.-M., et al., *Stability, electronic, and magnetic properties of the magnetically doped topological insulators Bi 2 Se 3, Bi 2 Te 3, and Sb 2 Te 3.* Physical Review B, 2013. **88**(23): p. 235131.

14. Hor, Y., et al., *Development of ferromagnetism in the doped topological insulator Bi 2− x Mn x Te 3.* Physical Review B, 2010. **81**(19): p. 195203.

15. Wimmer, S., et al., *Mn‐Rich MnSb2Te4: A topological insulator with magnetic gap closing at high curie temperatures of 45–50 K.* Advanced Materials, 2021. **33**(42): p. 2102935.

16. Vergniory, M., et al., *Exchange interaction and its tuning in magnetic binary chalcogenides.* Physical Review B, 2014. **89**(16): p. 165202.

17. Von Bardeleben, H., et al., *Ferromagnetism in Bi 2 Se 3: Mn epitaxial layers.* Physical Review B, 2013. **88**(7): p. 075149.

18. Janíček, P., et al., *Transport, magnetic, optical and thermodynamic properties of Bi2− xMnxSe3 single crystals.* Physica B: Condensed Matter, 2008. **403**(19-20): p. 3553-3558.

19. Wei, Z., et al., *Tuning of Electrical and Magnetic Transport Properties in Bi 2 Se 3 Topological Insulator Crystals Doped with Mn.* Journal of Superconductivity and Novel Magnetism, 2015. **28**: p.

2083-2088.

20. Zhao, W., et al., *Quantum oscillations of robust topological surface states up to 50 K in thick bulk-insulating topological insulator.* 2019. **4**(1): p. 1-6.

21. Wang, M., et al., *Efficiently enhancing electrocatalytic activity of α-MnO2 nanorods/N-doped ketjenblack carbon for oxygen reduction reaction and oxygen evolution reaction using facile regulated hydrothermal treatment.* Catalysts, 2018. **8**(4): p. 138.

22. Bake, A., et al., *Lamellae preparation for atomic-resolution STEM imaging from ion-beam-sensitive topological insulator crystals.* Journal of Vacuum Science & Technology A: Vacuum, Surfaces, and Films, 2022. **40**(3): p. 033203.

23. Zhang, D., et al., *Interplay between ferromagnetism, surface states, and quantum corrections in a magnetically doped topological insulator.* Physical Review B, 2012. **86**(20): p. 205127.

24. Tarasenko, R., et al., *Magnetic and structural properties of Mn-doped Bi2Se3 topological insulators.* Physica B: Condensed Matter, 2016. **481**: p. 262-267.

25. Wang, C., et al., *Antiferromagnetic order in MnO spherical nanoparticles.* Physical Review B, 2011. **83**(21): p. 214418.

26. Liang, D., et al., *Tunable structural and magnetic properties of NiAs-type MnxSb (1.00≤x≤1.30) compounds.* Journal of Alloys and Compounds, 2021. **856**: p. 158184.

27. Kriegner, D., et al., *Magnetic anisotropy in antiferromagnetic hexagonal MnTe.* Physical Review B, 2017. **96**(21): p. 214418.

Chapter 8. Conclusions and outlook

8.1 Summary of main results

The central hypothesis at the beginning of this thesis was that ion beam techniques can be used to engineer different levels of order and disorder at the surface of TIs to control electronic functionality. This led to a key related question: do topological states collapse upon disordering of the TI Sb_2Te_3 single crystal? This thesis has examined the effects of magnetic and non-magnetic disorders, in multiple forms, on the atomic structure and electronic and magnetic properties of the topological insulator Sb_2Te_3 using a combination of focused-ion beam and broad-beam ion beam technology.

In Chapter 3, a few novel device fabrication methods were developed to study the transport properties of single crystal Sb_2Te_3 from the nano-to-micro scale. The work identified two ways of minimising ion beam damage during device fabrication which has been described in detail. Both methods are generally suitable for vdW layer structured material. This will enable studying their transport properties at the nano/micro scale with controlled crystallographic orientations with the help of EBSD. The first method is to use the in-situ fracturing/exfoliation strategy which avoids the direct ion-beam milling of the front and back surfaces of the fabricated device structures. This is useful owing to the ion-beam sensitive nature of Sb_2Te_3 single crystals. The second method is ex-situ exfoliation followed by milling. This achieves a specific geometry with a desired thickness and crystallographic orientation, starting from the flakes of 2D materials. For TIs, maintaining surface crystallinity is critical as interesting transport properties originate from within the top few nanometers of the surface. During device fabrication, the ion-beam-sensitive nature of Sb_2Te_3 necessitates the development of a FIB lamella lift-out method suitable for ion -beam sensitive materials. The results show that the newly developed methods in this thesis allow for fabricating nearly "damage-free" nano/microstructures with a negligible effect of the ion beam on their crystal structure and transport properties.

Chapter 4 discusses the challenges of preparing high-quality TEM specimens from topological insulator materials such as Sb_2Te_3. The results show that topological insulator Sb_2Te_3 surfaces are ion beam sensitive; therefore, it is challenging to use the standard

general method to prepare a thin and damage-free FIB lamellae suitable for high-resolution STEM imaging. This thesis work developed a modified approach to fabricate thin FIB lamellae with minimal ion-beam damage by applying extra protective layers and milling and polishing at reduced energies. The work demonstrated that carefully selecting FIB milling parameters at each stage minimises the damage layer without needing a post-treatment. The FIB lamella preparation technique described in the current study enables the reliable preparation of high-quality TEM/STEM specimens necessary for studying the crystal structure at the atomic resolution level. This method is not only suitable to Sb_2Te_3 but can indeed be applied to a wide range of vdW materials and thin films that are sensitive to ion beams.

In Chapter 5, ion beams were deliberately used to create radiation damage which causes the formation of an amorphous region on the specific irradiated surface of single crystal Sb_2Te_3. The goal, in some sense, was opposite to the earlier chapters, which aimed to avoid ion-beam-induced damage described in the device fabrication. Instead, Chapter 5 built on the findings in the earlier chapters by aiming to systematically explore and harness the effects using carefully controlled irradiation that only modified very specific regions. It showed that by using top-down ion-beam irradiation of Sb_2Te_3 surfaces, it is possible to create various levels of disorder, and this modulates electronic properties. The Monte Carlo SRIM calculations were used for understanding the Ga interactions with Sb_2Te_3. The Sb_2Te_3 crystals were irradiated with a low energy Ga ion beam (8-30 keV), and experimentally characterised using EBSD maps combined with STEM imaging to understand the level of disorder. Then, focused and broad ion beams were used for further exploring the patterning of Sb_2Te_3 surfaces and characterising them with cAFM. These were combined with prototype device transport measurements and some theory calculations which explored the feasibility of using a focused ion beam to pattern topological surface and edge states. The results lay the foundation for the experimental realization in Chapter 6.

The work in Chapter 6 is the main scientific highlight of this thesis. It showed, in detail, that the amorphous, disordered regions formed by the ion beam become non-topological and provided a theory to support this. This demonstrates that it is possible to control the surface electronic properties of a topological insulator Sb_2Te_3 by modifying its surface with an ion beam. For Sb_2Te_3, it was found that the topological properties of the material

can be switched from topological to non-topological by changing the characteristic topological invariant $\mathbb{Z}_2$ from 1 to 0, which corresponds to the destruction of the topological surface states. Our experimental evidence shows that ion beams can be used to create patterns of conducting channels, which are essential for building topological electronic devices. This is a type of lithography, although it can be considered “inverse lithography” because the mask/pattern used is the inverse of the resulting conductivity map. Theoretical calculations support the observation of the transition from topological to non-topological upon introducing disorder at the surface of Sb_2Te_3. The results of this study provide insights into the behaviour of topological insulators and offer prospects for developing new electronic devices based on topological materials. With this recent discovery, it is possible to envision several future devices, as discussed in the section below on “Future Directions”.

Chapter 7 presented recent initial results that magnetic ion beams can also introduce an alternate form of order at the surface of Sb_2Te_3. Sb_2Te_3 crystals implanted with manganese show a certain magnetic order. Cross-sectional TEM showed, that as with Ga implantation, the Mn implantation also led to surface amorphization, however, small regions of crystallinity co-existed with the amorphous regions. This chapter shows the potential option of breaking time-reversal symmetry using the effect of magnetic ions in TIs. It shows the feasibility of introducing magnetism in the desired regions where transport properties of magnetically-patterned Sb_2Te_3 can be explored. As mentioned in the hypothesis of the thesis, this shows another way that an ion beam can be used to engineer order and disorder. In this case, Mn ions introduced a type of magnetic order in Sb_2Te_3. Future work is needed to establish whether this form of order can open a gap in the topological surface states and lead to anomalous Hall effects.

In summary, the results in Chapters 4-6 clearly show that the level of the disorder can be controlled using an ion beam, and the results allow for surface-engineering of device functionality. Moreover, the results of Chapter 7 show that magnetic ion beams can introduce a new form of magnetic order. This confirms the initial hypothesis because the proper selection of ion species and parameters enables the engineering of various levels of order and disorder at the surface of TIs. To be specific, ion beams can be used to engineer both a phase transition from order-to-disorder (crystal to glass), but also from disorder-to-order (magnetism). These are then connected to quantum transitions in the

topological electronic state itself.

8.2 Benefits to the broader research fields of 2D materials and surface electronics

Although this thesis focused on specific issues related to topological insulators, the techniques and knowledge developed in this work may have numerous applications in a broad range of research fields. Examples are given below:

- The device fabrication methods can also feasibly apply to other 2D materials and emerging vdW layer structured materials to study their nano/micro-scale transport properties. Custom designed devices of such vdW materials could help probe enhanced physical properties and discover new fascinating physical phenomena. For example, the FIB device fabrication work is ongoing for studying transport properties of NiFe/$FePS_3$ heterostructures.

- The custom-developed FIB lift-out process for preparing TEM lamellae is suitable for a wide range of ion-beam sensitive crystals and vdW materials and their thin films (and this has already been done in the following materials such as $MnBi_2Te_4$, Bi_2Te_3 etc.). The modified FIB lamella preparation method will enable high-quality TEM/STEM specimen preparation from ion-beam sensitive materials for studying the structure of materials at the atomic scale.

- The novel technique of using an ion-beam for introducing magnetism, or phase transitions, is a promising way for other similar types of quantum materials to explore the possibility of ion-beam lithography. Applications could include superconductors, Weyl semimetals, and Dirac topological semimetals. Our results indicate that it is possible to pattern nano-scale features on a crystal surface at a spatial precision approaching 10-20 nanometers. This is promising for exploring a wide range of materials for ion-beam lithography which is compatible with the modern electronics industry.

- Magnetic patterning of topological insulators could be an exciting way to enable

magnetic control of the electronic properties of such materials by introducing magnetic order in TIs.

8.3 Future directions and unresolved questions:

The work in this thesis opened the pathway to explore several related issues in the future, as outlined below:

- It should be possible to use magnetic ion beam doping for additional device functionalities (e.g., anomalous Hall effect), but this is a work in progress.

- The FIB device fabrication scheme could be optimised further by combining in-situ and ex-situ processes and fabricating electrical contacts via the lithography process. This would further reduce unintended ion-beam exposure of crystal surfaces.

- It is interesting to explore the ion-beam interaction with other topological materials to identify whether the ion-beam amorphisation process universally switches the topological invariant $\mathbb{Z}_2$ from 1 to 0.

- Better theoretical models of amorphous and TI states will be needed to build a more robust connection between theory and experiment.

The work also highlighted a major, unresolved fundamental question: Do amorphous topological insulators exist in real solids? The research indicates that, while these materials may certainly exist in theory, as explored in various disordered systems, it is unclear where one would find them in nature because the necessary conditions are extremely rare. The field of topological insulators has primarily focused on well-defined crystalline materials. There is a need to develop better models to explore whether disorder or amorphous structures might preserve topological properties in certain materials. Given the fundamental importance, the quest to find such a true amorphous topological insulator will continue.